Department of Chemistry
University College London

A Computational Study of the Structure and Properties of Titanates and Carbon Nitride

A thesis submitted for the degree of Doctor of Philosophy

by

Mohamed Kamal Hassan Ali Matar

July 2011

Declaration

I, Mohamed Matar, confirm that the work presented in this Ph.D. thesis is my own. Where information has been derived from other sources, I confirm that this has been indicated.

Abstract

This thesis presents results of a computational investigation focusing on two classes of materials:

- Those of interest as anodes in rechargeable Li ion batteries, particularly TiO_2 polymorphs and a novel Ti oxysulfide; and
- A graphitic carbon nitride, where the high pressure structural and electronic transformations, and intercalation properties are studied.

The first part of the work considers the Li intercalation in TiO_2 Brookite. Calculations identify stable sites and low energy configurations during the intercalation process up to full occupancy. It is demonstrated that Li intercalation is homogeneous but consists of three domains corresponding to different ordering patterns. It is shown that Li intercalation is strongly limited by the diffusion of Li ions, especially at high Li content, resulting in the absence of intercalation at normal conditions, and intercalation to high concentrations at elevated temperature or in the nanophase.

Later, Li intercalation in the TiO_2-B structure is investigated and the most favourable energy sites for Li ions in the structure have been identified including the energy favourable migration pathways. These have been studied by calculating the diffusion barriers in all possible directions within the substrate material.

Calculations indicate that the TiO_2-B structure has a lower density than other titanates, and the calculated cell voltage is in the range of 0.8 to 1.45 V for low Li content, with the z direction showing the highest mobility for Li ions; the TiO_2-B structure therefore yields a high Li mobility.

Calculations show that brookite is suitable to host Li ions, and yields relatively constant voltage values which are suitable for use in actual Li batteries (Brookite anode value

calculated as 1.7 V); TiO_2-B generates a voltage value which is lower than the brookite voltage which means it is a promising anode in rechargeable Li batteries.

In the second part of the thesis a graphitic carbon nitride of composition $C_6N_9H_3$.HCl is studied.

In the first part of the work, the interlayer bonding mechanism that takes place between consecutive layers at high pressure is analysed. Calculations performed also allowed identification of symmetrical hydrogen bonding, a feature which is rarely observed, and the formation of carbon-chlorine bonds (both observations at elevated pressures).

In the next stage of the study on Carbon Nitride, intercalation behaviour within the graphitic structure is examined (hence connecting this part of the work to the work performed on the TiO_2 substrates). Results indicate that the ability of the examined carbon nitride to act as an anode for rechargeable Li batteries is low because the intercalation energy is not constant as a function of the Li content, in addition to strong structural deformations occurring during intercalation. The combination of factors affecting the cyclabilty of intercalation/deintercalation is expected to make the substrate a poor rechargeable battery.

The final section of this thesis is dedicated to the study of the Li intercalation properties of a layered oxysulfide structure of composition $Y_4Ti_4O_{10}S_4$. Calculations indicate that the material appears to be unsuitable for use as an electrode for Li ion rechargeable batteries due to unsuitable Li intercalation energies, and large structural changes occurring within the substrate during the cycling process.

Table of Contents

DECLARATION **2**

ABSTRACT **3**

TABLE OF CONTENTS **5**

LIST OF FIGURES **9**

LIST OF TABLES **16**

ACKNOWLEDGEMENTS **18**

LIST OF PUBLICATIONS **19**

CHAPTER 1 ..... **20**

AN OVERVIEW OF THE THESIS **20**

CHAPTER 2 ..... **23**

BATTERIES **23**

2.1 Introduction **23**

2.2 Fundamentals of Batteries **23**

2.3 Battery types **25**

2.4 Rechargeable batteries **27**

2.5 Li-ion batteries **27**

CHAPTER 3 ..... **32**

COMPUTATIONAL METHODOLOGY **32**

3.1 Introduction **32**

3.2 Classical Methods **32**

3.3 Quantum Mechanical Methods 33
3.3.1 The Born-Oppenheimer approximation 34

3.4 Hartree Fock Theory 36

3.5 Density Functional Theory 36

3.6 Functionals 39
3.6.1 Local Density Approximation 39
3.6.2 Generalized Gradient Approximation (GGA) 40
3.6.3 Hybrid Functionals 41

3.7 Crystalline Solids 41

3.8 Periodic Boundary Conditions (PBC) 41

3.9 Bloch's Theorem 42

3.10 Basis Sets 43
3.10.1 Gaussian Type Orbitals 43
3.10.2 Plane Waves 44

3.11 Pseudopotentials 46

3.12 Computer Codes Employed 46
3.12.1 CASTEP 46

CHAPTER 4 48

Li INTERCALATION INTO TiO_2 POLYMORPHS 48

4.1 Introduction 48

4.2 Li Intercalation into Brookite 51
4.2.1 Introduction 51
4.2.2 Details of Calculations 53
4.2.3 Structure of Brookite 54
4.2.4 Li-insertion sites and structural relaxation 56
4.2.5 Ordering of the Li-ions 60
4.2.6 Diffusion of Li-ions 70
4.2.7 Summary 74

4.3 Li Intercalation into TiO_2-B 75
4.3.1 Introduction 75
4.3.2 Structural details of the TiO_2-B polymorph 76
4.3.3 Li-insertion sites 77
4.3.4 Lithium diffusion 80
4.3.5 Further Li intercalation 84
4.3.6 Summary and outlook 85

CHAPTER 5 86

THE HIGH PRESSURE BEHAVIOUR AND INTERCALATION PROPERTIES OF CARBON NITRIDES 86

5.1 High Pressure Behaviour of layered Carbon Nitride 87
5.1.1 Introduction. 87
5.1.2 Computational Details 90
5.1.3 Results and discussion 91

5.2 Li Intercalation into Carbon Nitride 115
5.2.1 Introduction 115
5.2.2 Structure 117
5.2.3 Computational Details 118
5.2.4 Results and Discussion 119
5.2.4.1 First Li intercalation 119
5.2.4.2 Further Li intercalation up to 12 128
5.2.5 Conclusion 138

5.3 Ion exchange properties of the layered Carbon Nitride 139
5.3.1 Introduction 139
5.3.2 Computational details 140
5.3.3 Trivalent cations 140
5.3.4 Divalent cations 147
5.3.5 Monovalent Cations 150
5.3.6 Conclusion 152

CHAPTER 6 153

Li INTERCALATION INTO A RUDDLESDEN–POPPER STRUCTURED OXYSULFIDE OF COMPOSITION $Y_4Ti_4O_{10}S_4$ 153

6.1 Introduction 153

6.2 Details of the Calculations 155

6.3 $Y_4Ti_4O_{10}S_4$ Structure 156

6.4 Results and discussion 159
6.4.1 $Y_4Ti_4O_{10}S_4$ structure 159
6.4.2 $LiY_4Ti_4O_{10}S_4$ 161
6.4.3 $Li_2Y_4Ti_4O_{10}S_4$ 165
6.4.4 $Li_3Y_4Ti_4O_{10}S_4$ 167
6.4.5 $Li_4Y_4Ti_4O_{10}S_4$ 171

6.5 Li intercalation energy and structural changes 172

6.6 Conclusions 179

CHAPTER 7 180

CONCLUSIONS AND PERSPECTIVES FOR FUTURE WORK 180

REFERENCES 185

List of Figures

Figure 2.1 Schematic diagram of a galvanic Daniel cell, one type of electrochemical cell or battery. 24

Figure 2.2 Charge –discharge operation of Li-ion cells[5]. 28

Figure 4. 1 The most stable polymorphs of TiO_2: (a) Anatase, (b) Rutile and, (c) Brookite 50

Figure 4.2 Ex situ XRD patterns of brookite TiO_2 at various lithium contents during initial cycle: (a) pristine brookite TiO_2, (b) $Li_{0.5}TiO_2$, (c) $Li_{0.9}TiO_2$, and (d) $Li_{0.3}TiO_2$ (after charge to 3 V). The * indicates the peak due to Mylar film. Reported from reference [55]. 52

Figure 4.3 Voltage vs Lithium composition for brookite TiO_2, for the first ten charge/discharge cycles carried out in the voltage range 1.0-3.0 V. Reported from reference[55]. 53

Figure 4.4 The structure of fully occupied brookite ($Li_{16}Ti_{16}O_{32}$) in polyhedral representation. Li in purple and oxygen in red. 55

Figure 4.5 Edge sharing motif in brookite. The Ti-ion is shown in black, O ions are shown in white. Equatorial O ions are denoted Oe, apical O-ions are denoted as Oa. 55

Figure 4.6 A Li insertion site in brookite. Here and in the following diagrams, O-ions are shown in red, Ti-ions in gray, Li ions in purple. The arrows indicate the structural relaxation upon intercalation.....57

Figure 4.7 Displacements of O-ions around the inserted Li-ion. Equatorial O-ions are denoted Oe, apical O-ions are denoted as Oa. 57

Figure 4.8 Displacement of the Ti-ions upon insertion of a Li-ion in brookite. Displacements of Ti-ions are indicated by arrows.....58

Figure 4.9 Insertion sites for further Li-intercalation at x=0.0625. Full red circles identify the most favourable sites; empty red circles show moderately favourable sites; full blue circles the most unfavourable sites, and empty blue circles moderately unfavourable sites. 59

Figure 4.10 Relaxed brookite structure of $LiTi_{16}O_{32}$ showing the 1st Li and the two most favourable sites A, B for the insertion of a 2nd Li ion. Site A corresponds to the 2nd Li in a neighbouring channel, B in the same channel as the 1st Li ion. 61

Figure 4.11 Estimate of relative stability for further Li intercalation at increasing concentrations (x=0.0625, 0.125, 0.3125) and considering A) the distances between O-ions. B) The distance between Ti-ions along the a-direction C) the distance between Ti-ions along the b-direction. 62

Figure 4.12 Lowest energy configurations of $Li_nTi_{16}O_{32}$ at n=2, 6, 8, 11, 13 and 14.....64

Figure 4.13 Volume change of a unit cell of $Li_nTi_{16}O_{32}$ as a function of Li concentration during intercalation. 65

Figure 4.14 Li intercalation energy in $Li_nTi_{16}O_{32}$ as a function of Li concentration.....66

Figure 4.15 Average intercalation energy as a function of nLi. 67

Figure 4. 16 Cell parameters a, b, c in Å of brookite during the Li intercalation.....68

Figure 4.17 Representation of the equilibrium cell angles during the intercalation process 69

Figure 4.18a. Migration pathway of Li between two favourable energy sites for x=0.0625 ($LiTi_{16}O_{32}$) b. Energy–position diagram; showing the presence of a local maximum which indicates that Li migration is an activated process, whose activation energy can be estimated by this energy diagram. 70

Figure 4.19 a) pathway between two favourable energy sites (A-X) for $Li_2Ti_{16}O_{32}$; b) corresponding energy profile 71

Figure 4.20 Li migration profile in brookite at n= 5 ($Li_5Ti_{16}O_{32}$). 72

Figure 4.21 Li migration profile at n= 15 ($Li_{15}Ti_{16}O_{32}$).....73

Figure 4.22 Energy – Distance profile for Li migration at concentrations n=1, 2, 5 and 15.....74

Figure 4.23 The structure of TiO_2-B in polyhedral representation.....76

Figure 4.24 1x2x1 Supercell of TiO_2-B employed in our calculations.....77

Figure 4.25 Available Li intercalation sites in a 1x1x2 supercell of TiO_2-B 79

Figure 4.26 Interstices of the TiO_2-B structure.....79

Figure 4.27 Li-ion (purple) in B site and possible diffusion patterns directions along *x*, *y* and *z*. Pink circles show the A and C sites, red is oxygen and grey is Ti. 81

Figure 4.28 a) Migration along *z* between two B sites. b) Calculated energy profile for this Li migration pathway. 82

Figure 4.29 a) Li migration pathway along *x* between two B sites, through the path BAAB b) calculated energy profile 82

Figure 4.30 a) Li migration pathway between two B sites along the *y* direction. b) calculated energy profile.....83

Figure 4.31 Relative intercalation energy in $Li_nTi_{16}O_{32}$ as a function of Li concentration 84

Figure 4.32 Relative intercalation energy of TiO_2-B and Brookite. 85

Figure 5.1 ILB0 phase a) Single layer b) Unit cell of $C_6N_9H_3$.HCl c) Stacking of layers in the z directions, highlighting the overlap of some triazine rings in adjacent layers.89

Figure 5.2 Unit cell parameters of the *g*-$C_6N_9H_3$·HCl structure as a function of increasing pressure. 92

Figure 5.3 ΔEnthalpy (eV) and unit cell volume ($Å^3$) as a function of applied pressure (GPa). 93

Figure 5.4 Cell parameters of *g*-$C_6N_9H_3$.HCl *a, b* and *c* as a function of applied pressure during compression. 94

Figure 5.5 Relative enthalpy of ILB0 and ILB1 phases as a function of applied pressure. 94

Figure 5.6 ILB1 structure at 70 GPa 96

Figure 5.7 One of the interlayer bonding pillars first formed at 70 GPa showing the labels of the atoms involved 103

Figure 5. 8 Equilibrium structure of the ILB1 phase at 90 GPa. 106

Figure 5.9 Equilibrium structure of the ILB1 phase obtained during pressure relief at 50 GPa, showing that only one of the nearly symmetric (N-H-N) H bonds is retained at this pressure. 106

Figure 5.10 Equilibrium structure of the ILB1 phase obtained during pressure relief at 0 GPa, where both N-H-N bonds have asymmetric nature. 107

Figure 5.11 Calculated band structures of ILB0 at 0GPa and ILB1 phases of $C_6N_9H_3$.HCl at 90, 50 , 0 GPa. The dashed line denotes the Fermi level. 112

Figure 5.12 Density of states of the ILB0 phase of the g-$C_6N_9H_3$.HCl structure at ambient pressure 113

Figure 5.13 Calculated band gap vs Pressure. 114

Figure 5.14 a). A single layer of the $C_6N_9H_3$ structure shows the large voids. B). Each unit cell contains two atomically flat layers of the Carbon Nitride solid. 117

Figure 5.15 Stable Li intercalation sites in g-$C_6N_9H_3$ 120

Figure 5.16 Environment of Li ion in the triangular cavities of the g-$C_6N_9H_3$ (A, B, C) 122

Figure 5.17 Dihedral angles employed to measure the extent of deformation in g-$C_6N_9H_3$ upon Li ion insertion.....125

Figure 5.18 Comparison of calculated band structures for g-$C_6N_9H_3$, and $LiC_{12}N_{18}H_6$ with 1 Li in site A 126

Figure 5.19 Density of states of the g-$C_6N_9H_3$ and $LiC_{12}N_{18}H_6$ structures, comparing sites A, B and C.....127

Figure 5.20 Stable Li configurations in the $Li_nC_{12}N_{18}H_6$ cell, for each value of n examined.....129

Figure 5.21 Lattice parameters change during Li intercalation as the number of Li ions inserted into the unit cell increases.....131

Figure 5.22 Fragment indicating the interlayer C-C bond between 2 triazine rings at Li =5 132

Figure 5.23 Dihedral angles (ABCD), (EFGH), as a function of the number of Li ions inserted into one carbon nitride unit cell.....133

Figure 5.24 Li intercalation energy as the number of Li ions inserted into the unit cell increases.....137

Figure 5.25 Relative intercalation energy of Brookite, TiO_2-B, g-$C_6N_9H_3$. 138

Figure 5.26 Simplest form of Porphyrins and an example of porphyrin (Heme).....139

Figure 5.27 $Al_2C_{12}N_{18}$ structure: a). perpendicular view (yellow represents the lower layer) b). side view, Al (pink), C (gray), N (blue).....142

Figure 5.28 Structure of $Ga_2C_{12}N_{18}$: a). Perpendicular (yellow atoms represent the lower layer) and b). Side view. Ga (brown), C (gray), N (blue).....144

Figure 5.29 Structure of $In_2C_{12}N_{18}$: a). perpendicular (yellow represent the lower layer) and b). side view. In (brown), C (gray), N (blue). 146

Figure 5.30 Equilibrium structure of $Ba_2C_{12}N_{18}H_2$: a). perpendicular (yellow atoms represent the lower layer), and b). Side view. Ba (green), C (gray), N (blue).....148

Figure 5.31 Equilibrium structure of $Cd_2C_{12}N_{18}H_2$; a). perpendicular (yellow atoms represent the lower layer), and b). side view. Cd (brown), C (gray), N (blue).....149

Figure 5.32 Structure of $Li_6C_{12}N_{18}$ a). perpendicular b). side view. Li (pink), C (gray), N (blue). 151

Figure 6.1 Ruddlesden-Popper structures AX $(ABX_3)_n$, corresponding to n=1, 2 and 3. *A* type ions are shown in green, *B*X_6 octahedra are shaded in red. 154

Figure 6.2 Crystallographic unit cell of the $Y_4Ti_4O_{10}S_4$ structure: Y (green), Ti (gray), S (yellow), and O (red).....156

Figure 6.3 Fragment of the $Y_4Ti_4O_{10}S_4$ structure showing the apical (Oa) and equatorial (Oe) oxygen ions. 157

Figure 6.4 2x2x2 supercell of $Li_4Y_4Ti_4O_{10}S_4$ indicating the rock salt layers, perovskite layers and Li ion sites (purple).....159

Figure 6.5 Band structure of $Y_4Ti_4O_{10}S_4$ 161

Figure 6.6 $LiY_4Ti_4O_{10}S_4$ structure with Li in site A, and details of the 4 coordinated window hosting the intercalated Li. 162

Figure 6.7 Band structure of $LiY_4Ti_4O_{10}S_4$. 165

Figure 6.8 Three possible configuration of Li concentration n=1. 166

Figure 6.9 $Li_3Y_4Ti_4O_{10}S_4$ structure. 168

Figure 6.10 Density of state of the $Li_nY_4Ti_4O_{10}S_4$ structure for increasing Li content (n=0-4) 170

Figure 6.11 $Li_4Y_4Ti_4O_{10}S_4$ structure.....171

Figure 6.12 Relative intercalation energy as a function of Li concentration (n). 173

Figure 6.13 The unit cell parameters of $Li_xY_4Ti_4O_{10}S_4$ structure 174

Figure 6.14 Unit cell volume as a function of Li concentration (n). 175

Figure 6.15 The Ti-Oe bond lengths as a function of Li concentration (n). 176

Figure 6.16 Ti-Oe and Ti-S bond lengths of as a function of Li concentration (n).....177

Figure 6.17 Oa-Ti-Oe angles as a function of Li concentration (n).....177

Figure 6.18 Trans Oe-Ti-Oe angles as a function of Li concentration (n). 178

Figure 6.19 Li-O distance and Y-S bond lengths as a function of Li concentration (n).178

List of Tables

Table 5.1 Analysis of bond lengths in compression and decompression calculations; the symbol * identifies nonbonding distances. Here and in the following tables, bold numbers correspond to the ILB1 phase. 98

Table 5.2 Net ionic charges in |e|, calculated using a Mulliken population analysis as a function of pressure in compression and decompression studies of $C_6N_9H_3$.HCl..101

Table 5.3 Mulliken population charge analysis during a compression-decompression loop of the C and N atoms forming one of the pillars of the ILB1 structure.....104

Table 5.4 C-N bond distances for the atoms of the pillar; the symbol (*) denotes nonbonding distances.....105

Table 5.5 Γ-Point phonons for the ILB1 phase at 90 GPa. The values highlighted correspond to symmetric H-bond stretching modes (2000-2200 cm^{-1}) and C-Cl stretching modes (965 and 1015 cm^{-1}).....108

Table 5.6 Γ-Point phonons for the ILB1 phase at 70 GPa. The values highlighted correspond to symmetric H-bond stretching modes (2000-2700 cm^{-1}) and C-Cl stretching modes (833 and 923 cm^{-1}).....109

Table 5. 7 Γ-Point phonons for the ILB1 phase at 50 GPa. The values highlighted correspond to symmetric H-bond stretching modes (2200-2700 cm^{-1}) and C-Cl stretching modes (797 and 943 cm^{-1}).....110

Table 5.8 Li fractional coordinates, cell parameters, and the intercalation energy for the unit cell of g-$C_6N_9H_3$ with 1 Li atom.....119

Table 5.9 Variation of unit cell angles and internal dihedral angles (degrees) (using the labelling of atoms of Figure 5.17) upon Li insertion.....124

Table 5.10 Relative intercalation energy, unit cell parameters and unit cell volume for subsequent Li intercalation process.....130

Table 5.11 Mulliken population charge for the Li ions in $Li_nC_{12}N_{18}H_6$ 135

Table 5.12 Mulliken population analysis for H, C, N atoms in the $Li_nC_{12}N_{18}H_6$ structure. 136

Table 6.1 Ti-X equilibrium bond distances as a function of Li concentration. 158

Table 6.2 Mulliken charge analysis of the $Y_4Ti_4O_{10}S_4$ structure. Labels A and B indicate the block of the structure (layer A or B in Figure 6.2.) where the ions are located; indices (e) and (a) refer to equatorial and apical oxygen ions. 160

Table 6.3 Lattice parameters as a function of Li concentration (n). 163

Table 6.4 Mulliken population charge analysis of the $LiY_4Ti_4O_{10}S_4$ structure. 164

Table 6.5 Mulliken population charge analysis of the $Li_2Y_4Ti_4O_{10}S_4$ structure. 167

Table 6.6 Mulliken population analysis of the $Li_3Y_4Ti_4O_{10}S_4$ structure 169

Table 6.7 Mulliken population charge analysis of the $Li_4Y_4Ti_4O_{10}S_4$ structure. 172

Acknowledgements

I would like to first thank my wife for her unconditional support and encouragement during all the stressful times that have passed during these years. We have been through a lot and without you I would not have been able to do this for our daughter; I dedicate this to you, my parents and to the rest of my family who always believed in me.

This research project started under the supervision of Dr. Marina Koudriachova whom I owe gratitude to and under whose guidance I began to examine Ti-O_2-based solids before continuing with Dr. Furio Corà.

Whilst there are many people I owe gratitude to on the academic front, foremost of them is my supervisor Dr. Furio Corà. Without your hard work, patience and generosity with your time this would not have been completed and I am truly grateful for your support both academic and otherwise.

I would also like to thank Professor Richard Catlow, Dr Claire Carmalt, Dr Scott Woodley, Dr Alexey Sokol for their support during the years, particularly when times were very difficult.

I would also like to thank Dr. Malek Deifallah for his unwavering friendship, loyalty and support.

Finally, I would like to acknowledge all my friends at the laboratory for making this such a great place to work.

List of Publications

- Marina V. Koudriachova, Mohamed Matar; Mechanism of Lithium Intercalation in TiO_2-brookite ECS Trans. 16, 63 (2009)
- Li intercalation in layered carbon nitrides, in preparation
- Cation exchange properties of carbon nitride materials, in preparation

Chapter 1

An Overview of the Thesis

This thesis presents the work performed during my PhD which is of a computational nature and is focused on two types of materials:

- Materials that could be used as anodes for rechargeable Li batteries such as Brookite, TiO_2-B, and Ti oxysulphides; and
- Carbon nitride materials that may be of potential interest in catalysis, sorption, microelectronics, batteries and as superhard materials.

The content of the thesis is organised as follows.

Chapter 2 begins by giving an introduction to the importance of energy sources and the developing awareness of the limitation of current fuel resources and their environmental impact. This leads on to a discussion on the necessity for finding new sources of clean, safe and environmentally friendly energy which are one of the key application areas discussed in the thesis and an introduction to rechargeable batteries which we discuss the properties/requirements for rechargeable batteries and in particular focus on Li- ion batteries.

Chapter 3 discusses the methods used to perform the computational research. Computational studies have proved to be an extremely helpful tool by providing in-depth detail of experimental observations at the atomic-level and allow us to make informed predictions on processes and materials; such methodology is therefore complementary to experimental work as is described later for rechargeable Li-ion batteries and carbon nitrides.

Chapter 4 presents research results concerning the Brookite and TiO_2–B structures. Brookite has an orthorhombic structure with *Pbca* symmetry. The structure represents a three dimensional network of TiO_6 octahedra sharing three edges each, with empty zigzag shaped channels along the *c*-direction which are potentially available for Li-intercalation. The analysis of the connectivity of the TiO_6 octahedra has been demonstrated to play an important role in understanding the mechanism of Li intercalation into titanates.

At room temperature, Li-uptake by polycrystalline brookite is negligible while the intercalation behaviour at elevated temperatures has not been investigated. In the nanophase, the reactivity of brookite towards Li increases with a decrease of the particle size. Recently, it has been shown that nanosized particles of brookite can intercalate Li-ions to high Li-concentrations (Li:Ti ratio of 0.9). The mechanism of Li-intercalation into brookite was studied and explained in the computational work.

The TiO_2-B structure contains edge-sharing TiO_2 octahedra and has a monoclinic structure with space group *C*2/*m*. The most favourable energy sites for Li intercalation have been investigated in addition to the identification of possible Li migration pathways by calculation of diffusion barriers in all possible directions within the structure.

Chapter 5 introduces a new set of materials studied in this thesis: Carbon Nitrides. Early theoretical predictions stated that a dense C_3N_4 phase, isostructural with the β-Si_3N_4 structure, may be less compressible than diamond, the hardest known material.

Experimentally, the synthesis of high density low compressibility C_3N_4 structures has not been possible and experimental research has generally been hampered by a lack of high pressure equipment. Now that such equipment has become more readily available, i.e. the diamond anvil cell, experimental research has accelerated. In line with such experimental work, theory is required to explain the high pressure transformation mechanisms of known carbon nitride precursors.

The thesis examines the compression of a layered Carbon Nitride of composition $C_6N_9H_3 \cdot xHCl$ from a structural and electronic perspective. Also examined are the effects that adatoms have on the material.

The work continues and extends previous theoretical work by examining the high pressure pathways adopted by the structure when compressed. The work performed found that at high pressure, interlayer bonds form between constituent layers. The results are compared with high pressure experiments and the thesis discusses the appearance of symmetrical hydrogen bonding and carbon- chlorine bonds under pressure.

The thesis later moves to examine the ability of the Carbon Nitride material to intercalate Li and hence examines its ability to act as electrode for rechargeable Li-ion batteries. In the final part of the study on Carbon Nitrides, some or all the acid protons of the structure are substituted with transition metal cations to examine any potential adsorption/catalytic properties of these structures.

The final Chapter of this thesis, Chapter 6, examines the Li intercalation mechanism in an oxysulfide structure of composition $Y_2Ti_2O_5S_2$, which is a Ruddlesden-Popper phase.

Again, the goal is to employ modelling in a predictive way to extend the investigation of Li intercalation in a host related to, but chemically distinct from, currently researched materials.

Chapter 2

Batteries

2.1 Introduction

Energy sources are essential in the 21st century; ever since the industrial revolution, the world demand for energy has been met by burning fossil fuels. However, there is now an increasing awareness that fossil fuel resources are in limited supply, and linked to long-lasting environmental damage. During the last years the oil price has raised dramatically, causing serious worries about our future energy supply. The petroleum crisis is an issue that will persist in the foreseeable future, because of the rate at which the world energy consumption grows. The need for clean, safe, and environmentally friendly sources of energy is increasing. Electricity generated from renewable sources, such as solar or wind energy, offers new possibilities. However, the use of electricity generated from intermittent, renewable sources requires efficient electrical energy storage. Electricity must be reliably available 24 hours a day. Thus, for large scale solar or wind-based electricity generation to be effective, the development of new energy storage systems will be critical to meeting continuous energy demands. Greatly improved electric energy storage systems are needed to progress from today's demands. Improvements in energy storage, reliability and safety are also needed to prevent premature, and sometimes catastrophic, device failure. Batteries are the leading energy storage technologies today. They are based on electrochemistry: batteries store energy in chemical reactants capable of releasing a flow of charge when required.

2.2 Fundamentals of Batteries

Batteries are devices used to convert chemical energy directly to electrical energy and vice versa. The simplest form of battery consists of a number of voltaic cells formed of two half cells connected in series by an electrolyte[1].

Chemical energy is converted to electrical energy through a chemical redox reaction. This chemical reaction is divided into two parts: the first is a reduction reaction, taking place at the positive electrode or cathode. The second half cell consists of an oxidation reaction taking place at the negative electrode or anode. The two half cells, anode and cathode, are connected by an electrolyte contained in a bridge. Each half cell has its own electromotive force, and the total electromotive force for the battery is the net difference between the potentials of the two half cells. The electrical driving force of the cell is measured in Volts and it is called the Open Circuit Voltage (OCV). The OCV (E) is related to the free energy of the overall chemical reaction (ΔG) taking place in the cell by the Nernst equation

$$\Delta G = - nF\,E \qquad (2.1)$$

Where F is Faraday's constant (charge of 1 mole of electrons), and n is the number of electrons exchanged in the redox process.

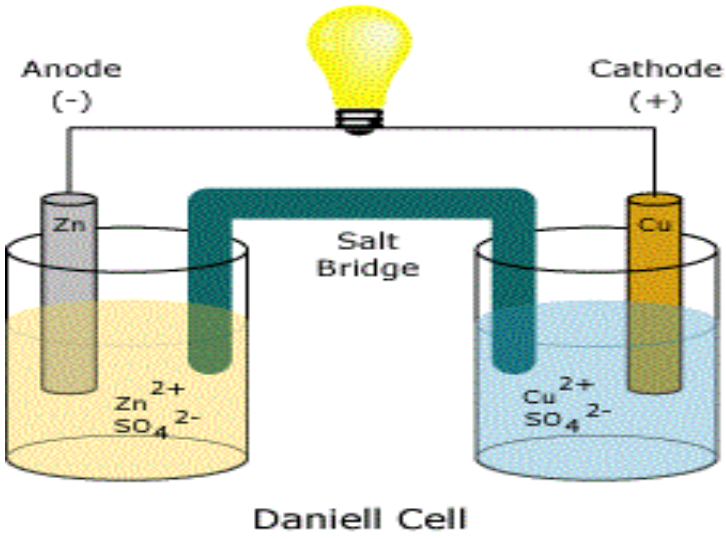

Figure 2.1 Schematic diagram of a galvanic Daniel cell, one type of electrochemical cell or battery[2].

The performance of the battery is characterized by the load cycle, charge cycle and life time, which depend on many factors including internal chemistry, current drain and temperature.

2.3 Battery types

Batteries are divided into two main groups, commonly referred to as primary, or disposable and secondary, or rechargeable.

Primary, or disposable, batteries are based on the transformation of the chemical energy of an initial set of reagents into electrical energy. The initial reactants are progressively exhausted, and the battery can't be restored once used. Disposable batteries can generate electrical current immediately after assembling; they are intended to be used once and discarded. These batteries have historic importance, as they represent the first generation of devices produced. The Daniel cell, schematically shown in Figure 2.1 is an example of disposable battery. Nowadays, the use of disposable batteries is greatly reduced and remains for devices where other electric power is at least intermittently available. Disposable primary cells cannot be recharged, since the chemical reactions employed are not easily reversible, and active materials may not return to their original forms. Examples of disposable batteries include zinc-cadmium and alkaline batteries. Generally, these have higher energy densities than rechargeable batteries but a high lifetime cost, and are associated with considerable environmental concern due to the use of toxic heavy metals.

Secondary batteries are instead rechargeable, because the chemical reactions employed to generate current are reversible. Recharging is accomplished by applying an external electrical energy to the cell which is led to restoring its original reactant composition. This type of battery must be charged before use; they are usually assembled with active materials in the discharged state. Rechargeable batteries can be recharged by applying electrical current, which reverses the chemical reactions that occur during its use. Chargers or rechargers are devices used to supply appropriate current to charge the

batteries. An example of rechargeable battery is the lead-acid battery used as car battery. Some portable rechargeable batteries include several "dry cell" types, which are sealed units and are therefore useful in appliances such as mobile phones and laptop computers. Examples of these kinds of battery are nickel-cadmium (NiCd), nickel-zinc (NiZn), nickel metal hydride (NiMH) and lithium-ion (Li-ion).

Batteries can be further classified with reference to the chemical reaction exploited and the design of the cell. In particular, we can divide batteries according to the type of electrolyte they employ.

Wet cell or flooded cell: These employ a liquid electrolyte which surrounds all the internal parts. Some wet cells can be classified as primary batteries, others as secondary. Wet cells are used in applications such as car batteries and as industry standby power for switchgears and telecommunications.

Dry cell: These do not contain liquids, but have a paste as electrolyte. The paste needs moisture for conduction. Dry cells have advantages, related to no leaking liquids and ease of handling. A common example for the dry cell is the zinc-carbon battery.

Molten Salt cells: These batteries use a molten salt as electrolyte; they have high energy and power density, useful properties for electric vehicles, but are more expensive to operate[3].

2.4 Rechargeable batteries

Whilst the need for rechargeable batteries is clear from an energy, environmental, and economic perspective, there are only a few types that are readily available and used industrially. This section looks at the main types available:

Lead Acid: One of the most used types of rechargeable batteries in the market. The battery relies on a solution-precipitation mechanism (PbO_2-Pb) but requires the presence of a large amount of sulphuric acid and water for the reaction to take place. The advantage of the lead acid battery is that it is low cost. Lead acid batteries are generally used in vehicles.

Nickel-Cadmium (Ni-Cd): the Nickel Cadmium battery was the first small sealed rechargeable cell. It consists of an alkaline (KOH) electrolyte, with Cd acting as the anode. Similar to Lead acid batteries, the reaction follows a solution-precipitation mechanism (Cd- $Cd(OH)_2$). Nickel-Cadmium batteries work at low temperatures and have high rate capabilities making them ideal for use in cellular phones and portable computers.

Nickel-Metal Hydride (Ni-MH): one of the motivations for the formulation of Nickel-Metal Hydride batteries was to replace the Nickel Cadmium batteries and hence negate the use of the Cd ion (a heavy metal). Nickel-Metal Hydride batteries are high energy storage and light weight but unfortunately have poor temperature capability but have found use in hybrid gasoline-electric vehicles.

Li Ion: Since Li ion batteries make up a large proportion of this thesis, a separate examination is provided below[4].

2.5 Li-ion batteries

Lithium batteries are rechargeable (secondary) batteries that have lithium metal or lithium compounds as anode. They exploit the intercalation energy of Li into an

inorganic host lattice to store and release chemical energy. Depending on the design and chemical compounds used, lithium cells can produce voltages from 1.5 V to about 3.7 V, over twice the voltage of an ordinary zinc-carbon or alkaline battery. Li-ion batteries are the current model of choice for portable applications, such as mobile phones, laptops, cameras, etc. Although they are more expensive than primary batteries, lithium cells provide much longer life, thereby reducing battery replacement costs.

The first commercial lithium-ion (Li-ion) battery appeared at the end of the 20th century. The operation of the Li–ion cell is shown in Figure 2.2. Both the anode and cathode are lithium intercalation compounds, incorporated into a polymer embodied electrode structure based on polyvinylidene difluoride (PVdF). The polymer allows the structure to breathe and accommodates the volume changes that occur in the active materials during charge and discharge. The cell operates by intercalation and de-intercalation of lithium ions into the anode and cathode, depending on whether the cell is being charged or discharged. There is no lithium metal in the cell, only Li ions. The electrolyte is a mixture of alkaline carbonate solvents with lithium hexaflurophosphate salt to provide conductivity[5] or can be solid polymers (e.g. polyethylene oxide, PEO) plus $LiPF_6$.

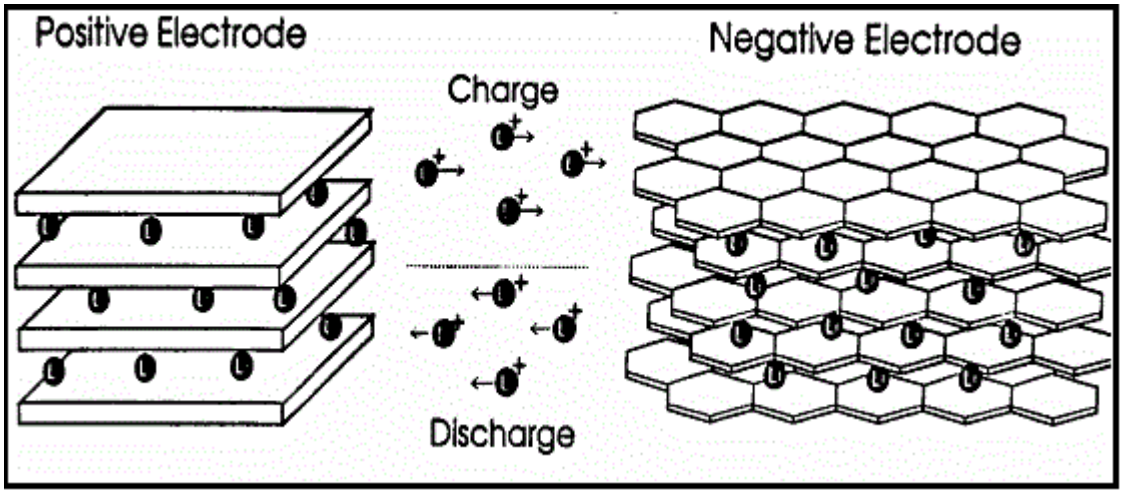

Figure 2.2 Charge –discharge operation of Li-ion cells[5].

For a new material to be considered suitable as an electrode, we must examine its ability to intercalate the Li ions reversibly. In our work we shall investigate a number of transition metal compounds based on Ti oxides and oxysulphides, and novel graphitic-type carbon nitride materials. High valence transition metal oxides have open structures capable of accommodating guest Li ions; the most common structures used for lithium batteries are metal oxides with flexible electronic structure, which can accommodate additional electrons. These properties result in a number of low energy sites for guest ions within the lattice structure, and the potential for high capacity lithium ion intercalation[6]. In addition the electrodes need to exhibit electronic as well as ionic conductivity. Cell voltage in Li-ion batteries is generated as the difference in Li intercalation energy between cathode and anode; maximum performance is therefore obtained by coupling a cathode material with very high Li intercalation energy, with an anode with low intercalation energy. The intercalation behaviour of Li ions in popular cathode materials such as $LiNiO_2$, $LiMnO_4$, $LiCoO_2$, $LiFeSiO_4$ and the olivine $LiFePO_4$ etc. is well documented with both experimental and computational studies[7,8].

The requirements of the cathode materials in rechargeable Li batteries are as follows:

- Contain redox active transition metal ions, that react with Li reversibly and rapidly
- Good electronic conductor, and stable structure
- Low cost and environment friendly.

There are two classes of compounds on which research and commercialization are concentrated: The first class of materials is based on layered compounds with close-packed anion lattices in which alternate layers between the anion sheets are occupied by redox-active transition metal ions and lithium then inserts itself into the vacant intersties of the remaining layers. Examples of these materials are $LiTiS_2$, $LiCoO_2$, $LiNi_{1-y}Co_yO_2$, and recently $LiNi_yMn_yCo_{1-2y}O_2$.

The second class of materials have open structure like vanadium oxides, manganese dioxide and also transition metal phosphates such as olivine $LiFePO_4$.

The first class has the advantage of compact lattice which provide high energy density storage, while the second class is potentially low cost[4].

In the last decade, Lithium batteries have been introduced in the market, with new cathode materials, such as the ($LiMn_2O_4$)[9] Spinels whose cubic close-packed anion lattice is closely related to the α-$NaFeO_2$ layer structure, and only differs in the distribution of the cations between the octahedral and tetrahedral sites[10,11]. The discharge occurs in two steps around 4 and 3 V; the cell is constructed in the discharged state and must be charged before use.

Substituted nickel oxides such as $LiNi_{1-y-z}Co_yAl_zO_2$, are the first candidate materials for the cathode of advanced rechargeable lithium batteries in large scale systems, as required for hybrid electric vehicles. In the charging process of these mixed oxides[12], first the nickel is oxidised to Ni^{4+} then the cobalt to Co^{4+}. Mn, and especially Ni and Co are expensive and environmentally toxic; among transition metal ions, Fe would represent a better choice from both economic an environmental perspectives: it is not surprising, therefore, that intensive research[13,14,15] has been performed in order to investigate the suitability of iron oxides as materials for rechargeable lithium batteries. $LiFeO_2$ shows difficult lithium removal; recent work has also been done on other iron oxide materials such as FeOCl[16], $FePS_3$[17], $KFeS_2$[18] and FeS_2[19] but the reversibility of Li intercalation in these materials remains an unsolved issue. Much more promising are the metal phosphate materials, such as olivine structured $LiFePO_4$, which have been known for decades but only recently have been considered as suitable cathodes.

Anode materials represent the source of Lithium in the discharge process; the current material of choice is graphitic carbon, and alternatives have received less attention than new cathodes. Li intercalation in graphitic carbon yields LiC_6. The need to develop more efficient and effective batteries to meet current global demand motivates a renewed effort in the search for alternative electrode materials.

An important characteristic of electrode performance is the open circuit voltage (OCV), which is the voltage difference between electrodes in equilibrium. In practice, it is

approximated as the voltage observed under low current discharge. The OCV is determined by the difference in the chemical potential of lithium between anode and cathode and can be obtained from simulations. Slow Li diffusion may however prevent ions from reaching their thermodynamically stable sites, so that the OCV cannot be reached. Therefore, to design new batteries, we need to understand the stable sites and diffusion pathways of the Li ions, with key factors including high-energy density and reversible structure changes on Li intercalation for a large range of insertion concentrations.

Monte Carlo treatment and first principles calculations provide the basis upon which previous simulations have been performed on the thermodynamics of Li insertion in electrode materials. In addition, diffusion mechanism and energy barriers present in the migration pathway have been examined. Theoretical models are able to provide configurationally averaged estimates of intercalation energies, which are assumed to be valid over a range of insertion concentrations.

Lithium insertion into electrode materials is often accompanied by changes in electronic structure, as the lithium atoms ionize upon intercalation and donate at least part of their valence 2s electron to the host lattice. Computer simulations therefore need to account for changes in the electronic structure upon intercalation. This can be done through quantum mechanical calculations, which provide information about electronic states.
The fundamentals of the computational methods that can be applied to study Li-ion batteries are described in chapter 3.

Chapter 3

Computational Methodology

3.1 Introduction

The goal of computational chemistry is to develop and apply software programs which are able to investigate problems of chemical interest. It is now a mature science that can not only assist in the interpretation of experimental observations, but also predict new phenomena in advance of experiment. It is the predictive capability that makes computational chemistry particularly attractive. Simulation can in fact be performed to screen new materials of potential interest so that experimental effort, more demanding in terms of time and cost, can concentrate on the systems of highest potential impact.
Computational chemistry can be divided into two main branches, classical methods, which are sometimes very useful and computationally faster, and quantum methods. The main features of both will be discussed in the following sections.

3.2 Classical Methods

Classical methods use the laws of classical physics to describe the atomic-level behaviour of the systems of interest. Electrons are not treated explicitly; rather the interaction between neighbouring atoms is described as a function of interatomic distances and angles. The ensemble of functions and parameters used to represent the potential energy surface is commonly referred to as force field (FF). These energy contributions contain parameters, often system dependent, which need to be determined, either empirically or making reference to quantum mechanical results.

Classical calculations using force fields are computationally fast, and can be used with structures containing thousands and in some case even millions of atoms[20]. On the other hand these methods are limited to certain classes of systems, for which reliable force

field parameterisations are available. A non-exhaustive list of general-validity force-field methods available in the literature are MMI-4, AMBER, CHARMM, GROMOS, UFF [21,22].

3.3 Quantum Mechanical Methods

In contrast to classical methods, quantum chemical techniques aim to describe explicitly the electrons of the system.

This thesis employs ab initio Quantum Mechanical (QM) calculations to investigate the internal energy and the electronic properties of solids[23]. Such QM calculations provide information about electronic states and are in principle 'parameter-free'; although some techniques do include parameters these are not system-dependent.

QM simulations attempt to find solutions to the time-independent Schrödinger equation

$$\hat{H}\Psi = E\Psi \qquad \textbf{(3.1)}$$

where Ψ is the many-body wavefunction, which is a function of all the electronic and nuclear coordinates of the system, including electron spins. E is the total energy of the system. $\hat{H}$ is the many-body Hamiltonian. For a system of electrons and nuclei with position vectors r_i, R_A the Hamiltonian for N electrons and M nuclei can be expressed as

$$\hat{\mathrm{H}} = -\sum_{i=1}^{N}\frac{1}{2}\nabla_i^2 - \sum_{A=1}^{M}\frac{1}{2M_A}\nabla_A^2 - \sum_{i=1}^{N}\sum_{A=1}^{M}\frac{Z_A}{r_{iA}} + \sum_{i=1}^{N}\sum_{j>i}^{N}\frac{1}{r_{ij}} + \sum_{A=1}^{M}\sum_{B>A}^{M}\frac{Z_A Z_B}{R_{AB}} \qquad \textbf{(3.2)}$$

The $\hat{H}$ operator is the sum of the kinetic energy of electrons, nuclei, and the Coulomb interaction among all the charged particles.

The Schrödinger equation can be solved exactly only for 1 electron systems; any system with 2 or more electrons requires approximations.

3.3.1 The Born-Oppenheimer approximation

This approximation is based on the fact that electrons are much lighter than nuclei, hence they move faster[24]. For instance, in the hydrogen atom the average speed of the electron is faster than the proton average speed by approximately 1000 times[25]. Electrons are affected by the nuclei positions, but the difference in speed enables them to adapt instantaneously to any change in the nuclear coordinates. We can therefore separate the motion of electrons from the motion of the nuclei. The Schrödinger equation can be solved for the electrons in the field of fixed nuclei as indicated in the equation below

$$\hat{H}_e(R)\psi_e(r,R) = E_e(R)\psi_e(r,R) \qquad \textbf{(3. 3)}$$

Where $\hat{H}_e$ is the electronic Hamiltonian operator, it is a sum of the kinetic energy of the electrons, electrostatic interactions between charged particles and the exchange forces between the electrons so that equation 3.2 becomes

$$\hat{H}_e(R) = -\sum_{i=1}^{N} \frac{1}{2}\nabla_i^2 - \sum_{i=1}^{N}\sum_{A=1}^{M}\frac{Z_A}{r_{iA}} + \sum_{i,j}^{N}\sum_{i,j}^{N}\frac{1}{r_{ij}} \qquad \textbf{(3.4)}$$

The solution of equation 3.3 for the electronic wavefunction yields the electron wavefunction

$$\Psi_e = \Psi_e(\{r_i\};\{R_A\}) \qquad \textbf{(3.5)}$$

The total energy for fixed nuclei can be written as

$$E_{tot}(\{R_A\}) = \mathrm{Ee} + \sum_{\mathrm{A}=1}^{\mathrm{M}} \sum_{\mathrm{B}\rangle \mathrm{A}}^{\mathrm{M}} \frac{\mathrm{ZAZB}}{\mathrm{RAB}} \qquad \textbf{(3.6)}$$

In virtue of the Born-Oppenheimer approximation, the motion of nuclei described within the average field of the electrons and the corresponding nuclear Hamiltonian can be written as

$$\hat{\mathrm{H}}_N = \sum_{A=1}^{M} \frac{1}{2M_A} \nabla_N{}^2 + E_{tot}(\{R_A\}) \qquad \textbf{(3.7)}$$

The second parameter in equation 3.7 represents the potential for nuclear motion. So the nuclei in Born-Oppenheimer approximation move on the potential energy surface (PES) obtained by solving the electronic problem.

The solutions of the nuclear Schrödinger equation

$$\hat{\mathrm{H}}_N \psi_N = E \psi_N \qquad \textbf{(3.8)}$$

is represented by the equation

$$\psi_N = \psi_N \{R_A\} \qquad \textbf{(3.9)}$$

which describes the nuclear system. The energy E in the Born-Oppenheimer approximation (equation 3.8) describes the total energy as kinetic energy of nuclei plus the Coulombic interaction of the nuclei in the average field of the electrons. If the nuclear position is changed, the electronic wavefunction and total energy change as well. The wavefunction $\Psi_e(r, R)$ is the electron many-body function.

Two main solution strategies exist to calculate $\Psi_e(r, R)$, that factorise the many-body problem into a product of one-electron solutions; these are the Hartree Fock (HF) & Density Function (DF) theories.

3.4 Hartree Fock Theory

In the Hartree Fock (HF) theory the many-body electron wavefunction is the product of a series of single electron wavefunctions, each of them depending on the coordinates and spin of a single electron. The anti-symmetric nature of the wavefunction with respect to the exchange of two electrons, which is necessary to satisfy Pauli's Exclusion Principle, is achieved by expressing the many electron wavefunction as a linear combination of products of anti-symmetrised 1-electron wavefunctions using Slater determinants[26]. The wavefunction of lowest energy, which corresponds to the "best" wavefunction according to the variational principle, is found by solving the equations with respect to all the 1-electron wavefunctions.

In the Hartree Fock theory, an electron is described as moving through the mean-field generated by all the other electrons in the system, and therefore electron-electron correlation effects are not considered. This approximation leads to an over-estimation of the total energy. Methods that are designed to expand the Hartree Fock theory by accounting for electron-electron correlation effects are referred to as post Hartree Fock approaches[27]. These approaches give a more complete approximation of the wavefunction, which is represented as a combination of different Slater determinants including occupied orbitals as well as empty orbitals.

3.5 Density Functional Theory

Density Functional Theory (DFT) is currently the method of choice for electronic structure calculations in condensed matter physics, widely applied because of its advantages in calculating the total energy of a system compared with the Hartree Fock theory[28].

The theoretical foundations of DFT are expressed in the theorems of Hohenberg and Kohn[29,30]. They stated that the ground-state energy of a closed shell system can be expressed as a functional of the total electron density only. Basing the energy on the total electron density means that there are fewer variables to calculate in DFT than in Hartree Fock. The total electronic density of the system depends on three spatial coordinates for closed shell systems and six for open shell (α spin x, y, z and β spin x, y, z).

The energy of a system in DFT, depends on the total electron density, and contains contributions arising from the kinetic energy of the electrons (T [ρ]), the nuclei-electron interactions ($V_{ne}[\rho]$), and the electron-electron interaction ($V_{ee}[\rho]$), as shown in equation (3.10)

$$E[\rho] = T[\rho] + V_{ne}[\rho] + V_{ee}[\rho] \qquad \textbf{(3.10)}$$

The nuclear-nuclear interactions are constant under the Born-Oppenheimer approximation. The goal of DFT calculations is to determine the ground-state electron density$\rho_o(r)$ of the system under investigation. The correct solution for $\rho(r)$ is the one that minimizes the ground-state energy. In other words, starting from a trial electron density, $\rho_t(r)$ describing the electrons in the system, and satisfying the condition

$$\int \rho_t(r)dr = N \qquad \textbf{(3.11)}$$

where N is the number of electrons in the system, the variational principle assures that the energy of the system calculated as a function of ρ_t will be higher than the actual energy of the system investigated, and therefore,

$$E[\rho_t] \geq E[\rho_o]. \qquad \textbf{(3.12)}$$

The practical method to calculate $\rho(r)$ is defined by the Kohn-Sham (KS) approach[31], and consists of a diagonalisation of the Hohenberg and Kohn (HK) Hamiltonian in a given basis set, which provides 1 electron orbitals analogous to those of the HF theory (basis sets are discussed in section 3.11). The exact DFT solution and form of the functional is known only for a fictitious system of non-interacting electrons, known as a uniform electron gas and we use this model to approximate the electronic kinetic energy in the DFT solution given by the KS orbitals.

$$T_f[\rho] = -\frac{1}{2}\sum_{i}^{N}\left\langle \Phi_i \mid \nabla^2 \mid \Phi_i \right\rangle \qquad \textbf{(3.13)}$$

where ϕ_i are the occupied 1-electron (molecular) orbitals. All the components of the total energy of the system in equation 3.10 are explicitly written in the form given below

$$E[\rho] = T_f[\rho] + V_{ne}[\rho] + J[\rho] + E_{xc}[\rho] \qquad \textbf{(3.14)}$$

In equation (3.14), J [ρ] is the classical Coulombic electron-electron repulsion and $E_{xc}[\rho]$ is called the exchange and correlation functional. It can be described as the error involved in treating the electron-electron interaction as classical particles and obtaining a value for the kinetic energy from equation (3.13)[32]. The correlation part of $E_{xc}[\rho]$ accounts for the correlated motion of electrons in a system.

$$E_{xc}[\rho] = (T[\rho] - T_f[\rho]) + (V_{ee} - J[\rho]) \qquad \textbf{(3.15)}$$

The HK theory is formally correct, i.e. exact. However, the exact form of the E_{xc} functional is unknown; several working formulations have been proposed, that will be discussed in the following sections. Results are known to depend on the type of functional employed.

3.6 Functionals

The E_{xc} term must contain the exchange energy, correlation energy and the difference between the kinetic energies of non-interacting and interacting systems. In order to calculate the exchange-correlation functionals, different approximations have been proposed such as the local density approximation (LDA) and the generalized gradient approximation (GGA).

3.6.1 Local Density Approximation

LDA is the simplest functional approximation; in this formulation the exchange-correlation contribution to the energy in each point of space, r, depends only on the electron density in r, $\rho(r)$, and its value is the same as that calculated for a uniform electron gas of the same density, $\rho(r)$[33]. The correlation part of $E_{xc}[\rho]$ has been parameterised[34,35], while the exchange part can be calculated exactly. Thereby, the local exchange correlation energy E*xc* is written as a function of the local charge density as below:

$$E_{XC}^{LDA}[\rho(r)] = \int \rho(r)\varepsilon_{XC}(\rho(r))dr \qquad \textbf{(3.16)}$$

where $\varepsilon_{xc}(\rho(r))$ represents the exchange-correlation energy per electron at point r in a uniform gas of density ρ, and can be divided into exchange and correlation contributions as follow;

$$\varepsilon_{xc}(\rho(r)) = \varepsilon_{x}(\rho(r)) + \varepsilon_{c}(\rho(r)) \qquad \textbf{(3.17)}$$

The LDA approximation is successful with materials characterised by a slow change in the electron density such as metals, but the exchange energy is underestimated and the correlation energy is overestimated, which leads to an underestimation of bond lengths.

The accuracy of the LDA approximation can be improved by more complex functionals; the most common are referred to as Generalized Gradient Approximation (GGA).

3.6.2 Generalized Gradient Approximation (GGA)

The generalised gradient approximation (GGA) improves the LDA by incorporating a dependence of E_{xc} on the local gradients of the charge densities, which can be written as

$$E_{XC}[\rho(r)] = \int f_{xc}(\rho(r), |\nabla\rho(r)|)dr \qquad \textbf{(3.18)}$$

Also in GGA the E_{xc} term can be split into exchange and correlation contributions, and each part can be calculated separately.

The GGA functionals contain parameters, which are obtained either from first-principles, a method mastered by Perdew (for instance the PW and PBE functionals)[36,37,38], or by fitting to experimental data (for instance the case of BLYP proposed by Becke)[39,40].

Functionals that include second derivatives of the local density have also been proposed and they are called meta-GGA. However, whilst accuracy may be increased, all these cases are "local" in the mathematical meaning, i.e. the exchange and correlation functional in a point r is expressed in a Taylor expansion of the electronic density, using only the values (total density, first and eventually second derivatives) in the point r.

GGA functionals usually show great improvement of results compared to LDA; in particular they improve the LDA overestimation of the atomisation energies for molecules and solids, equilibrium bond lengths and lattice parameters, vibrational frequencies and bulk moduli[41].

3.6.3 Hybrid Functionals

Hybrid exchange functionals are currently the most widely used in molecular studies, and are becoming more and more common for solids. The hybrid functionals are obtained by mixing HF and DFT formulation of the exchange forces; they are "non-local", and include orbital dependent terms. B3LYP is an example of these hybrid functionals[42]. In this way, unlike LDA and GGA functionals, electron self-interaction can be accounted for DFT.

$$E_{xc} = \alpha(E_x^{HF} - E_x^{DFT}) + E_c^{DFT} \qquad \textbf{(3.19)}$$

The mixing parameter α in equation (3.19) corresponds to the amount of HF exchange included in E_{xc}. The value of α in the B3LYP functional, proposed by Becke, is α = 0.2 (determined by fitting to experimental data).
The extent of HF-mixing required to accurately model a system depends on the system and its properties[43].

3.7 Crystalline Solids

Crystalline solids are characterised by periodicity; as for molecules, also for solids a many-body wavefunction can be mapped into the product of many effective single-particle wavefunctions. However, there still remains the difficult task of handling an infinite number of non interacting electrons in the electrostatic potential of an infinite number of nuclei in a solid material.

3.8 Periodic Boundary Conditions (PBC)

The study of solids at an atomic level is a complex task; hence we use Periodic Boundary Conditions (PBC) to simplify our goal of studying crystalline systems[44]. PBC allow us to model macroscopic systems where the changes occurring in one cell can be generalised to those occurring throughout the system[45]. The "box" or unit cell is repeated in space to

form an infinite lattice. When one atom moves in the original box, its image is repeated in all other "boxes". Each box however is not bound by any walls and hence atoms in motion can move from one cell to the next.

Using PBC, it should be noted that atoms which appear far from each other may in fact be very close to the periodic repetition in adjacent boxes. Furthermore, interactions between an atom and its own image(s) in repeated boxes may occur. However, for simulated systems far from phase transition points, PBC exert no strong influence on the calculated properties[45].

3.9 Bloch's Theorem

The number of electrons in the crystal structure is one important issue to be considered in the calculations; obviously a solid contains a very large number of electrons, but using the PBC settings, calculations are performed on the unit cell only thus making the problem tractable. According to Bloch's Theorem[46], the one-electron wavefunction in a regularly repeating lattice (i.e. under periodic boundary conditions) is given by

$$\Psi_{n,k}(r) = exp^{(i\underline{k}.\underline{r})} U_{n,k}(r) \qquad \textbf{(3.20)}$$

where $exp^{i\underline{k}.\underline{r}}$ represents phase factor, $\underline{r}$ is the position and $\underline{k}$ is the wave vector. For any lattice vector a_i of the simulation cell

$$\Psi_{n,k}(r+a_i) = exp^{(i\underline{k}.\underline{r})} \Psi_{n,k}(r) \qquad \textbf{(3.21)}$$

where $U_{n,k}(r)$ has lattice periodicity of the cell

$$U(r+a_i) = U(r) \qquad \textbf{(3.22)}$$

3.10 Basis Sets

The one-electron wavefunctions or orbitals that appear in the HF and KS solutions can be expressed by a linear combination of a finite set of atomic functions known as basis functions[47,30]; these represent the wavefunction and/or electron density of the system in real space. Two types of basis functions are used most frequently in solid-state calculations: Gaussian Type Orbitals (GTOs) and Plane Waves.

3.10.1 Gaussian Type Orbitals

GTOs make reference to the correct solution (atomic orbitals) for the H atom; the orbitals are expressed as product of angular and radial components, in which the angular part is given by the spherical harmonics, and the radial part is expressed as a contraction of Gaussian functions

$$\phi(r) = \sum_{i=1}^{N} c_i e^{-\alpha_i r^2} \qquad \textbf{(3.23)}$$

where the exponential (α_i) determines the radial extent of the Gaussian function and the sum determines the type of orbital. The correct solutions for the H atom have a simple, rather than quadratic exponential decay, $e^{-\alpha r}$; hence GTOs do not reproduce correctly the cusp of the electron density on the nucleus.

A more correct radial description can be achieved by using linear combinations of more GTOs; and this is particularly important for core electrons. One of the advantages of using Gaussian functions is that most calculations, such as of multi-centre integrals, can be performed analytically. Atom centred GTOs are normally used, which are identified as atomic orbitals. The simplest type of basis set, which includes the minimum number of functions to represent all the electrons in a neutral atom, is called minimal, or Single Zeta (SZ). In order to improve the variational flexibility of the basis set, the number of

functions can be doubled or tripled; the new basis sets are called Double Zeta (DZ) and Triple Zeta (TZ) respectively.

In case of heavy atoms, often only the valence electrons are described by multiple atomic orbitals (AOs), while core electrons are treated with a minimal basis set. In this case the basis sets are named as DZV, TZV for doubled and tripled valence respectively[47] .

3.10.2 Plane Waves

The second type of basis set commonly used for solids are plane waves, which represent waves propagating with a constant frequency, amplitude, perfectly periodic, and obey Bloch's theorem (equation 3.22).

A periodic function u(r) can be expanded as a Fourier series in the form:

$$u_i(r) = \sum_G \varepsilon \ \exp^{i\mathbf{G}.\mathbf{r}} \qquad \textbf{(3.24)}$$

where G are the reciprocal lattice vectors defined by the condition $exp^{i\mathbf{G}.\mathbf{a}_i} = 1$, ($i$=1,2,3).

From equation 3.20 and equation 3.24 the electronic wavefunction in solids can be written as:

$$\psi_{i.k}(r) = \sum_G c_{i,k+G} \exp^{i(k+G).r} \qquad \textbf{(3.25)}$$

Two important parameters appear in this equation: the first is the number of K points. Usually, a small K point number is chosen to calculate the wavefunctions, since the wavefunctions and other properties such as Hamiltonian Eigenvalues vary smoothly over the Brillouin zone[48].

The second parameter is the energy cut-off used to define the periodic wavefunction basis set. The plane-wave basis set includes only the plane waves corresponding to kinetic energies that are less than some particular cut-off value E_{cut}, according to the equation:

$$E_{cut} = \frac{\hbar^2}{2M}(K+G)^2 \qquad \textbf{(3.26)}$$

The choice of the cut off energy is very important to ensure that the calculated properties are well converged.

Plane waves provide an alternative way of representing atomic orbitals in periodic systems. The main difference between plane waves and GTO basis sets is that plane waves are already periodic and obey directly the Bloch's theorem, for the description of the entire crystal lattice. Furthermore, the number of plane waves used does not depend on the number of constituent atoms but on the size of the unit cell. However, since plane waves do not resemble the correct shape of the orbitals, we need very large numbers to achieve chemical accuracy.

Both plane wave and GTO basis sets have a common feature that the greater the number of basis functions used, the greater the accuracy. The optimal number of basis functions depends on how strongly the electron density changes in space; the stronger the changes, the more plane waves are needed to describe the system. Since this effect is most pronounced for core electrons, for systems containing heavy atoms the Hamiltonian matrix will be large. Pseudopotentials are introduced in such a way to reproduce the properties of the valence electrons accurately while avoiding an explicit description of the core electrons[49].

3.11 Pseudopotentials

Pseudopotentials are used in plane wave calculations; the potential of the core electrons and nuclei is replaced by an effective potential which acts upon the valence electrons. The justification for using pseudopotentials arises from the fact that only the valence electrons are responsible for the chemical bonding properties of a system. In this way we are able to simplify the description of the electrons.

Hamann *et al*. extended the concepts of pseudopotentials to the Norm-Conserving Pseudopotentials (NCPP) approach[50] in which the all electron wavefunction is replaced by a soft nodeless pseudo-wavefunction inside the core radius; with the restriction that the pseudo-wavefunction must have the same norm (electronic charge) as the all-electron wavefunction within the chosen core radius.

Ultrasoft pseudopotentials represent an extension of pseudopotentials[51]; they allow a smoother wavefunction and hence lower energy cut-off. This approximation removes the constraint of norm-conservation, and localized atom augmentation charges are introduced to compensate the resulting charge deficit. Transferability is guaranteed even for large core radii, by allowing more than one reference energy per quantum state[52].

3.12 Computer Codes Employed

The calculations performed throughout the thesis employ one computer code: CASTEP [66].

3.12.1 CASTEP

The CASTEP code performs electronic structure calculations using DFT and plane wave basis sets.

The electron-ion potentials are described by ab initio pseudopotentials within either norm-conserving or ultrasoft formulations.

The energy minimization is used to calculate self-consistently the electronic wavefunctions and the corresponding charge density.
Using CASTEP code it is possible to calculate the total energy, forces and stress effects on crystal structures, and also investigate the electronic charge densities and band structures.
The code can use Density Functional Perturbation Theory (DFPT) for the calculation of phonon frequencies and eigenvectors, which can be used to give the Gibbs free energy, entropy, enthalpy, Debye temperature, heat capacity, and a measurement of phase stability.

The accuracy of these calculations, as in general of all computational studies, depends on the level of theory chosen and on a number of user-defined parameters, such as the number of K-points, the quality of the pseudopotentials, the basis set cut off, the functional employed, etc. While the effect of numerical accuracy can be checked, and in general we have always chosen parameters that converge relative energies to at least 1 meV/ atom, the effect of the level of theory employed is less easily predictable, and there are many examples of qualitatively (not only quantitatively) incorrect computational results due to a wrong choice.

Most of the calculations have been performed on local Linux clusters; the most demanding calculations have been run on national facilities: HPCx first, and HECToR since 2009, under the UK's HPC Materials Chemistry Consortium (funded by EPSRC via grants EP/D504872 and EP/F067496) whom we are very grateful to.

Many calculations discussed in this thesis have been very demanding in terms of CPU time; for instance one geometry optimization for the $Li_xTi_{16}O_{32}$ unit cell required 24 hours on 128 cores on HECToR. Relatively small supercells of the host systems (about 40 atoms) required in excess of 1 week CPU time on local cluster resources. It is estimated that larger supercells of up to 200 atoms as appropriate to represent for example the Li intercalation in realistic conditions will require in excess of 1 month CPU time on local resources, and are suitable for parallel execution using 32-128 cores.

Chapter 4

Li intercalation into TiO_2 Polymorphs

Notes: *Results discussed in this chapter refer to the first part of the PhD work, performed under the supervision of Dr. Marina Koudriachova.*

4.1 Introduction

Rechargeable Li batteries are of interest because they provide efficient energy storage with high energy density and high voltage. The main factors affecting the efficiency of the electrodes in these batteries are the capability to uptake and release reversibly Li ions during the charge and discharge processes, the stability of the structure during the intercalation process and the rate of diffusion of the Li-ions.

The charge–discharge performance depends on the voltage difference between the anode and the cathode, the ability of the electrode to accept large numbers of Li ions and the number of charge and discharge cycles.

It is preferable for Li batteries to have high and constant voltage, obtained by combining a low voltage for the anode and a high voltage for the cathode.

Titanium dioxide is one of the most interesting materials for anodes because of the chemical properties of Ti, a transition metal ion capable of accommodating electron density donated by intercalated Li atoms, and because the structures of TiO_2 polymorphs are open enough to provide space for the Li ions.

Titanium dioxide (TiO_2) is cheap and non-toxic, and one of the few known transition-metal bearing materials that intercalate Li at low voltages, and therefore may be a suitable anode material in Li rechargeable batteries[53,54,55]. It exists in a large number of

polymorphic structures, of which the most stable are rutile, anatase and brookite[56,57,58]. These polymorphs show different intercalation behaviour[59,60,61], which in addition has been shown to depend on particle size and operating conditions[62,63].

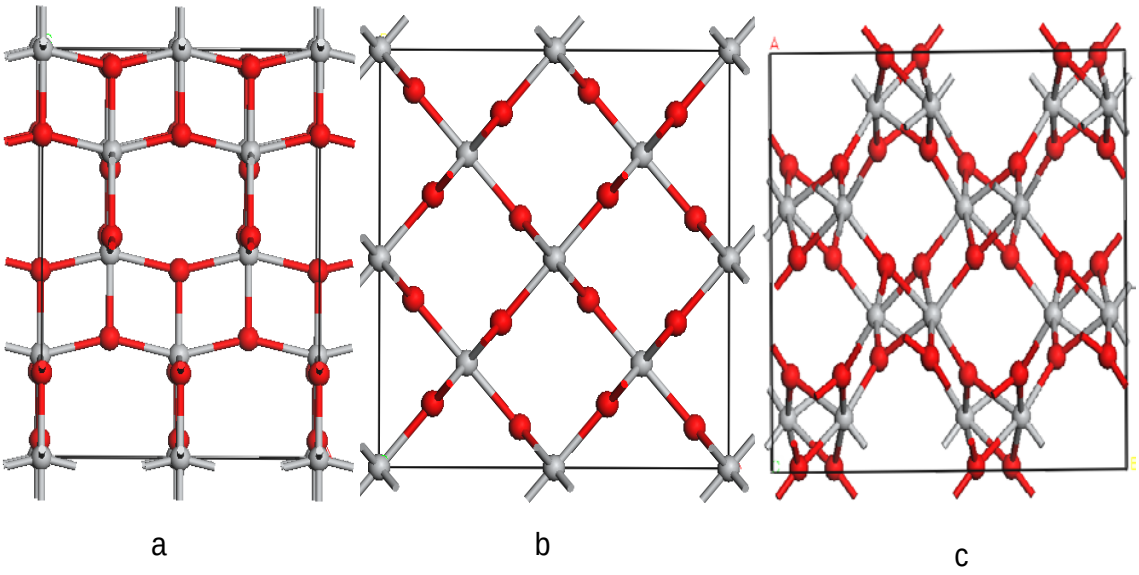

Figure 4.1 shows a structural comparison of the most stable polymorphs of TiO_2: (a) anatase, (b) rutile and, (c) brookite; it is clear that they all have interstitial sites available, and are good candidates for intercalation, however the details of the interstitial sites differ among polymorphs. The polymorphic behaviour of TiO_2 has been subject of extensive computational studies[64].

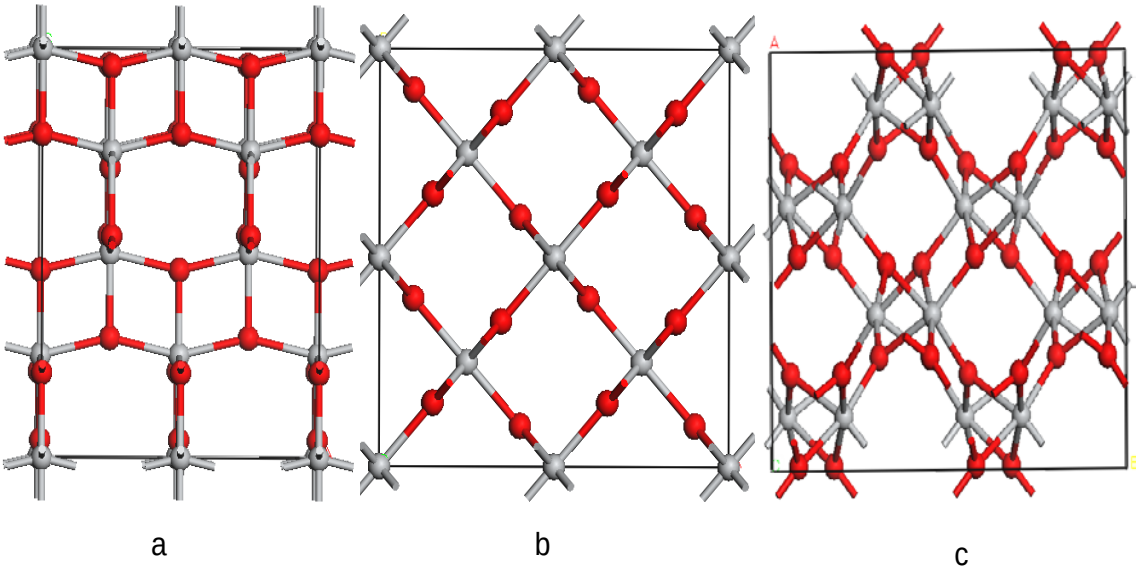

Figure 4.1 The most stable polymorphs of TiO_2: (a) Anatase, (b) Rutile and, (c) Brookite

It was found that in the anatase structure at room temperature Li intercalation is efficient, but at elevated temperature the electrode ages more rapidly. Intercalation into rutile behaves differently, with low intercalation at room temperature, while at elevated temperature the electrode performance increases[53,58]. The behaviour difference is related to the anisotropy of Li diffusion in the structures, as well as to the deformations induced by Li intercalation and the existence of stable ordered superstructures inside the host lattice.

This chapter investigates the intercalation process into two other polymorphs of TiO_2: Brookite and TiO_2-B, which have received less attention than anatase and rutile structures as Li intercalation hosts in the literature.

Section 4.2 investigates the Brookite structure and predicts the most favourable energy sites and possible Li arrangements in the structure; it also studies the Li diffusion mechanism, and compares the theoretical results with experimental work. Section 4.3 considers the Li intercalation in TiO_2-B; again characterising the most favourable intercalation sites within the structure, identifying the pathways for Li diffusion and calculating the diffusion barriers for this process in different crystallographic directions.

4.2 Li Intercalation into Brookite

4.2.1 Introduction

At room temperature, anatase intercalates Li-ions reversibly to yield Li_xTiO_2, up to a value of x at least equal to 0.5[53,56,58], while Li-uptake by both polycrystalline rutile and brookite is negligible. At elevated temperature, anatase and rutile intercalate to high Li-insertion concentrations (x=1)[58]. The intercalation behaviour of Brookite at elevated temperatures has not been investigated yet. In the nanophase, the reactivity of both rutile and brookite towards Li increases with a decrease of the particle size[54,55]. Li insertion into mesoporous rutile proceeds at room temperature and follows the same sequence of phase transformations as for the polycrystalline material at elevated temperature[55,58,59,60]. Specially tailored nanostructures of rutile may show different intercalation behaviour[57]. Using *ab initio* simulations the intercalation behaviour of rutile and anatase and its temperature dependence was fully explained by accounting for the effect of Li-ion diffusion[59,60,63]. It has been shown that Li-intercalation into rutile is strongly limited by highly anisotropic diffusion of the Li-ions, so that intercalation proceeds only when diffusion is activated (elevated temperature, small particle size)[59,60]. Recently, it has been shown that nanosized particles of brookite can also intercalate Li-ions to high Li-concentrations (x=0.9)[54]. The mechanism of Li-intercalation into rutile and anatase has been studied in detail using various experimental and theoretical techniques; this should be contrasted with brookite, where very little is currently known about the mechanism of Li-insertion and diffusion, and the corresponding structural changes. There is a strong indication that upon Li-intercalation, the structure of brookite is preserved, in contrast to rutile and anatase and some other titanates (ramsdellite-structured TiO_2 and spinel-structured $Li_{0.5}TiO_2$), however the evidence is indirect[54]. The X-Ray Diffraction (XRD) patterns at different stages of intercalation/deintercalation, which have been analysed only qualitatively, show two major reflections of brookite at all Li-concentrations examined but the quality of the pattern precludes any quantitative analysis[54] (see Figure 4.2). For the whole range of insertion concentrations a steady monotonic decline of the equilibrium voltage with Li-concentration x is observed[54] (see Figure 4.3).

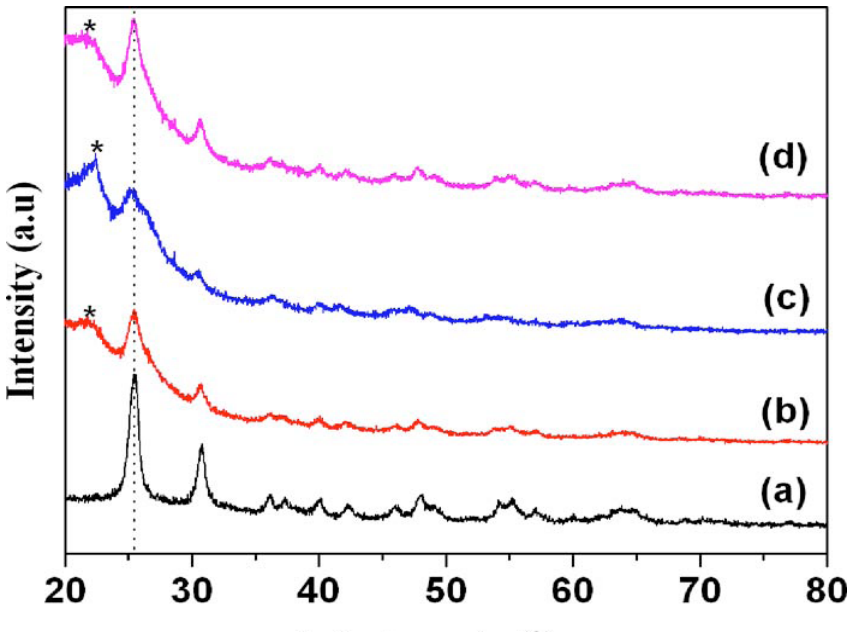

Figure 4.2 Ex situ XRD patterns of brookite TiO_2 at various lithium contents during initial cycle: (a) pristine brookite TiO_2, (b) $Li_{0.5}TiO_2$, (c) $Li_{0.9}TiO_2$, and (d) $Li_{0.3}TiO_2$ (after charge to 3 V). The * indicates the peak due to Mylar film. Reported from reference [54].

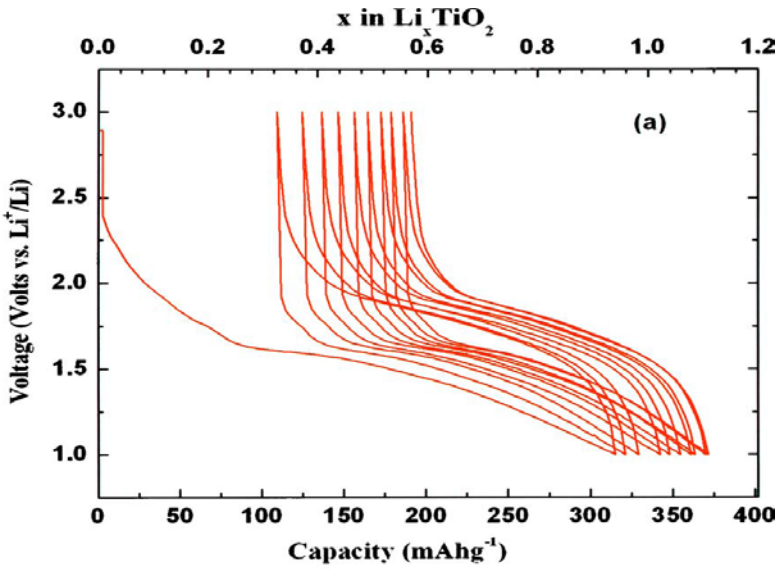

Figure 4.3 Voltage vs Lithium composition for brookite TiO_2, for the first ten charge/discharge cycles carried out in the voltage range 1.0-3.0 V. Reported from reference[54].

This shape is characteristic of a single phase insertion, while phase transformations manifest themselves by steps and plateaux in the equilibrium voltage profile.

Further detail on the Li-insertion into brookite is given by the electrochemical data (Figure 4.3), which shows a sharp drop in cell voltage (to 1.6 eV) upon Li-insertion up to x=0.25, followed by a steady further decline to 1 eV, possibly through two reversible processes corresponding to ordering of the inserted Li-ions.

Despite a significant irreversible capacity loss upon initial discharge (of approximately 0.32 Li)[54], the stable capacity of brookite on further cycling is reported to be higher than that of other titanates, making nanostructured brookite an attractive electrode material (anode) for rechargeable Li batteries.

Ab initio simulations have played an important role in developing a detailed atomistic picture of the processes underlying Li-insertion in various materials as they provide reliable thermodynamics and invaluable information on the changes in the electronic structure and local geometry[59,61,63].

Based on first principles calculations, a simple model relating lattice morphology of these materials to their intercalation has been developed[62,63]. Here, first principles calculations are applied to predict the Li-intercalation behaviour of brookite and in particular its structural behaviour, and to elucidate the underlying mechanisms.

4.2.2 Details of Calculations

All calculations were performed within the pseudopotentials plane wave formalism[65,66] using the CASTEP code. Electron exchange and correlation effects were treated within

the spin polarized Generalized Gradient Approximation (GGA)[67] of DFT using the Perdew-Burke-Ernzerhof (PBE) functional with ultrasoft pseudopotentials to replace the core electrons[68]. Reciprocal space was sampled on a regular net with a consistent spacing of 0.05 $Å^{-1}$, corresponding to 1x1x2 unique K-points in the first Brillouin Zone of a $Ti_{16}O_{32}$ cell. Plane wave cut-off energy of 380 eV was found to converge the total energy to 0.01 eV per formula unit. The size and shape of the cell and all internal degrees of freedom were fully relaxed with respect to the total energy and all calculations were performed in P1 symmetry. The lowest energy configurations have been sought for a number of Li-insertion concentrations using supercells $Li_nTi_{16}O_{32}$, n=1-16.

The nature of the insertion process has been determined by comparing the thermodynamic stability of homogeneous and possible coexisting phases[60].

4.2.3 Structure of Brookite

Brookite TiO_2 has an orthorhombic structure with *Pbca* symmetry and cell parameters *a*=9.18 Å, *b*=5.46 Å, *c*=5.15 Å[69]; the calculated values of the lattice parameters in our computational work are *a*=9.23 Å, *b*=5.47 Å, *c*=5.15 Å. The structure represents a three dimensional network of TiO_6 octahedra sharing three edges each, with empty zigzag shaped channels along the c-direction, which are potentially available for Li-intercalation, see Figure 4.4. The edge sharing motif underlying the structure of brookite is shown in Figure 4.5, together with the local crystallographic directions. The analysis of the connectivity of TiO_6 octahedra has been demonstrated to play an important role in understanding the electronic mechanism of Li-insertion into titanates[59,60,61]. The discussion on Li intercalation in brookite therefore starts by examining the structural features of the TiO_2 backbone.

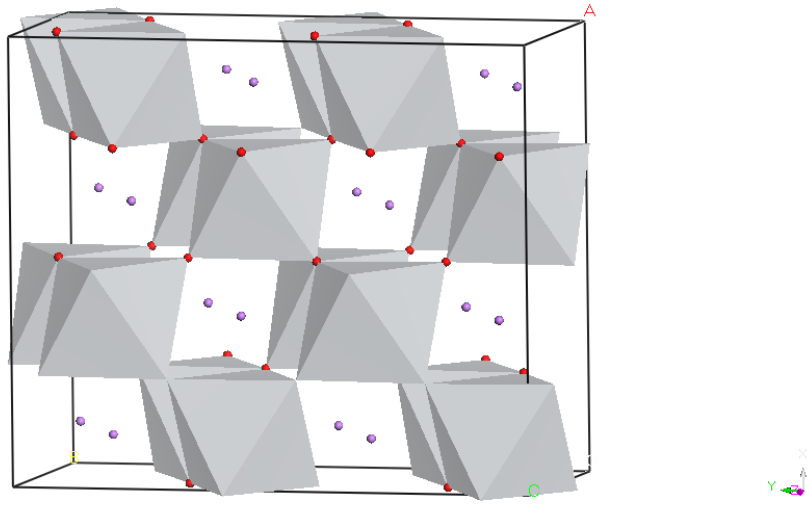

Figure 4.4 The structure of fully occupied brookite ($Li_{16}Ti_{16}O_{32}$) in polyhedral representation. Li in purple and oxygen in red.

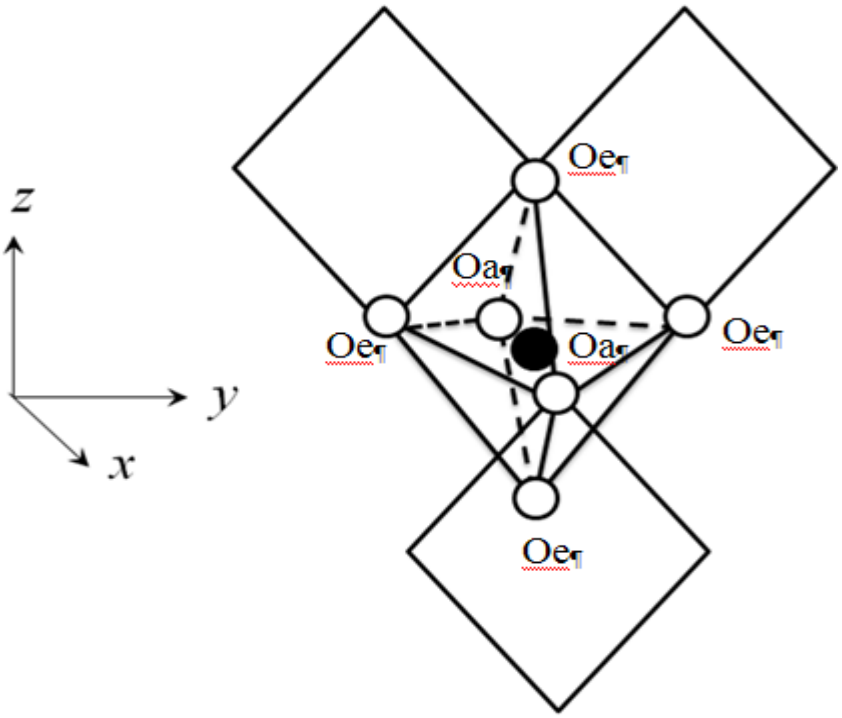

Figure 4.5 Edge sharing motif in brookite. The Ti-ion is shown in black, O ions are shown in white. Equatorial O ions are denoted Oe, apical O-ions are denoted as Oa.

4.2.4 Li-insertion sites and structural relaxation

The first step in the investigation is to analyse the geometry of the interstitial sites in brookite, which can potentially accommodate Li-ions, and compare them with a typical Li-O and Li-Ti environment in other polymorphs of Li_xTiO_2. This comparison allows the establishment of the type of sites and the possible Li-coordination at various Li-concentrations, and the detection of a number of stable Li-phases.

The sites available for Li-insertion are in the open channels being formed by six oxygen ions, with separations across the interstitial site of 3.49(x2)Å, 4.24(x2)Å and 4.84(x2)Å, and four Ti-ions at 4.75(x2) Å and 5.44(x2) Å (Figure 4.6 and Figure 4.7). Distances between a Li ion located at the centre of the interstice and it's O and Ti neighbours are half of the distances reported above. Comparison of the above geometry with the typical distances in other polymorphs suggests that insertion of Li-ions into brookite results in strong distortions of the local structure.

The primary source for such distortions is the strong electrostatic repulsion between the Li^+ ions and the closely spaced neighbouring Ti^{+4} ions. The Li-Ti repulsion is usually well screened for Li-Ti distances above 2.8 Å. Therefore, considerable displacements of the Ti-ions neighbouring a guest Li are expected in brookite, where Li-Ti distances of 2.37 Å are available in the undistorted lattice.

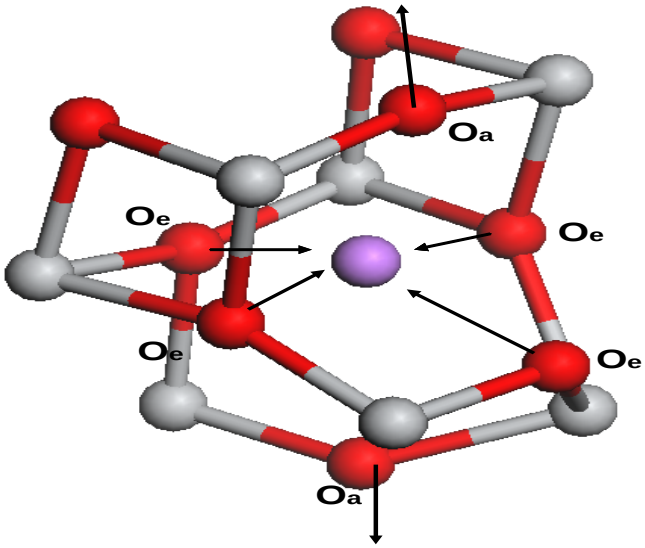

Figure 4.6 A Li insertion site in brookite. Here and in the following diagrams, O-ions are shown in red, Ti-ions in gray, Li ions in purple. The arrows indicate the structural relaxation upon intercalation.

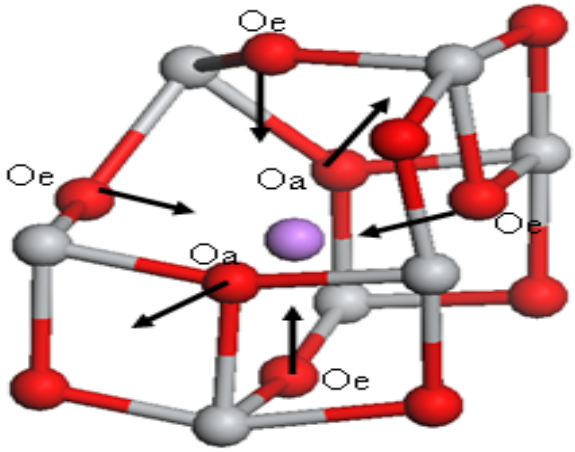

Figure 4.7 Displacements of O-ions around the inserted Li-ion. Equatorial O-ions are denoted Oe, apical O-ions are denoted as Oa.

The Ti-Ti distances across the insertion site (4.75 Å and 5.44 Å) are too short to place a Li-ion between them without considerable deformations. The resulting relaxation of the TiO_2 lattice affects the size of the neighbouring vacant interstitials, influencing the

ability to accommodate Li-ions upon further intercalation (Figure 4.7). The sites with larger Ti-Ti separations will be clearly more suitable for insertion of Li-ions, as electrostatic repulsion will be reduced. It has been demonstrated that in the rutile structure, where Li-intercalation also involves significant displacements of the neighbouring Ti-ions, the resulting ordering of Li-ions on the sites opened by this distortion governs the intercalation behaviour. Similar effects can be expected for Li-intercalation in brookite.

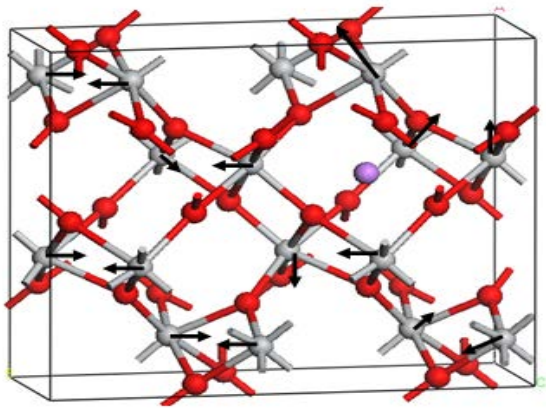

Figure 4.8 Displacement of the Ti-ions upon insertion of a Li-ion in brookite. Displacements of Ti-ions are indicated by arrows.

Direct calculations confirm that Li-occupancy results in strong deformations of the insertion site. At x=0.0625 (one Li-ion added to the $Ti_{16}O_{32}$ supercell) the shortest O-O distance across the site increases from 3.49 Å to 3.65 Å. The Ti-Ti separations across the Li intercalation site increase from 4.75 and 5.44 Å to 4.97 and 5.65 Å. The effect of these deformations on the neighbouring vacant sites is illustrated in Figure 4.8 and Figure 4.9, where the purple dot indicates the position of the Li ion; neighbouring interstitial sites closed by the deformation are shown in Figure 4.9 as blue circles and the sites opened by the deformation as red circles. Full circles represent the sites where the relaxation is largest. The correlation expected between intercalation energy and dimension of the interstitial site indicates the red circles as being the favourable positions for further intercalation.

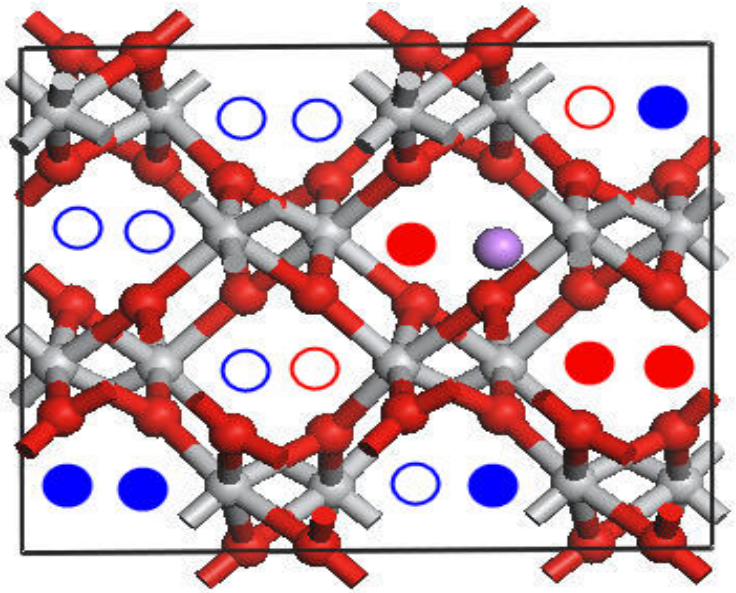

Figure 4.9 Insertion sites for further Li-intercalation at x=0.0625. Full red circles identify the most favourable sites; empty red circles show moderately favourable sites; full blue circles the most unfavourable sites, and empty blue circles moderately unfavourable sites.

Another source of local distortions is associated with Li-ions adopting a suitable O-coordination. Typically, Li-ions in titanates are coordinated to four to six neighbouring oxygen ions at approximately 1.8-2.1Å, with both coordination number and Li-O distances increasing with increasing Li-insertion concentration. In brookite, minor displacements of the O-ions (resulting in 2% contraction of the longest O-O distance) are only possible if Li-ions adopt a five-fold O-coordination. For the four-fold coordination the required change in some O-O distances is up to 6%, and for a six-fold coordination it is as much as 14%. Hence, it is likely that five-fold O-coordination will be adopted by the Li-ions over the whole range of insertion concentrations.

These simple considerations are confirmed by our ab initio simulations. The lowest concentration considered corresponds to one Li-ion added to $Ti_{16}O_{32}$ (a doubled unit cell along the *b*-direction, x=0.0625). At this concentration, the Li-ion inserted initially into a

tetrahedral site moves into an asymmetric position (at 0.403*a*, 0.691*b*, 0.449*c* or symmetry equivalent sites) to adopt a five-fold O-coordination and Li-O bond distances of 1.81 Å, 1.85 Å, 2.01 Å, 2.04 Å, and 2.15 Å; the 6th Li-O distance is 2.6 Å, clearly larger than the others.

In general, the geometry of an occupied Li-site closely resembles that in orthorhombic $Li_{0.5}TiO_2$, which is a phase adopted by lithiated anatase at x=0.5[58]. However, in anatase the orthorhombic phase is formed at intermediate Li concentrations (x=0.5); it is preceded by a tetragonal anatase phase with Li-ions coordinated to four O-ions (x<0.0625), and followed by a rock-salt like phase with Li ions coordinated to six O-ions (x=1).

Direct calculations in brookite confirm that at all Li-concentrations (x = 0.0625-1), Li ions are coordinated to five O-ions, at distances that gradually approach 2 Å with increasing Li-concentration. At x = 0.0625 the inserted Li-ion adopts an asymmetric position in the c-channels, being coordinated to five O-ions at 1.81-2.15 Å. The sixth Li-O distance decreases with x rapidly; since it various from 2.6 Å to 2.2 Å as a function of Li content. In the fully relaxed configuration at x=1 (16 Li-ions in the $Ti_{16}O_{32}$ supercell) Li-ions are coordinated to five O-ions at distances equal to 1.99 Å, 2.00 Å. 2.01 Å, 2.02 Å, 2.09 Å and the sixth O-ion is at 2.22 Å, which indicates an increased interaction with the 6th oxygen in brookite similar to what observed in other TiO_2 polymorphs. The results confirm that no phase transformation is expected to occur during the intercalation of Li into brookite.

4.2.5 Ordering of the Li-ions

The ability of vacant sites to accommodate Li in $Li_{0.0625}TiO_2$ is illustrated by Figure 4.10. The sites preferable for further Li-intercalation (red circles) have O-geometry close to that of a typical five-fold O-coordinated site and separations between Ti-ions across the site enlarged compared to undoped brookite. Closed red circles denote the most favourable sites for further insertion. Open red circles denote sites which have more suitable geometry than in pure brookite, but less than the full red positions; open blue

circles denote sites with the geometry close to that in undoped brookite, and full blue circles denote the most unfavourable sites, which are closed by the deformations.

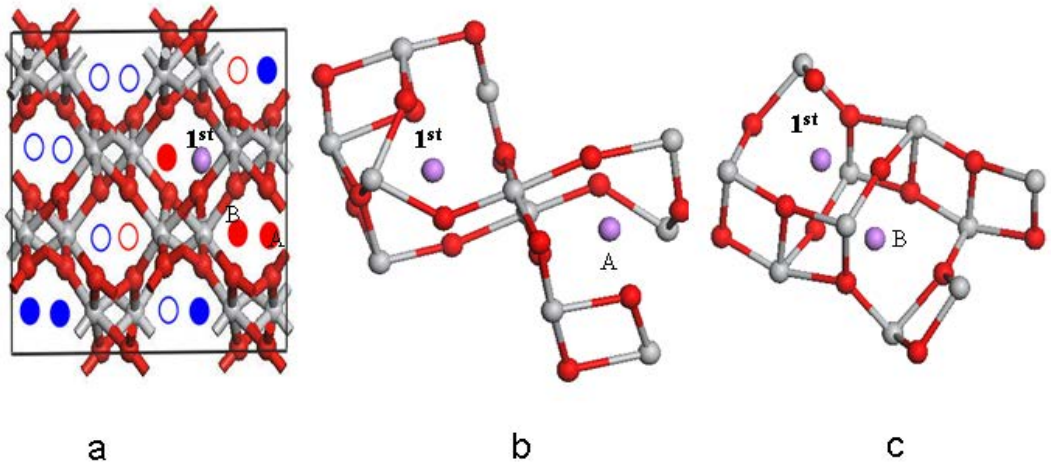

Figure 4.10 Relaxed brookite structure of $LiTi_{16}O_{32}$ showing the 1st Li and the two most favourable sites A, B for the insertion of a 2nd Li ion. Site A corresponds to the 2nd Li in a neighbouring channel, B in the same channel as the 1st Li ion.

As shown in Figure 4.10, the most preferable sites for further intercalation sites are located either in the same *c*-channel as the occupied site along a zigzag chains (site B) or in an adjacent channel (site A). Full optimization of various configurations at x=0.125 and x=0.1875 (two and three Li-ions per $Ti_{16}O_{32}$ supercell) confirmed that occupancy of the above sites is favoured over the others by about 0.02 eV and 0.03 eV per Li-ion respectively. The fragments of the fully relaxed structures with two Li-ions in the same *c*-channel and in the neighbouring *c*-channels are shown in Figure 4.10.

A similar analysis has been performed for higher Li-concentrations as shown in Figure 4.11 for x=0.125 and x=0.3125 (not the lowest energy configuration).

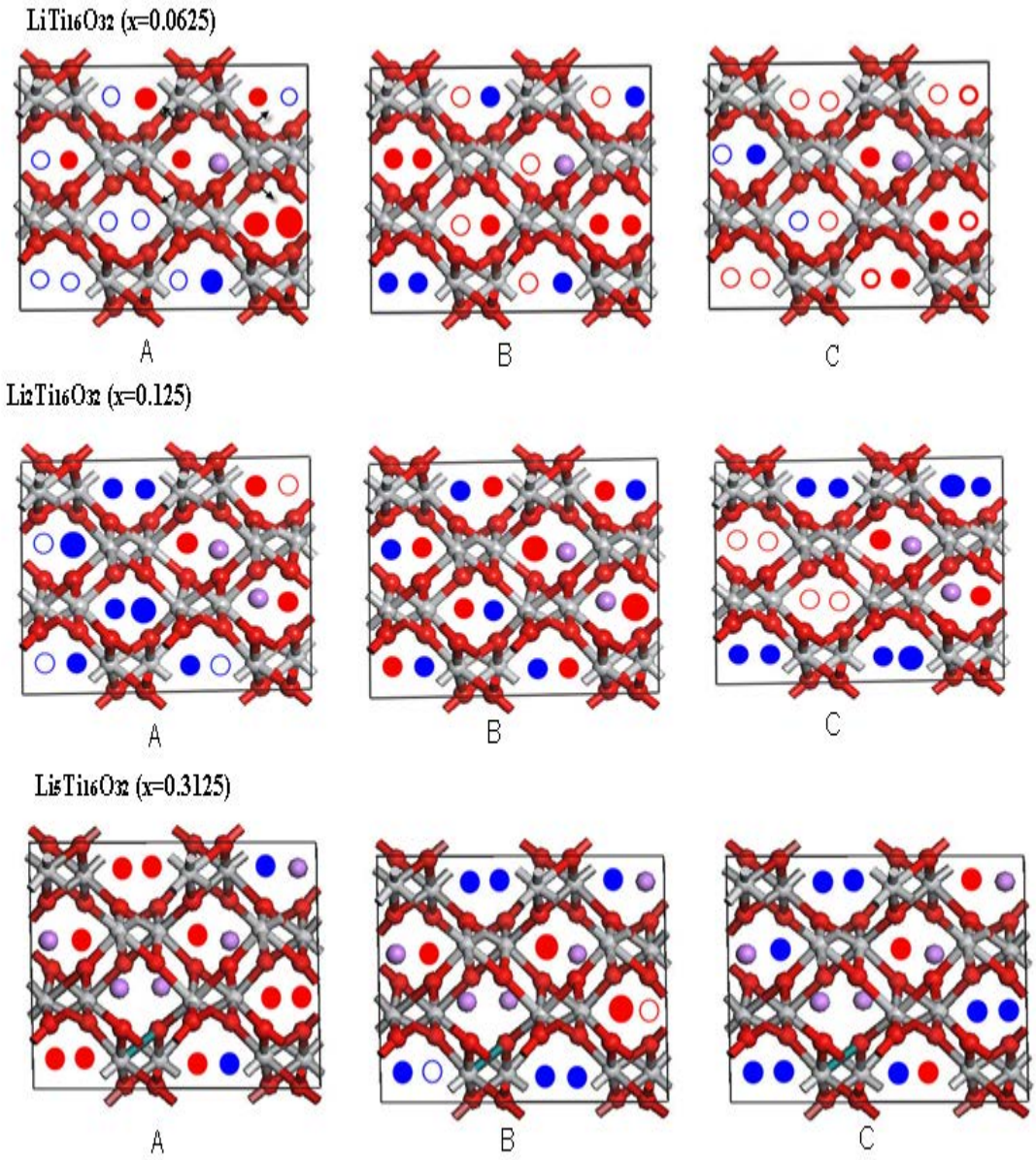

Figure 4.11 Estimate of relative stability for further Li intercalation at increasing concentrations (x=0.0625, 0.125, 0.3125) and considering A) the distances between O-ions. B) The distance between Ti-ions along the a-direction C) the distance between Ti-ions along the b-direction.

In this concentration range the most favourable sites for intercalation are ordered in a zigzag chain, while the unfavourable sites are outside the chain. Thus, Li-insertion into brookite will consist of at least two domains: once Li occupies a site in one of the zigzag chains, occupancy of the other sites along the same zigzag chain is expected to occur before occupancy of the remaining sites.

It is clear from Figure 4.11 that more sites have "improved" O-geometry as Li-concentration increases. This trend is due to a structure expansion on increasing Li content, which requires less expansion of the interstices to accommodate further Li ions. At x=0.3125 the geometry of nearly all vacant sites does not require additional O-displacements upon Li-occupancy. At the same time, the number of sites "closed" by displacements of Ti-ions along the a-direction, and especially, the *b*-direction increases. At x=0.375 all the sites are closed by the distortion associated with displacements of Ti-ions along the *b*-direction, and the ordering pattern of Li-ions is therefore expected to change.

In order to verify the predicted ordering of Li-ions, the lowest energy configurations were sought over the complete range of Li-concentration from x=0 to x=1. At each concentration (n*0.0625, where n is a number of Li-ions added to the $Ti_{16}O_{32}$-supercell, n =1, 2 ...16) various representative configurations were fully relaxed and their computed energies compared. A representative selection of lowest energy configurations are displayed in Figure 4.12. As predicted, at $1 \leq n \leq 6$ Li ions occupy positions in zigzag chains. Despite full occupancy in zigzag chains corresponds to n=8, at n=7 the occupancy pattern changes dramatically, because at n=6 the vacant sites in zigzag chains are closed by the displacements of Ti-ions as discussed above. At n=7 Li-ions are separated in different channels, being randomly distributed over two available sites. At n=8 half of the positions in every *c*-channel is occupied by Li-ions.

This configuration is more stable than the configuration corresponding to completely filled zigzag chains by almost 0.07eV per Li-ion. At $10 \leq n \leq 15$ Li-ions occupy the remaining sites; there is a slight tendency for Li-ordering even at these concentrations, however the difference in total energy between various structures at a given

concentration does not exceed thermal energy at normal conditions and therefore will not be considered here. Hence, a random occupancy of the available sites is expected.

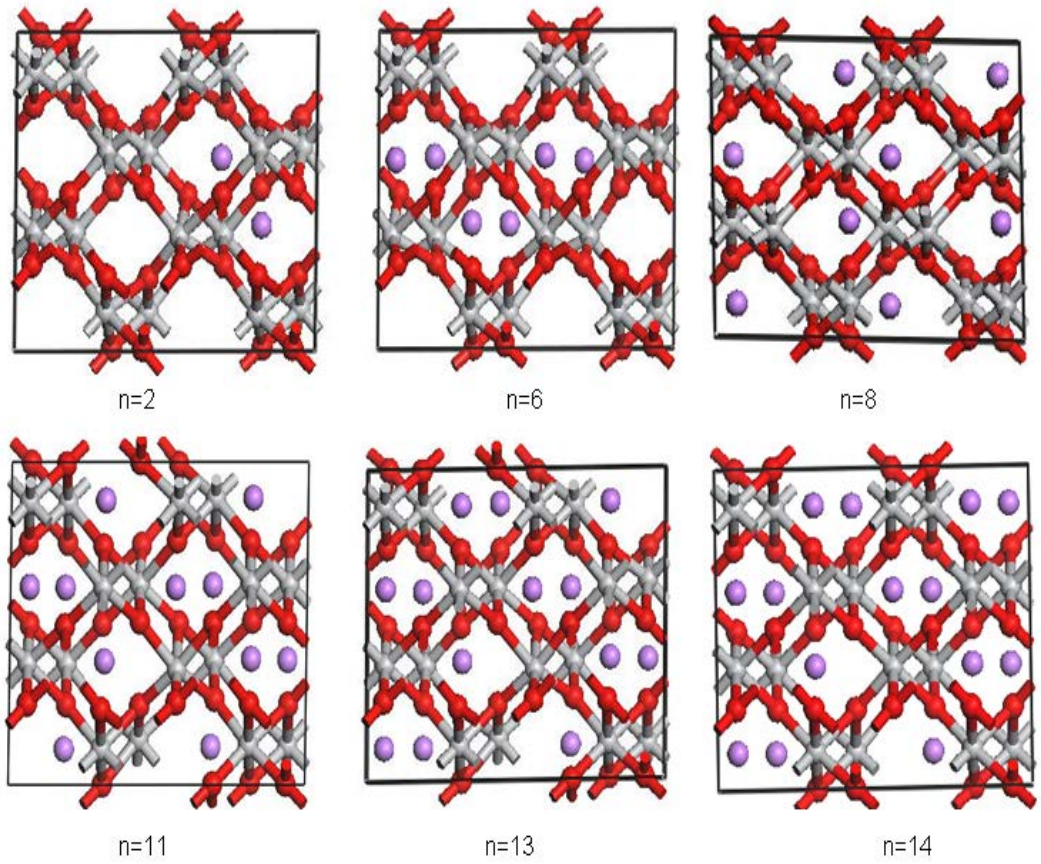

Figure 4.12 Lowest energy configurations of $Li_nTi_{16}O_{32}$ at n=2, 6, 8, 11, 13 and 14.

Figure 4.13 shows the volume of the unit cell during the intercalation process. The volume increases with increasing Li concentration from 523.94 $Å^3$ to a maximum of 557.45 $Å^3$ (an expansion of 6.39 %). We note in the figure a small discontinuity at Li concentration of 6-8 ions. The reason behind this is that the Li ions insert into sites which are already 'open' due to the deformation of the cell during Li filling to 6 ions, while as discussed above the ordering pattern changes at n=7.

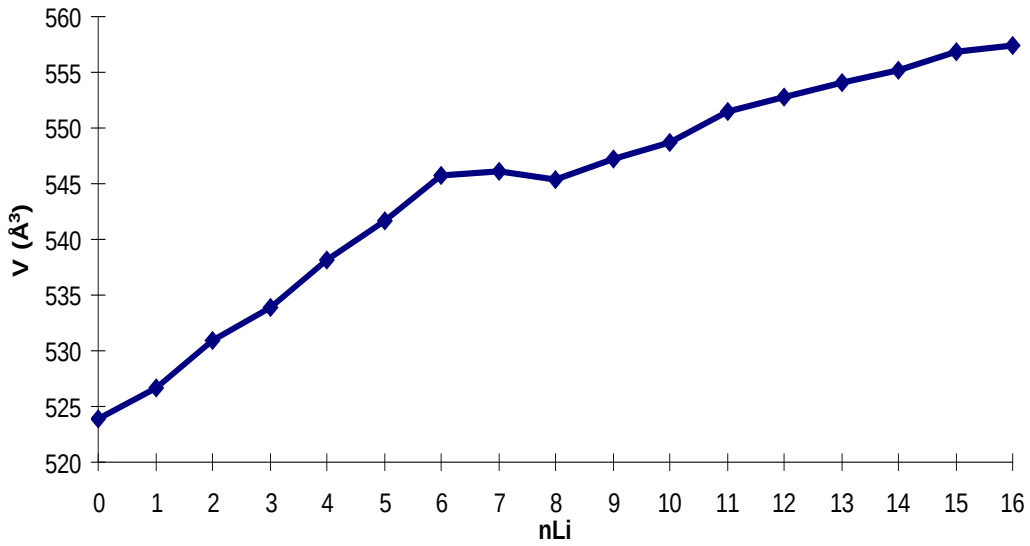

Figure 4.13 Volume change of a unit cell of $Li_nTi_{16}O_{32}$ as a function of Li concentration during intercalation.

Let us now examine the intercalation energy associated with the Li insertion, calculated using the following equation:

$$\mathbf{E_n = [E\ (Li_nTi_{16}O_{32}) - E\ (Li_{n-1}Ti_{16}O_{32}) - E\ (Li)]} \qquad \mathbf{(4.1)}$$

where E_n is the intercalation energy and n is the number of Li ions in the system. A graphical plot of the results is shown in Figure 4.14. The energy of metallic Li has been calculated consistently with that of the TiO_2 and Li_xTiO_2 phases.

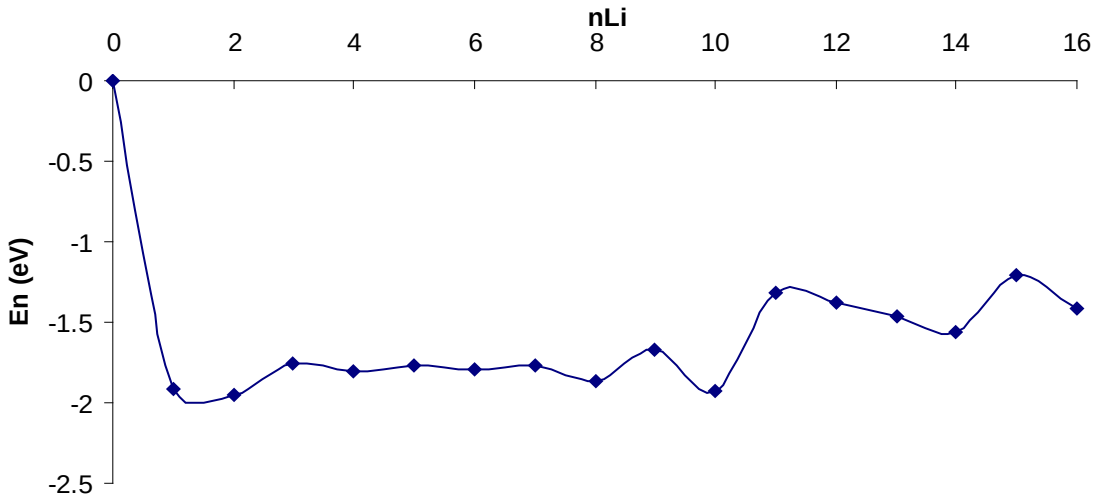

Figure 4.14 Li intercalation energy in $Li_nTi_{16}O_{32}$ as a function of Li concentration.

As we see in Figure 4.14, the Li intercalation is energetically favourable (E_n<0) up to a value of n=16, corresponding to composition $LiTiO_2$. Intercalation of the first Li ion in the supercell yields intercalation energy of -1.91 eV. Insertion of a second Li ion yields slightly larger change in energy of -1.95 eV, with the increase being an indication of cooperative distortions. Beyond two Li ions however, we find that intercalation up to 8 Li ions yields lower energies (energy average -1.79 eV). These low energies are due to the zigzag arrangement of Li ions in the unit cell; the structure has already 'opened' local minima that can host the Li atoms are accessible due to the cell deformation.

At a concentration of 9 Li ions the intercalation energy is -1.67 eV which is relatively low, and may be due to the stable arrangement of Li atoms at n=8 corresponding to a $Li_{0.5}TiO_2$ phase. At a concentration of 10 Li ions however, we see more favourable energy and this is likely due to the opening of a stable site once 9 Li ions are in the cell. Concentrations of 11 to 16 Li ions yield relatively lower energies with the average - 1.39 eV for intercalation due to the shielding effect of Li ions which prevent further Li intercalation.

Overall, the calculated intercalation energy averaged over the whole range of Li content from 0 to full occupation is -1.66 eV, consistent with brookite being a suitable anode material for Li batteries.

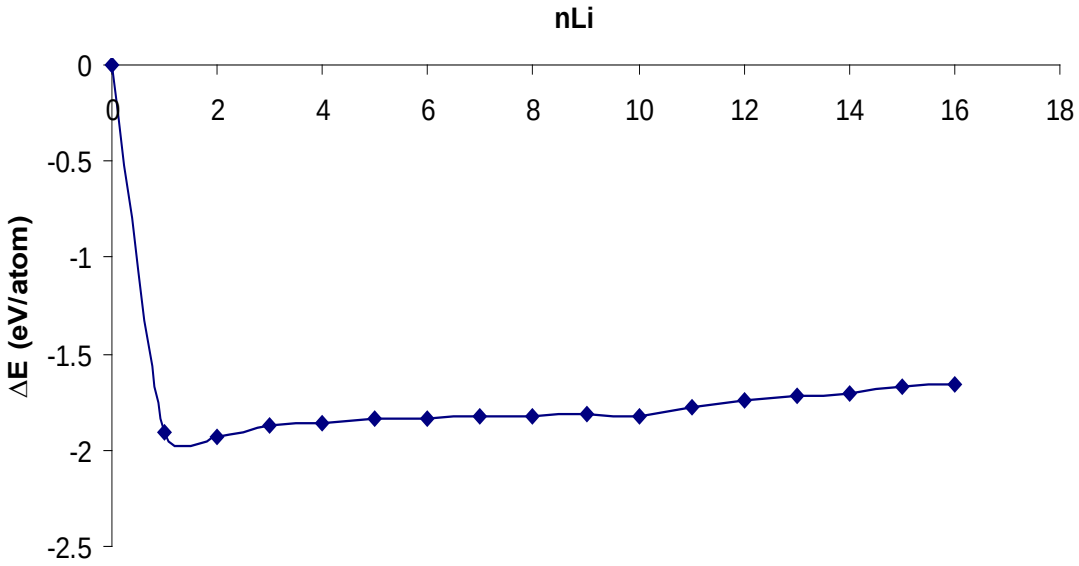

Figure 4.15 Average intercalation energy as a function of nLi.

Equation 4.1 yields the evolution of the intercalation energy as a function of Li concentration. A second quantity of interest is the average intercalation energy, which can be calculated using equation 4.2 below:

$$\langle E_n \rangle = [E(Li_nTi_{16}O_{32}) - E(Ti_{16}O_{32}) - n\,E(Li)] / n \qquad (4.2)$$

For completeness, the variation of <En> with nLi is shown in Figure 4.15. The averaging process makes <En> smoother than En in equation 4.1 and we only observe a small monotonic decrease of <En> on increasing Li content.

Figure 4.15 shows that the average intercalation energy decreases with increasing Li loading, consistently with the most favourable sites being occupied first. The average intercalation energy in the range n=0 - 16 (x=0-1) is -1.8 eV ($LiTiO_2$ Composition).

Figure 4.16 shows the changes in the cell parameters during the intercalation process. The *a*, *b* cell parameters expand monotonically on insertion of Li, with the exception of the concentration n= 8 due to the change in the intercalation mechanism as discussed earlier. The *c* lattice parameter expands when intercalation opens one of the zigzag chains of the structure (i.e. between n=1, 2 and n=7, 8), while it contracts when the new Li ions occupy a zigzag chain that is already partially occupied by Li ions. Cell angles are also reported for the complete series in Figure 4.17. Changes in the cell angles are more erratic as a function of intercalation but in any case small and not relevant.

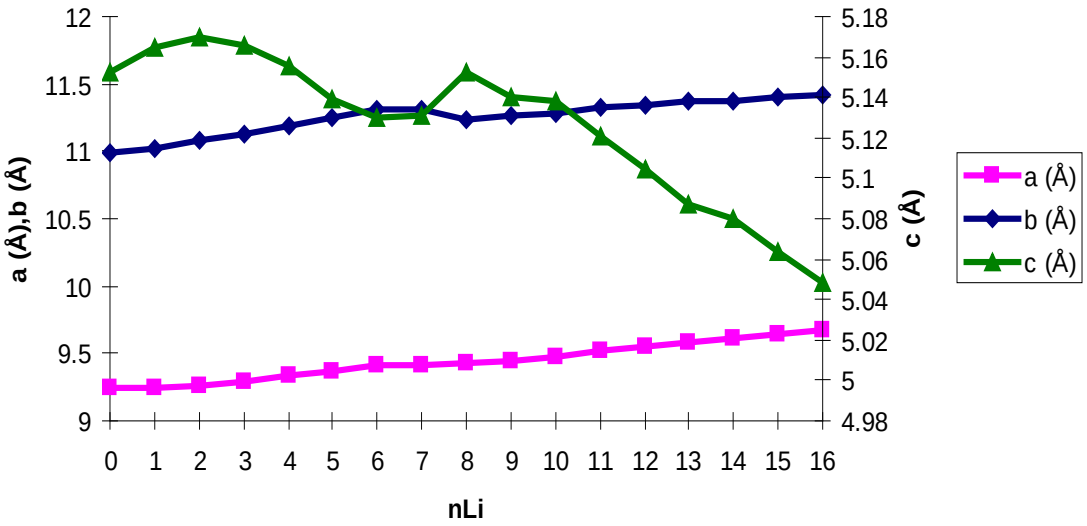

Figure 4.16 Cell parameters a, b, c in Å of brookite during the Li intercalation.

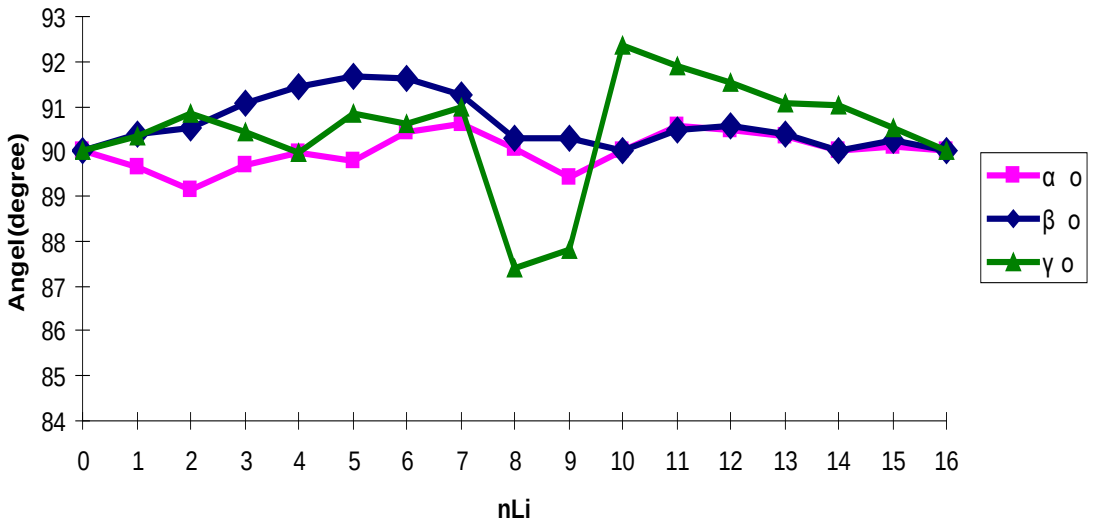

Figure 4.17 Representation of the equilibrium cell angles during the intercalation process.

Upon lithiation of brookite the geometry of the TiO_6 octahedra becomes gradually more regular. However, even at x=1, Ti-ions are still slightly off centre in the TiO_6 octahedra, forming bonds of 1.99, 2.03 Å (Ti-Oa), and 2.03, 2.09, 2.1, 2.1 Å (Ti-Oe). The Ti-Oe bonds as well as pairs of Ti-Oa and Ti-Oe bonds are coplanar. At x=1 all O-Ti-O angles are close to 90^o (Oe-Ti-Oe: 89^o, 89^o, 90^o, 91.7^o; Oa-Ti-Oe: 88^o, 89^o, 91^o, 92^o, Oa-Ti-Oa: 87^o, 90^o, 91^o, 92^o). Li-ions are separated by about 2.9 Å, Li-Ti distances are 2.54, 2.84, 2.84, 2.88, 2.89, and 2.89Å. Li-ions are coordinated to six neighbouring O-ions at 1.99, 2.00, 2.01, 2.02, 2.09 and 2.22 Å. Compared to the parent structure of brookite (x= 0), the structure at x= 1 expands by about 6%. This is in contrast to rocksalt $LiTiO_2$, formed upon lithiation of $Li_{0.5}TiO_2$ spinel and anatase, where the structure contracts upon intercalation. This indicates that neither the packing of Ti and Li polyhedra in brookite is optimal, nor are the interactions between Li-ions efficiently screened by the lattice.

Examination of the intercalation energies given in Figure 4.13, suggests that Li intercalation is energetically favourable and it proceeds homogeneously, with a plateau of intercalation potential between x= 0.125 and x= 0.5. Local maxima of intercalation energy exist at concentration n=9 and n= 11 suggesting that two phase equilibria may be present at these loadings. However, energy differences are small and may be repressed

by thermal effects. Therefore, at normal conditions, Li-insertion is likely to proceed homogeneously in the whole range of insertion concentrations.

4.2.6 Diffusion of Li-ions

The homogeneous nature of Li-insertion into brookite, together with the strong site preference at $0<x\leq0.5$, implies that the intercalation behaviour of brookite observed experimentally may be strongly limited by accessibility of the intercalation sites. The latter depends on the operating temperature and the particles size. In calculations the accessibility is characterized by barriers for diffusion of Li-ions between the stable sites.

To complete the computational characterization of the process, such migration barriers were calculated for a number of lowest energy configurations, by fixing a Li-ion in positions along the pathway from one stable site to another, while the positions of all other ions were fully relaxed.

At low Li insertion concentrations n= 1, x= 0.0625 the Li ion is fixed in positions along two favourable energy sites as shown in Figure 4.18.

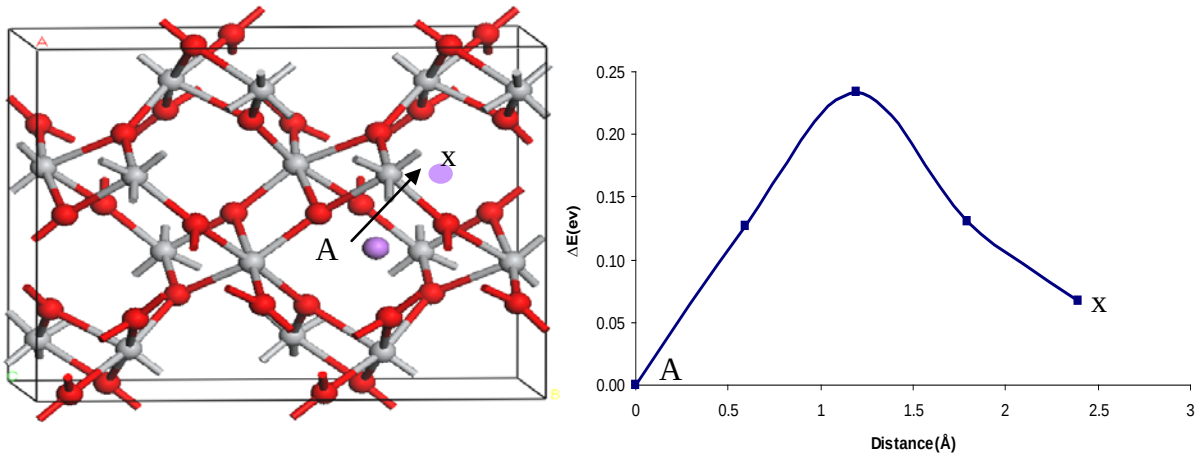

Figure 4.18a. Migration pathway of Li between two favourable energy sites for x=0.0625 ($LiTi_{16}O_{32}$) b. Energy–position diagram; showing the presence of a local maximum which indicates that Li migration is an activated process, whose activation energy can be estimated by this energy diagram.

The two sites A and X examined are similar, but not symmetry equivalent. The calculated diffusion path between the two favourable energy sites shows an energy barrier of 0.23 eV which represents the activation energy for the Li migration at low concentration. This computational process has been repeated for different Li concentrations.

At Li concentration of n= 2, x= 0.125 the diffusion barrier increases dramatically to 0.58 eV, as shown in Figure 4.19 where we report the migration path and the corresponding energy profile. The increase in activation energy is consistent with the presence of cooperation Li-Li effects during the intercalation, discussed earlier when considering intercalation energies.

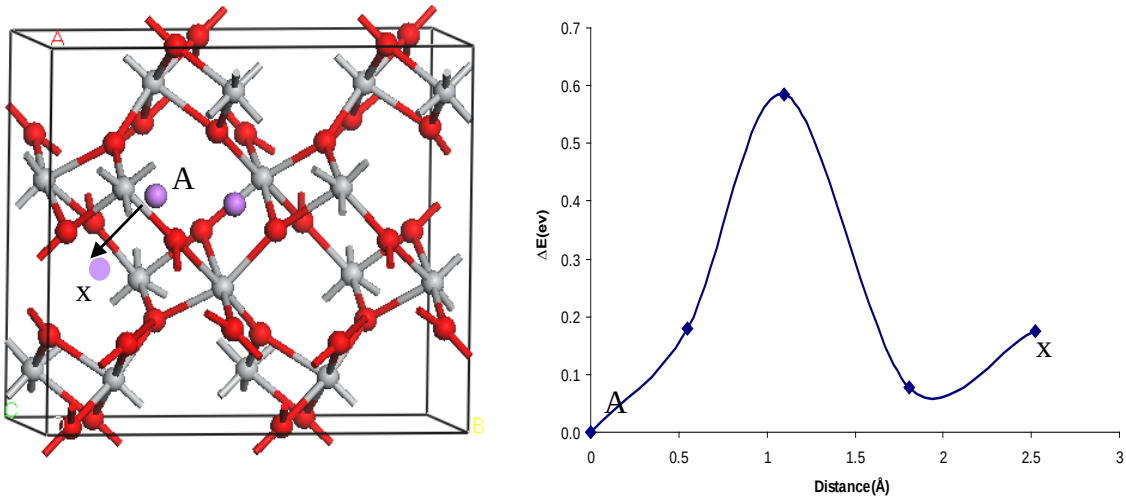

Figure 4.19 a) pathway between two favourable energy sites (A-X) for $Li_2Ti_{16}O_{32}$; b) corresponding energy profile.

We notice in Figure 4.19 that the minimum energy position at the end of the migration path does not corresponding exactly with point X. The end-point (X) of the migration path was chosen as the stable intercalation site for n= 1; the fact that this is no longer the final minimum for the Li disposition examined at n=2 indicates again the presence of cooperative Li-Li effects.

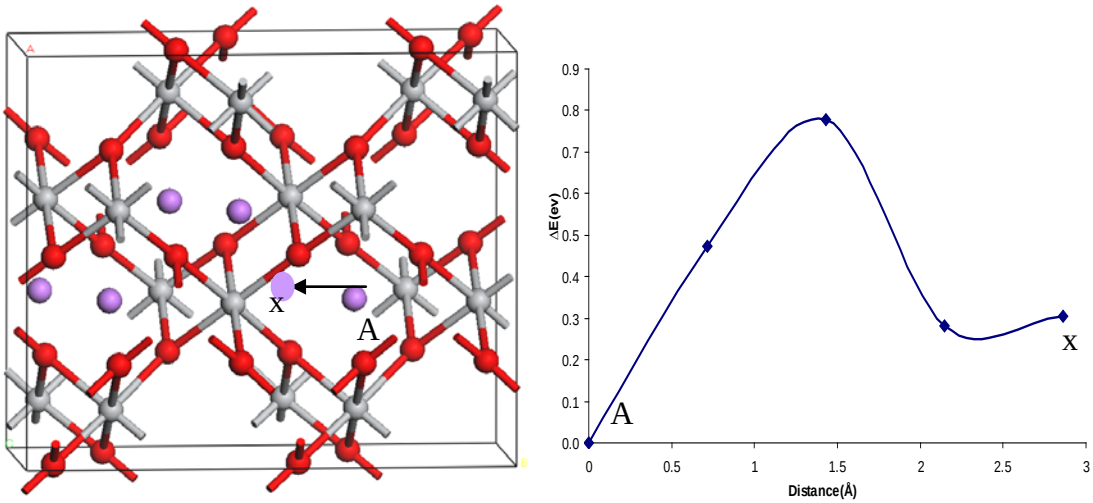

Figure 4.20 Li migration profile in brookite at n= 5 ($Li_5Ti_{16}O_{32}$).

Similar calculations have been repeated for all values of n between 1 and 16. Representative migration paths considering to n=5 and n=15 are shown in Figure 4.20 and Figure 4.21.

At concentration of n=5, x=0.3125 the energy barrier is equal to 0.78 eV, according to the Li arrangement show in Figure 4.20. The diffusion behaviour with relatively high activation barriers indicates that at normal conditions Li-ions may not be able to reach their most stable sites, or be trapped in metastable sites of the structure. This prediction is in line with the negligible Li-insertion observed into polycrystalline brookite, and the improved behaviour in nanostructured brookite anodes. At concentrations between Li= 7 to 14 (x= 0.4375 to 0.875) the energy barriers further increase, to over 1.1 eV, which is an indication of trapping of Li-ions in their positions in the zigzag chains. At very high Li-concentrations n=15 (x=0.9375) shown in Figure 4.21, the diffusion barrier exceeds 1.1 eV indicating that the phase at x= 1 is may be unattainable in practice.

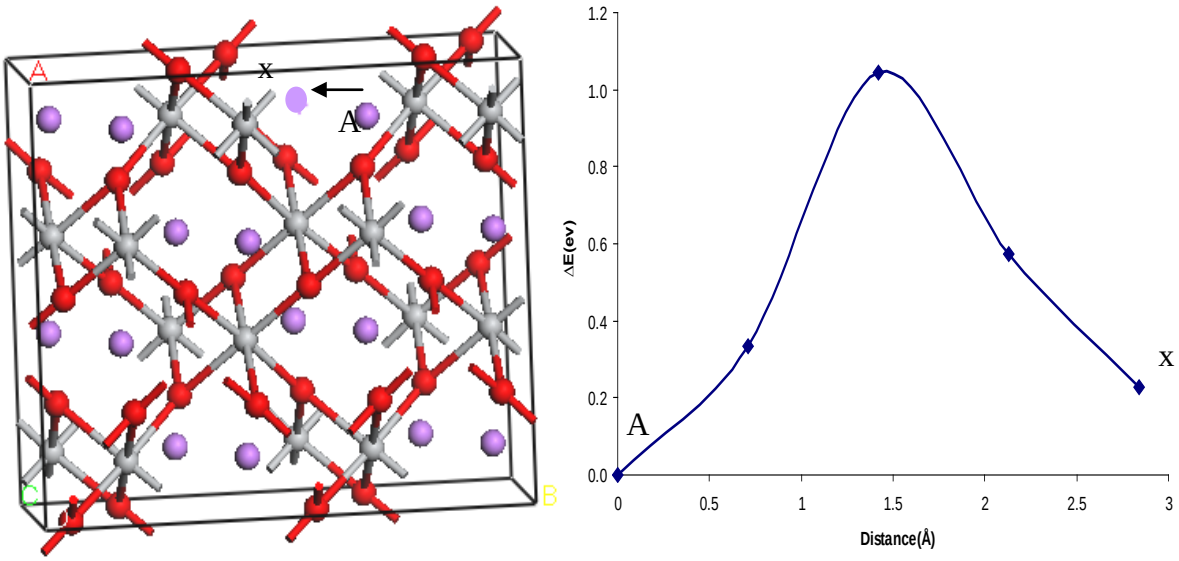

Figure 4.21 Li migration profile at n= 15 ($Li_{15}Ti_{16}O_{32}$).

The evolution of the calculated migration profiles as a function of Li concentration is clear in Figure 4.22, which reports the energy vs distance profile of the migration path for n= 1, 2, 5 and 15. It is noted not only that the activation energy increases with n, but also the length of the Li migration path changes, an indication of long ranged Li-Li interactions in the solid. The location of stable intercalation sites depends in practice on the local distribution of Li surrounding the site examined.

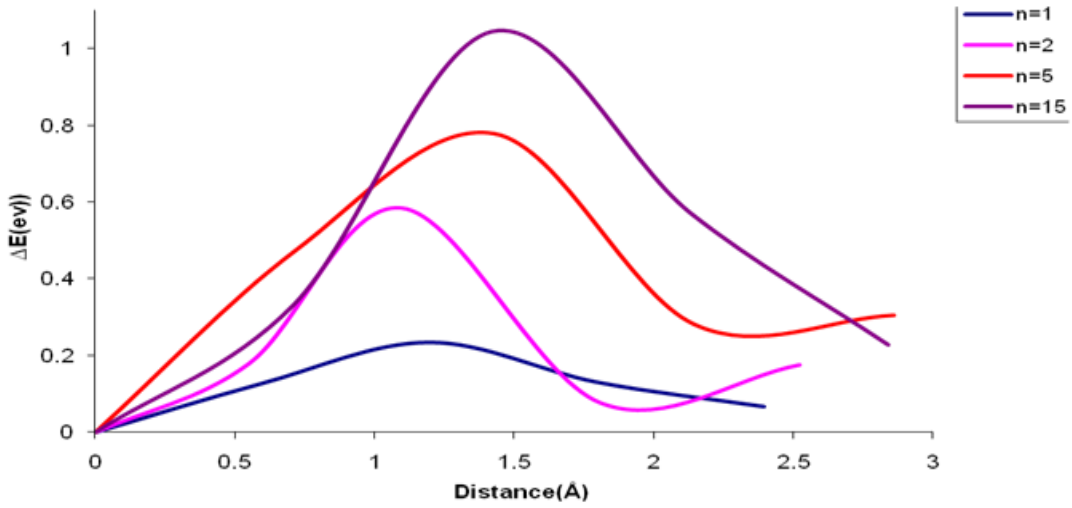

Figure 4.22 Energy – Distance profile for Li migration at concentrations n=1, 2, 5 and 15.

4.2.7 Summary

Using *ab initio* simulations, the intercalation behaviour of brookite structured titania has been studied with respect to Lithium to yield Li_xTiO_2. The stable sites and the lowest energy configurations were identified and their computed energies were used to elucidate the mechanism of Li-intercalation thermodynamically, up to full occupancy of the available intercalation sites (x=1). It was demonstrated that Li intercalation is homogeneous but consists of three domains, corresponding to different ordering patterns: the occupancy of zigzag chains at $0<x\leq0.375$, configurations with maximum separation between Li-ions (x=0.435, 0.5); and random site occupancy at x>0.5. It is shown that Li-intercalation is strongly limited by the diffusion of Li-ions, especially at high Li content, resulting in the absence of intercalation at normal conditions, and intercalation to high concentrations at elevated temperature or in the nanophase.

4.3 Li Intercalation into TiO_2-B

4.3.1 Introduction

The B polymorph of TiO_2 is one of the new materials investigated as anodes for Li-ion batteries, and is receiving increasing attention[70,71,72]. The interest in TiO_2-B[73] is due to its improved ability to intercalate Li ions compared with rutile[74,75], anatase and brookite[76]. TiO_2-B has a high theoretical capacity and shows good electrochemical properties[77,78,79]. In this section of the thesis the lithium ion intercalation into the TiO_2-B structure is investigated and the energy barriers for Lithium intercalation and diffusion are calculated in a similar way to the study of brookite in the previous section. To do so, the TiO_2-B structure is first analysed and the most favourable intercalation sites are evaluated based on the local environment of the empty interstices of the lattice. These data cannot be obtained reliably from XRD experiments because of the weak X-ray scattering power of the light Lithium ions within the host; the mechanism of intercalation and diffusion affects electrochemical properties like the charge/discharge rate. Earlier computational studies are available, comparing TiO_2-B[80,81,82] to other titanates which suggest that Li can be inserted in sites with four, five and six fold coordination with oxygen ions[83].

As for brookite discussed earlier, the ab initio simulation code CASTEP was used to model the intercalation of Li in TiO_2-B using Density Functional Theory. All calculations were performed using the pseudopotential plane-wave formalism[65,66]. Electron exchange and correlation effects were treated within the Generalized Gradient Approximation (GGA) using the Perdew and Wang functional (PW91)[67]and ultrasoft pseudopotentials[68]. Reciprocal space was sampled using a regular net with a consistent spacing of 0.05 $Å^{-1}$. Plane wave cut-off energy of 380 eV was found to converge the total energy to within 0.01 eV per formula unit. The size and shape of the cell and all internal degrees of freedom were fully relaxed with respect to the total energy. While this work was being carried out, a similar study by M. Islam et al.[84] was performed using a different set of computational parameters[85,86]. This section compares the results obtained here with those of ref [84]. Because of this recent publication, only the initial stages of Li

intercalation in TiO_2-B are discussed here, which were obtained prior to the publication of ref [84].

4.3.2 Structural details of the TiO_2-B polymorph

According to previous studies, the TiO_2-B structure was assumed to be iso-structural with VO_2-B[81] in that it contains corner and edge-sharing TiO_2 octahedra and the most favourable site for Li insertion is slightly off-centre in the z channel. TiO_2-B has a monoclinic structure with space group *C2/m* and calculated cell parameters a = 12.269 Å, b = 3.76 Å, c = 6.612 Å and $\alpha = 90.0^o$, $\beta = 106.9^o$ and $\gamma = 90.0^o$ compared with the experimental cell parameters a = 12.179 Å, b = 3.741 Å, c = 6.525 Å and $\alpha = 90.0^o$, $\beta = 107.1^o$ and $\gamma = 90.0^o$[87]. Figure 4.23 represents the polyhedral form of the TiO_2-B structure.

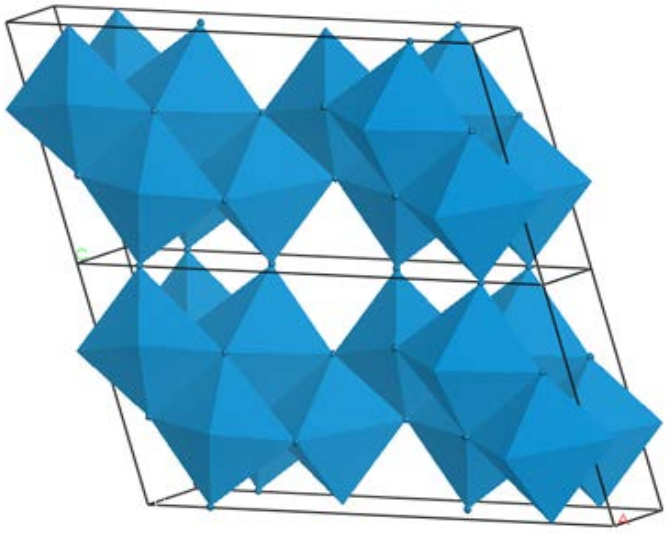

Figure 4.23 The structure of TiO_2-B in polyhedral representation.

As already discussed in the section on brookite, the connectivity of TiO_6 octahedra plays an important role in understanding the mechanism of Li-insertion into titanates[59,60]. The GGA approximation employed in our calculations yields slightly overestimated bond distances compared to experiment, however, this error is small and systematic, and unlikely to affect results on Li intercalation. In order to identify the most favourable sites for Li intercalation in the TiO_2-B polymorph, we used a 1x2x1 supercell of the crystallographic unit cell, shown in Figure 4.24, with composition $Ti_{16}O_{32}$.

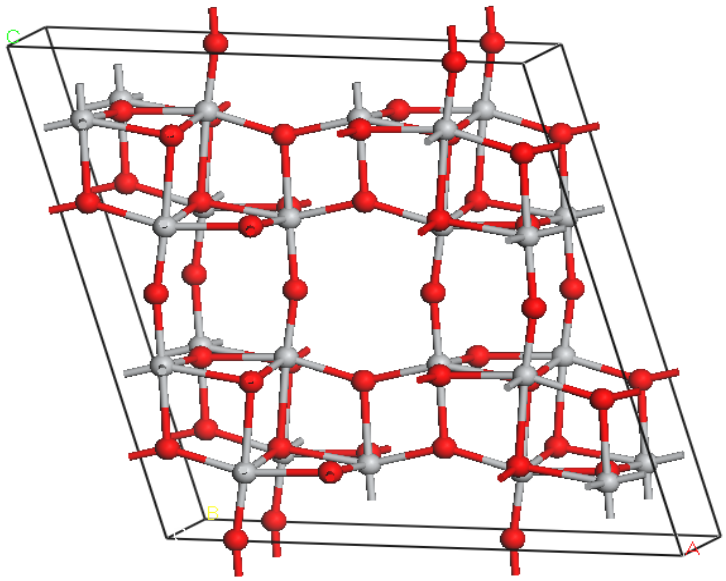

Figure 4.24 1x2x1 Supercell of TiO_2-B employed in our calculations.

4.3.3 Li-insertion sites

As the first step in this investigation, the geometry of interstitial sites in TiO_2-B structure, which can potentially accommodate Li-ions was examined, and compared with a typical Li-O and Li-Ti environment. This gives an indication of possible Li-coordination at various Li-concentrations and a possible number of stable Li-phases. As mentioned in the previous section, Li-ions are coordinated to four, five or six neighbouring oxygen ions at approximately 1.8-2.1Å, with the coordination number as well as the Li-O distances increasing with Li-concentration. The changes in Li-O coordination are typically associated with a collective distortion of the host lattice, and

sometimes phase transformations. The required deformations are minor and result from accommodation on Ti of the electron charge density donated by the Li-ions upon intercalation, and from the site of Li^+ ions.

As done for brookite, the interstices with the most appropriate local environment for intercalating Li ions[88] were first identified. Three possible sites available for the Li-ions in the TiO_2-B structure are indicated as A, B, C in Figure 4.25, and further highlighted in Figure 4.26. The B site is four fold coordinated and it is located in the middle of the cage of Ti, O ions along the *b* axis; the interstice is at the centre of a square-planar arrangement of the oxygen atoms. The C site is 5 fold coordinated to oxygen within the same plane of B but oriented along the *a* axis. The A site is also 5 fold coordinated and lies between the bridging oxygens; it points along the *c* axis. Site A and C provide a trigonal bipyramidal environment for Li.

Having identified the possible Li intercalation sites, actual calculations have been performed with one Li ion in each of the three interstices, to rank their relative stability. The position labelled B corresponds to the site with most favourable intercalation energy in the structure, with intercalation energy of -0.87 eV: The next stable energy site is A which is located at a position of five fold coordination, with intercalation energy of -0.68 eV; the least favourable energy site is C which is also five fold coordinated, with intercalation energy of -0.58 eV. We found in agreement with the recent work by Islam and coworkers[84] that in the B site, the Li ion is located very slightly off-centre in the interstice along the *b* axis with average Li-O distances of 2.47 Å. These results are in agreement with recent neutron diffraction studies, which indicate that the Li ion occupies off-centre B sites in bulk Li_xTiO_2-B for $x \leq 0.25$[84]. This is similar to what was observed in rutile[89].

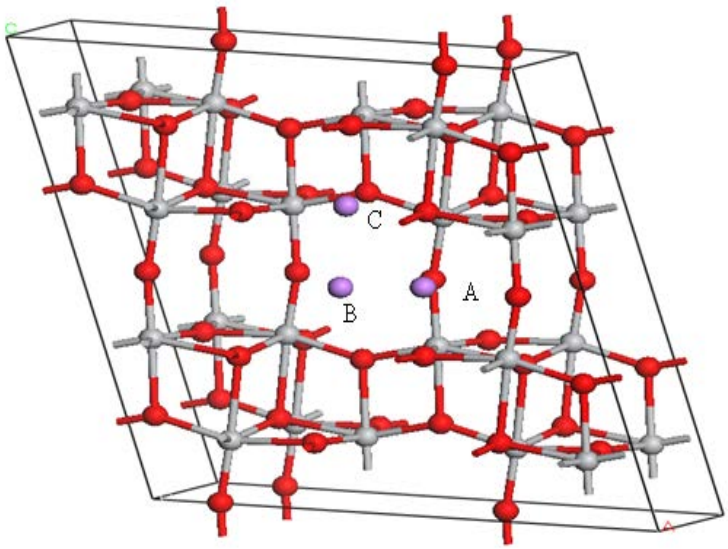

Figure 4.25 Available Li intercalation sites in a 1x1x2 supercell of TiO_2-B.

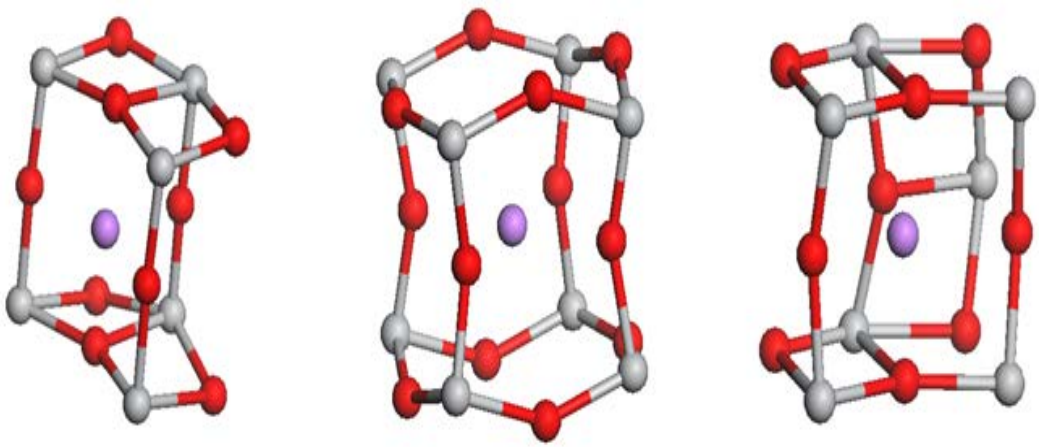

Figure 4.26 Interstices of the TiO_2-B structure.

The intercalation energy in TiO_2-B, -0.87 eV per Li ion at the initial stage of the intercalation (compared to -1.41 eV found by Islam and co-workers[84]), is considerably smaller than the one found earlier for brookite, of -1.91 eV for n=1.

If confirmed, this result is very important: the Li intercalation energy in the anode of a battery needs to be as low as possible; hence TiO_2-B is much more suitable than brookite for such applications.

4.3.4 Lithium diffusion

As already discussed for brookite, the mechanism and the energy barriers for Li diffusion plays an important role for Li battery performance. This section examines the process in TiO_2-B.

The relative energy calculated for Li in the interstitial sites of TiO_2-B showed that position B is the most favourable site, so that upon intercalation the first Li ion is expected to occupy this position.

At low Li values, we need to consider B-B migration pathways. As shown in Figure 4.27, adjacent B sites along the *x* crystallographic direction are connected through an A type interstice; along the *y* direction adjacent B sites are connected via a C type interstice, while along *z* two B sites are separated by a 4 member ring of TiO_6 octahedra. The Li migration profile along each of these directions is also examined.

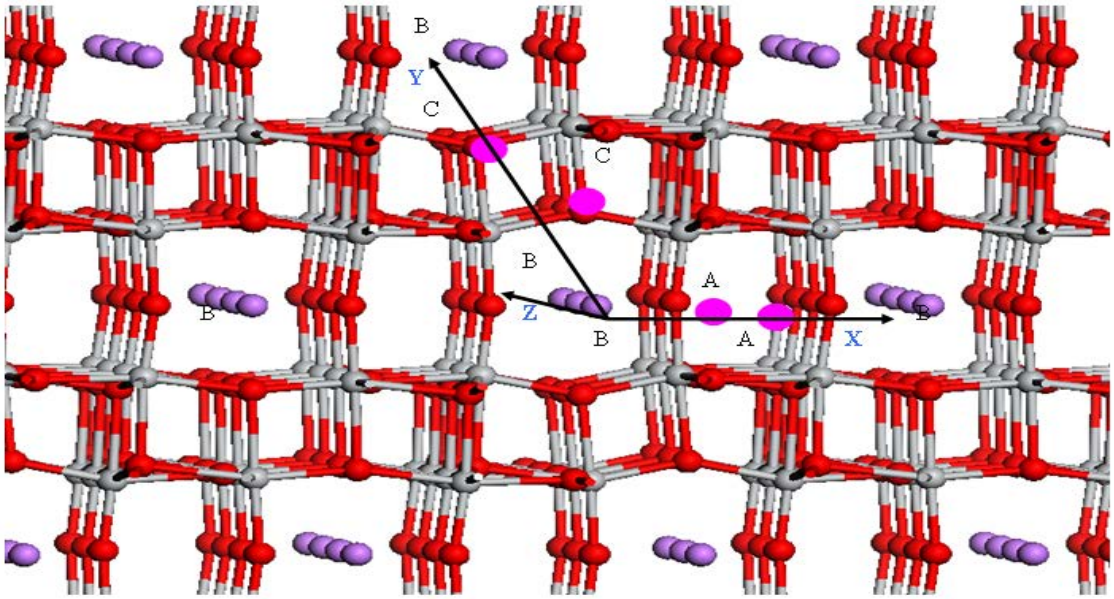

Figure 4.27 Li-ion (purple) in B site and possible diffusion patterns directions along *x*, *y* and *z*. Pink circles show the A and C sites, red is oxygen and grey is Ti.

Figure 4.28 represents the initial and final B type interstices, for migration along *z*; the highest energy on the pathway is related to Li passing through the 4 member window. The energy profile for the diffusion pathway is shown in Figure 4.28.b, and yields a calculated diffusion barrier of 0.32 eV; the path is linear along the *z* direction.

For the *x* pathway, the migration of the Li-ion between B sites through the A position occurs in zigzag shape, as shown in Figure 4.29.a; the energy profile between the two B sties is shown in Figure 4.29.b. The calculations show that migration along *x* is unfavourable, the highest barrier is related to Li passing through a Ti_4O_4 window of 8 atoms members (4 Ti, 4 Oxygen) with an activation barrier of 0.99 eV.

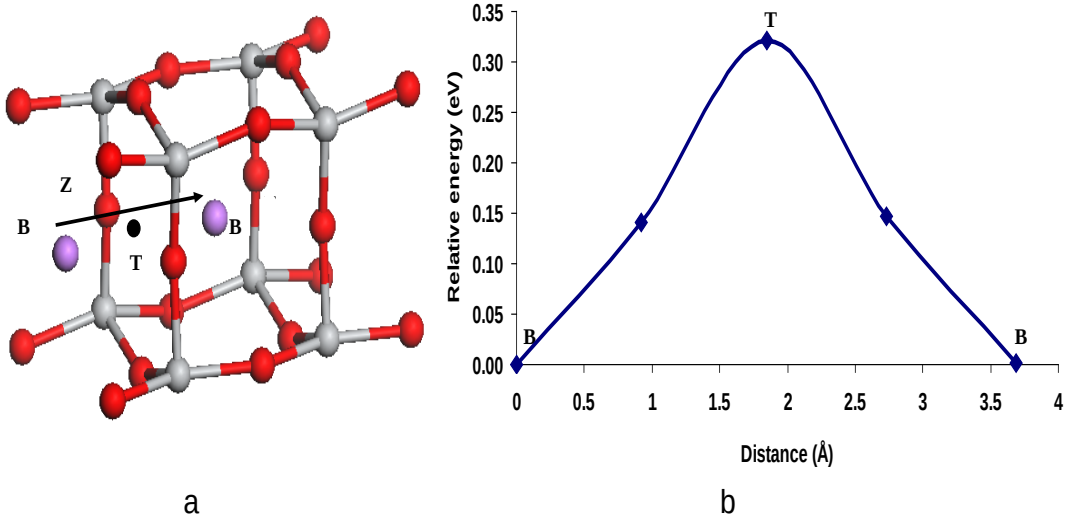

Figure 4.28 a) Migration along *z* between two B sites. b) Calculated energy profile for this Li migration pathway.

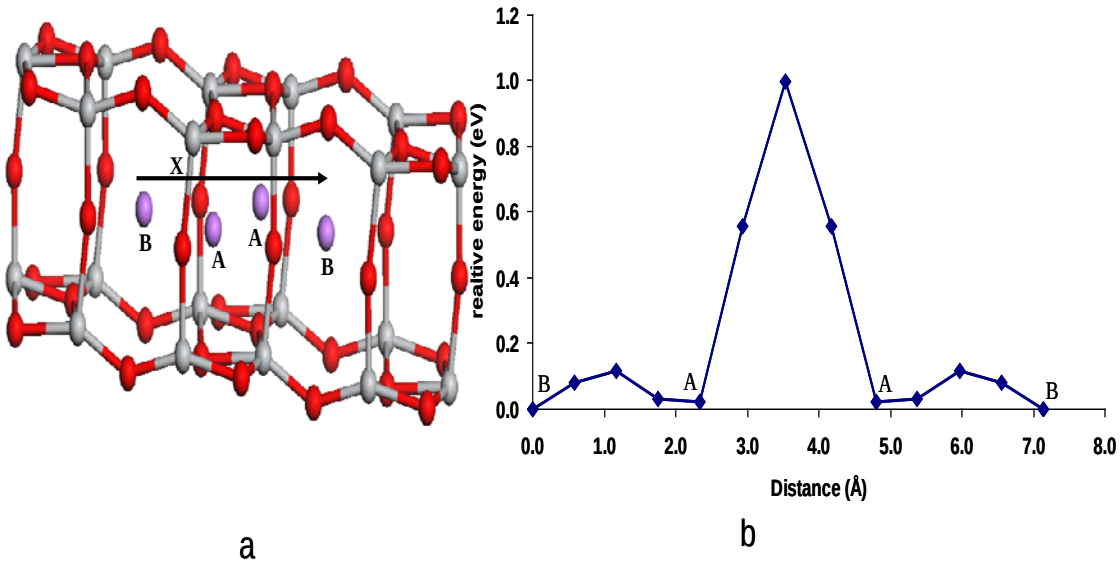

Figure 4.29 a) Li migration pathway along *x* between two B sites, through the path BAAB b) calculated energy profile.

The migration of the Li-ion between B sites along *y* occurs through a path BCCB, also with a zigzag shape (see Figure 4.30.a.). The energy profile is shown in Figure 4.30.b; the highest energy barrier for this migration path is of 0.56 eV, between the two C interstices.

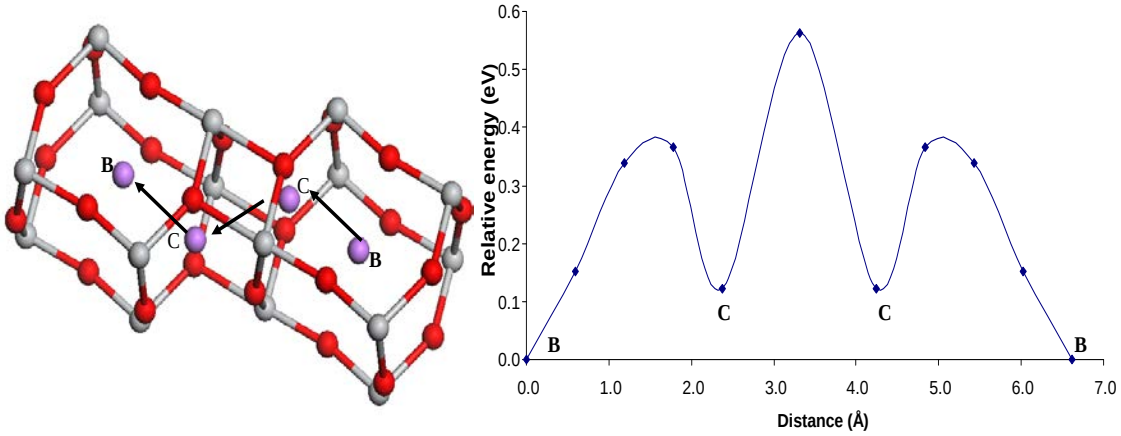

a b

Figure 4.30 a) Li migration pathway between two B sites along the *y* direction. b) Calculated energy profile.

In summary, these electronic structure calculations have made it possible to calculate the energy profile and mechanism of Li intercalation in TiO_2-B at low Li concentration. It is found that among the pathways indicated in Figure 4.28 the most favourable is in the *z* direction, with an energy barrier 0.32 eV. Migration in the y direction has energy barrier of 0.56 eV, while along *x* it has a barrier of 0.99 eV. The preferential migration in the *z* direction is in agreement with recent work[84]. The calculated migration energy is also in agreement with previous experimental and theoretical[59,90,91]data which state that the activation energy is ≤0.5 eV for related TiO_2 materials[83,92].

4.3.5 Further Li intercalation

We have investigated the intercalation energy associated with random Li insertion for Li content up to 6 in the $Ti_{16}O_{32}$ cell of TiO_2-B employed. A graphical plot of the intercalation energy, calculated using equation 4.1 is shown in Figure 4.31.

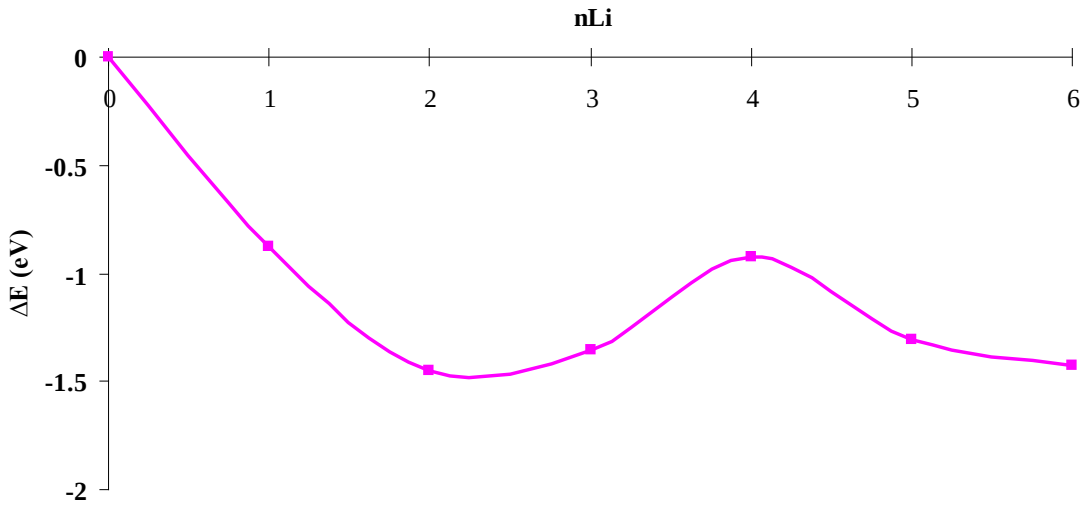

Figure 4.31 Relative intercalation energy in $Li_nTi_{16}O_{32}$ as a function of Li concentration.

We see in Figure 4.31 that Li intercalation is energetically stable (E_n<0) up to a value of n= 6, corresponding to composition $Li_{0.375}TiO_2$.

The Li intercalation energy of first Li ion of -0.87 eV corresponds to composition $Li_{0.0625}TiO_2$, the insertion of the first 6 Li ions into the supercell yields stable intercalation energy with average of -1.2 eV; only occupation of B sites occurs in this range. With further Li insertion, structural distortions increase, and as a consequence positions C, A become more stable than B to host further Li ions so that more intercalation sites need to be considered. Since these results are in general agreement with the recent work by Islam[93], it was decided not to replicate that work, not to consider in full detail further Li intercalation in TiO_2-B.

4.3.6 Summary and outlook

Using ab initio simulations the intercalation behaviour of brookite and TiO_2-B with respect to Lithium have been studied. The stable sites and the lowest energy configurations were identified and their computed energies were used to elucidate the mechanism of Li-intercalation. It was found that the TiO_2-B structure has lower density than other titanates like rutile, anatase and brookite, and the calculated cell voltage is in the range of 0.8 and 1.45 V for low Li content, lower than in brookite, hence more suitable for application in anodes. These calculations found that the most favourable energy site is the square planar site signed as B, and a relatively low favourable energy site signed as A is a five fold coordinated with oxygen atom, and the lowest favourable energy site signed as C. From these data it is found that the *z* direction shows the highest mobility for Li-ions so that the TiO_2-B structure has enough Li mobility for its use as an anode in rechargeable lithium batteries.

The intercalation energy of the brookite and TiO_2-B structures up to the 6th Li ion is compared in Figure 4.32; which shows that the TiO_2-B structure has lower intercalation energy than brookite across this range of Li concentration, which makes it more suitable as an anode material; however brookite has a more constant intercalation energy in this concentration range, which may make it more suitable for real-life applications.

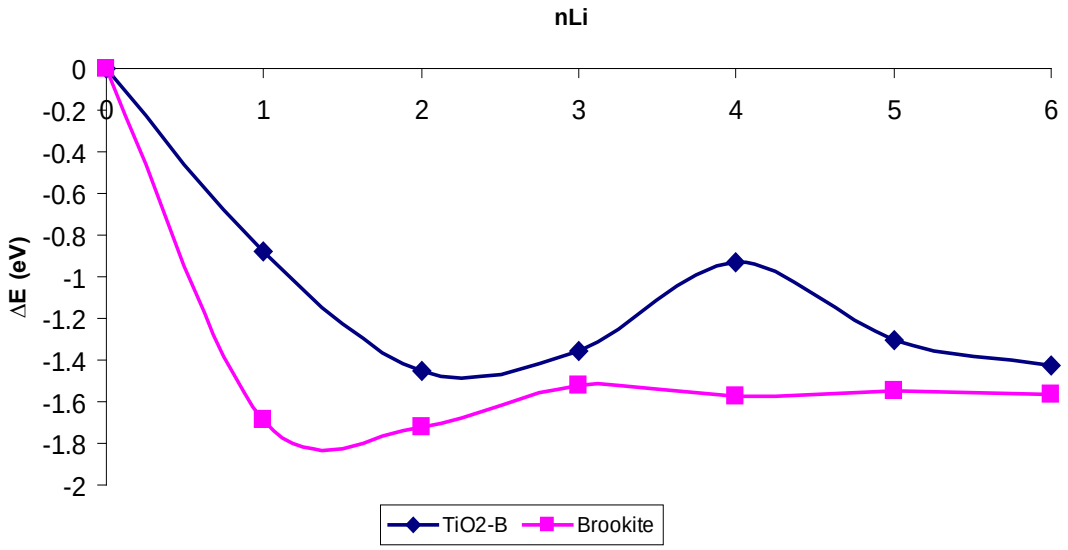

Figure 4.32 Relative intercalation energy of TiO_2-B and Brookite.

Chapter 5

The High Pressure Behaviour and Intercalation Properties of Carbon Nitrides

This chapter considers the properties of a layered (graphite-like) carbon nitride material of composition $C_6N_9H_3$.HCl recently synthesized experimentally. The discussion is split into three main parts:

- The study of the material under hydrostatic compression. In particular, the computational work initiated by Dr. Deifallah[94,112] is continued by examining the high pressure intra- and interlayer distortion mechanisms;
- Following the theme of this thesis the intercalation properties of graphitic $C_6N_9H_3$ are examined to compare with the earlier findings performed on the Ti-based structures; and
- The structural behaviour of graphitic $C_6N_9H_3$ upon replacing the framework H atoms from the bridging NH groups with metal cations are examined.

To begin, a general introduction to carbon nitrides is provided since these materials are significantly different to those already encountered in this thesis.

5.1 High Pressure Behaviour of layered Carbon Nitride

5.1.1 Introduction.

The study of the high pressure behaviour of carbon nitrides has received great attention, ever since theoretical work predicted that a dense phase of composition C_3N_4 might exhibit super-hard properties comparable to, if not superior, to those of diamond. Several low compressibility structures have been identified theoretically but to date experimental high pressure synthesis has not been successful in unequivocally synthesizing them[95,96].

In recent years, work has shown that layered forms of carbon nitride (analogous to graphite) may be amongst the most stable conformations. Indeed, experimentally such layered forms have been synthesised and we refer to these below.

The C_3N_4 composition is the smallest C:N ratio that can have long-range order within a crystalline solid with C and N atoms that alternate with chemical valences of 4 for carbon and 3 for nitrogen. Layered carbon nitrides can be imagined as obtained from graphite by replacing C atoms with N and creating voids in the layered to satisfy the lower coordination number of N. Such layers graphite-like solids are indicated with a prefix g- in the composition (e.g. g-C_3N_4). The substitution of carbon with nitrogen leads to heterocyclic aromatic compounds that possess properties different to the pure carbon form, both structurally and electronically, and the materials may exhibit promising mechanical and electrical properties for modern applications[97].

The high pressure behaviour of graphite is well understood[98,99]and it has been shown that when graphite is compressed at low temperature, the layers buckle and sp^3 bonding begins to appear[100,101]. There have been previous suggestions that C,N-based layered solids may undergo similar structural changes upon compression yielding dense structures of high bulk modulus and low compressibility[98, 99,102].

Certain molecular C,N-contains structures such as the Liebig's melem $(C_6N_7(NH_2)(NH))_n$ phase contains large planar units whereby C and N atoms alternate[103]. The existence of

fully condensed graphitic C_3N_4 structures has been suggested theoretically[101,104] and a nanocrystalline structure of this type has been prepared by chemical vapour deposition but its structure has not been fully characterised[105,106].

A fully condensed layered structure has been synthesised which does not conform to a C_3N_4 backbone, but $C_6N_9H_3$; it contains large intraframework voids (see Figure 5.1) [99]. Such relatively well-crystallised versions of these layered graphitic materials with C:N ratios close to 3:4 were prepared by high-P,T synthesis methods from heterocyclic aromatic precursors (melamine & cyanuric chloride), in the P = 0.5 - 1.5 GPa pressure range at up to T ~ 500^oC[107]; condensation of the precursors generates HCl as by product, which was found to remain within the structure upon synthesis. In fact the synthesised composition is best indicated as $C_6N_9H_3{\cdot}x$HCl with x ~1. It is possible that the inclusion of Cl^- in the synthesis process may help direct the structure to produce voids: unlike pure carbon graphite, the $C_6N_9H_3{\cdot}x$HCl materials were found to contain large interstices where the H atoms decorate the interior of the intralayer voids forming –N(H) groups and thus satisfying the N atoms' valency requirements. The Cl^- ions are hosted in the interstices of these layers. Relatively recently, the compressional behaviour of $C_6N_9H_3{\cdot}x$HCl was examined by Wolf *et al.*[108] and later by our colleagues[94].

It was proposed that the solid examined had an AB stacking sequence of the layers with $P6_3/m$ symmetry and the individual layers contained large 24 atom $C_{12}N_{12}$ triangular cavities as shown in Figure 5.1. For subsequent reference, we denote the structure as ILB0 (where ILB indicates Inter-Layer Bonding).

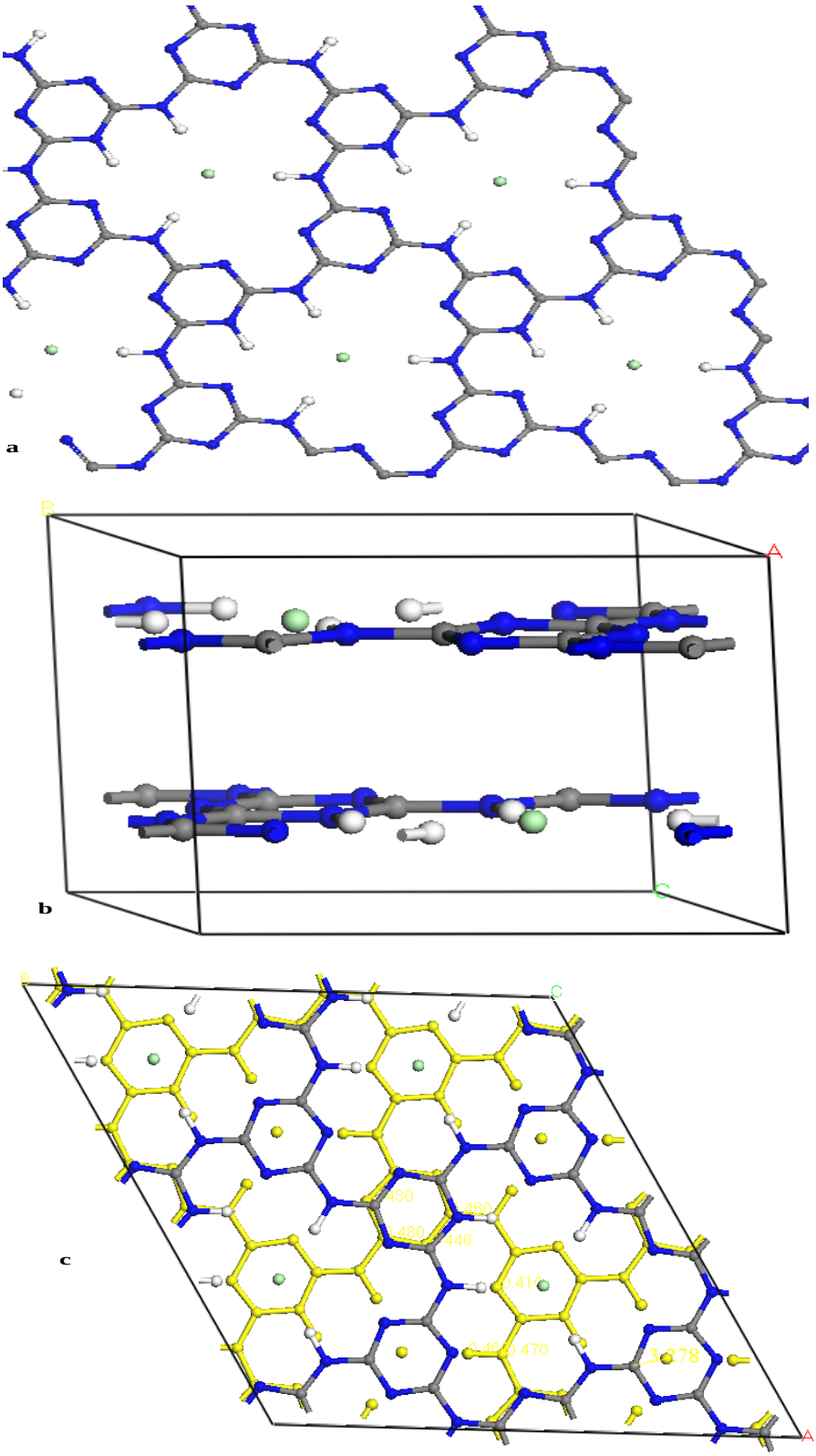

Figure 5.1 ILB0 phase a) Single layer b) Unit cell of $C_6N_9H_3$.HCl c) Stacking of layers in the z directions, highlighting the overlap of some triazine rings in adjacent layers.

It is important to note that some of the triazine rings in adjacent layers are located directly above each other, whereas others are lie on top of the triangular ($C_{12}N_{12}$) voids (Figure 5.1.c).
Previous work showed that upon compression the $C_6N_9H_3{\cdot}x$HCl material is more easily compressed in the direction perpendicular to the layers, as expected for a graphitic compound, and above 10 GPa it exhibits buckling of the layers. The nature of the buckling mechanism showed that the layers relieved pressure via primarily bending the bridging-NH groups that link triazine rings. At approximately 45 GPa the material forms interlayer bonds to yield a dense structure (referred to as ILB1).

In this chapter the computational work is extended, and the structural behaviour of $C_6N_9H_3{\cdot}$HCl to pressure up to 90 GPa and the properties during decompression are examined further. It specifically examines the structural distortions within the covalently-bonded C, N, H layers and the formation of new 3-dimensional structures that appear as a result of high-pressure polymerisation pathways.

5.1.2 Computational Details

The calculations were performed using the CASTEP code[109,110]. The LDA functional and ultra-soft pseudopotentials[111] were utilized. The cut-off value for the plane wave expansion has been determined in previous work by considering the convergence of the energy using a series of single energy point calculations. The cut-off has been chosen to be 450 eV; additional plane waves were considered not necessary to describe the valence orbitals[94].

High pressure calculations have been performed under hydrostatic pressure (P), in the range between 0 and 90 GPa. Full geometry optimisations have been performed at each P, in which the enthalpy H = E + PV is minimised. In the formulation of H, E is the internal energy and V the unit cell volume, while pressure is estimated during the calculation from its thermodynamic definition of $P = -\partial E/\partial V$.

The initial structural model for the solid used in our calculations is that proposed by Zhang et al[99], and confirmed both computationally[94,112] and experimentally in recent work[102]. A proton-ordered version of the 40-atom crystallographic unit cell is employed in all the calculations. All geometry optimisations are carried out within space group P1 to allow for atomic displacements of atoms from the averaged positions implied by the *P6₃/m* structure. The choice of a general symmetry also allowed exploring a wider range of possible structural transformations during compression, within the constraints of periodic overall symmetry, than would be permitted within the higher symmetry space group[94].

5.1.3 Results and discussion

In order to identify the transformation mechanisms of the *g*-$C_6N_9H_3$·HCl structure under compression, we first refer to a comparison between the experimental and computational data. The layered ambient pressure structure corresponds to a local minimum in the potential energy surface; any chemical or structural transformation in the material under pressure is therefore likely to require a non-zero activation barrier in order to take place. Experimentally, this energy is provided by both temperature and pressure terms of the free energy, while in a static computational work, as the present one, the temperature contribution is neglected (i.e. we consider enthalpies instead of free energies) and all the activation energy for pressure-induced transformations must be provided by the PV term of the enthalpy. It is therefore expected that the onset of any transformation be shifted to higher values of P compared with experiment. To investigate this topic in greater detail, we performed a further series of calculations on g-$C_6N_9H_3$.HCl, at increasing values of pressure.

The comparison below of g-$C_6N_9H_3$.HCl, upon applying P from the ambient pressure phase has been discussed in depth in Dr. Deifallah's thesis[112] , hence in this section we present only an overview of the results discussed there.

The investigation began by examining the structure in its original status as flat parallel layers, before gradually increasing the pressure in steps of 10 GPa to 90 GPa. Each

calculation has started from the geometry-optimised structure at the previous pressure reading. Under this gradual increase of pressure, the unit cell lattice parameters, volume and enthalpy, can be monitored. The lattice parameter changes are shown in Figure 5.2.

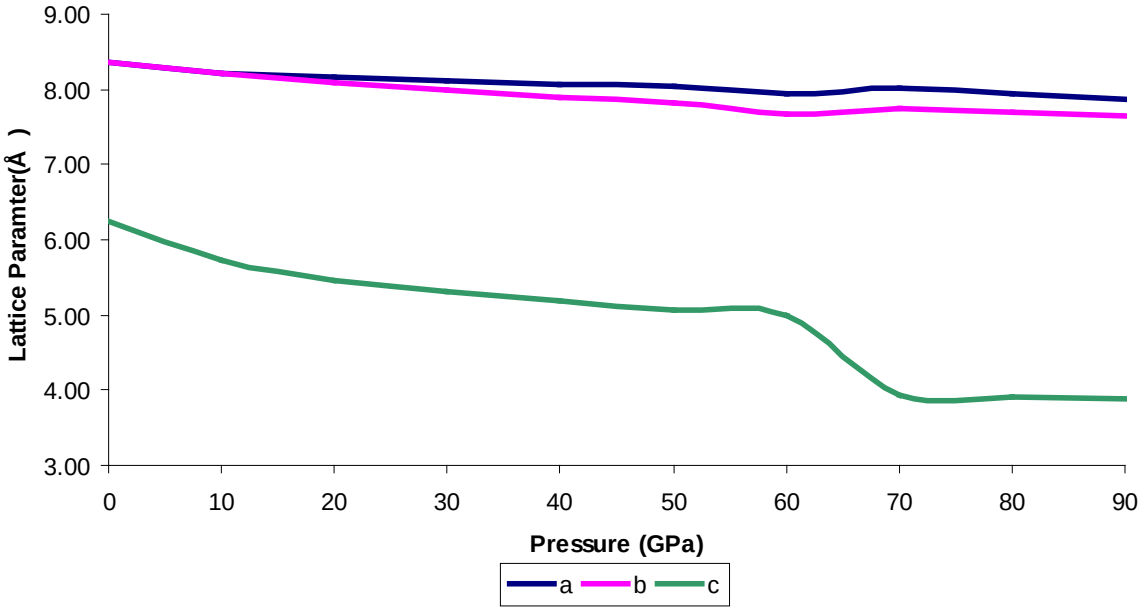

Figure 5.2 Unit cell parameters of the *g*-$C_6N_9H_3$·HCl structure as a function of increasing pressure.

The *a* and *b* unit cell parameters are equal at ambient pressure; however this equivalence typical of the hexagonal structure of g-$C_6N_9H_3$·HCl is lost already at 10 GPa. The *b* unit cell parameter reduces more rapidly than the *a* lattice parameter, and the difference between the two lattice parameters increases as a function of pressure. The *c* lattice parameter which corresponds to the interlayer separation decreases more rapidly than *a* and *b* from 0 to 60 GPa, before dropping sharply between the pressures of 60 and 70 GPa. Calculated unit cell volume (V) and enthalpy (ΔH) are shown in Figure 5.3. The discontinuity observed at 70 GPa is attributed to a pressure induced structural transformation, consisting in the formation of interlayer bonding between triazine rings that are above each other in the structure, forming a pillared phase that in ref [94] has been labelled as ILB1. A picture of this new phase is shown in Figure 5.6.

In addition to the above observations from the previous work, from analysis of these calculations, addition structural features in the carbon nitride framework under pressure are noticeable: the formation of symmetrical N-H-N hydrogen bonds and of carbon-chloride bonds; these feature remain throughout the pressure regime in which the ILB1 phase is stable, i.e. above 70 GPa in the compression study.

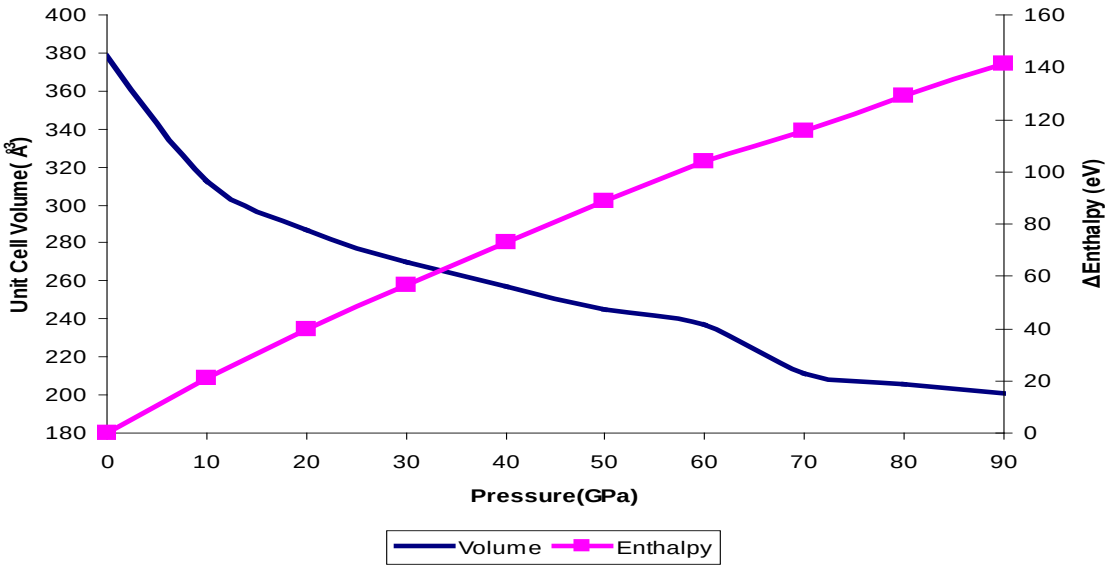

Figure 5.3 ΔEnthalpy (eV) and unit cell volume (Å^3) as a function of applied pressure (GPa).

We now examine the decompression process from 90 GPa; i.e. starting with the optimised ILB1 phase with interlayer bonding, and gradually reducing pressure in steps of 10 GPa. Each calculation has been started from the geometry-optimised structure at the immediately higher value of pressure. Under this gradual relief of pressure, the interlayer bonding of the *g*-$C_6N_9H_3$.HCl material is retained to ambient pressure and the layers remain buckled indicating that the ILB1 phase obtained at the highest pressure may be recoverable to ambient conditions. The lattice parameters change during decompression is shown in Figure 5.4. During decompression the *a*, *b*, and *c* lattice parameters increase by 11.3%, 15.7% and 11.9% respectively, but do not result in the original structure first examined at 0 GPa since the interlayer bonding is retained. It is of interest that the anisotropy observed in the compression study, with easier compressibility in the *z* direction typical of layered solids, is no longer present once

interlayer bonding is formed. The ILB1 structure has therefore a three dimensional behaviour. In order to examine the stability of the two phases, ILB0 and ILB1, their enthalpies as a function of pressure are reported in Figure 5.5.

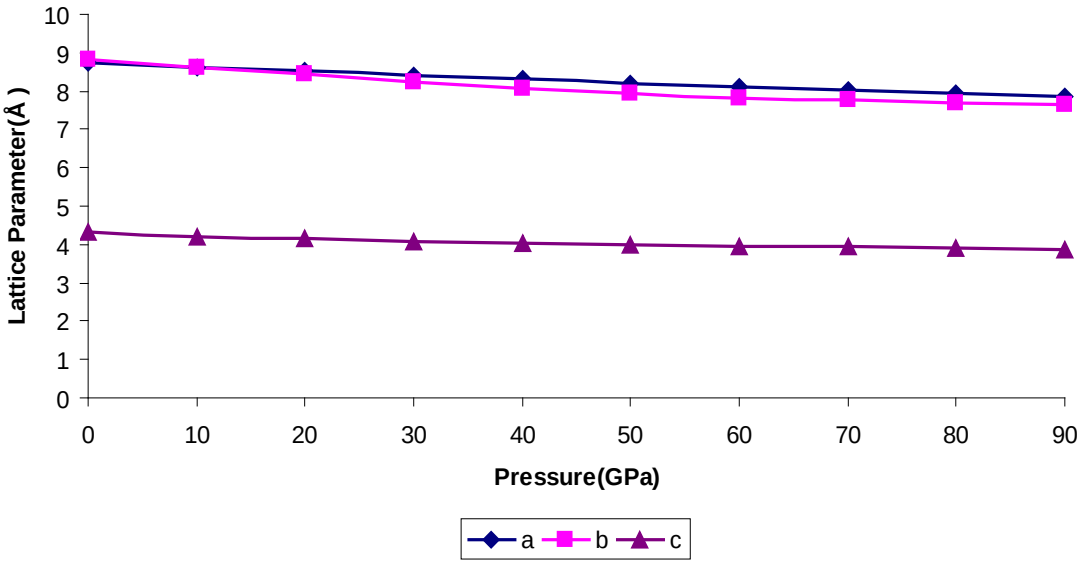

Figure 5.4 Cell parameters of *g*-$C_6N_9H_3$.HCl *a*, *b* and *c* as a function of applied pressure during compression.

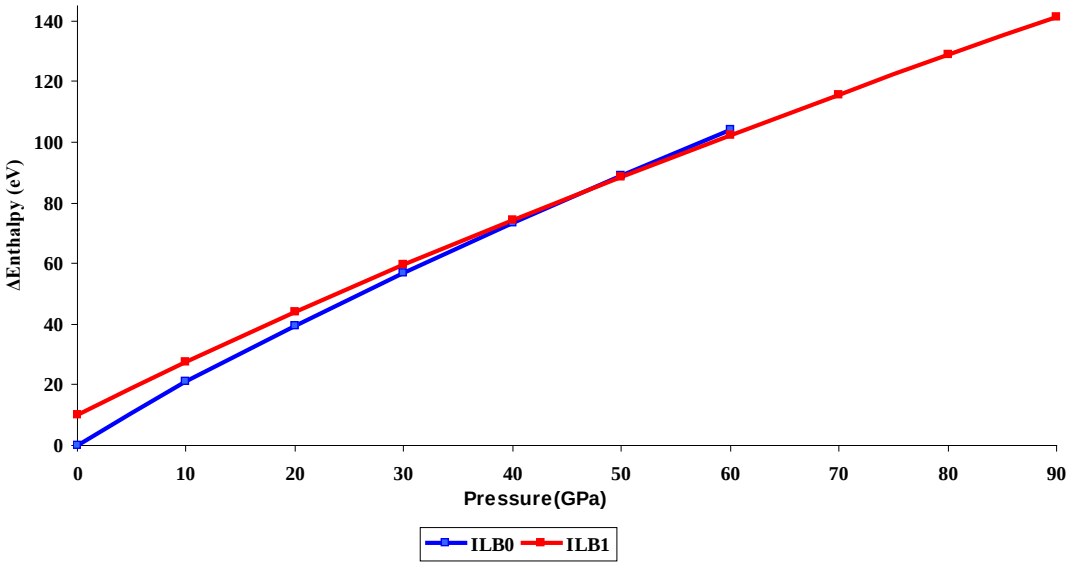

Figure 5.5 Relative enthalpy of ILB0 and ILB1 phases as a function of applied pressure.

Examining the results shown above, we can predict that the pressure at which the two phases (ILB0, ILB1) are isoenthalpic is 47 GPa. The ILB0 phase is thermodynamically stable below 47 GPa, after which the pillared ILB1 phase with interlayer bonding becomes thermodynamically stable.
The presence of HCl in the *g*-$C_6N_9H_3$.HCl structure has a retarding effect on the phase transition; the isoenthalpic point between ILB0 and ILB1 phases for the HCl free material g-$C_6N_9H_3$ was calculated as 7 GPa[94,112]. The Cl^- ions in the structure play therefore an important role on the mechanism of structural deformation under pressure.

In order to understand the mechanism of the structural of transformation and the role of the Cl^- ions, it is necessary to investigate the interatomic behaviour during pressure increase and relief.

The ILB1 structure obtained at pressure of 70 GPa is shown in Figure 5.6. Other than the occurrence of interlayer bonding, it contains a number of other interesting features. First, two interlayer H- bonds exist (labelled N_2-H_1-N_{12} and N_3-H_4-N_{11} in Figure 5.6) in which the two N-H bond distances are similar, and hence can be classified as symmetric N-H-N hydrogen bonds.

Second, the Cl^- ions yield two short C-Cl bonds that may suggest they are not chemically inert under these pressure conditions but form C-Cl bonds with the carbon nitride framework.

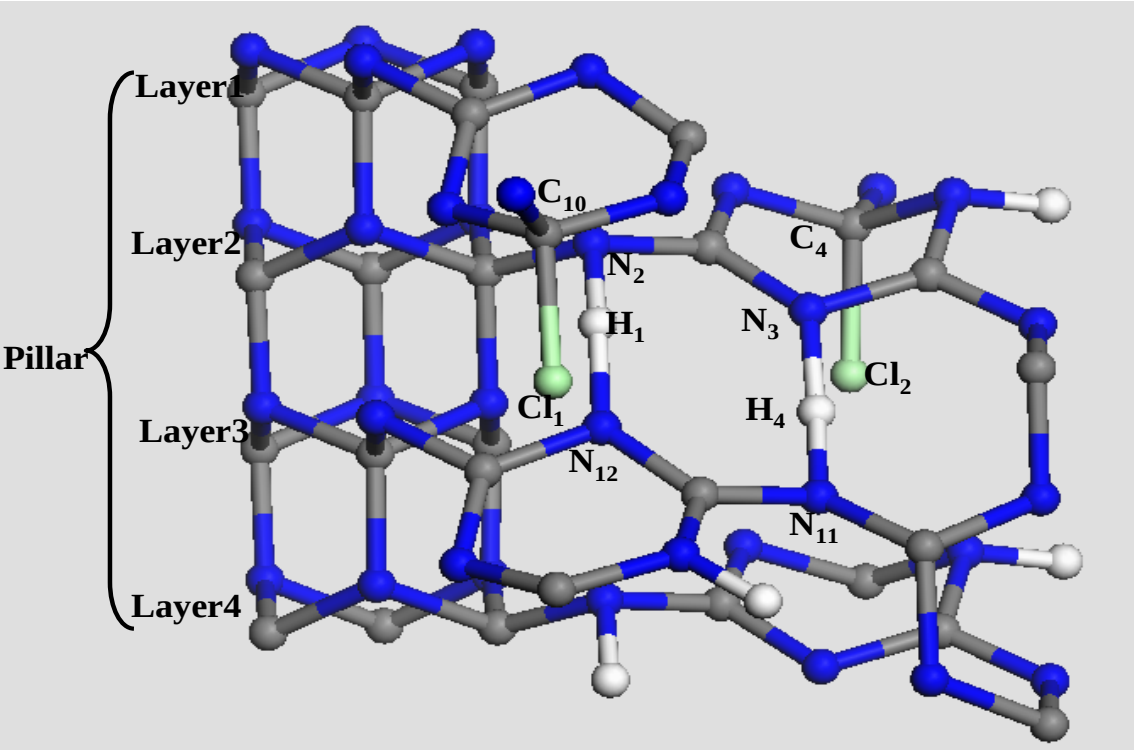

Figure 5.6 ILB1 structure at 70 GPa.

Symmetric hydrogen bonds have been observed spectroscopically in formic acid at high pressures (12 GPa)[113]. Each hydrogen atom forms a partial covalent bond with two atoms rather than one. Symmetric hydrogen bonds have also been postulated in ice at high pressure (ice-X)[114,115,116]. Symmetric N-H-N hydrogen bonds have been reported in some organic compounds upon decreasing the N—N separation in a range between 2.526 to 2.635 Å; the maximum N-N separation that enables a symmetric H bond is 2.65 Å[117]; even in these conditions it was found that in some systems the N-H-N unit is asymmetric with a distinct H bond donor and acceptor N atom[118,119]. In the case shown in Figure 5.6, the separations across the symmetric H bonds are N_2-N_{12} = 2.373 Å and N_3-N_{11}= 2.369 Å.

Symmetric hydrogen bond has also been identified in potassium hydrogen maleate by diffraction and computational work and the results have confirmed that the symmetric (or close to symmetric) hydrogen bonds are a common feature for materials under pressure[120].

We have performed phonon calculations and Mulliken Population analysis in order to investigate the nature of the symmetric hydrogen bond and of the carbon chloride bonds in the material under pressure.

Table 5.1 presents the equilibrium bond lengths for the structures optimised during the compression and decompression processes. Starting from the known ambient pressure phase and increasing pressure, we observe that the NH bond lengths (N_2-H_1), (N_{11}-H_4) at ambient condition are ~ 1.06 Å while the H bond acceptor N has a distance of over 3 Å. The NH bonds shorten slightly upon applying P up to ~ 50 GPa; conversely the non-bonded distances between H and the H-bond acceptor N decrease much more appreciably, up to ~2.3 Å. This shortening is associated with a reorientation of the NH bond from the plane of the $C_6N_9H_3$ layer towards the interlayer region enabling a more effective H- bonding geometry. At 70 GPa and above, compression produces two nearly symmetric N-H-N bonds, with both NH bond distances in the range of 1.1-1.2 Å.

	0 GPa	**10 GPa**	**20 GPa**	**30 GPa**	**40 GPa**	**50 GPa**	**60 GPa**	**70 GPa**	**80 GPa**	**90 GPa**
	Compression									
N_2-H_1	1.070	1.065	1.060	1.059	1.053	1.053	1.058	**1.162**	**1.162**	**1.159**
N_{12}-H_1	3.194*	3.348*	2.684*	2.589*	2.521*	2.670*	2.382*	**1.270**	**1.270**	**1.243**
C_{10}-Cl_1	3.53*	2.889*	2.692*	2.577*	2.494*	2.770*	2.374*	**1.646**	**1.646**	**1.640**
C_4-Cl_2	3.278*	3.590*	2.889*	2.799*	2.738*	2.550*	2.674*	**1.647**	**1.647**	**1.643**
N_{11}-H_4	1.064	1.063	1.063	1.062	1.061	1.059	1.060	**1.193**	**1.193**	**1.171**
N_3-H_4	3.224*	3.364*	2.587*	2.500*	2.440*	2.662*	2.310*	**1.227**	**1.227**	**1.220**
	Decompression									
N_2-H_1	**1.056**	**1.080**	**1.092**	**1.112**	**1.136**	**1.159**	**1.164**	**1.164**	**1.163**	**1.159**
N_{12}-H_1	**1.861***	**1.623***	**1.537***	**1.451***	**1.373***	**1.311***	**1.284***	**1.267**	**1.252**	**1.243**
C_{10}-Cl_1	**1.797**	**1.754**	**1.730**	**1.700**	**1.673**	**1.659**	**1.652**	**1.646**	**1.642**	**1.640**
C_4-Cl_2	**1.797**	**1.759**	**1.733**	**1.706**	**1.686**	**1.670**	**1.658**	**1.647**	**1.634**	**1.632**
N_{11}-H_4	**1.078**	**1.105**	**1.120**	**1.138**	**1.171**	**1.204**	**1.204**	**1.194**	**1.182**	**1.171**
N_3-H_4	**1.663***	**1.480***	**1.421***	**1.375***	**1.312***	**1.253**	**1.233**	**1.226**	**1.222**	**1.220**

Table 5.1 Analysis of bond lengths in compression and decompression calculations; the symbol * identifies nonbonding distances. Here and in the following tables, bold numbers correspond to the ILB1 phase.

Under further compression the symmetric hydrogen bonds (or close to symmetric) are shortened, and the protons (H_1, H_4) move closer to the centre of the N-N unit. The N-H-N unit above 70 GPa is close to symmetric (we can denoted this geometry as semi-symmetric), but it is not linear (at 70 GPa the NHN angles are 164°, 168°).

In the decompression process, i.e. starting from the phase obtained at the highest pressure of 90 GPa and gradually decreasing pressure, the semi-symmetric hydrogen bond is stretched and the protons move towards one side (the original nitrogen atoms N_2, N_{11}).

The semi- symmetric hydrogen bond lengths at 90 GPa are (1.159-1.243) Å, and (1.171-1.220) Å and they are stretched to (1.164-1.267) Å, (1.194-1.226) Å at 70 GPa. Further pressure relief causes a more traditional asymmetric H bond, where we recognise one donor (N_2-H_1 or N_{11}-H_4) and one acceptor (N_{12} or N_3) nitrogen with significantly different N-H distances. The final geometry at ambient pressure is however different from the original one, since the NH bonds remain out of the $C_6N_9H_3$ layers and engaged in some interlayer H bond.

Appreciable changes occur also in the C-Cl distances. While in the original ambient pressure phase the Cl^- ions are located near the centre of the $C_{12}N_{12}$ interstices of the structure, with negligible C-Cl interactions (all C-Cl distances are above 3 Å), above 70 GPa in the compression study we observe two short C-Cl bonds: C_{10}-Cl_1 of 1.646 Å and C_4-Cl_2 of 1.647 Å, which remain nearly constant on further increases of pressure. This behaviour may indicate that the Cl^- ions are not inert under compression, and may become engaged in C-Cl bonds under compressive stress, thus contributing to an increase of the coordination number of C and its rehybridisation from sp^2 to sp^3. The shorter C-Cl bond lengths formed upon compression are retained on relieving pressure, with just a gradual increase of bond distances from 1.6 to ~ 1.8 Å on returning to ambient conditions.

There is therefore a pronounced hysteresis in the structure that after completing a compression- decompression loop does not return to the original ambient pressure phase.

The changes to the bonding pattern between C-N, N-H, and C-Cl ions upon pressure cannot be categorised based on bond distances alone. To this goal we have measured the net ionic charges on all the atoms involved in the structural changes discussed above, using a simple Mulliken population analysis of the equilibrium electron densities, for each pressure studied upon compression and decompression loops. Values are summarised in Table 5.2.

	0 GPa	**10 GPa**	**20 GPa**	**30 GPa**	**40 GPa**	**50 GPa**	**60 GPa**	**70 GPa**	**80 GPa**	**90 GPa**
	Compression									
N_2	-0.47	-0.45	-0.44	-0.43	-0.42	-0.4	-0.42	**-0.48**	**-0.44**	**-0.49**
N_3	-0.47	-0.46	-0.44	-0.43	-0.43	-0.4	-0.42	**-0.45**	**-0.45**	**-0.44**
N_{11}	-0.42	-0.39	-0.42	-0.42	-0.42	-0.4	-0.42	**-0.45**	**-0.44**	**-0.45**
N_{12}	-0.63	-0.39	-0.42	-0.42	-0.42	-0.39	-0.41	**-0.44**	**-0.44**	**-0.43**
H_1	0.42	0.41	0.38	0.37	0.36	0.35	0.35	**0.36**	**0.36**	**0.36**
H_4	0.56	0.43	0.4	0.39	0.38	0.37	0.37	**0.37**	**0.37**	**0.37**
C_4	0.5	0.5	0.49	0.47	0.46	0.47	0.43	**0.23**	**0.23**	**0.22**
C_{10}	0.53	0.48	0.48	0.47	0.46	0.48	0.45	**0.22**	**0.21**	**0.2**
Cl_1	-0.63	-0.56	-0.53	-0.49	-0.46	-0.45	-0.38	**0.14**	**0.17**	**0.19**
Cl_2	-0.62	-0.57	-0.52	-0.49	-0.45	-0.42	-0.37	**0.08**	**0.1**	**0.11**
	Decompression									
N_2	**-0.48**	**-0.47**	**-0.47**	**-0.47**	**-0.47**	**-0.48**	**-0.48**	**-0.48**	**-0.49**	**-0.49**
N_3	**-0.48**	**-0.47**	**-0.46**	**-0.45**	**-0.45**	**-0.45**	**-0.45**	**-0.45**	**-0.45**	**-0.44**
N_{11}	**-0.5**	**-0.49**	**-0.49**	**-0.48**	**-0.47**	**-0.46**	**-0.45**	**-0.45**	**-0.44**	**-0.45**
N_{12}	**-0.5**	**-0.5**	**-0.49**	**-0.48**	**-0.46**	**-0.45**	**-0.44**	**-0.44**	**-0.44**	**-0.43**
H_1	**0.44**	**0.41**	**0.39**	**0.39**	**0.37**	**0.37**	**0.36**	**0.36**	**0.36**	**0.36**
H_4	**0.42**	**0.4**	**0.39**	**0.38**	**0.37**	**0.37**	**0.37**	**0.37**	**0.37**	**0.37**
C_4	**0.31**	**0.29**	**0.28**	**0.27**	**0.26**	**0.25**	**0.24**	**0.23**	**0.23**	**0.22**
C_{10}	**0.32**	**0.29**	**0.28**	**0.26**	**0.25**	**0.24**	**0.23**	**0.22**	**0.21**	**0.2**
Cl_1	**-0.06**	**-0.02**	**0.01**	**0.03**	**0.07**	**0.1**	**0.12**	**0.14**	**0.17**	**0.19**
Cl_2	**-0.04**	**-0.01**	**0.01**	**0.03**	**0.04**	**0.06**	**0.07**	**0.08**	**0.1**	**0.11**

Table 5.2 Net ionic charges in |e|, calculated using a Mulliken population analysis as a function of pressure in compression and decompression studies of $C_6N_9H_3$.HCl.

The ambient pressure values of the net charges on C, N, H and Cl^- atoms are consistent with their relative electronegativity, and Cl^- being a negatively charged ion, not bonded to the carbon nitride backbone. The net charge of Cl^- is -0.6, less than the formal value of -1, because some overlap of the Cl^- electron density with that of the H's lining the $C_{12}N_{12}$ cavity edges takes place.

Charges on N (-0.4, -0.6), C (+0.5) and H (~ +0.4) are consistent with polarised C-N and N-H bonds. The structure becomes less polar upon compression; in particular the net charge of Cl^- decreases most rapidly due to increased Cl-H overlap, but no substantial change occurs up to 70 GPa, where we observe abrupt changes on Cl, from -0.4 to +0.1.

Combined with the short C-Cl bond distances, we conclude that indeed C-Cl bonds are formed in this structure. The C atoms involved in the C-Cl bonds (C_4 and C_{10}) also have a significant decrease of net charge at 70 GPa, as they accept one of the electrons originally on the Cl^- ions to form the C-Cl bonds.

The C-Cl bonds appear to be retained upon decompression until ambient conditions, this result is indicative that a structure with C-Cl bonds is a stable minimum in the potential energy surface; cleavage of a C-Cl bond, once formed, is a process that requires a significant activation energy, which is not provided in a series of static energy minimisations.

The formation of symmetric N-H-N bonds at 70 GPa and above is not reflected in substantial changes of the N and H net charges, consistent with such H-bond interaction having a large electrostatic, not only covalent, component.

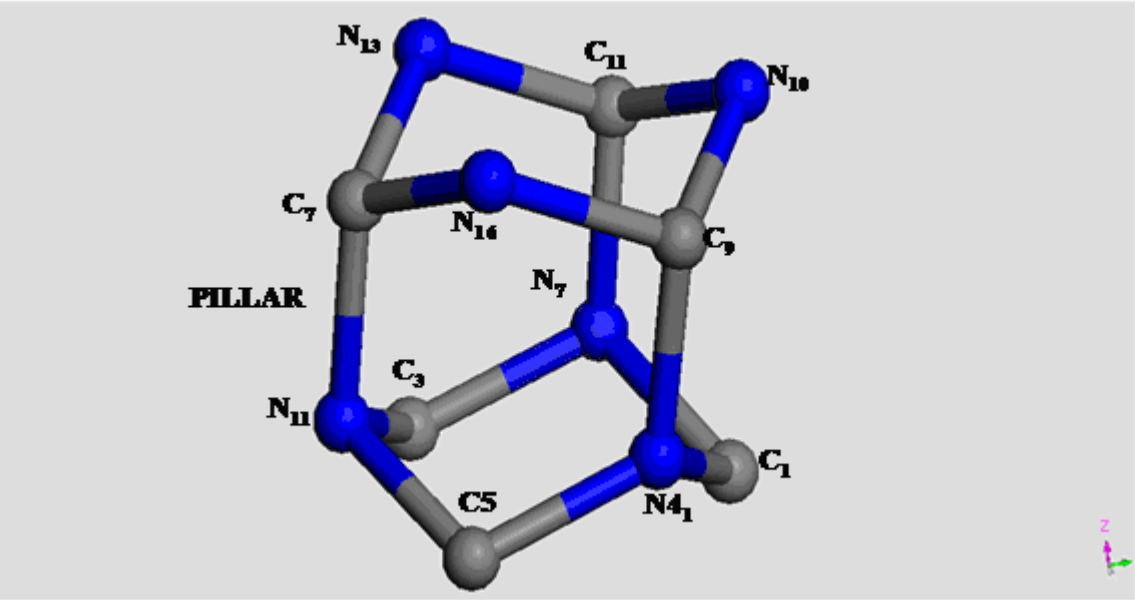

Figure 5.7 One of the interlayer bonding pillars first formed at 70 GPa showing the labels of the atoms involved

The other major reconstruction observed at 70 GPa is the formation of the interlayer bonding and of pillars running perpendicular to the layer orientation. A label of the atoms involved, and equilibrium structure at 70 GPa, is shown in Figure 5.7, which highlights the interlayer bonding features in one of the pillars found between overlapping triazine rings in adjacent layers.

The net atomic charges, derived from Mulliken population analysis of the atoms belonging to the pillar are presented in Table 5.3. Small net charges due to the different electronegativity of C and N but consistent with the covalent nature of C-N bonds in the carbon nitride framework are observed. Net charges decrease slightly on increasing pressure, and there is no substantial change, not even above 70 GPa when interlayer bonding is observed. Such behaviour is not surprising, since interlayer bonding causes a change of C-N bonding from sp^2 to sp^3, but the atom types involved are the same, as the strict alternation of C and N in the structure present before interlayer bonding is retained also over interlayer bonding is created.

		0 GPa	10 GPa	20 GPa	30 GPa	40 GPa	50 GPa	60 GPa	70 GPa	80 GPa	90 GPa
		Compression									
Layer 1	**C_{11}**	0.48	0.48	0.48	0.47	0.47	0.44	0.45	**0.41**	**0.41**	**0.41**
	N_{10}	-0.44	-0.42	-0.41	-0.40	-0.40	-0.42	-0.39	**-0.35**	**-0.35**	**-0.35**
	C_9	0.46	0.46	0.43	0.42	0.42	0.42	0.41	**0.43**	**0.42**	**0.42**
	N_{16}	-0.50	-0.49	-0.47	-0.46	-0.45	-0.46	-0.45	**-0.38**	**-0.38**	**-0.38**
	C_7	0.48	0.44	0.47	0.47	0.47	0.47	0.47	**0.40**	**0.40**	**0.40**
	N_{13}	-0.43	-0.42	-0.42	-0.42	-0.41	-0.40	-0.42	**-0.35**	**-0.35**	**-0.35**
Layer 2	**N_7**	-0.43	-0.42	-0.42	-0.41	-0.41	-0.42	-0.42	**-0.36**	**-0.36**	**-0.36**
	C_1	0.50	0.45	0.48	0.48	0.48	0.48	0.48	**0.44**	**0.44**	**0.43**
	N_4	-0.51	-0.47	-0.47	-0.46	-0.46	-0.45	-0.45	**-0.37**	**-0.36**	**-0.36**
	C_5	0.50	0.45	0.44	0.43	0.43	0.42	0.42	**0.42**	**0.42**	**0.42**
	N_1	-0.43	-0.43	-0.44	-0.43	-0.43	-0.44	-0.42	**-0.37**	**-0.36**	**-0.36**
	C_3	0.48	0.48	0.43	0.43	0.42	0.42	0.41	**0.42**	**0.42**	**0.42**
		Decompression									
Layer 1	**C_{11}**	**0.43**	**0.42**	**0.42**	**0.42**	**0.42**	**0.41**	**0.41**	**0.41**	**0.41**	**0.41**
	N_{10}	**-0.36**	**-0.36**	**-0.35**	**-0.35**	**-0.35**	**-0.35**	**-0.35**	**-0.35**	**-0.35**	**-0.35**
	C_9	**0.43**	**0.43**	**0.43**	**0.43**	**0.43**	**0.43**	**0.42**	**0.43**	**0.42**	**0.42**
	N_{16}	**-0.40**	**-0.40**	**-0.40**	**-0.39**	**-0.39**	**-0.39**	**-0.38**	**-0.38**	**-0.38**	**-0.38**
	C_7	**0.43**	**0.42**	**0.42**	**0.42**	**0.41**	**0.41**	**0.41**	**0.40**	**0.40**	**0.40**
	N_{13}	**-0.36**	**-0.37**	**-0.36**	**-0.36**	**-0.36**	**-0.35**	**-0.35**	**-0.35**	**-0.35**	**-0.35**
Layer 2	**N_7**	**-0.37**	**-0.36**	**-0.36**	**-0.35**	**-0.35**	**-0.36**	**-0.36**	**-0.36**	**-0.36**	**-0.36**
	C_1	**0.44**	**0.44**	**0.44**	**0.44**	**0.44**	**0.44**	**0.44**	**0.44**	**0.44**	**0.43**
	N_4	**-0.39**	**-0.39**	**-0.38**	**-0.38**	**-0.37**	**-0.37**	**-0.37**	**-0.37**	**-0.36**	**-0.36**
	C_5	**0.42**	**0.42**	**0.42**	**0.42**	**0.42**	**0.42**	**0.42**	**0.42**	**0.42**	**0.42**
	N_1	**-0.38**	**-0.37**	**-0.37**	**-0.37**	**-0.37**	**-0.37**	**-0.37**	**-0.37**	**-0.37**	**-0.36**
	C_3	**0.43**	**0.43**	**0.43**	**0.43**	**0.43**	**0.43**	**0.43**	**0.42**	**0.42**	**0.42**

Table 5.3 Mulliken population charge analysis during a compression-decompression loop of the C and N atoms forming one of the pillars of the ILB1 structure.

	0 GPa	**10 GPa**	**20 GPa**	**30 GPa**	**40 GPa**	**50 GPa**	**60 GPa**	**70 GPa**	**80 GPa**	**90 GPa**
	compression									
C_{11}-N_7	3.130*	2.908*	2.852*	2.772*	2.713*	2.528*	2.635*	**1.456**	**1.456**	**1.438**
C_9-N_4	3.130*	2.970*	2.861*	2.773*	2.703*	2.503*	2.591*	**1.453**	**1.453**	**1.434**
C_7-N_1	3.134*	2.947*	2.826*	2.755*	2.701*	2.499*	2.638*	**1.454**	**1.454**	**1.433**
	decompression									
C_{11}-N_7	**1.631**	**1.569**	**1.537**	**1.514**	**1.496**	**1.481**	**1.468**	**1.456**	**1.447**	**1.438**
C_9-N_4	**1.643**	**1.56**	**1.53**	**1.505**	**1.488**	**1.475**	**1.463**	**1.453**	**1.443**	**1.434**
C_7-N_1	**1.622**	**1.562**	**1.532**	**1.511**	**1.494**	**1.48**	**1.467**	**1.454**	**1.443**	**1.433**

Table 5.4 C-N bond distances for the atoms of the pillar; the symbol (*) denotes nonbonding distances.

The equilibrium interlayer bond distances as a function of pressure for the C and N atoms making up one pillar are reported in Table 5.4. Once formed at 70 GPa, interlayer bonds compress on further application of pressure, and are retained during the whole decompression cycle. At ambient pressure the C-N bonds equal 1.62-1.64 Å, which is typical of a C-N single bond, and much shorter than the interlayer separation in the original ILB0 phase.

In summary, in the ILB1 phase (shown in Figure 5. 8) we observe a number of new structural features not present in the original ILB0 phase:

- Interlayer N-H-N hydrogen bonding, of a nearly symmetric nature under pressure.
- C-Cl bonds.
- C-N interlayer bonds generating pillars in the structure.

Upon decompression, we observe an intermediate region below 60 GPa in which the pillar and C-Cl bonds of ILB1 are retained, but the N-H-N interlayer H bonds are weakened and less symmetric. Between 50 and 60 GPa only one symmetric H bond is retained (Figure 5.9), while both are lost below 50 GPa; the structural changes are highlighted in Figure 5.10.

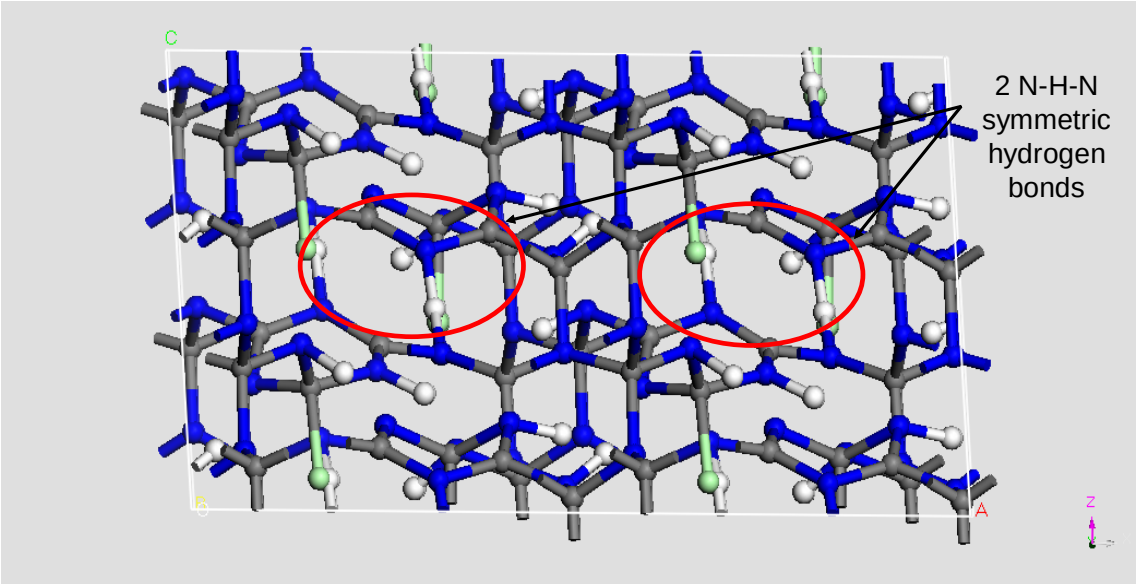

Figure 5. 8 Equilibrium structure of the ILB1 phase at 90 GPa.

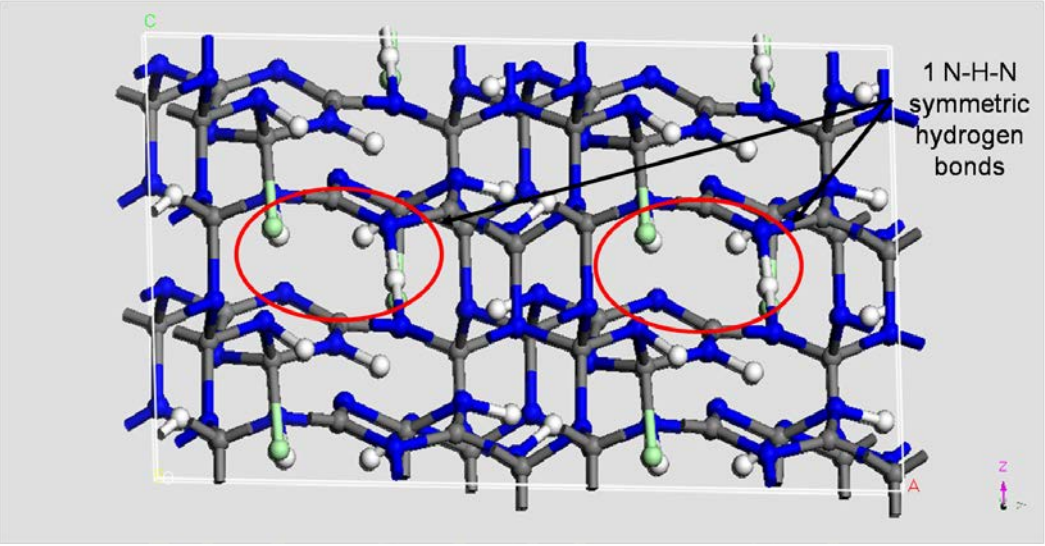

Figure 5.9 Equilibrium structure of the ILB1 phase obtained during pressure relief at 50 GPa, showing that only one of the nearly symmetric (N-H-N) H bonds is retained at this pressure.

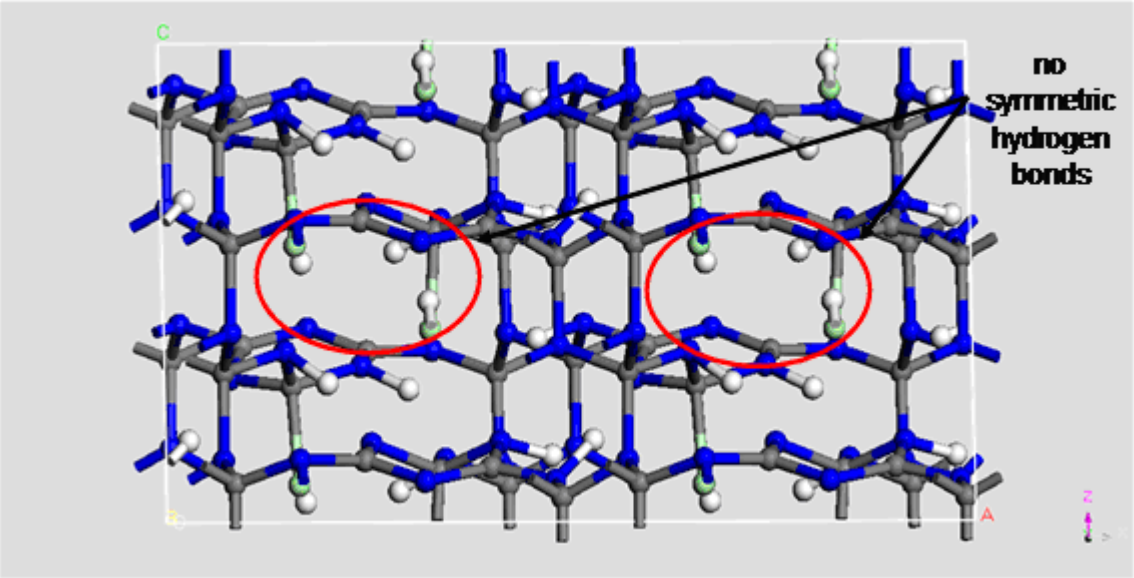

Figure 5.10 Equilibrium structure of the ILB1 phase obtained during pressure relief at 0 GPa, where both N-H-N bonds have asymmetric nature.

Phonon calculations have been carried out to confirm that the new features observed in the ILB1 phase correspond to real minima of the Potential Energy Surface (PES), in particular the (semi) symmetric H bond. The phonon calculations have been performed using CASTEP, fully optimised structures at each pressure, and the same computational parameters of the calculations discussed so far. However, to ensure that the higher coordination numbers are not an artefact of the LDA functional, we have also repeated the phonon calculations (and geometry optimisations) at 50, 70 and 90 GPa using the PBE (GGA) functional. The phonon spectrum in the Γ point of reciprocal space, obtained with the PBE functional, is reported in Table 5.5-Table 5. 7 at the three pressures examined.

N	Freq (cm^{-1})	N	Freq (cm^{-1})	N	Freq (cm^{-1})	N	Freq (cm^{-1})	N	Freq (cm^{-1})	N	Freq (cm^{-1})
1	-25.42	**21**	487.92	**41**	722.78	**61**	1015.51*	**81**	1242.38	**101**	1515.60
2	-23.98	**22**	498.31	**42**	733.73	**62**	1033.42	**82**	1251.84	**102**	1576.86
3	-13.41	**23**	506.24	**43**	738.76	**63**	1034.60	**83**	1262.02	**103**	1615.68
4	162.35	**24**	529.79	**44**	764.19	**64**	1050.43	**84**	1269.04	**104**	1634.62
5	208.82	**25**	537.91	**45**	793.58	**65**	1070.31	**85**	1272.31	**105**	1652.02
6	232.35	**26**	547.96	**46**	799.24	**66**	1097.78	**86**	1289.92	**106**	1675.69
7	266.47	**27**	554.74	**47**	813.15	**67**	1101.15	**87**	1293.07	**107**	1699.90
8	269.90	**28**	571.97	**48**	813.92	**68**	1108.99	**88**	1302.09	**108**	1729.41
9	317.05	**29**	579.06	**49**	845.93	**69**	1117.65	**89**	1318.72	**109**	1764.82
10	336.61	**30**	588.06	**50**	868.94	**70**	1132.53	**90**	1339.76	**110**	1810.21
11	361.60	**31**	601.67	**51**	885.86	**71**	1135.14	**91**	1341.07	**111**	1833.53
12	377.25	**32**	602.70	**52**	906.73	**72**	1145.34	**92**	1351.71	**112**	1864.62
13	384.84	**33**	626.64	**53**	923.38	**73**	1165.19	**93**	1359.41	**113**	1968.70
14	394.13	**34**	626.95	**54**	924.39	**74**	1167.07	**94**	1390.08	**114**	1995.68*
15	405.68	**35**	636.93	**55**	932.56	**75**	1181.41	**95**	1405.33	**115**	2228.47*
16	409.19	**36**	659.37	**56**	951.87	**76**	1192.07	**96**	1426.26	**116**	2262.18*
17	424.78	**37**	669.98	**57**	955.05	**77**	1201.57	**97**	1434.20	**117**	2798.79
18	447.31	**38**	670.96	**58**	965.36*	**78**	1205.56	**98**	1458.66	**118**	3304.35
19	462.06	**39**	684.12	**59**	982.70	**79**	1224.06	**99**	1467.06	**119**	3391.07
20	482.67	**40**	709.38	**60**	992.73	**80**	1229.16	**100**	1494.94	**120**	3630.06

Table 5.5 Γ-Point phonons for the ILB1 phase at 90 GPa. The values highlighted correspond to symmetric H-bond stretching modes (2000-2200 cm^{-1}) and C-Cl stretching modes (965 and 1015 cm^{-1}).

N	Freq (cm^{-1})	N	Freq (cm^{-1})	N	Freq (cm^{-1})	N	Freq (cm^{-1})	N	Freq (cm^{-1})	N	Freq (cm^{-1})
1	-25.72	**21**	461.03	**41**	685.72	**61**	989.79	**81**	1214.95	**101**	1490.89
2	-21.36	**22**	475.48	**42**	712.78	**62**	996.04	**82**	1216.56	**102**	1554.56
3	-7.98	**23**	491.86	**43**	725.93	**63**	1015.00	**83**	1233.01	**103**	1584.81
4	120.60	**24**	502.67	**44**	729.04	**64**	1028.30	**84**	1234.87	**104**	1600.31
5	154.57	**25**	506.16	**45**	743.79	**65**	1042.77	**85**	1245.27	**105**	1643.33
6	188.86	**26**	527.74	**46**	755.94	**66**	1046.80	**86**	1254.58	**106**	1671.76
7	217.97	**27**	534.27	**47**	776.06	**67**	1061.39	**87**	1264.09	**107**	1683.77
8	257.79	**28**	565.34	**48**	785.64	**68**	1072.00	**88**	1275.14	**108**	1705.20
9	285.38	**29**	576.75	**49**	815.03	**69**	1077.30	**89**	1287.07	**109**	1738.16
10	314.92	**30**	579.46	**50**	833.21*	**70**	1089.68	**90**	1303.87	**110**	1800.27
11	332.47	**31**	585.25	**51**	853.84	**71**	1097.81	**91**	1323.62	**111**	1816.47
12	338.33	**32**	588.84	**52**	867.33	**72**	1103.57	**92**	1335.65	**112**	1826.95
13	365.52	**33**	605.03	**53**	887.68	**73**	1114.56	**93**	1350.21	**113**	1995.26*
14	370.28	**34**	613.25	**54**	901.35	**74**	1122.12	**94**	1366.03	**114**	2123.21*
15	382.74	**35**	615.53	**55**	910.35	**75**	1133.63	**95**	1384.12	**115**	2566.91
16	397.53	**36**	628.30	**56**	923.03*	**76**	1143.64	**96**	1394.86	**116**	2772.25*
17	411.76	**37**	640.17	**57**	930.75	**77**	1169.11	**97**	1401.73	**117**	3150.94
18	425.36	**38**	652.32	**58**	933.16	**78**	1174.48	**98**	1419.49	**118**	3286.59
19	438.53	**39**	662.20	**59**	959.11	**79**	1180.97	**99**	1438.60	**119**	3428.06
20	443.07	**40**	681.58	**60**	963.89*	**80**	1196.72	**100**	1474.44	**120**	3464.46

Table 5.6 Γ-Point phonons for the ILB1 phase at 70 GPa. The values highlighted correspond to symmetric H-bond stretching modes (2000-2700 cm^{-1}) and C-Cl stretching modes (833 and 923 cm^{-1}).

N	Freq (cm^{-1})	N	Freq (cm^{-1})	N	Freq (cm^{-1})	N	Freq (cm^{-1})	N	Freq (cm^{-1})	N	Freq (cm^{-1})
1	-34.60	**21**	443.30	**41**	670.95	**61**	940.41	**81**	1168.14	**101**	1472.67
2	-23.59	**22**	451.37	**42**	698.79	**62**	943.33*	**82**	1177.86	**102**	1522.74
3	-18.51	**23**	454.05	**43**	706.79	**63**	975.51	**83**	1197.61	**103**	1552.21
4	114.33	**24**	476.85	**44**	723.11	**64**	983.19	**84**	1202.19	**104**	1577.17
5	160.76	**25**	500.83	**45**	738.59	**65**	993.31	**85**	1203.17	**105**	1632.55
6	203.06	**26**	506.53	**46**	752.80	**66**	998.07	**86**	1224.71	**106**	1637.98
7	223.54	**27**	513.77	**47**	757.17	**67**	1003.60	**87**	1241.21	**107**	1665.82
8	245.55	**28**	530.94	**48**	770.36	**68**	1015.72	**88**	1242.66	**108**	1700.01
9	274.20	**29**	559.59	**49**	797.18*	**69**	1028.39	**89**	1266.53	**109**	1721.35
10	294.98	**30**	569.68	**50**	811.30	**70**	1041.24	**90**	1277.44	**110**	1766.12
11	297.95	**31**	572.66	**51**	814.43	**71**	1046.72	**91**	1311.65	**111**	1775.07
12	329.43	**32**	580.47	**52**	837.65	**72**	1052.00	**92**	1327.78	**112**	1805.18
13	346.74	**33**	590.77	**53**	847.38	**73**	1064.15	**93**	1337.61	**113**	2263.74*
14	362.36	**34**	602.77	**54**	871.63	**74**	1077.68	**94**	1343.60	**114**	2389.85*
15	365.55	**35**	607.07	**55**	878.63	**75**	1082.82	**95**	1360.60	**115**	2731.08*
16	378.50	**36**	620.16	**56**	886.51	**76**	1093.37	**96**	1385.48	**116**	2789.48
17	386.47	**37**	633.64	**57**	893.92	**77**	1121.53	**97**	1404.33	**117**	3306.80
18	401.45	**38**	641.57	**58**	906.50	**78**	1132.10	**98**	1414.40	**118**	3338.51
19	405.83	**39**	655.75	**59**	916.74	**79**	1141.31	**99**	1441.20	**119**	3387.19
20	414.98	**40**	662.47	**60**	922.55	**80**	1159.69	**100**	1460.22	**120**	3427.79

Table 5. 7 Γ-Point phonons for the ILB1 phase at 50 GPa. The values highlighted correspond to symmetric H-bond stretching modes (2200-2700 cm^{-1}) and C-Cl stretching modes (797 and 943 cm^{-1}).

None of the phonon spectra contains imaginary modes; the 3 lowest frequencies can be interpreted as numerical zeros within the tolerances chosen and correspond to their rigid translations of the lattice. The C-Cl bonds and the symmetrical H bonds discussed when analysing the equilibrium structures are therefore true features of compressed $C_6N_9H_3$.HCl, in both LDA and PBE calculations.

The phonon analysis at 90 GPa further shows that the frequencies associated to the semi-symmetric hydrogen bond are calculated as 2262, 2228, and 1995 (cm^{-1}), while the frequencies of the carbon chloride bonds are 1015 and 965 (cm^{-1}). In particular, the H-bond stretching frequencies in the nearly symmetric configuration discussed here are considerably red-shifted compared to N-H stretching vibrations not involved in H bonding, which occur at over 3400 cm^{-1} in this pressure range (highest modes in Table 5.5Table 5. 7).

In the structure at 50 and 70 GPa only 1 of the two N-H-N bonds is symmetric; the second N-H stretching occurs at much higher frequency of ~ 2700cm^{-1}. The symmetric H bonds should be sufficiently clear to be observed experimentally in this region of the spectrum.

Let us now consider the band structure in $C_6N_9H_3$.HCl. It is well known that the LDA functional generally underestimates the value of the band gap. Even so, comparisons of the band structures at different pressures are significant. A selection of calculated band structures obtained during the compression/decompression cycle is reported in Figure 5.11 .

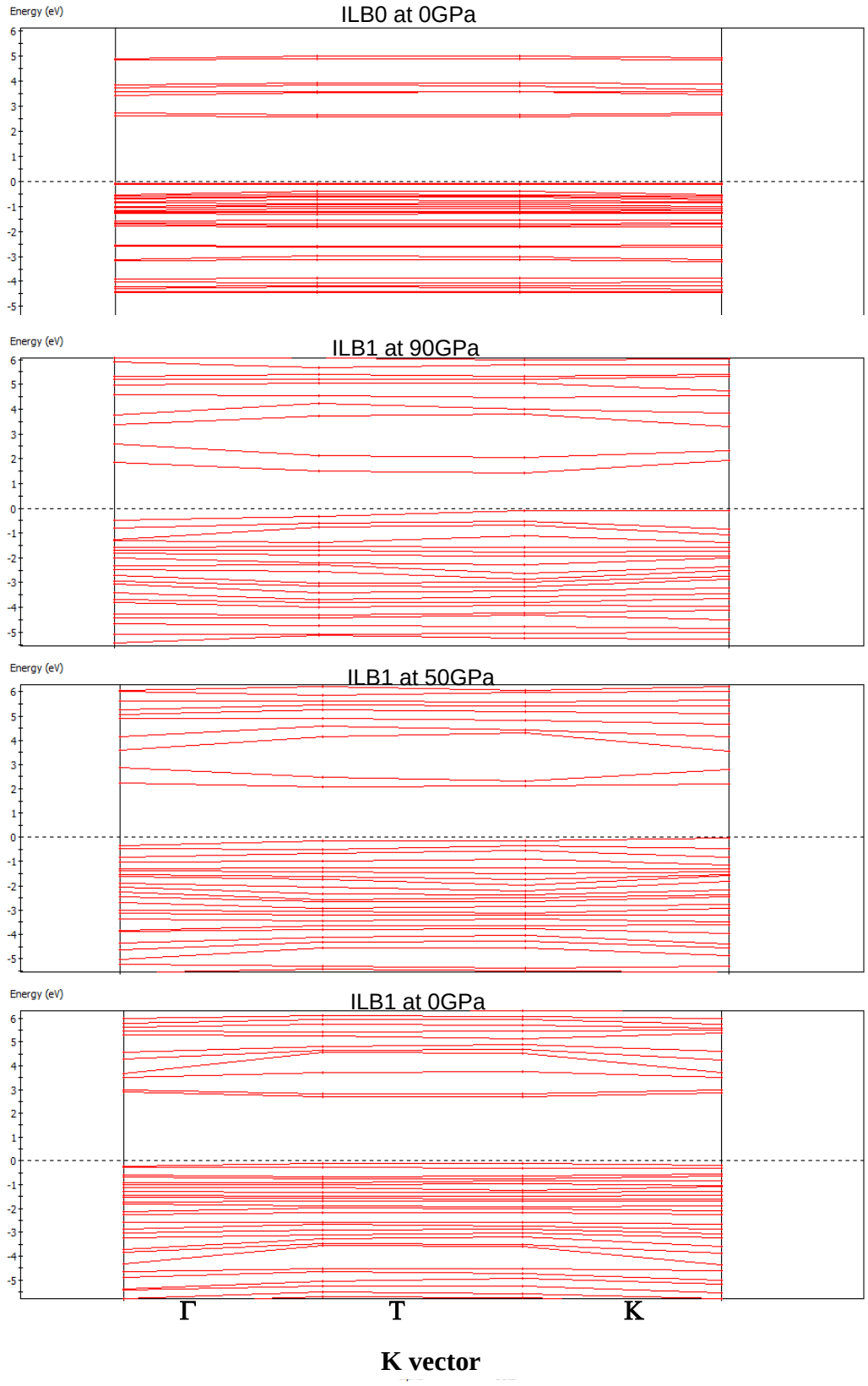

Figure 5.11 Calculated band structures of ILB0 at 0GPa and ILB1 phases of $C_6N_9H_3$.HCl at 90, 50 , 0 GPa. The dashed line denotes the Fermi level.

The band structure of the solid is shown for the ILB0 phase at ambient pressure, and for ILB1 at pressures of 90, 50 and 0 GPa i.e. during the decompression part of the work. The band gaps are estimated as 2.65 eV, 1.90 eV, 1.85 eV, and 2.70 eV respectively. Application of pressure therefore contributes to reducing the band gap, but the material remains an electronic insulator at all pressure conditions examined here.

An example of density of states corresponding to the ILB0 material at ambient pressure is also reported for completeness in Figure 5.12.

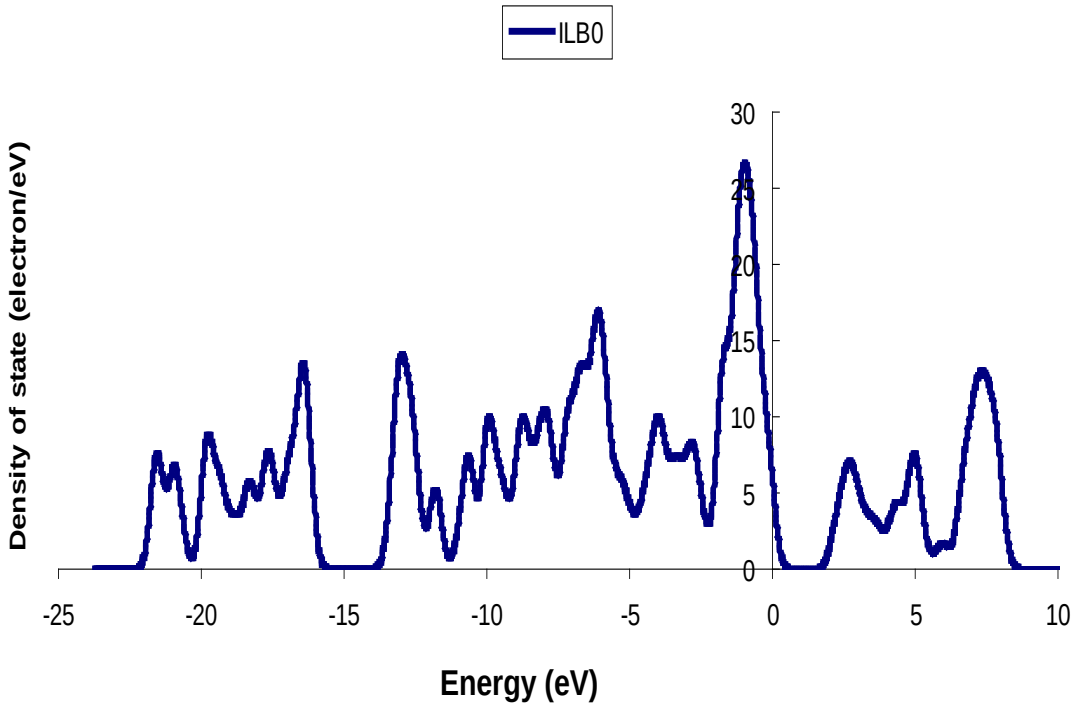

Figure 5.12 Density of states of the ILB0 phase of the g-$C_6N_9H_3$.HCl structure at ambient pressure

Figure 5.13 represents the variation of the calculated band gap energy during the increase and subsequent relief of pressure. The figure shows that between 0 and 50 GPa, the pressure increase causes a decrease in the bad gap from 2.65 eV to 1.6 eV. The band gap increases at 60 GPa, possibly indicative of the forthcoming sp^2 to sp^3 rehybridisation of the layer, even if the latter only occurs at 70 GPa. After the discontinuity at 60 GPa, the gap decreases again on increasing pressure. The value during decompression is less smooth, but shows a trend to larger band gap at lower pressure.

At all values of pressure, including ambient pressure the value of the band gap is larger in the decompression (blue line in Figure 5.13) than in the compression (purple line) part of the work. These correspond to sp^3- hybridised ILB1 and sp^2- hybridised ILB0 phases, since some interlayer bonding and sp^3 hybridisation of C and N atoms is retained on decompressing the ILB1 phase.

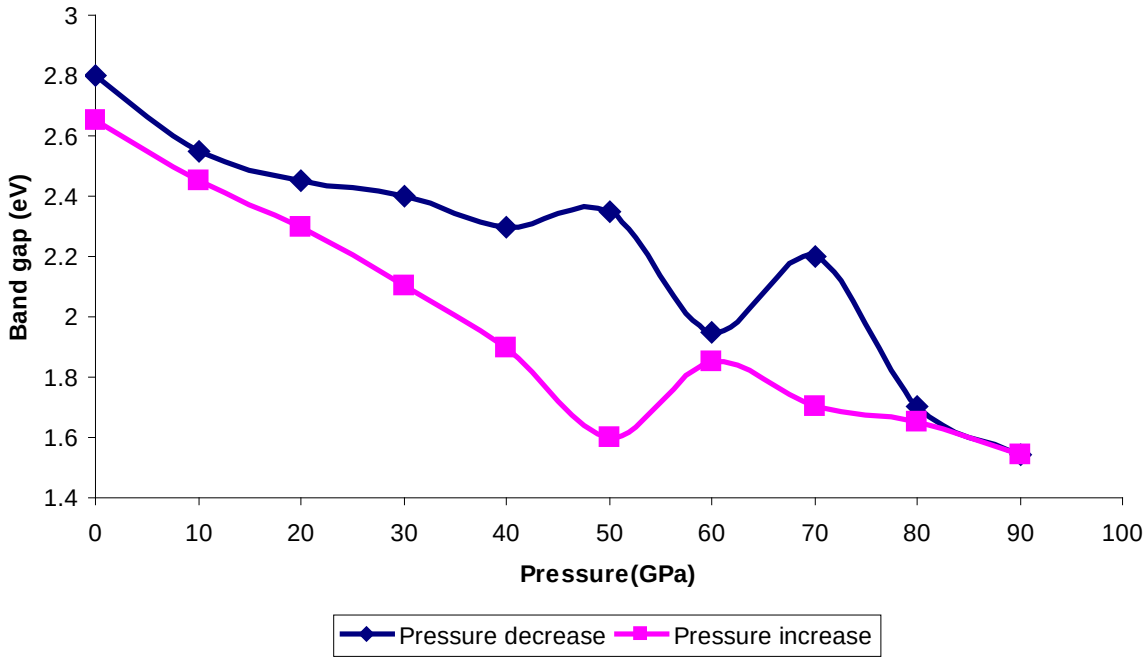

Figure 5.13 Calculated band gap vs Pressure.

5.2 Li Intercalation into Carbon Nitride

5.2.1 Introduction

Searching for new materials that can provide alternative energy storage devices are vital to meeting today's global social demand. As has been amply seen in earlier chapters, electrochemical energy storage methods attract much research, with focus on rechargeable batteries.

The current implementation of rechargeable Li-ion batteries employs carbon (graphite) as anode. Carbon based materials can adopt a wide variety of structures and shapes with different chemical and electronic properties. Graphite is the stable allotrope of carbon at ambient conditions; its structure consists of stacking carbon sheets, containing sp^2 hybridised carbon atoms in interconnecting hexagons. Changing synthesis conditions can lead to a further host of carbon structures[121,122]which can intercalate Li ions in the interlayer spacing[123,124,125] as required in rechargeable batteries[126,127,128].

When searching for new electrode materials for rechargeable Li ion batteries, one of the aims is to deliver materials that are able to host the greatest amount of Li ions per unit of mass or volume and retain their structural integrity during intercalation and de-intercalation.

Li intercalation in graphite has been achieved via chemical and electrochemical methods[129,130] and yields a stable phase of composition LiC_6. Upon Li intercalation, the graphite structure deforms[131,132]; the process initially involves an expansion of the interlayer separation, of less than 10%[133], between the layers where Li is intercalated. The intercalation is staged, i.e. a full layer is occupied before neighbouring interlayer spaces are filled. The increased interlayer separation is in principle beneficial for the intercalation process, as it provides larger spaces for the migration and intercalation of further Li ions, although it causes strains in the device that may limit its lifetime. The theoretical capacity of graphite (corresponding to formation of the LiC_6 phase) is 372 $mAhg^{-1}$; although an irreversible capacity of 1000 $mAhg^{-1}$ has

been reached upon higher Li intercalation, followed by a structure collapse after few intercalation /deintercalation cycles[130,134]. Carbon Nano Tubes (CNT), which can be imagined as folded graphite sheets, are one of the promising structures for Li batteries and have found a vast range of applications since they were first discovered in 1991 by Iijima[122]. Li intercalation in CNTs has been investigated, and was found theoretically and experimentally that the Li ions are preferably adsorbed on the outer surface of the CNTs, although the Li ions can also be inserted into CNT; it is therefore very difficult to provide a complete view of the intercalation mechanism[135].

Theoretical calculations have shown that upon adsorption of Li ions on CNT walls, there is a partial electron transfer that leads to net ionic charges of Li of 0.7 |e|; and the CNT acts as Li ion attractor[135].

Li adsorption was calculated as stable on the outer wall of CNTs compared with the inner walls; also, diffusion of Li inside a CNT is nearly barrier less (the activation energy is of only ~0.04 eV), which suggests that the residence time of Li inside CNTs is very short[136,137].

Other carbon structures derived from pyrolitic reactions of organic precursors are less ordered. The Li intercalation ability into such structures can be higher than in graphite, which is explained by the existence of different types of intercalation mechanism. The higher ability to accommodate Li ions makes the deintercalation process slower and more difficult, which is not suitable for Li ion batteries[138,139,140].

The carbon nitride investigated earlier in this chapter shares the layered sp^2 structure of graphite, contains additional voids within the layer which may favour Li migration, and has heteronuclear rings (C_3N_3 rather than C_6 in graphite), which may favour intercalation processes. It is therefore of interest to explore whether the layered carbon nitride compound may provide interesting features as electrode for rechargeable Li-ion batteries. The next section examines computationally the Li intercalation and migration in this new host.

5.2.2 Structure

As mentioned in section 5.1, the layered structure[94,141] examined in this chapter consists of sheets of composition $C_6N_9H_3$: For the purpose of Li intercalation, we ignore the interstitial HCl ions and study the framework of composition $C_6N_9H_3$ only. The $C_{12}N_{12}$ holes are large enough to host adsorbed ions; in this case Li. The Li intercalation can therefore exploit both interlayer space and intralayer voids.

The fully optimized structure of $C_6N_9H_3$ has cell parameters $a = b = 8.5639$ Å, and $c = 6.0296$ Å, and adopts hexagonal $P6_3/m$ symmetry.

The structure at ambient pressure has flat layers as shown in Figure 5.14.a; most layered carbon nitride materials examined are believed to buckle due to repulsion between closely associated lone pairs on the nitrogen atoms. The large cavities found within $C_6N_9H_3$ allow for that this electronic repulsion to be avoided allowing the layers to remain planar[94].

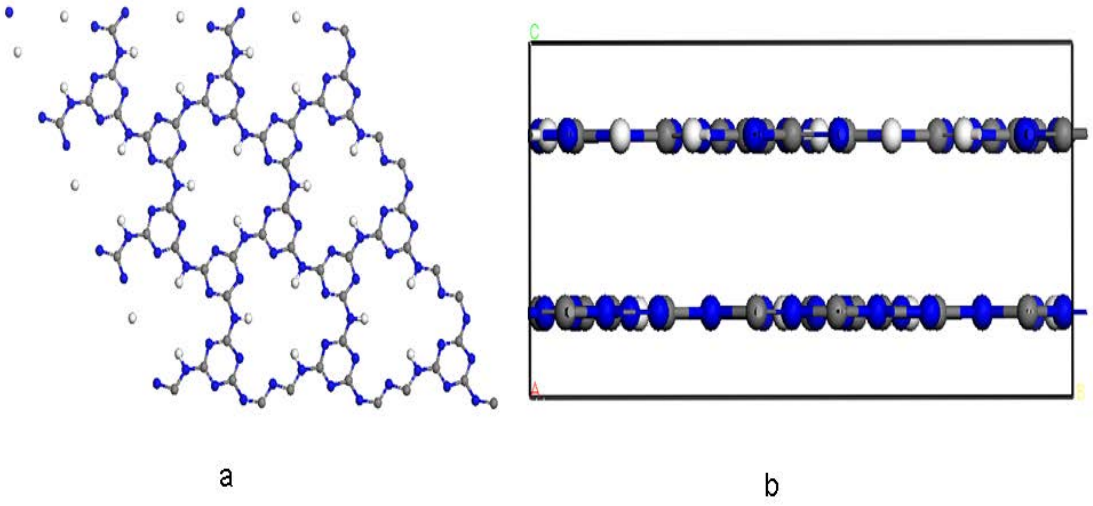

Figure 5.14 a). A single layer of the $C_6N_9H_3$ structure shows the large voids. B). Each unit cell contains two atomically flat layers of the Carbon Nitride solid.

5.2.3 Computational Details

The computational work was performed using the same technique and parameters as discussed in section 5.1 for the host material: the CASTEP code, the LDA functional and ultra-soft pseudopotentials; the cut-off value for the plane wave expansion was 450 eV and reciprocal space was sampled on a regular net with a consistent spacing of 0.04 $Å^{-1}$, corresponding to 4x3x4 K-points in the first Brillouin zone of a $C_{12}H_{18}H_6$ cell. As in chapter 4, the Li intercalation energy has been calculated as

$$\mathbf{E=E\ (Li.\ host)-E\ (host)-E\ (Li)} \qquad (5.1)$$

where E (Li. host), and E (host) are the unit cell energies of the host system after and before the Li intercalation. The energy of lithium metal, E (Li) was obtained by optimisation of body-centred cubic (Im3m) unit cell, stable at room temperature, using the same parameters employed for the carbon nitride work, but a k-point mesh of 25x25x25. The equilibrium lattice parameter is calculated as 3.491 Å, very close to the experimental value of 3.51 Å.

The lowest energy configurations have been sought for a number of Li-insertion concentrations using unit cells of a composition $Li_nC_{12}N_{18}H_6$, n=1-12. The nature of the insertion process has been determined by comparing the thermodynamic stability of homogeneous and possible coexisting phases. All calculations have been performed in *P1* symmetry.

5.2.4 Results and Discussion

5.2.4.1 First Li intercalation

In order to understand the Li intercalation into the g-$C_6N_9H_3$ structure and identify the stable intercalation sites, one Li ion was inserted into one unit cell of the structure in different possible positions and full geometry optimisations were performed. Comparison of the relative energies makes it possible to identify the stable intercalation sites.

The results show that there are three possible sites that are favourable for Li insertion. In Figure 5.15 these sites are denoted as 'A', 'B' and 'C'. Equilibrium cell parameters and intercalation energy for the cell with Li in site A, B and C are summarised in Table 5.8; it can be seen there that sites A and B have similar intercalation energy of -1.89 and -1.81 eV, while in C this value reduces to -1.50 eV.

It should be noted that alike Li adsorption into graphite, insertion of Li ions into g-$C_6N_9H_3$ causes some local deformation of the host material, reflected in the changes of the lattice parameters upon Li insertion, see Table 5.8.

	Fractional Coordinates of Li	a(Å)	b(Å)	c(Å)	Intercalation Energy(eV)
Original Structure	----------	8.564	8.564	6.030	----------
Site A	(0.678,0.831,0.497)	8.504	8.471	6.495	-1.89
Site B	(0.631,0.575,0.577)	8.384	8.567	5.734	-1.81
Site C	(0.312,0.405,0.297)	8.388	8.441	5.702	-1.50

Table 5.8 Li fractional coordinates, cell parameters, and the intercalation energy for the unit cell of g-$C_6N_9H_3$ with 1 Li atom.

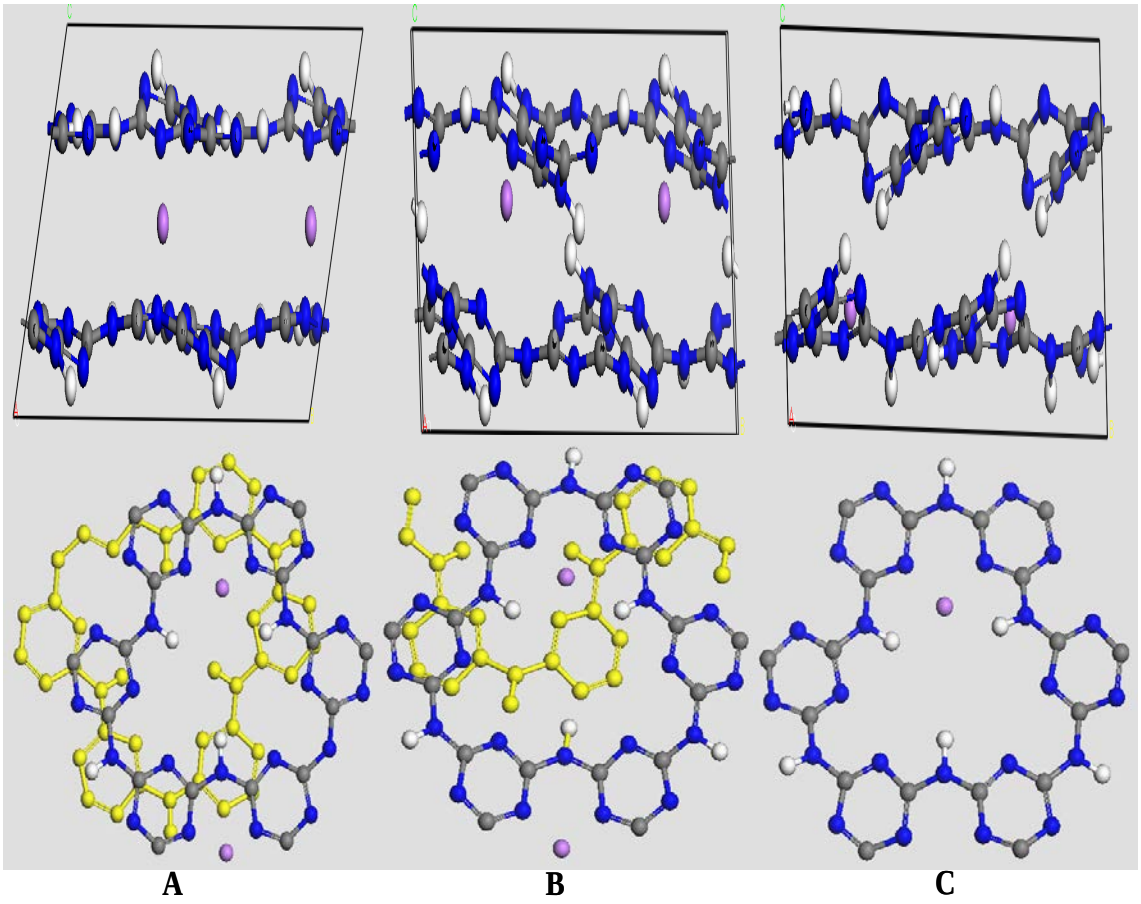

Figure 5.15 Stable Li intercalation sites in g-$C_6N_9H_3$

Let us consider the local Li environment in the 3 sites. In site A, the Li ion is located in the middle of the interlayer space at z=0.497, hence roughly equidistant from the layer above (at z= 0.75) and below (at z= 0.25). Site A corresponds to one of the triangular cavities of the upper layer, with Li displaced towards one of the corners where it can achieve a more effective interaction with the basic N atoms (see Figure 5.15.A). This site has a coordination number of 4, with Li bond distances of 2.021, 2.021 Å (upper layer), 2.018 and 2.025 Å (lower layer). In site B, Li is still hosted in the interlayer space, but it is now closer to one that the other layer, at fractional coordinate z=0.577.

Again, site B corresponds to one of the corners of the triangular cavity, but Li is now located next to one of the bridging NH groups of the adjacent layer, with a coordination number of 3.

The closest Li-N bond distances are 1.875 and 1.917 Å from two N atoms of the triangular void, and 1.972 Å from one N atom of the triazine ring (see Figure 5.15. B).

In site C , Li is instead located within one of the graphitic layers at fractional coordinate z= 0.297; site C is within one of the triangular voids, shifted to one of the vertices where Li has coordination number of 2, with equilibrium Li-N bond distances of 1.886 and 1.933 Å (see Figure 5.15.C).

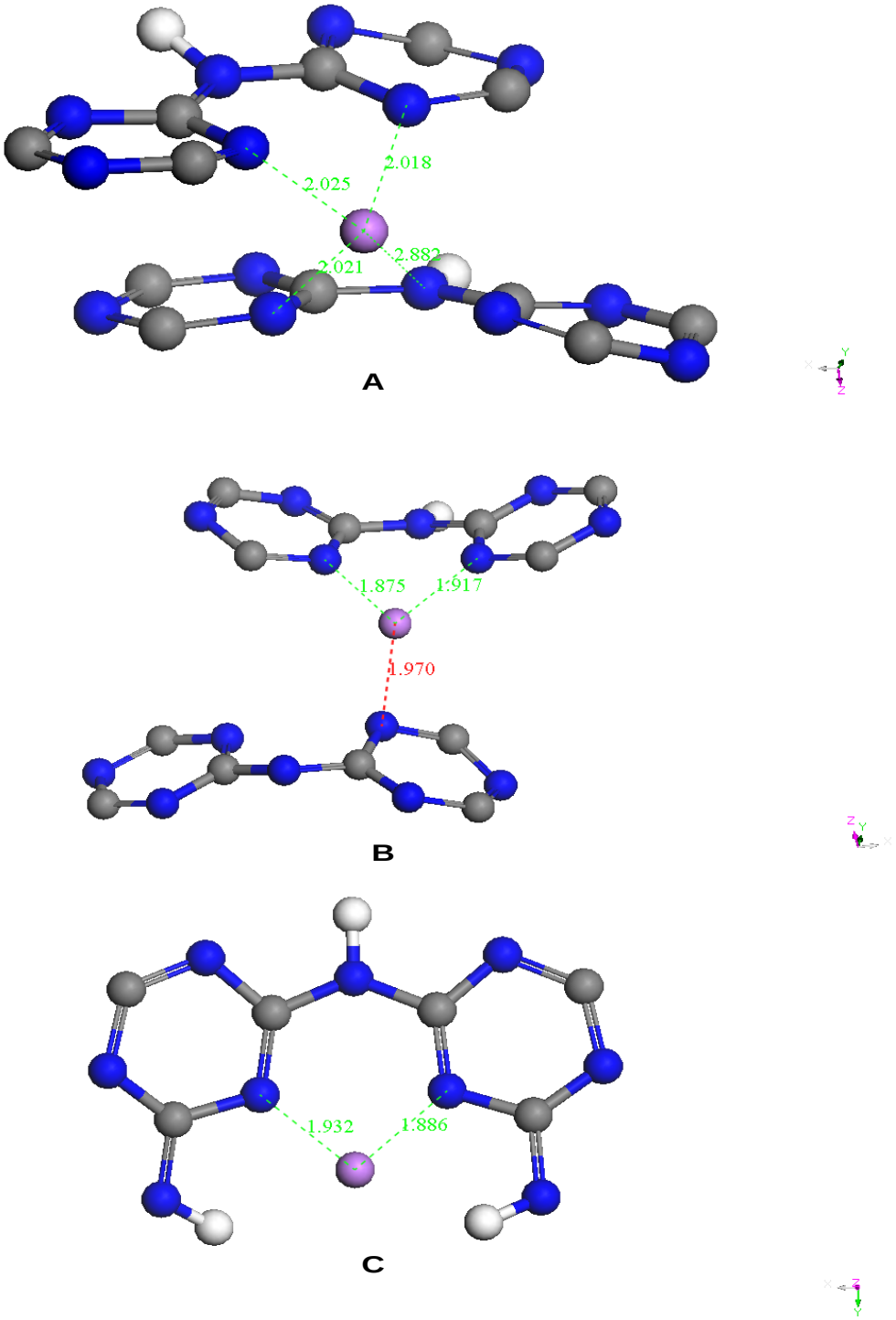

Figure 5.16 Environment of Li ion in the triangular cavities of the g-$C_6N_9H_3$ (A, B, C)

Li intercalation into g-$C_6N_9H_3$ leads to significant deformations of the host lattice. The effect on the lattice parameters can be analysed using the data of Table 5.8. Occupation of site A causes a large expansion along the *c* direction, similar to what observed for intercalation in graphite and consistent with the occupation of the interlayer space pushing the layers apart. Such an expansion is not observed for sites B and C, which instead cause a contraction of the structure upon intercalation. Not only do the lattice parameters change; the cell also changes shape, as observed by comparing the cell angles (reported in Table 5.9). In particular, Li intercalation in site A causes a large shear of adjacent layers, which enables Li to be sandwiched between the corners of two triangular voids in adjacent layers. Finally intercalation is accompanied by some buckling of the layers, which as in previous sections has been monitored via dihedral angles in the layer (as indicated in Figure 5.17), reported in Table 5.9.

Li concentration		α°	β°	γ°	ABCD°	EFGH°
Li=0		90.0	90.0	120.0	0.02	0.02
Li=1	**Site A**	60.0	106.6	119.4	0.22	2.03
	Site B	89.0	100.9	121.3	1.94	4.62
	Site C	97.9	81.5	118.7	2.39	7.61
Li=2		100.8	95.9	123.0	2.34	35.69
Li=3		105.3	103.5	120.1	4.80	0.85
Li=4		103.5	103.5	119.8	5.17	4.40
Li=5		103.8	104.3	119.1	3.16	6.88
Li=6		87.2	107.0	120.3	25.41	36.13
Li=7		84.4	110.7	120.2	24.35	34.29
Li=8		86.2	107.6	120.8	19.01	13.43
Li=9		87.1	109.2	120.8	44.00	22.48
Li=10		94.1	99.2	120.0	56.12	37.08
Li=11		85.1	110.7	120.1	56.30	6.00
Li=12		89.3	104.0	120.9	53.79	2.66

Table 5.9 Variation of unit cell angles and internal dihedral angles (degrees) (using the labelling of atoms of Figure 5.17) upon Li insertion

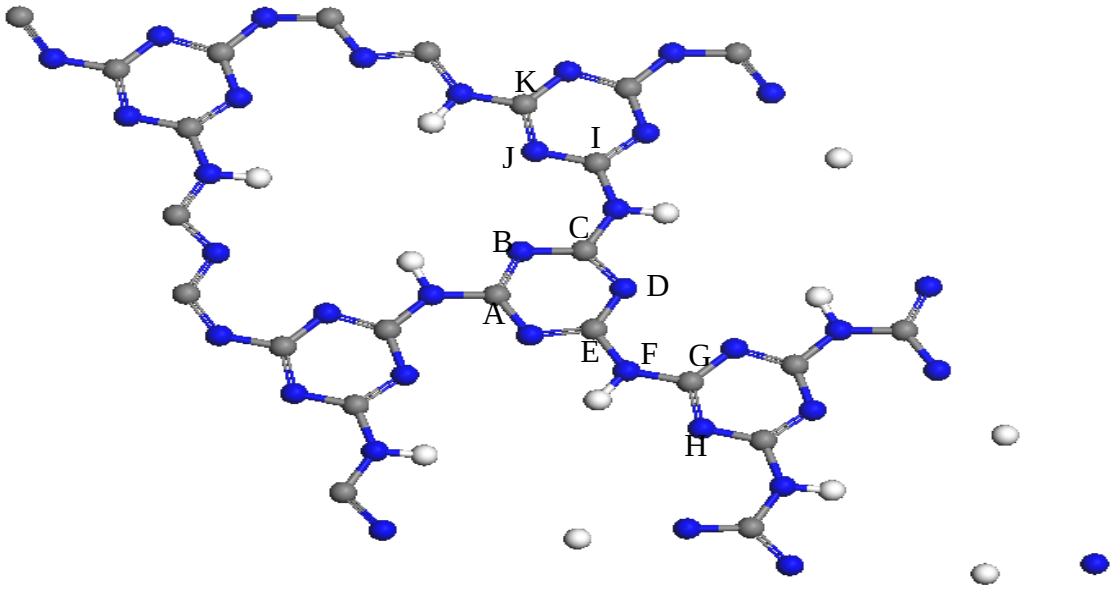

Figure 5.17 Dihedral angles employed to measure the extent of deformation in g-$C_6N_9H_3$ upon Li ion insertion

Let us now examine what is the effect of Li insertion on the electronic structure of the solid. To this goal, in Figure 5.18 and Figure 5.19 we report band structure and density of states for the material without Li and with 1 Li in site A, B and C. It is clear in Figure 5.18 and Figure 5.19 that Li ionises upon intercalation, and donates its electron to the conduction band of the carbon nitride host. The shift in the position of the bands before and after intercalation is an artefact of the convention adopted in CASTEP to assign the zero of the energy to the Fermi level, which for n=0 is the top of the valance band, whilst it is at the bottom of the conduction band for n=1. After accounting for this change of the energy zero, it appears from Figure 5.19 that the valance and conduction bands have very similar features before and after Li intercalation, and appear insensitive to the location of Li in site A, B or C. The electronic change accompanying the Li intercalation is therefore a rigid occupation of the conduction band states. The donated electrons is delocalised across the carbon nitride host, which changes from insulator to metal upon intercalation.

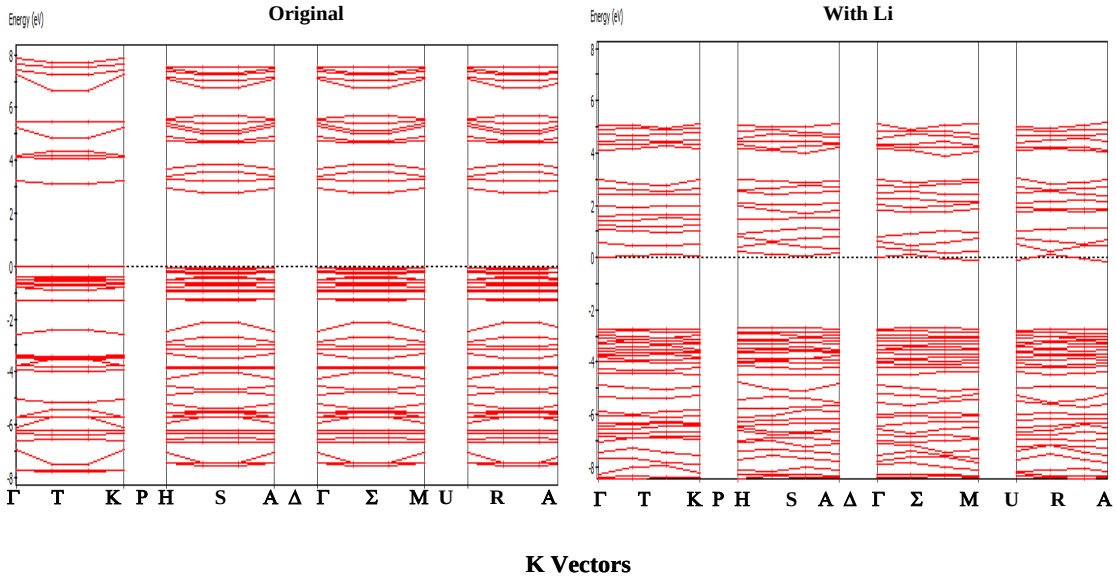

Figure 5.18 Comparison of calculated band structures for g-$C_6N_9H_3$, and $LiC_{12}N_{18}H_6$ with 1 Li in site A

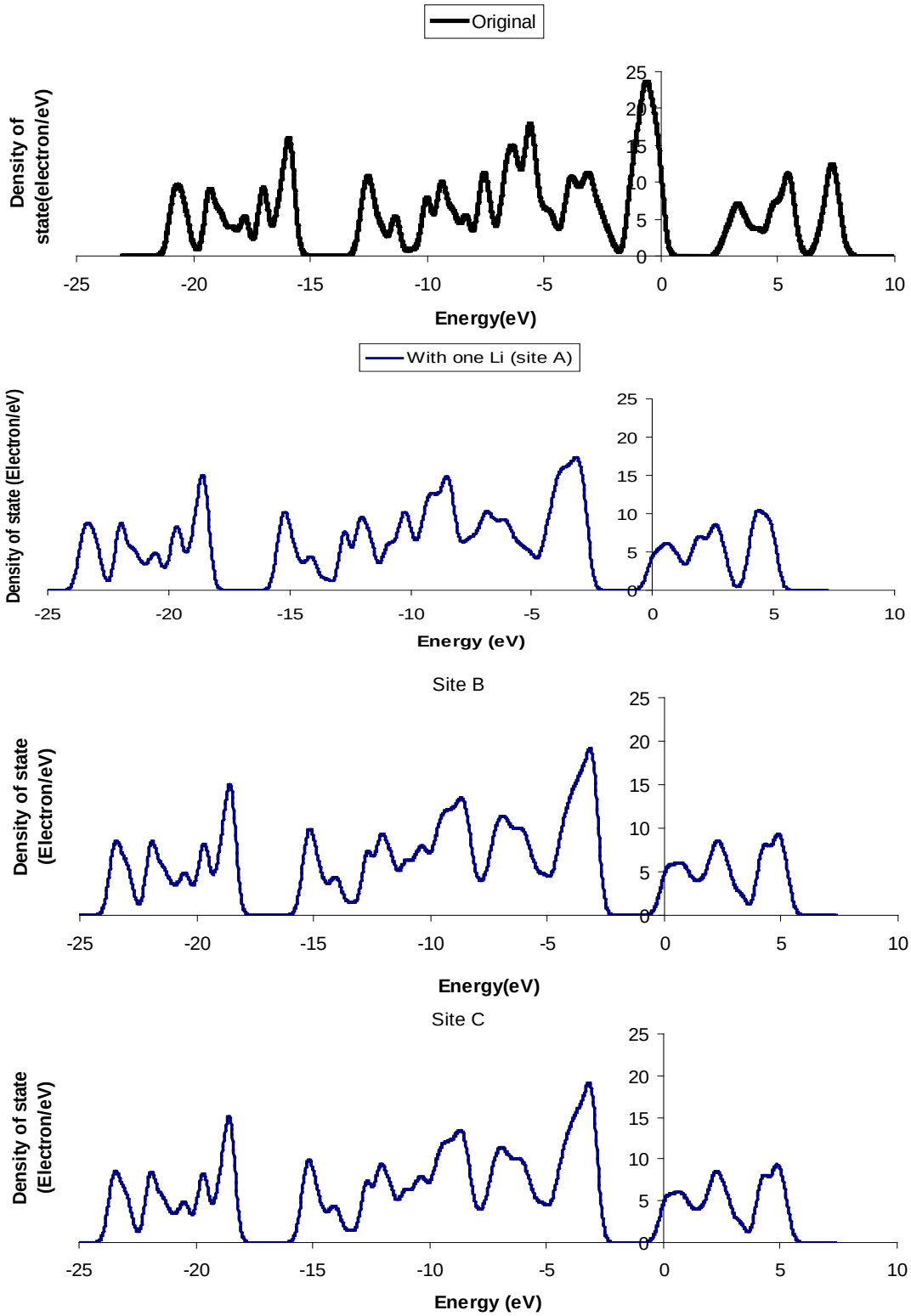

Figure 5.19 Density of states of the g-$C_6N_9H_3$ and $LiC_{12}N_{18}H_6$ structures, comparing sites A, B and C

5.2.4.2 Further Li intercalation up to 12

After considering the first Li intercalation process, we now study how the features of the Li intercalation in the graphitic carbon nitride phase vary as a function of the Li content. To this goal, geometries and energies of phases with up to 12 Li ions per unit cell are calculated, corresponding to the composition $Li_nC_{12}N_{18}H_6$ (n=1-12). It is useful to notice that this range of Li content corresponds to a much higher ratio between Li and heavy framework atoms than is achievable to intercalate reversibly in graphite (where reversible intercalation occurs up to a Li : C ratio of 1 : 6).

The structures of the most stable Li intercalation positions for all n values examined is summarised in Figure 5.20, while the relative intercalation energy, unit cell parameters and volumes are reported in Table 5.10. Unit cell angles, dihedral angles and triazine angles correspond to Li ion concentration n=1 to 12 are reported in Table 5.9. The variation of the cell parameters is also shown schematically in Figure 5.21.

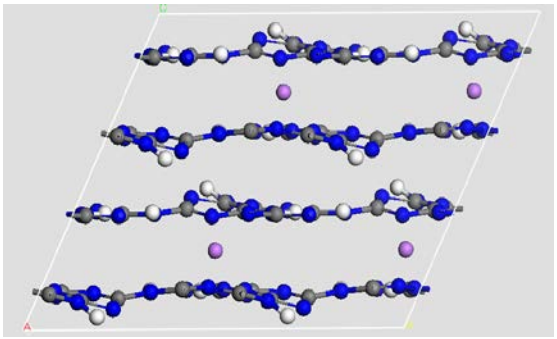

n= 1

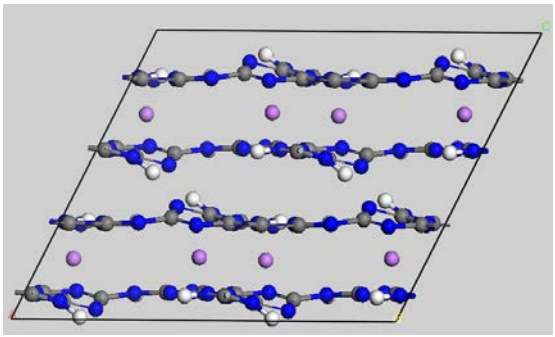

n= 2

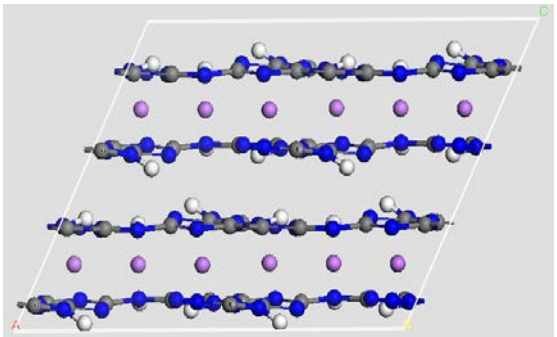

n= 3

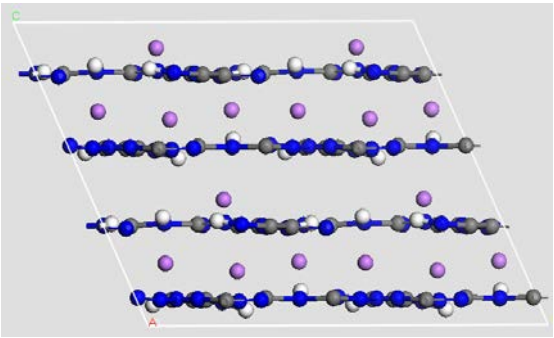

n= 4

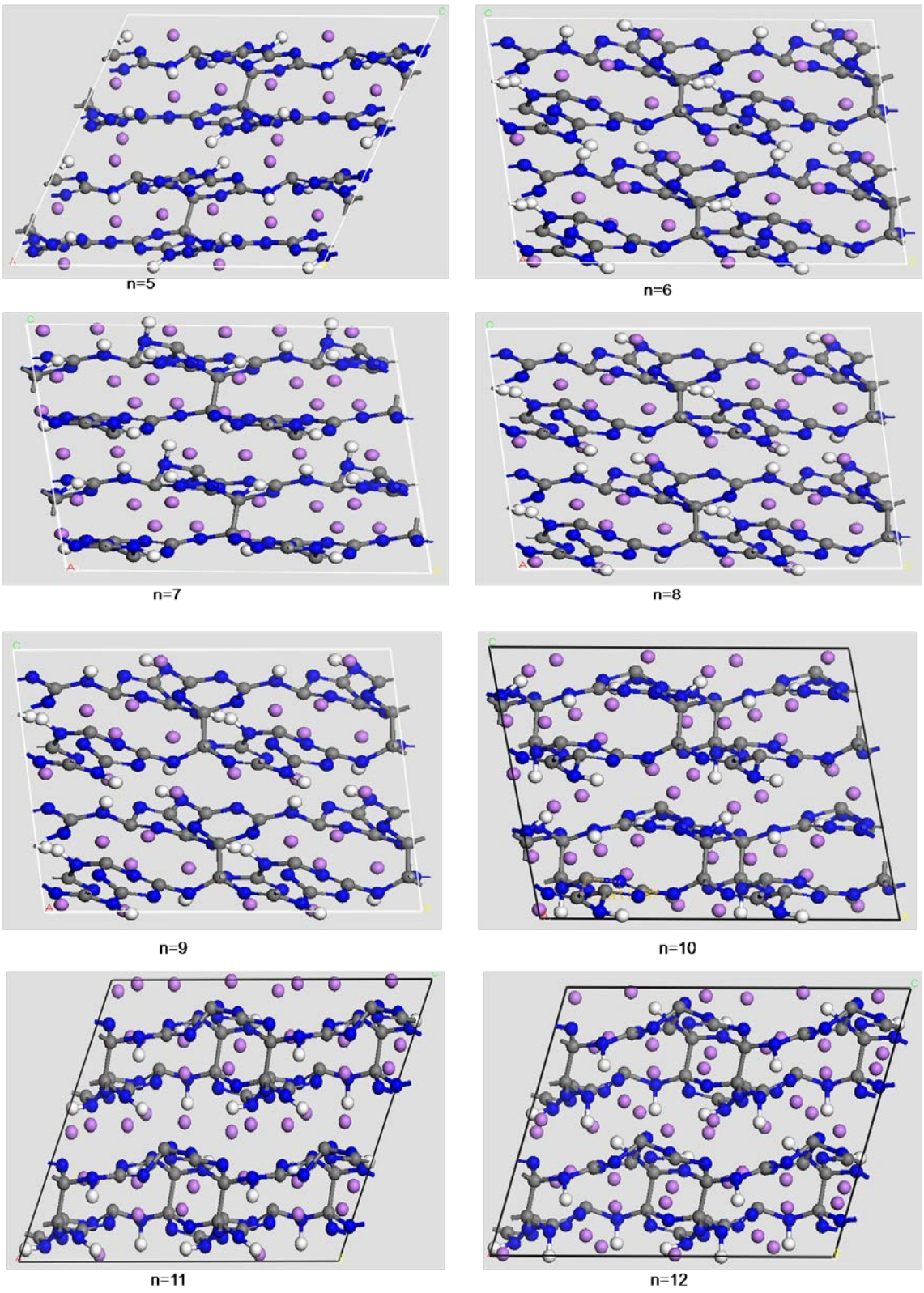

Figure 5.20 Stable Li configurations in the $Li_nC_{12}N_{18}H_6$ cell, for each value of n examined

		Relative Intercalation Energy (eV)	a (Å)	b (Å)	c (Å)	V (Å^3)
Li=0			8.56	8.56	6.03	382.93
Li=1	**Site A**	-1.89	8.50	8.47	6.49	352.30
	Site B	-1.81	8.38	8.56	5.73	343.76
	Site C	-1.50	8.38	8.44	5.70	349.20
Li=2		-1.94	8.60	8.53	6.34	342.11
Li=3		-2.23	8.60	8.58	6.13	338.83
Li=4		-0.33	8.65	8.59	6.22	355.11
Li=5		-1.20	8.48	8.43	6.63	363.75
Li=6		-0.49	7.69	8.75	6.10	340.79
Li=7		-0.40	7.86	8.78	6.47	356.40
Li=8		-0.76	8.54	8.82	6.12	377.40
Li=9		-0.27	8.63	8.42	6.38	372.59
Li=10		-0.14	8.60	8.42	6.04	368.35
Li=11		-0.21	8.52	8.58	6.06	356.34
Li=12		0.30	8.71	8.60	5.92	365.78

Table 5.10 Relative intercalation energy, unit cell parameters and unit cell volume for subsequent Li intercalation process

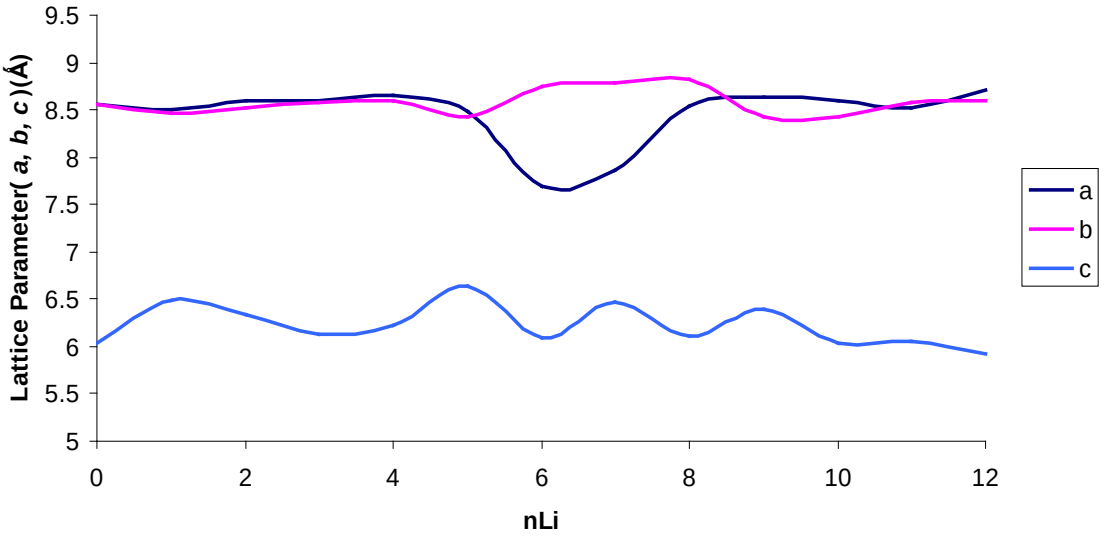

Figure 5.21 Lattice parameters change during Li intercalation as the number of Li ions inserted into the unit cell increases

Overall, changes are relatively small and affect mostly the initial intercalation stages; the cell volume first contracts from 383 $Å^3$ at (n=0) to 352 (n=1) and 342 $Å^3$ (n=2), and then expands gradually (even if not linearly) upon further Li intercalation.

Looking at Figure 5.20, it can be seen that the Li intercalation in the layered carbon nitride is staged, similar to the behaviour observed in graphite. The first 3 Li ions occupy the same interlayer space and the case n=3 is stable with a staged structure in which one interlayer plane is fully occupied and one fully vacant. Only from the 4^{th} Li in the unit cell, the second interlayer space is occupied. The staged phase observed at n=3 is clearly still evident for n=4 and n=5.

Upon further increases of Li content, the Li ions appear to cluster and form intermetallic (Li-Li) bonds, which may be indicative of the formation of metallic Li nanoclusters in the interlayer space.

The layered structure of the host carbon nitride is retained up to n~5 after which internal distortions become important, which can be classified as buckling of the layers (n>6), coupled with the formation of interlayer C-C bonds. A fragment of the structure at n=5, highlighting the interlayer C-C bond, is shown in Figure 5.22. It is important here to stress on the different types of interlayer bonding compared to what observed earlier in section 5.1. While the application of pressure causes the formation of C-N interlayer bonds, here during Li intercalation the interlayer bond involves two C atoms, whose sp^3 hybridisation is stabilised in the anionic framework formed during intercalation.

As in earlier sections, buckling is monitored by the measurement of dihedral angles, which are summarised in Table 5.10 and plotted in Figure 5.23 as a function of Li content.

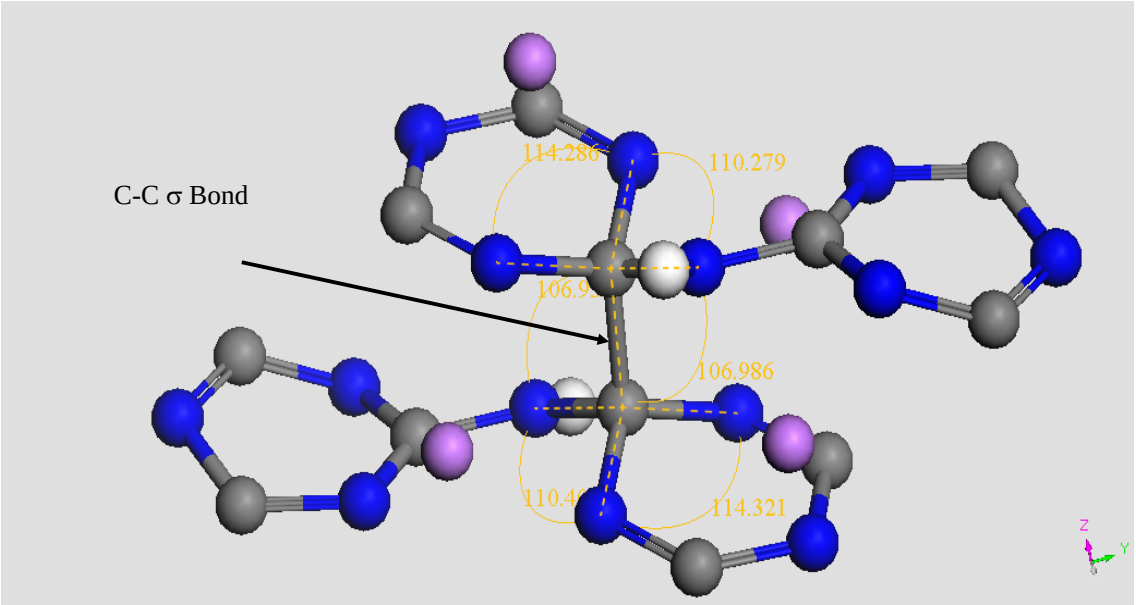

Figure 5.22 Fragment indicating the interlayer C-C bond between 2 triazine rings at Li =5

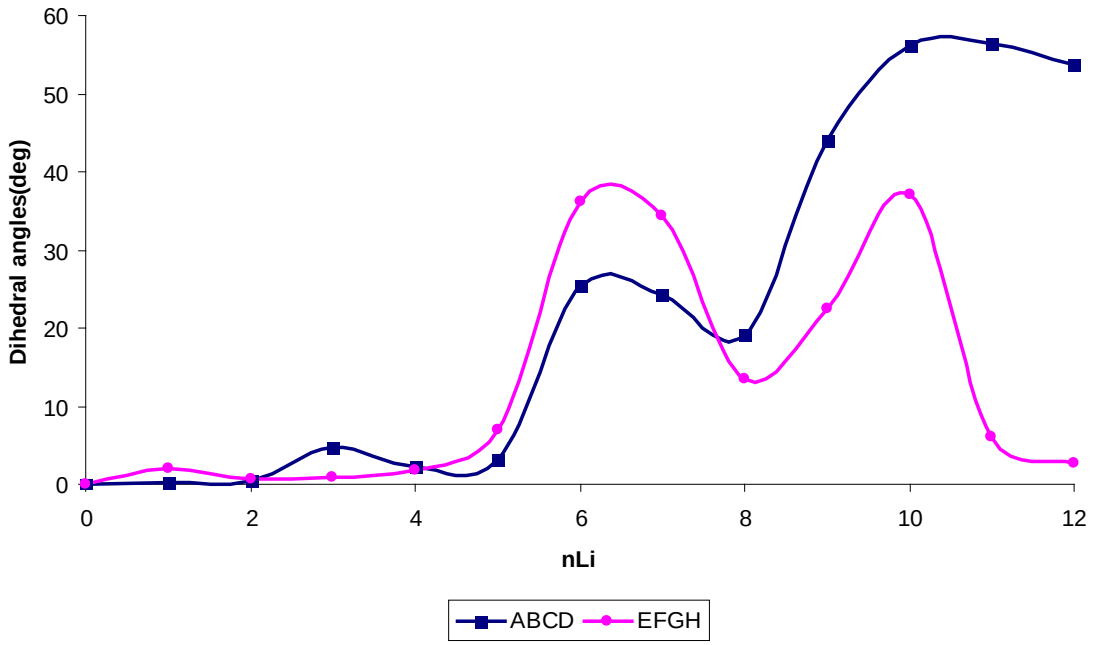

Figure 5.23 Dihedral angles (ABCD), (EFGH), as a function of the number of Li ions inserted into one carbon nitride unit cell.

In agreement with the visual inspection of the equilibrium structures of Figure 5.20, the dihedral angles (ABCD, EFGH) are found to be small (less than 10°) up to n=5, while they jump to 30° or more for n ≥ 6.

It is believed that the different staging observed here in the layered carbon nitride host compared to graphite is due to a more ionic character of the CN material, which creates greater electrostatic repulsion between Li ions. The basic character of the triazine nitrogens, each with a lone pair pointing towards the empty spaces, ensures a better environment for Li^+ than that achievable in graphite.

Upon insertion, Li fully ionises; the Li net charges as a function of n, calculated with a Mulliken scheme, are summarised in Table 5.11 and support the fully ionic nature of Li at each Li content. The donated electrons occupy the conduction band of the host carbon nitride; however upon increasing the electron density, the structure deforms and sp^3 hybridisation of C and N becomes more stable than sp^2; this feature causes the appearance of C-C interlayer bonds at n ≥ 5.

Only for n≥10 do we see in Table 5.11 that some of the Li have significantly less than formal charge, which may represent the onset of the formation of metallic nanoclusters, in which some of the Li electron density is no longer donated to the carbon nitride host, but located on the Li clusters.

The Mulliken analysis of charges is completed in Table 5.12, where we report the charge of C, N and H atoms as a function of n. At n=0 the net charges are +0.48 |e| for C, +0.5 for H and -0.47/-0.53 for N.

Increasing n up to 5 causes a relatively uniform decrease of the C, N and H charges, confirming that the electrons donated from Li occupy the bottom of the CB, in delocalised states. At n=6, however, we observe that the charge of two C atoms, those labelled as C6 and C10 in Table 5.12, decreases dramatically. This is a clear indication that electrons become localised on these two C atoms. The combination of structural and electronic changes confirms the change of hybridization from sp^2 to sp^3 of these C atoms that how have carbanion-type nature, with 2 unshared electrons forming a lone pair. On further increases of n, another pair of C atoms (labelled as C8 and C2) undergoes a similar modification.

Let us now examine the intercalation energy as a function of Li content. Data are reported in Table 5.10 and shown in Figure 5.24. It can be seen there that the energy becomes more favourable on increasing Li content, and increases from -1.89 eV for n=1 to -1.94 eV at n=2. The fully staged phase at n=3 corresponds to a smaller energy gain and has intercalation energy of -1.48 eV. From n=4 onwards the energy is of 1 eV or less, and it is stable up to n=11; the intercalation energy is small, and has a minimum at n=4, corresponding to the initial occupation of the second interlayer space; this local maximum may indicate small kinetic barriers to overcome. The variation of intercalation energy observed as a function of n indicates that the carbon nitride material is expected to behave similarly to graphite as electrode in electrochemical processes, but is able to accommodate a higher number of Li atoms per unit of mass (the phase with n=11 corresponds to a ratio between Li and heavy atoms in the host material of ~1:3, while the intercalation in graphite needs to stop at a Li:C ratio of 1:6).

	$Li_nC_{12}N_{18}H_6$											
	n1	**n2**	**n3**	**n4**	**n5**	**n6**	**n7**	**n8**	**n9**	**n10**	**n11**	**n12**
1st	1.10	1.09	1.14	1.10	1.11	0.99	0.95	0.99	0.99	1.07	1.06	0.93
2nd		1.09	1.09	1.07	1.16	1.10	1.21	1.22	1.12	0.93	0.98	1.01
3rd			1.09	1.07	1.06	1.05	1.06	1.08	0.93	1.14	1.12	0.91
4th				1.18	1.06	1.22	1.10	0.97	1.05	0.95	0.95	1.16
5th					0.99	1.07	1.01	1.00	0.88	0.73	0.68	0.88
6th						1.07	1.01	0.89	0.89	1.02	0.99	0.77
7th							1.02	1.01	0.91	0.93	1.03	1.00
8th								0.99	1.00	0.96	0.91	0.98
9th									1.03	0.97	0.94	0.96
10th										0.80	0.92	0.96
11th											1.00	0.96
12th												0.87

Table 5.11 Mulliken population charge for the Li ions in $Li_nC_{12}N_{18}H_6$.

	$Li_nC_{12}N_{18}H_6$											
	n1	**n2**	**n3**	**n4**	**n5**	**n6**	**n7**	**n8**	**n9**	**n10**	**n11**	**n12**
H1	0.47	0.42	0.42	0.44	0.39	0.37	0.39	0.34	0.33	0.29	0.27	0.21
H2	0.45	0.47	0.44	0.43	0.39	0.32	0.33	0.35	0.32	0.29	0.33	0.31
H3	0.47	0.41	0.42	0.37	0.34	0.33	0.33	0.26	0.31	0.26	0.29	0.26
H4	0.50	0.42	0.42	0.43	0.34	0.36	0.38	0.36	0.33	0.30	0.26	0.23
H5	0.42	0.47	0.44	0.40	0.39	0.30	0.33	0.34	0.31	0.28	0.23	0.26
H6	0.46	0.41	0.42	0.40	0.39	0.34	0.33	0.27	0.31	0.23	0.17	0.29
C1	0.45	0.44	0.37	0.35	0.36	0.38	0.34	0.36	0.28	0.27	0.24	0.22
C2	0.44	0.38	0.37	0.35	0.37	0.32	0.24	**-0.02**	**-0.01**	**-0.13**	**-0.28**	**-0.15**
C3	0.44	0.40	0.37	0.37	0.37	0.37	0.35	0.26	0.28	0.28	0.20	0.17
C4	0.46	0.42	0.38	0.25	0.33	0.27	0.09	0.18	0.19	0.25	0.15	0.23
C5	0.45	0.41	0.38	0.34	0.32	0.27	0.37	0.27	0.26	0.25	0.27	0.25
C6	0.44	0.45	0.38	0.35	0.39	**-0.04**	**-0.07**	**0.33**	**0.27**	**-0.14**	**-0.18**	**-0.21**
C7	0.42	0.44	0.37	0.30	0.36	0.29	0.31	0.31	0.30	0.28	0.24	0.22
C8	0.45	0.38	0.37	0.36	0.36	0.34	0.36	**-0.06**	**-0.09**	**-0.06**	**-0.02**	**-0.20**
C9	0.45	0.40	0.37	0.35	0.42	0.36	0.35	0.31	0.32	0.34	0.28	0.17
C10	0.47	0.42	0.38	0.36	0.36	**-0.14**	**-0.21**	**-0.24**	**-0.24**	**0.22**	**0.00**	**-0.23**
C11	0.47	0.41	0.38	0.36	0.32	0.42	0.37	0.32	0.30	0.25	0.26	0.24
C12	0.43	0.45	0.38	0.33	-0.19	0.27	0.34	0.26	0.28	0.29	0.22	0.23
N1	-0.60	-0.54	-0.60	-0.62	-0.79	-0.68	-0.63	-0.64	-0.73	-0.70	-0.66	-0.72
N2	-0.51	-0.52	-0.54	-0.54	-0.52	-0.53	-0.55	-0.57	-0.62	-0.68	-0.70	-0.72
N3	-0.60	-0.60	-0.62	-0.63	-0.69	-0.71	-0.76	-0.69	-0.72	-0.93	-0.93	-0.92
N4	-0.47	-0.60	-0.60	-0.61	-0.66	-0.73	-0.74	-0.77	-0.78	-0.86	-0.90	-0.90
N5	-0.49	-0.51	-0.50	-0.51	-0.52	-0.54	-0.55	-0.56	-0.63	-0.60	-0.67	-0.66
N6	-0.50	-0.59	-0.60	-0.62	-0.59	-0.73	-0.79	-0.78	-0.77	-0.68	-0.80	-0.76
N7	-0.46	-0.48	-0.62	-0.63	-0.61	-0.63	-0.78	-0.74	-0.74	-0.81	-0.80	-0.79
N8	-0.53	-0.48	-0.50	-0.60	-0.63	-0.68	-0.67	-0.68	-0.65	-0.64	-0.62	-0.69
N9	-0.46	-0.50	-0.61	-0.68	-0.62	-0.66	-0.87	-0.78	-0.81	-0.82	-0.82	-0.74
N10	-0.46	-0.59	-0.60	-0.61	-0.63	-0.59	-0.61	-0.66	-0.71	-0.78	-0.74	-0.72
N11	-0.53	-0.52	-0.54	-0.56	-0.63	-0.57	-0.54	-0.59	-0.66	-0.60	-0.65	-0.66
N12	-0.46	-0.60	-0.62	-0.62	-0.60	-0.73	-0.70	-0.74	-0.79	-0.76	-0.78	-0.79
N13	-0.47	-0.60	-0.60	-0.61	-0.67	-0.66	-0.66	-0.71	-0.73	-0.91	-0.89	-0.88
N14	-0.49	-0.51	-0.50	-0.50	-0.54	-0.60	-0.59	-0.57	-0.63	-0.60	-0.55	-0.63
N15	-0.49	-0.59	-0.60	-0.63	-0.66	-0.56	-0.69	-0.73	-0.74	-0.69	-0.75	-0.94
N16	-0.60	-0.48	-0.62	-0.75	-0.71	-0.73	-0.69	-0.81	-0.76	-0.78	-0.78	-0.85
N17	-0.52	-0.48	-0.50	-0.49	-0.53	-0.52	-0.63	-0.55	-0.57	-0.58	-0.67	-0.72
N18	-0.59	-0.50	-0.61	-0.75	-0.75	-0.76	-0.79	-0.86	-0.80	-0.74	-0.78	-0.74

Table 5.12 Mulliken population analysis for H, C, N atoms in the $Li_nC_{12}N_{18}H_6$ structure.

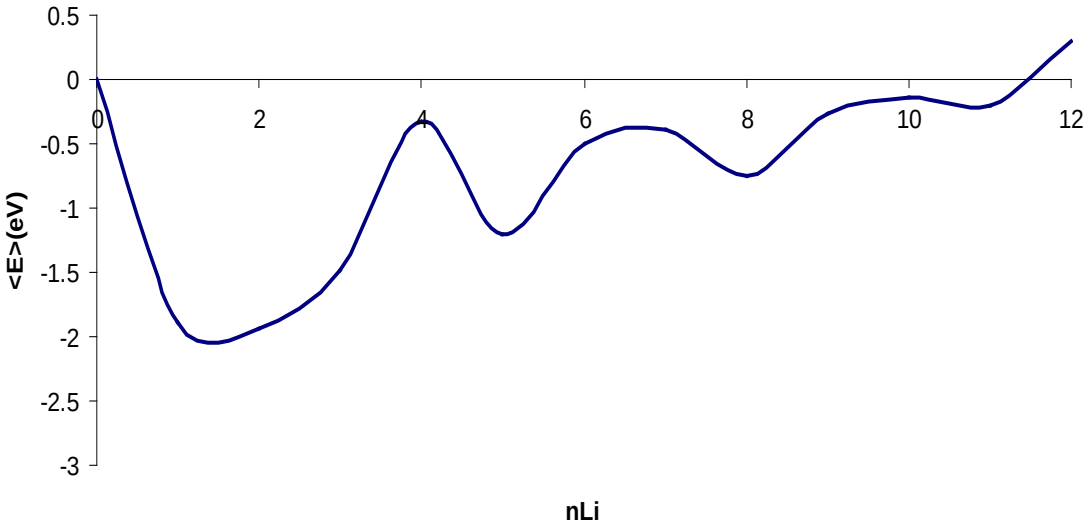

Figure 5.24 Li intercalation energy as the number of Li ions inserted into the unit cell increases.

To complete the characterization of the Li intercalation in the layer carbon-nitride, we have attempted to remove some of the Li ions from the stable structure at high values of n, in particular from the structures containing C-C interlayer bonds. We noticed that this process leaves the C-C interlayer bond also at values of n where it is no longer expected to occur.

Such observation has two consequences: first, it confirms that high values of Li intercalation lead to irreversible changes, and hence are not suitable for reversible electrochemical applications such as in rechargeable batteries. Second, it suggests an alternative direction to the application of pressure to achieve 3D connectivity in the host carbon nitride, the process examined in the initial sections of this chapter. Because of the negative charge on the CN framework once Li is intercalated, transformation of the C and N atoms from sp^2 to sp^3 is easier, and the change can be retained upon removal of Li. There is obviously interest in passing this information to our experimental colleges, to see whether such sequence of processes can be implemented in new experimental work.

5.2.5 Conclusion

It is found that the g-$C_6N_9H_3$ structure is able to accommodate up to 12 Li ions per crystallographic cell; however intercalation is irreversible, and may be not be able to continue after the 3rd Li due to the low intercalation energy at the concentration of n=4. Figure 5.25 compares the relative intercalation energy found here in g-$C_6N_9H_3$ to our earlier work on the intercalation in the brookite and the TiO_2-B structures.

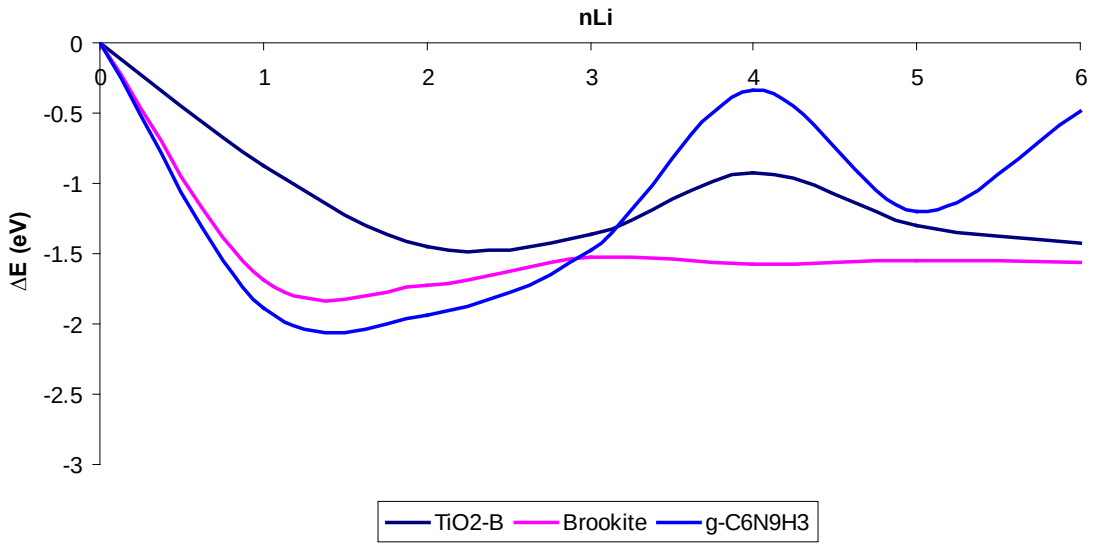

Figure 5.25 Relative intercalation energy of Brookite, TiO_2-B, g-$C_6N_9H_3$.

It shows that intercalation of the first Li atom into g-$C_6N_9H_3$ is more favourable than in brookite and TiO_2-B. Intercalation of further Li atoms above three is lower in the graphitic material. The relative intercalation energy in brookite shows a straight line around -1.55 eV, whereas TiO_2-B and even more so the carbon nitride material give a fluctuating relative intercalation energy that may be indicative of staging and kinetic barriers.

5.3 Ion exchange properties of the layered Carbon Nitride

5.3.1 Introduction

The planar nature of the $C_6N_9H_3$ layers, with cavities lined up by basic N atoms reproduces the main structural and electronic features of polycyclic ligands such as porphyrins (see Figure 5.26), which are essential in the coordination chemistry of transition metal ions and enable both adsorption and catalytic properties of biological relevance, for instance the O_2-transport function of the Heme group.

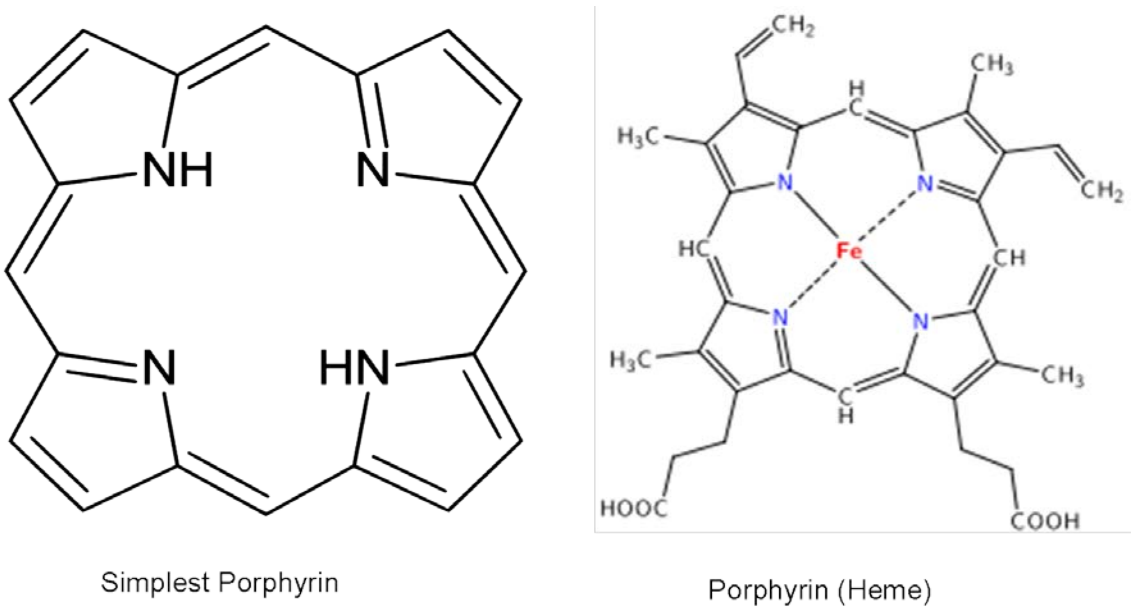

Figure 5.26 Simplest form of Porphyrins and an example of porphyrin (Heme)[142].

It is therefore of interest to use computational methods predictively to see whether the layered carbon nitride system studied here can provide an extended host for 2-dimensionally extended transition metal complexes. This would have potentially transformative applications in sorption and catalysis.

We note that the original $C_6N_9H_3$ system contains bridging NH groups, whose H's are potentially exchangeable by other cations (the same process that leads from a porphyrin molecule to the Heme group, described in Figure 5.26).

The process that we consider is therefore the proton exchange of the NH protons with metal ions of different charge, up to 3+ when replacing all three NH protons in one of the triangular cavities of $C_6N_9H_3$. The author is interested in characterising the structure stability of such a metal-exchanged carbon nitride layer and its ability to hold cations in the triangular voids, similar to a porphyrin complex.

5.3.2 Computational details

The calculations started with the fully optimized structure discussed in section 5.2. All computational parameters are the same as in section 5.1 and 5.2 in order to keep the calculation parameters the same to perform comparisons.

The energy of the metal oxides has been calculated for their stable polymorph at ambient conditions, as will be mentioned in detail in the following subsections. The energy of a single water molecule has been calculated using a cell with P1 symmetry.

5.3.3 Trivalent cations

The bulk structure of g-$C_6N_9H_3$ contains three protons decorating each triangular cavity, as mentioned before when replacing all acid protons of the layer, charge neutrality is achieved when a 3+ cation is hosted in each cavity: Each unit cell of $C_6N_9H_3$ contains two cavities, and in this work the acid hydrogens have been replaced in both simultaneously.

- **Al^{3+}**

Calculations have been initiated by replacing the six protons with two Al^{3+}, positioned in the centre of the triangular cavity in each layer. The process can be described according to the equation below:

$$\mathbf{Al_2O_3 + C_{12}N_{18}H_6 \rightarrow Al_2C_{12}N_{18} + 3H_2O} \qquad \textbf{(5.2)}$$

The energy of one Al_2O_3 unit cell was calculated using the hexagonal corundum structure; the calculated lattice parameters are a=b= 4.69 Å, c= 12.80 Å.

The calculations performed on the $Al_2C_{12}N_{18}$ structure showed that one of the Al ions is located in a tetrahedral coordinate ion environment with four nitrogen atoms, belonging to three carbon nitride layers; one Al-N bond is connected with the upper layer and one with the lower layer, and the other two bonds are connected to two nitrogen atoms in the Al ion plane. The second Al ion forms four bonds with nitrogen atoms in a square planar shape environment, two bonds connect to the Al ion from the upper layer and the other two bonds from the lower layer. Figure 5.27 presents the side and perpendicular views of the geometry optimised structure.

The calculated cell parameters are a = 7.85 Å, b = 8.38 Å, c = 5.77 Å, α = 81.43°, β = 114.31°, γ = 118.89°, V= 302.51 $Å^3$. The lattice parameter a, b and c decrease by 8.3%, 2.2 % and 4.3% respectively compared to the original acid form $C_6N_9H_3$, which lead to a decrease in the unit cell volume by 21%. This large contraction may be due to the strong electrostatic interaction between Al^{3+} and the framework, which includes interlayer components.

The replacement 3 protons by the Al^{3+} causes a strong deformation of the g-$C_6N_9H_3$ as the structure is strongly buckled; the tetrahedral Al ion is located in one cavity of the CN layers, and is shifted to a corner where it interacts strongly with two N atoms, as already observed earlier for Li+.

The tetrahedral Al ion is coordinated to 4 N atoms with bond lengths equal to 1.852, 1.917, 1.940, 1.959Å. The square planar Al ion coordinated to 4 N atoms with bond lengths equal to 1.875, 1.902, 1.928, 1.935 Å. The difference in the 4 Al-N bond distances is due to the rigidity of the carbon nitride framework, which prevents the 4 nitrogens to be optimal Al-N distance. Other compounds with tetrahedral Al-N environments exist, such as the wurtzite structure AlN, where the equilibrium Al-N distances of 1.89 Å[143].

The calculated energy of reaction 5.2 has the value of 9.17 eV, which is very large and indicates that a full exchange of the acid framework protons with AL^{3+} is practically impossible to achieve. The high formation energy is due to the small ionic radius of Al^{3+}, 0.50Å, which does not enable an effective interaction with the 3 nitrogen atoms of the triangular cavities in the carbon nitride backbone. To understand whether the cation size is indeed an important factor, we used larger 3+ ions such as Ga^{3+} and In^{3+} in the ion exchange reaction. These results are discussed below.

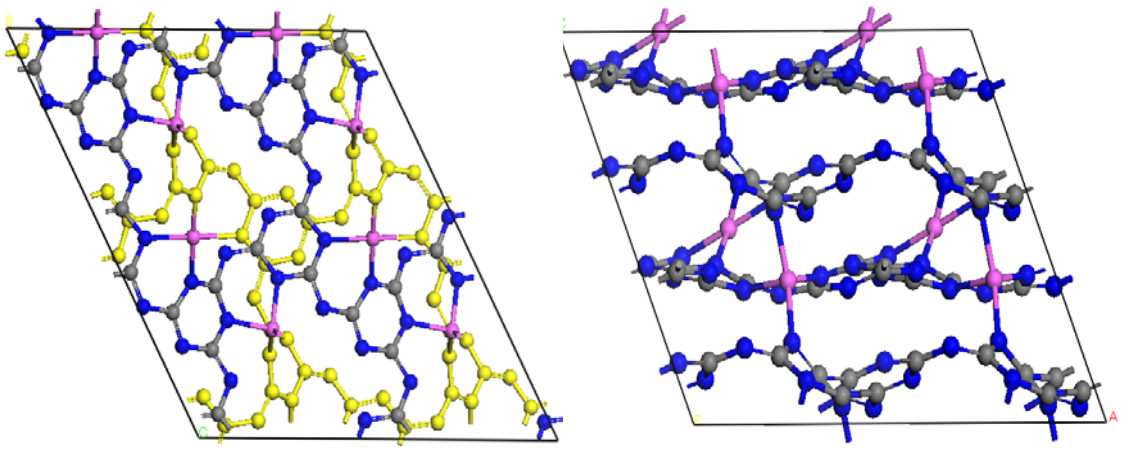

Figure 5.27 $Al_2C_{12}N_{18}$ structure: a). perpendicular view (yellow represents the lower layer), and b) side view, Al (pink), C (gray), N (blue).

- **Ga^{3+}**

Let us consider the ionic exchange of the 6 acid protons of the $C_6N_9H_3$ unit cell with two Ga^{3+} ions, according to reaction 5.3:

$$\mathbf{Ga_2O_3 + C_{12}N_{18}H_6 \rightarrow Ga_2C_{12}N_{18} + 3H_2O} \qquad \mathbf{(5.3)}$$

As for Al^{3+}, the calculations were initiated with both Ga^{3+} ions in the centre of the triangular cavities. The geometry optimised $Ga_2C_{12}N_{18}$ structure (perpendicular and side views) is shown in Figure 5.28; the energy of Ga_2O_3 has been calculated for the system with monoclinic symmetry and the calculated cell parameters are *a*= 12.11 Å, *b*= 3.04 Å, *c*= 5.77 Å and $\alpha = \gamma = 90°$, $\beta = 76.16°$ (compared with experimental values of *a*=12.23 Å, *b*= 3.04 Å *c*= 5.8 A and $\alpha = \gamma = 90°$, $\beta = 103.7°$[144]).

The calculated lattice parameters of the $Ga_2C_{12}N_{18}$ structure are *a* = 8.00 Å, *b* = 8.43 Å, *c* = 5.79 Å, α=80.27°, β = 115.12°, γ = 119.37°, and V= 307.79 $Å^3$.
Similar to the case of Al^{3+}, the calculations show that the lattice parameters of $Ga_2C_{12}N_{18}$ contract with respect to the acid form $C_{12}N_{18}H_6$: *a*, *b* and *c* decrease by 6.6%, 1.57 % and 3.9 % respectively, which leads to a decrease in the unit cell volume by 19.6%, but the Ga-containing solid is as expected less compact than the Al-containing one.
As for Al^{3+} the compression is due to the increased electrostatic interaction of the carbon nitride framework with the 3+ charge of Ga than the 1+ of H.
The calculations found that both Ga^{3+} ions are coordinated to 4 N atoms: one of the gallium ions is located in the plane of the layers, towards a corner of the triangular cavity. This Ga has a tetrahedral coordination environment, with four nearest neighbour nitrogen atoms; as for Al^{3+} discussed earlier, the tetrahedral environment spans three carbon nitride layers, with two N atoms in the central layer, one above and one below. The Ga-N bond lengths are 1.903, 1.938, 1.954 and 2.005 Å.

The second gallium ion is located in the interlayer space and is coordinated to 4 nitrogen atoms in a square planar environment: two bonds are connected with the upper layer and

the other two with the lower layer. The equilibrium Ga-N bond lengths are 1.923, 1.949, 2.008 and 2.010 Å.

The energy of reaction 5.3 has been calculated as 6.89 eV; this value is still very large, but substantially lower than that calculated earlier for Al^{3+}(9.17), configuring our initial hypothesis that the ionic size of the exchanged cation has a larger influence on whether the ionic exchange can or not take place on energetic grounds.

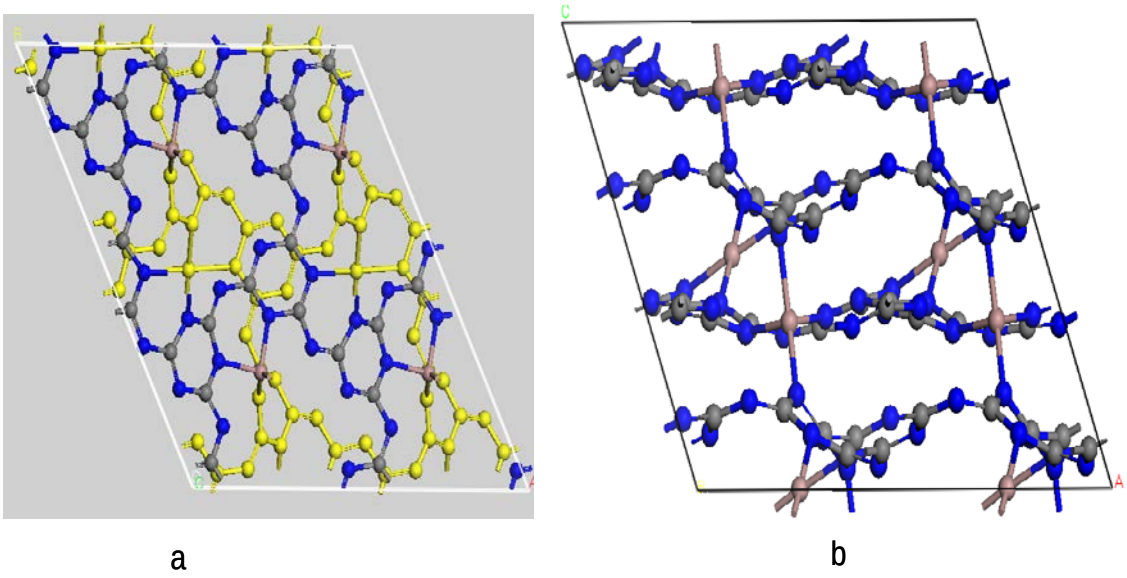

Figure 5.28 Structure of $Ga_2C_{12}N_{18}$: a) perpendicular (yellow atoms represent the lower layer) and b) side view. Ga (brown), C (gray), N (blue).

- **In^{3+}**

In case of indium, we follow the same procedure adopted for Al and Ga, by replacing the six protons by two In^{+3} ions, which are initially located in the centre of the triangular cavities in each layer. The formation energy for the In-containing solid is calculated as:

$$\mathbf{In_2O_3 + C_{12}N_{18}H_6 \rightarrow In_2C_{12}N_{18} + 3H_2O} \qquad \mathbf{(5.4)}$$

Full geometry optimizations have been performed and the calculated equilibrium lattice parameters for the $In_2C_{12}N_{18}H_6$ structure (shown in Figure 5.29) are a = 7.70 Å, b = 8.44 Å, c = 6.90 Å, α = 79.51°, β = 123.93°, γ= 117.17°, V = 329.56 $Å^3$.

The equilibrium volume is larger than for Al^{3+} and Ga^{3+} but still smaller than the acid form; there is however an expansion in the c direction.

These calculations found that both In^{3+} ions are located in the interlayer space, in 6-fold coordination; the 6 nearest neighbour N atoms are located there in the upper layer, with bond lengths of 2.153, 2.334 and 2.425 Å, and three in the lower layer, at distances of 2.153, 2.333 and 2.428 Å. Also for In^{3+} the equilibrium position is shifted to one corner of the triangular cavities.

The reference energy of the In_2O_3 structure to be used in equation 5.4 has been calculated using a cell with monoclinic symmetry, which yields equilibrium lattice parameters a= 12.10 Å, b= 3.32 Å, c= 6.80 Å and $\alpha = \gamma = 90°$, β= 106.36° (compared with experimental values of a=10.116 Å[145].

The energy of reaction 5.4 is calculated as 4.88 eV per cell (2 In^{3+} ions); the larger In^{3+} ion achieves therefore a more effective interaction with the $[C_6N_9]^{3-}$ backbone than the smaller Al^{3+} and Ga^{3+} ions, confirmed by its increased coordination number. The full replacement of the acid protons by In^{3+} is still however very unfavourable on energetic grounds; more importantly, our calculations show that however large a cation we employ

in the ion-exchange process, the size of the triangular cavities in the carbon nitride framework is too large to achieve a planar, porphyrin-like coordination of the cation in the plane of graphitic layer; the extraframework ion interact preferentially with nitrogen atoms in adjacent layers. It is also evident that corners of the triangular cavities provide stable environments for the extraframework cations that are in close proximity to two nitrogens of the carbon nitride backbone. It is therefore of interest to examine incomplete ion-exchange process, where ions with formal charge less than 3+ are employed. In the next section we examine Ba and Cd as representative (larger) 2+ cations and Li^+ as representative 1+ cation

Figure 5.29 shows the structure of $In_2C_{12}N_{18}$ shows that the Indium ion is octahedrally coordinated to 6 nitrogen atoms three of them from one layer and the other three from the parallel layer.

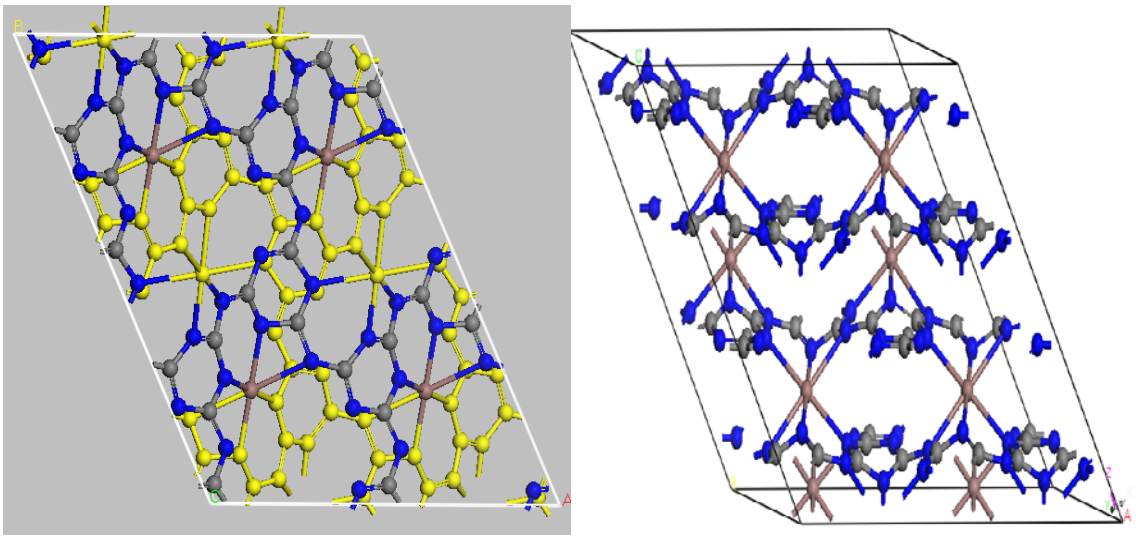

Figure 5.29 Structure of $In_2C_{12}N_{18}$: a) perpendicular (yellow represent the lower layer), and b) side view. In (brown), C (gray), N (blue)

5.3.4 Divalent cations

- **Ba^{2+}**

In this set of calculations, we employed two barium ions Ba^{2+} to replace four protons of the $C_{12}N_{18}H_6$ unit cell. Geometry optimisations were started with each Ba ion in the centre of one triangular cavity from which 2 protons have been removed. The replacement energy is calculated using equation 5.5 below:

$$\mathbf{2BaO + C_{12}N_{18}H_6 \rightarrow Ba_2C_{12}N_{18}H_2 + 2H_2O} \qquad \mathbf{(5.5)}$$

The calculated equilibrium lattice parameters of the $Ba_2C_{12}N_{18}H_2$ structure are a = 8.28 Å, b = 8.35 Å, c = 8.28 Å, α = 75.27°, β = 64.39°, γ = 119.48°, V = 361.19 $Å^3$. The larger Ba^{+2} ion causes an overall expansion of the unit cell, with the effect particularly pronounced for the c lattice parameter, which increases by 37.28 % compared to the acid form.

The reference energy of BaO has been calculated for a cubic rock salt lattice, whose equilibrium lattice parameters are calculated as 5.44 Å (experimental 5.52 Å[146]). The reaction energy calculated according to equation 5.5 yields the value of -1.02 eV. The close association achieved between Ba^{2+} and each of the deprotonated N sites causes' in this case negative (favourable) substitution energy, indicating that ion exchange of the framework protons is indeed possible.

Figure 5.30 represents the optimised structure of $Ba_2C_{12}N_{18}H_2$. It shows that both barium ions lay roughly in the carbon nitride layers, shifted towards one corner of the triangular cavities. Ion-exchange causes a significant buckling of the layers that appear to form pockets around the Ba^{2+} ions. This process is obviously driven by the electrostatic interaction between Ba^{2+} and the basic nitrogen atoms lining the edge of the triangular cavities. Overall, Ba^{2+} is in fourfold coordination, with equilibrium bond distances of 2.729, 2.735, 2.743, and 2.766Å. All 4 nitrogen atoms involved belong to the same layer (and the same cavity) hosting the Ba ion.

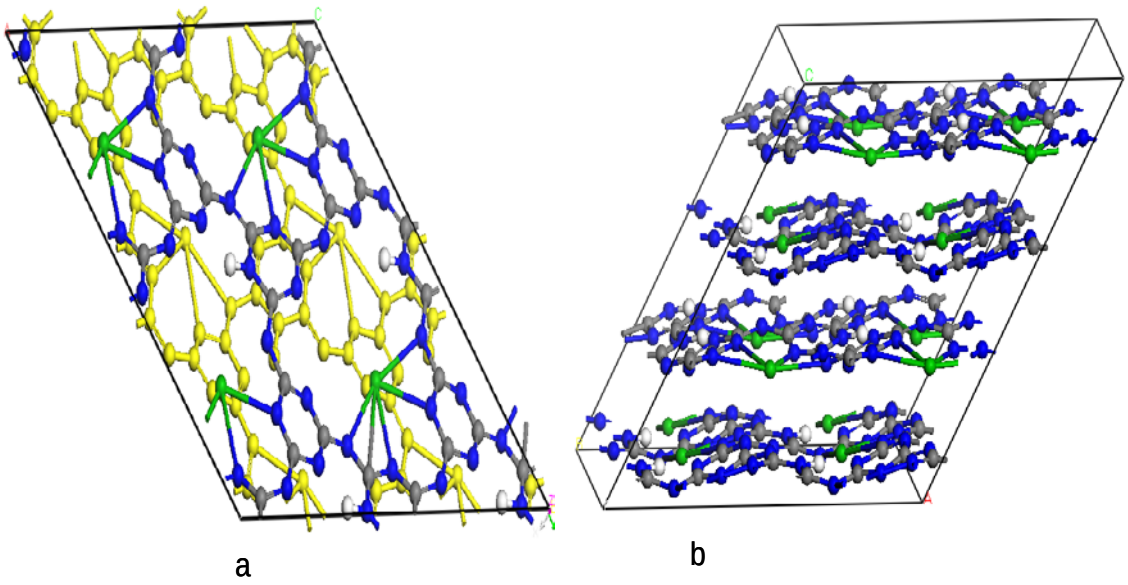

Figure 5.30 Equilibrium structure of $Ba_2C_{12}N_{18}H_2$: a) perpendicular (yellow atoms represent the lower layer), and b) side view. Ba (green), C (gray), N (blue)

Because of its large ionic size, Ba^{2+} is located closer to the centre of the triangular cavity, but the system cannot be described as porphyrin-like because of the buckling in the carbon nitride host.

- **Cd^{2+}**

Similarly to Ba^{2+}, two protons in each cavity were replaced with Cd^{2+} ions. The formed reaction corresponds to

$$2CdO+C_{12}N_{18}H_6 \rightarrow Cd_2C_{12}N_{18}H_2+2H_2O \qquad (5.6)$$

The calculated equilibrium unit cell parameters of $Cd_2C_{12}N_{18}H_2$ are a = 8.42 Å, b = 8.40 Å, c = 6.95 Å, α = 117.57°, β = 85.85°, γ = 121.34°, V = 362.70 Å^3. Compared to the acid form, in the Cd-containing material the lattice parameter a, b decrease by 1.65 %,

1.93 % respectively, while the *c* lattice parameter increases by 13.2 %. The total unit cell volume shrinks by 5.28%.

The reference energy of CdO has been calculated for the cubic polymorph, with lattice spacing of 5.67 Å. Figure 5.31 shows the equilibrium structure of $Cd_2C_{12}N_{18}H_2$. Unlike Ba^{2+}, the Cd^{2+} ions are located in the interlayer space and have fourfold coordination, with the nearest neighbour nitrogen atoms belong to two layers. However, one of the Cd ions can be associated more closely with one of the carbon nitride layers.

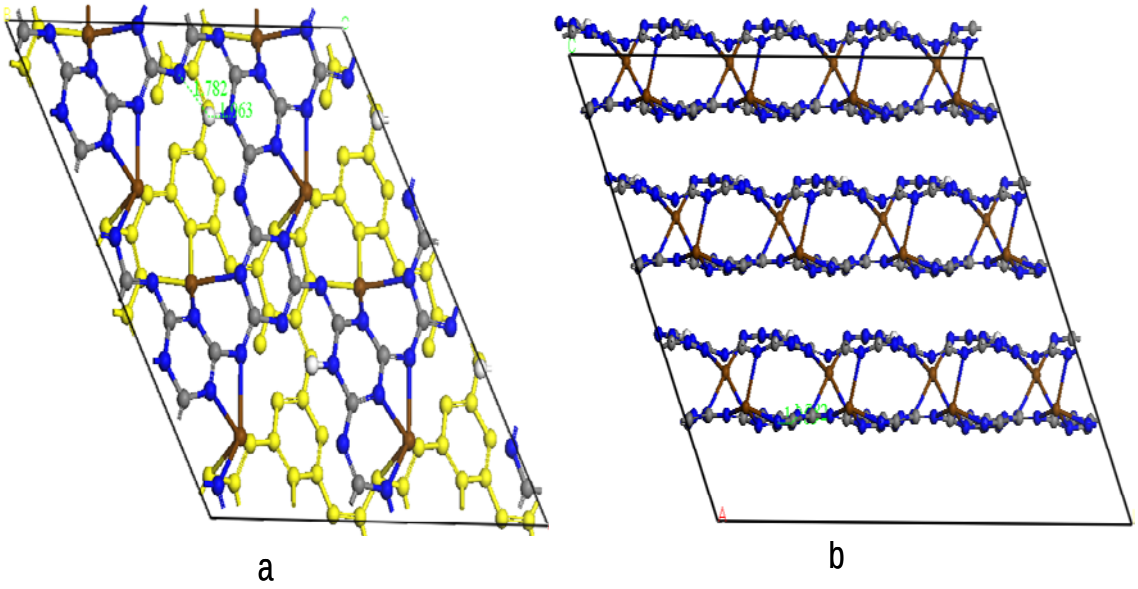

Figure 5.31 Equilibrium structure of $Cd_2C_{12}N_{18}H_2$; a) perpendicular (yellow atoms represent the lower layer), and b) side view. Cd (brown), C (gray), N (blue)

The equilibrium Cd-N bond distances are 2.214, 2.308, 2.313 and 2.361 Å, for the 1st and 2.120, 2.160, 2.272 and 2.299 Å for the 2nd Cd ion.

The calculated energy of reaction 5.6 yields the value of 2.71 eV; this is higher than for Ba^{2+}, and reflects the trend between reaction energy and cationic size already discussed for the trivalent ions.

5.3.5 Monovalent Cations

- **Li^{+1}**

In case of the Li^+ monovalent ion, the ion exchange product has been simulated by replacing all six protons of the acid form with 6 Li^+ cations.
Geometry optimisations have been started with the Li^+ ions in the carbon nitride planes, with a 1:1 association between Li^+ and each deprotonated N of the framework.
Replacement energies are calculated using equation 5.7 below:

$$3Li_2O + C_{12}N_{18}H_6 \rightarrow Li_6C_{12}N_{18} + 3H_2O \qquad (5.7)$$

The fully exchanged $Li_6C_{12}N_{18}$ system retains the hexagonal symmetry of the parent $C_{12}N_{18}H_6$ compared, with optimised lattice parameters $a = b$=8.41 Å and c = 6.07 Å, very similar to those of the acid form.

Figure 5.32 represents the equilibrium structure of $Li_6C_{12}N_{18}$. The Li ions remain in the carbon nitride layer, and occupy each corner of the triangular cavities, where they achieve a coordination number of 2, with Li-N bond distances of 1.840 and 1.843 Å. The layers are atomically flat upon replacement of H^+ by Li^+.
Replacement of H^+ by Li^+ causes therefore only minor perturbations to the carbon nitride lattice.

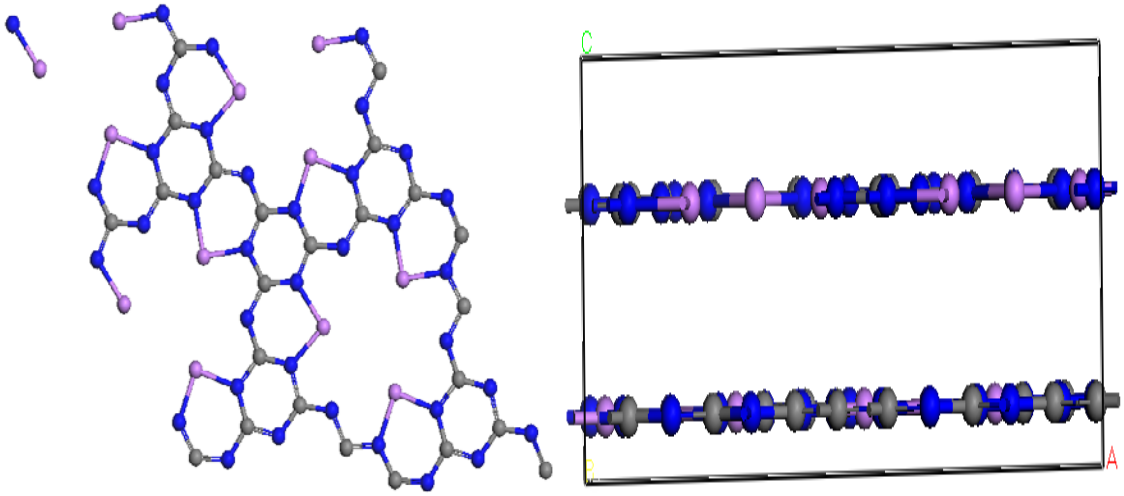

Figure 5.32 Structure of $Li_6C_{12}N_{18}$ a) perpendicular b) side view. Li (pink), C (gray), N (blue)

The reference energy of Li_2O has been calculated using a tetragonal unit cell with lattice parameters $a=b=$ 4.00 Å, $c=$ 4.06 Å.

The reaction energy calculated according to the equation 5.7 yields the value of -0.09 eV, indicating a favourable process.

5.3.6 Conclusion

These calculations show that the replacement of the acid protons in the $C_6N_9H_3$ network by the extraframework cations is possible, but requires an accurate choice of the cation. The triangular cavities of the carbon nitride host are very large, and do not enable an effective contact of a monatomic cation, in its centre with all basic nitrogens lining the perimeter of the cavity.

Because of this size mismatch, all cations examined here move towards a corner of the cavity, where they achieve a strong interaction with two basic nitrogen atoms. The most important parameter to understand the calculated ion-exchange energies is the size of the cation employed: the larger the ion, the more effective its interaction within the triangular cavity. Trivalent cations replace all acid protons in each cavity, a situation that incurs a large energetic penalty, even in the case of large In^{3+} ions.

When divalent cations are used, and replace only 2 of the protons in one cavity, the electrostatic interaction is more similar to that in the original framework, and replacement with a large ion like Ba^{2+} becomes energetically favourable.

The other replacement that appears possible on energetic grounds is that 3 protons by monovalent cations (e.g. Li^+). In this case, each Li^+ can interact strongly with two framework nitrogen atoms and yield a stable ion-exchanged material.

The original goal of finding porphyrin-like behaviour appears therefore impossible (at least using monatomic cations as done here), but our calculations have shown that the carbon nitride solids may have useful ion-exchange properties.

Chapter 6

Li intercalation into a Ruddlesden–Popper structured oxysulfide of composition $Y_4Ti_4O_{10}S_4$

6.1 Introduction

As discussed in chapter 4 of the thesis, the Li intercalation in different polymorphs of TiO_2 is of potential interest in the search for anode materials for Li ion batteries[147,148,149]. Examining the behaviour of materials related to TiO_2 may indicate new directions of research[150,151], and is particularly suited for modern electronic structure calculations that can be used to screen for interesting response properties in advance of experiment.

A Ti-based oxysulfide of composition $Y_4Ti_4O_{10}S_4$ has recently been synthesised and characterised in Oxford [157]; its behaviour towards Li intercalation will be examined computationally here, in an analogous way to the study of brookite and TiO_2-B of chapter 4. The compound has a layered Ruddlesden Popper structure with a site ordered distribution of oxide and sulphide ions. Ruddlesden Popper (RP) phases, of general composition $A_{n+1}B_nX_{3n+1,}$ or $AX(ABX_3)_n$, are layered materials in which n layers of perovskite structured compound are separated by one atomic layer of rock-salt structured material. The first 3 members (n= 1, 2, 3) of the RP series are shown in Figure 6.1[152].

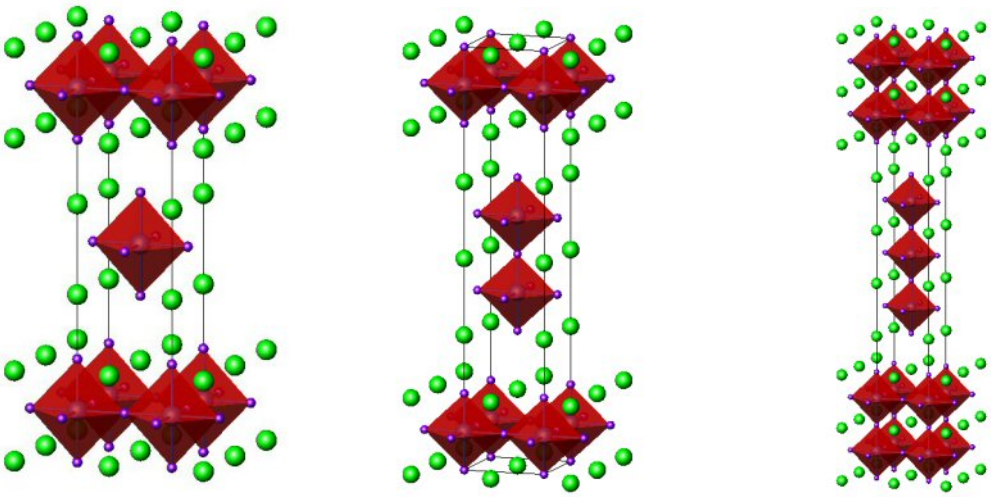

Figure 6.1 Ruddlesden-Popper structures AX $(ABX_3)_n$, corresponding to n=1, 2 and 3. *A* type ions are shown in green, *B*X_6 octahedra are shaded in red.

The oxysulfide examined here corresponds to the case n=2 in which oxide (O^{2-}) and sulphide (S^{2-}) ions separate in different layers[153,154]. The rock-salt layer has composition Y_2S_2, while the perovskite block consists of a bilayer of Ti_2O_5 stiochiometry, and contains empty interstices in the middle. It is these empty cationic sites that enable the intercalation of Li. Some features related to the intercalation chemistry of RP materials are known from experiment, for instance insertion of alkali metals in $H_2Sr_2Ta_2TiO_{10}$ (as an example) led to exfoliation or increased the separation between the slabs[155]. Some RP phases, such as $Sr_3Ru_2O_7$[156], undergo topotactic oxidative intercalation of fluorine into the rock salt layers, again indicating the availability of interstitial sites for ion intercalation in this family of compounds.

This chapter investigates Lithium intercalation into the vacant sites of the perovskite layer of $Y_4Ti_4O_{10}S_4$ to yield $Li_nY_4Ti_4O_{10}S_4$, with reduction of the Ti ions.

Experimental work demonstrated that under thermodynamic control the intercalation occurs into the perovskite slab, whereas under kinetic control insertion takes place into the rock-salt layers. Lithium intercalation was carried out by reacting the oxysulphide powders with excess n-BuLi (2.5 M in hexane) or Li naphthalide (0.5 M in THF) at between 20 and 50 °C for 0.5 – 11 days.

The products were analysed chemically and using Powder X-Ray Diffraction (PXRD)[157]. The PXRD patterns of the Li intercalation at 50 °C were indexed on the tetragonal unit cell of the starting material in space group *I4/mmm* suggesting that the intercalation is topotactic. The experimental data have shown that the structures at low Li concentration (n) (between 0 – 1.2) and at high Li concentration (between 3 – 3.7) are body centred tetragonal *I4/mmm*, while at intermediate Li concentration from 1.4 to 2.6 there is a symmetry lowering distortion to body centred orthorhombic (*Immm).* The *a* cell parameter increases by 2-3 % whereas the *c* cell parameter decreases by 1-2 % upon Li intercalation.

6.2 Details of the Calculations

As in the previous chapters, the calculations were performed within the pseudopotential planewave formalism using the CASTEP code[65,66]. Electron exchange and correlation effects were treated within the Generalized Gradient Approximation (GGA)[158] using the Perdew-Burke-Ernzerhof (PBE) functional with ultrasoft pseudopotentials to replace the core electrons[159]. Reciprocal space was sampled on a regular net with a consistent spacing of 0.06 $Å^{-1}$, corresponding to 4x4x1 unique K-points in the first Brillouin zone of a $Y_2Ti_2O_5S_2$ cell. The planewave cut-off energy has been calculated by performing a series of full optimisation calculations, where the cut off has been varied between 380 - 600 eV. The internal energy converges upon increasing the energy cut-off, the value of 450 eV has been chosen, at which the energy is converged to within 0.02 eV per atom.
The energy of lithium metal, E (Li) was obtained by optimisation of body-centred cubic (*Im3m*) Li metal, using a K-point mesh of 25x25x25. Calculations for the Li-intercalated phases have been performed as spin polarised.

The size and shape of the cell and all internal degrees of freedom were fully relaxed with respect to the total energy. All possible configurations corresponding to Li intercalated in the empty interstices of the Ti_2O_5 sublayer have been calculated for Li concentrations n= 0-4 in the crystallographic unit cell of composition $Li_nY_4Ti_4O_{10}S_4$.

6.3 $Y_4Ti_4O_{10}S_4$ Structure

The $Y_4Ti_4O_{10}S_4$ structure is a Ruddlesden-Popper (R-P) type n=2 phase, in which the perovskite-like layers Ti_2O_5 are separated by rock salt layers Y_2S_2. The oxygen ions are exclusively located in the perovskite layer while the sulphide ions occupy the sites in the rock salt layer. The structure contains Ti ions which are reduced from 4+ to 3+ oxidation state during the Li intercalation.

The Li intercalation occurs in the centre of the Ti_2O_5 layers, in the empty sites of the perovskite block. Each crystallographic unit cell of the material contains two perovskite layers, which we can identify as A and B (see Figure 6.2). Correspondingly we label as A and B the Li intercalation sites depending on the layer occupied by Li; the stiochiometry of the structure limits the Li intercalation to 4 ions per crystallographic unit cell.

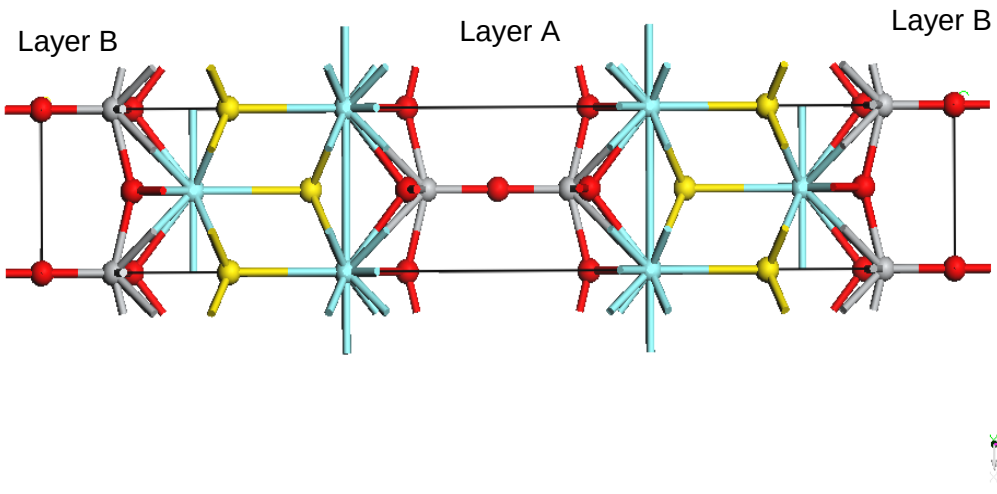

Figure 6.2 Crystallographic unit cell of the $Y_4Ti_4O_{10}S_4$ structure: Y (green), Ti (gray), S (yellow), and O (red).

A fragment of the original structure highlighting the atomic environments is shown in Figure 6.3. The Ti ions are approximately octahedrally coordinated to 5 O ions and one S ion. The Ti-S bond is oriented perpendicularly to the layer orientation. This environment defines a set of 4 equatorial O atoms, denoted as Oe_1 and Oe_2; the 5th O (trans to S) is apical and denoted as Oa. Conversely, the Y ions are coordinated to 4 oxygens, 4 equatorial S and 1 axial S ions. A summary of the Ti-X equilibrium bond distances is given in Table 6.1. For completeness, in Figure 6.4 we also show an expansion of the structure along the layers, highlighting the Li intercalation sites.

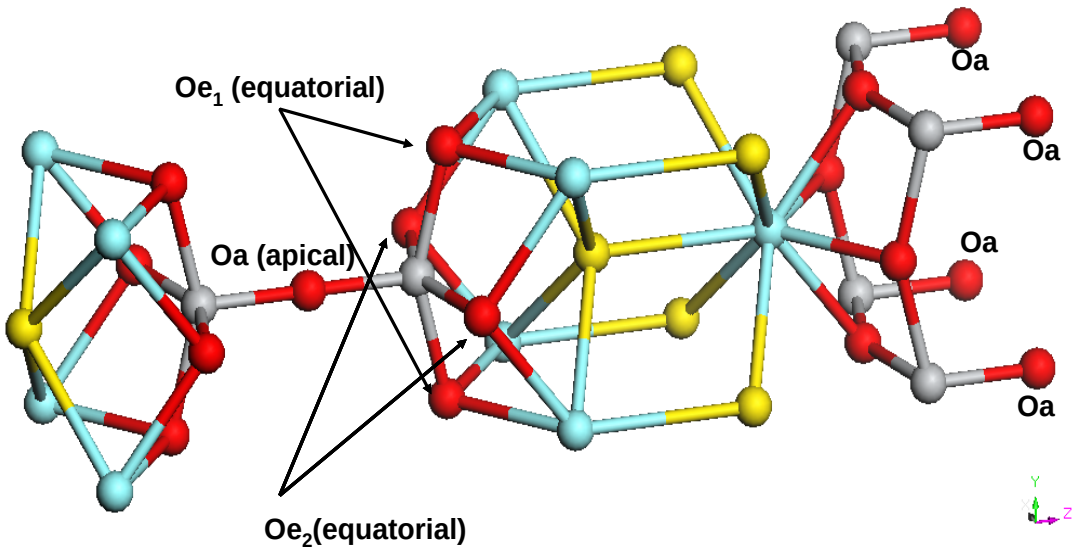

Figure 6.3 Fragment of the $Y_4Ti_4O_{10}S_4$ structure showing the apical (Oa) and equatorial (Oe) oxygen ions.

Li_n	Ti	Oe_1	Oe_1	Oe_2	Oe_2	Oa	S
n =0	**Ti1**	1.954	1.954	1.954	1.954	1.811	2.916
	Ti2	1.954	1.954	1.954	1.954	1.811	2.916
	Ti3	1.954	1.954	1.954	1.954	1.811	2.916
	Ti4	1.954	1.954	1.954	1.954	1.811	2.916
n=1	**Ti1**	1.969	1.969	1.993	1.993	1.811	2.882
	Ti2	1.963	1.946	1.942	1.943	1.912	2.680
	Ti3	1.970	1.970	1.993	1.995	1.810	2.888
	Ti4	1.662	1.945	1.942	1.944	1.912	2.674
n=2	**Ti1**	1.924	1.924	1.979	1.979	1.939	2.661
	Ti2	1.924	1.924	1.979	1.979	1.939	2.661
	Ti3	1.924	1.924	1.979	1.979	1.939	2.661
	Ti4	1.924	1.924	1.979	1.979	1.939	2.661
n=3	**Ti1**	1.988	1.988	1.973	1.973	1.992	2.46
	Ti2	1.994	1.994	2.004	2.001	1.899	2.632
	Ti3	1.993	1.993	2.002	2.001	1.905	2.619
	Ti4	1.989	1.989	1.973	1.973	2.011	2.486
n=4	**Ti1**	2.004	2.004	2.004	2.004	1.997	2.447
	Ti2	2.004	2.004	2.004	2.004	1.997	2.447
	Ti3	2.004	2.004	2.004	2.004	1.997	2.447
	Ti4	2.004	2.004	2.004	2.004	1.997	2.447

Table 6.1 Ti-X equilibrium bond distances as a function of Li concentration.

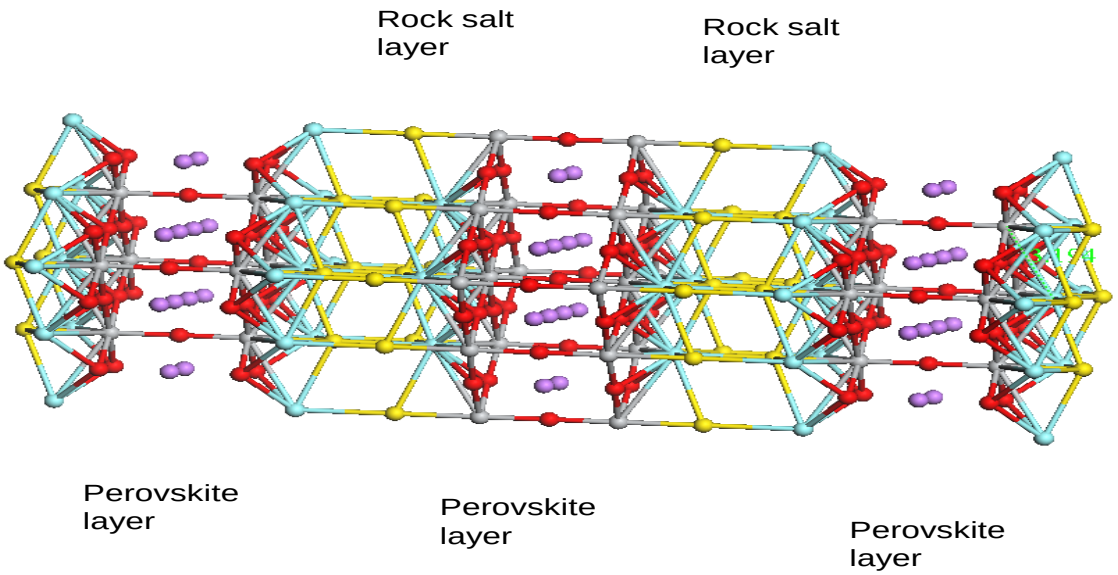

Figure 6.4 2x2x2 supercell of $Li_4Y_4Ti_4O_{10}S_4$ indicating the rock salt layers, perovskite layers and Li ion sites (purple).

6.4 Results and discussion

6.4.1 $Y_4Ti_4O_{10}S_4$ structure

The calculations confirm the experimental data as the $Y_4Ti_4O_{10}S_4$ structure has a tetragonal structure with *I4/mmm* symmetry; the calculated cell parameters are *a*= *b*= 3.785 Å, *c*= 23.047 Å and the unit cell volume V= 330.257, compared to experimental values of *a*= *b*= 3.770 Å, and *c*= 22.806 Å[160].

The equilibrium bond distances (Table 6.1) are in substantial agreement with experiment: Ti-Oe bonds are calculated as 1.954 Å, compared to 1.943 Å from experiment, the apical Ti-Oa bond is 1.811 Å compared to 1.794 Å, and Ti-S is 2.916 Å compared to 2.874 Å.

Comparison of the bond distances shows the Ti-Oa bond to be much shorter than the equatorial Ti-Oe ones, which corresponds to a stronger Ti-Oa bond and an off-centering displacement of the Ti ion towards Oa in its coordination octahedron, typical of many compounds of Ti^{+4}, such as the ferroelectric perovskite $BaTiO_3$.

The Ti displacement towards Oa is clear in the structural representation of Figure 6.3. A Mulliken population analysis has been performed on the $Y_4Ti_4O_{10}S_4$ structure in order to understand the charge distribution in the solid, and serve as reference to analyse the effect of Li intercalation. Results are shown in Table 6.2; we note that the charge of the axial Oa ions (O9 and O10 in the table) is lower than that of the equatorial ions, indicating a more covalent Ti-Oa bond than the Ti-Oe ones and consistent with the shorter bond distance.

$Y_4Ti_4O_{10}S_4$									
Atom No.	**charge**	**Atom No.**	**charge**	**Atom No.**	**charge**	**Atom No.**	**charge**	**Atom No.**	**charge**
Oe1(A)	-0.96	Oe6(A)	-0.96	S1	-1.52	Ti1(B)	1.04	Y1	2.7
Oe2(B)	-0.96	Oe7(B)	-0.96	S2	-1.52	Ti2(A)	1.04	Y2	2.7
Oe3(A)	-0.96	Oe8(A)	-0.96	S3	-1.52	Ti3(B)	1.04	Y3	2.7
Oe4(B)	-0.96	Oa9(B)	-0.62	S4	-1.52	Ti4(A)	1.04	Y4	2.7
Oe5(B)	-0.96	Oa10(A)	-0.62						

Table 6.2 Mulliken charge analysis of the $Y_4Ti_4O_{10}S_4$ structure. Labels A and B indicate the block of the structure (layer A or B in Figure 6.2.) where the ions are located; indices (e) and (a) refer to equatorial and apical oxygen ions.

The band structure of $Y_4Ti_4O_{10}S_4$ is shown in Figure 6.5. The dashed line is the Fermi level and the calculated band gap yields the value of 1.68 eV, consistent with the small band gap insulating nature for the oxysulfide. The small gap is confirmed by the density of states, shown in Figure 6.10. The bottom of the conduction band is formed by the Ti-3d energy levels.

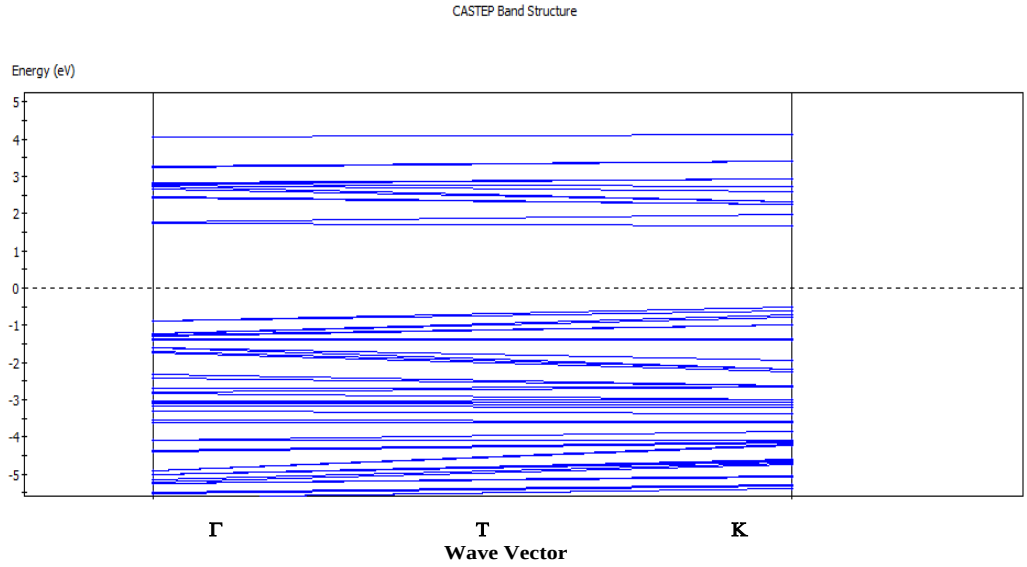

Figure 6.5 Band structure of $Y_4Ti_4O_{10}S_4$

In order to investigate the mechanism of Li intercalation in $Y_4Ti_4O_{10}S_4$ and its effect on the host system, different Li configurations have been calculated, to find the most stable Li arrangement as a function of Li content. Results are discussed in separate subsections for each Li content.

6.4.2 $LiY_4Ti_4O_{10}S_4$

The first Li intercalation corresponds to Li concentration n=1. The Li ion intercalates in the centre of the perovskite layer. Rather than occupying the 12 coordinated site of the perovskite layer, the small ionic radius of Li causes a considerable displacement of Li towards a side, and the equilibrium intercalation site corresponds to one of the 4-coordinated windows at the edge of the site. The equilibrium cell for the system hosting the Li ion and $LiY_4Ti_4O_{10}S_4$, and a fragment that describes the four coordinated window are shown in Figure 6.6. For future reference, we use the label A to represent the perovskite layer that hosts the first intercalated Li.

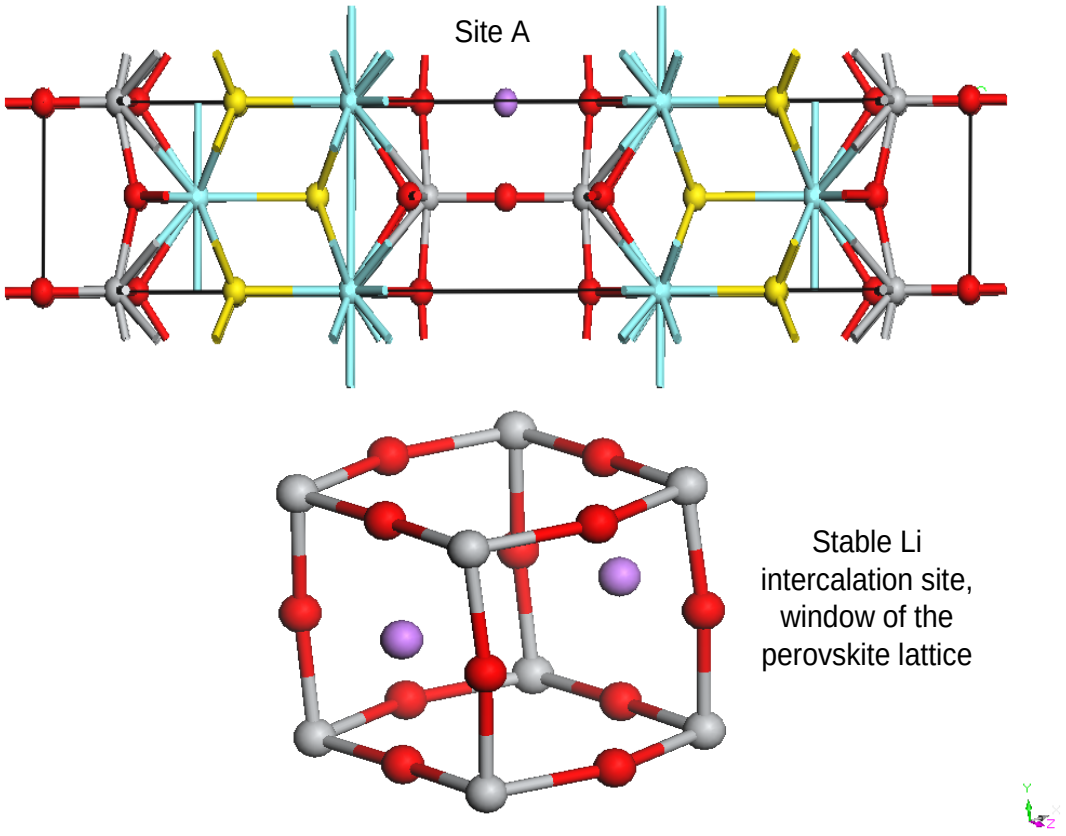

Figure 6.6 $LiY_4Ti_4O_{10}S_4$ structure with Li in site A, and details of the 4 coordinated window hosting the intercalated Li.

The calculated intercalation energy is of -2.40 eV, according to the equation

$$|E| = [E(Li\,Y_4Ti_4O_{10}S_4) - E(Y_4Ti_4O_{10}S_4) - E(Li)] \quad (6.1)$$

The calculated unit cell parameters are a = 3.819 Å, b = 3.872 Å, c = 22.662 Å and the unit cell volume V= 335.28 $Å^3$.

To highlight the effect of Li intercalation on the oxysulphide structure, in Table 6.3 we summarise the equilibrium lattice parameters and cell volume as a function of Li content. We note here that the effect of the 1st Li intercalation is very pronounced. Firstly, it causes a symmetry lowering from tetragonal (*I4/mmm*) to orthorhombic (*Pmm2*).

Second, the structure expands in *a* and *b* directions and contracts appreciably (nearly 0.5 Å) along *c*, i.e. the layers are closer to each other.

Li_n		a(Å)	b(Å)	c(Å)	V(Å^3)
n=0		3.785	3.785	23.047	330.257
n=1		3.819	3.874	22.666	335.275
n=2	**config 1**	3.905	3.905	22.310	340.199
	config 2	3.845	3.947	22.307	338.517
	config 3	3.904	3.905	22.267	339.432
n=3		3.974	3.944	21.932	343.771
n=4		4.008	4.008	21.573	346.490

Table 6.3 Lattice parameters as a function of Li concentration (n).

Experimentally the symmetry lowering from tetragonal to orthorhombic is observed in a similar interval, the structure is tetragonal for n= 0.66, while tetragonal and orthorhombic phases coexist for n= 1.32. When the temperature is raised above 200°C the tetragonal symmetry is produced in a single phase indicating that the reaction switches from kinetic to thermodynamic control at this temperature.

The Mulliken population analysis for the structure with Li concentration of n= 1 is reported in Table 6.4. It shows that Li is fully ionised, while the additional electron is shared between 2 Ti ions, labelled as Ti2 and Ti4 in Table 6.4, whose charge decreases from ~1 to ~0.5 |e|; conversely, the charges of Ti ions labelled Ti1 and Ti3 does not change.

The two Ti ions that are partially reduced are those in layer A where Li is intercalated. The effect of intercalation reduces to a lesser extent also the charge of O and S ions of Layer A; in particular the apical oxygen bonded to Ti2, labelled O10 in Table 6.4, changes from -0.62 to -0.85.

$LiY_4Ti_4O_{10}S_4$											
Atom No.	**charge**	**Atom No.**	**charge**	**Atom No.**	**charge**	**Atom No.**	**charge**	**Atom No.**	**charge**	**Atom No.**	**charge**
Li1	1.2	Oe1(A)	-0.98	Oe6(A)	-0.98	S1	-1.51	Ti1(B)	1.01	Y1	2.72
		Oe2(B)	-0.98	Oe7(B)	-1.01	S2	-1.42	Ti2(A)	0.55	Y2	2.71
		Oe3(A)	-1.01	Oe8(A)	-0.95	S3	-1.51	Ti3(B)	1.01	Y3	2.72
		Oe4(B)	-0.94	Oa9(B)	-0.62	S4	-1.41	Ti4(A)	0.54	Y4	2.71
		Oe5(B)	-0.98	Oa10(A)	-0.85						

Table 6.4 Mulliken population charge analysis of the $LiY_4Ti_4O_{10}S_4$ structure.

The conduction band electron localised on Ti2 occupies a level of antibonding character between Ti2-O10. Upon reduction of Ti2, the Ti2-O10 bond weakens and makes O10 more ionic; it also affects the environment of the Ti2 ion that is in a much more symmetric environment when reduced. The reduced off–centering of Ti2 is clear when comparing Figure 6.6 with Figure 6.3 (x=0). The axial O10-Ti2-S2 bond distances change from 1.811 and 2.916 Å to 1.912 and 2.680 Å upon intercalation. Such modification is common to other reactions causing $d^{(0)} \rightarrow d^{(1)}$ changes in the electronic configuration of transition metal ions[161,162].

It is clear that the electronic effects of intercalation are largely confined to layer A where Li is hosted, while the second layer, B, is nearly identical to the Li free case.

The band structure of $LiY_4Ti_4O_{10}S_4$ is shown in Figure 6.7; blue and red lines refer to alpha and beta spin levels. We see that an alpha spin level at the bottom of the conduction band is now occupied, yielding a metallic system where the Fermi level is inside the conduction band. The picture is confirmed by the DOS shown in Figure 6.10.

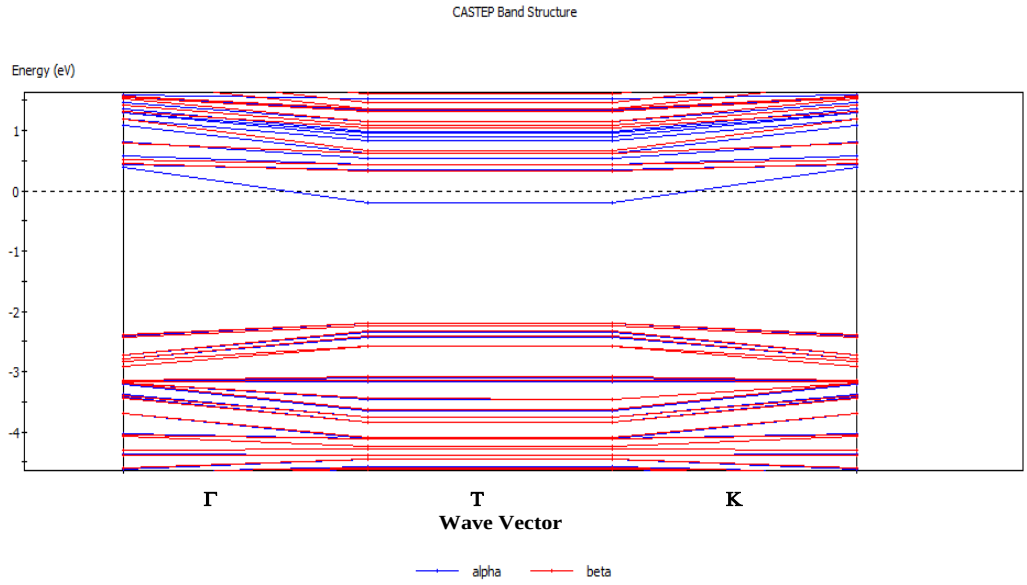

Figure 6.7 Band structure of $LiY_4Ti_4O_{10}S_4$.

6.4.3 $Li_2Y_4Ti_4O_{10}S_4$

The second Li intercalation has two possible sites for the Li insertion: either in the same layer (A) where the 1st Li is hosted or the other perovskite layer of the structure (B). These two possibilities produce three distinct configurations, shown in Figure 6.8. The system with one Li per layer may in fact have the Li ions occupying 4 coordinated windows oriented parallel or perpendicular to each other. We have optimised all 3 cases, with results summarised in Table 6.3.

The lattice parameters, and most importantly the overall symmetry of the system, differ in the 3 cases. In particular, configuration 1 yields a tetragonal cell (*I4/mmm*), while configuration 2 is orthorhombic (*Immm*).

In configuration 3 the *a* and *b* lattice parameters are very similar to each other, and the structure is tetragonal (*P4/mmm*) within the numerical accuracy of the calculations. The

intercalation energy, with respect to the structure with one Li ion, is calculated as -1.57, -2.39 and -2.33 eV for configurations 1, 2 and 3 respectively. It is clear that case 1, with both Li ions in the same layer, is unstable, while the two geometries with 1 Li per layer have very similar energy, and we may expect both of them to be present, although it is reassuring to notice that the most stable case (config2) is consistent with the orthorhombic structural determination obtained experimentally for n=1.98.

We finally note that the 2nd Li intercalation causes a further expansion of the cell along *a* and *b* directions, and contraction along *c*.

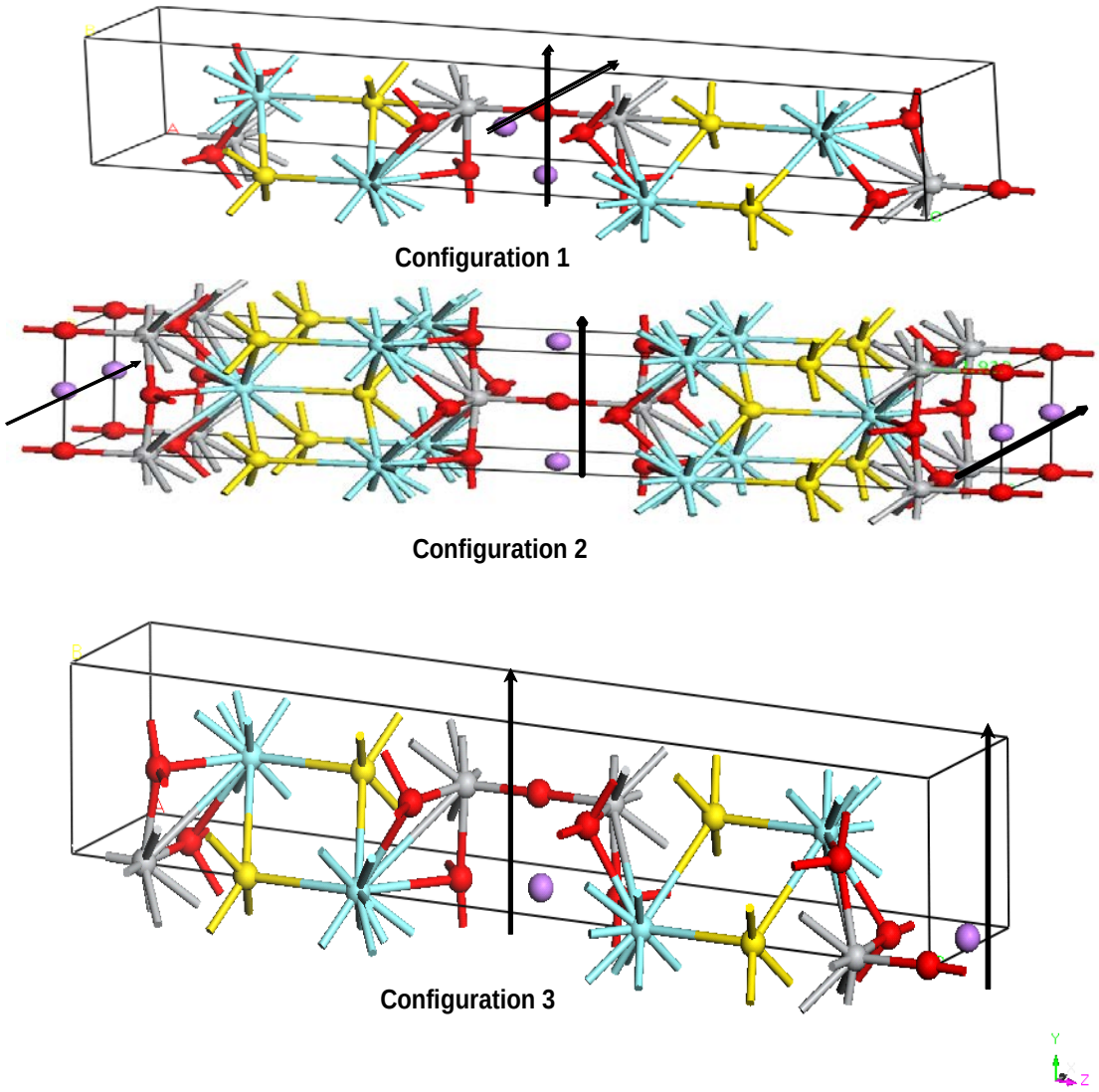

Figure 6.8 Three possible configuration of Li concentration n=1.

A Mulliken population analysis has been calculated for the stable configuration 2 and it is shown in Table 6.5. When 1 Li is hosted in each perovskite layer, all Ti ions are partially reduced and the rehybridisation effect discussed in the previous section for the Ti2-O10 bond affects now all the Ti ions.

The density of states (Figure 6.10) shows that the electrons donated by Li occupy the bottom of the conduction band and yield a metallic system.

$Li_2Y_4Ti_4O_{10}S_4$											
Atom No.	**charge**	**Atom No.**	**charge**	**Atom No.**	**charge**	**Atom No.**	**charge**	**Atom No.**	**charge**	**Atom No.**	**charge**
Li1	1.18	O_e1(A)	-0.99	O_e6(A)	-0.99	S1	-1.41	Ti1(B)	0.50	Y1	2.72
Li2	1.18	O_e2(B)	-0.99	O_e7(B)	-0.99	S2	-1.41	Ti2(A)	0.50	Y2	2.72
		O_e3(A)	-0.99	O_e8(A)	-0.99	S3	-1.41	Ti3(B)	0.50	Y3	2.72
		O_e4(B)	-0.99	O_a9(B)	-0.83	S4	-1.41	Ti4(A)	0.50	Y4	2.72
		O_e5(B)	-0.99	O_a10(A)	-0.83						

Table 6.5 Mulliken population charge analysis of the $Li_2Y_4Ti_4O_{10}S_4$ structure.

6.4.4 $Li_3Y_4Ti_4O_{10}S_4$

The third Li intercalation has only one possible configuration, in which layer A is fully occupied and only half of the Li sites in layer B are filled. This structure is shown in Figure 6.9.

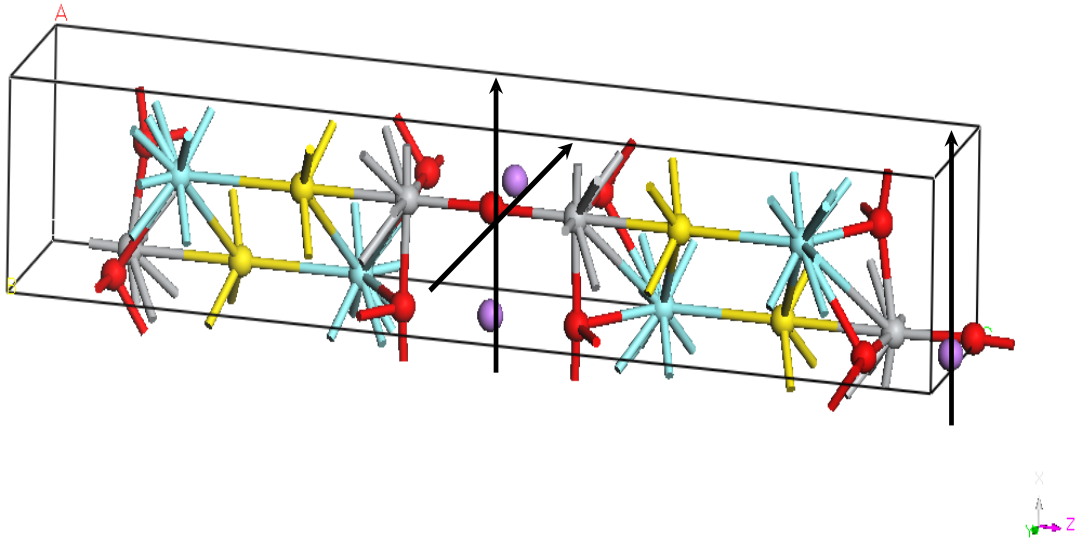

Figure 6.9 $Li_3Y_4Ti_4O_{10}S_4$ structure.

The calculated cell parameters of $Li_3Y_4Ti_4O_{10}S_4$ are *a* = 3.974 Å, *b* = 3.943 Å, *c* = 21.931 Å, α = 90.0°, β= 90.0°, γ= 90.0° and the unit cell volume V= 343.8 $Å^3$. The symmetry is orthorhombic *(Pmm2*). These values show that intercalation of the third Li ion causes a further deformation of the structure.

The calculated intercalation energy (relative to the phase with n=2) is -1.73 eV.

$Li_3Y_4Ti_4O_{10}S_4$											
Atom No.	**charge**	**Atom No.**	**charge**	**Atom No.**	**charge**	**Atom No.**	**charge**	**Atom No.**	**charge**	**Atom No.**	**charge**
Li1	1.02	Oe1(A)	-1.02	Oe6(A)	-1.01	S1	-1.38	Ti1(B)	0.47	Y1	2.73
Li2	1.01	Oe2(B)	-1.02	Oe7(B)	-1.04	S2	-1.27	Ti2(A)	0.08	Y2	2.73
Li3	1.17	Oe3(A)	-1.04	Oe8(A)	-0.99	S3	-1.37	Ti3(B)	0.46	Y3	2.75
		Oe4(B)	-1.00	Oa9(B)	-0.83	S4	-1.29	Ti4(A)	0.14	Y4	2.73
		Oe5(B)	-1.02	Oa10(A)	-1.02						

Table 6.6 Mulliken population analysis of the $Li_3Y_4Ti_4O_{10}S_4$ structure

The Mulliken population analysis for the $Li_3Y_4Ti_4O_{10}S_4$ is shown in Table 6.6; it shows that the Ti ions (Ti2, Ti4) in layer A are further reduced, while the Ti ions (Ti1, Ti3) in layer B are unmodified with respect to the structure with n=2. Once more the electron is confined to the same layer hosting the Li ion.

The DOS for the structure with n=3 is shown in Figure 6.10, where it is compared with the DOS for n= 0 - 4. It shows that further intercalation of Li causes a nearly rigid filling of the conduction band.

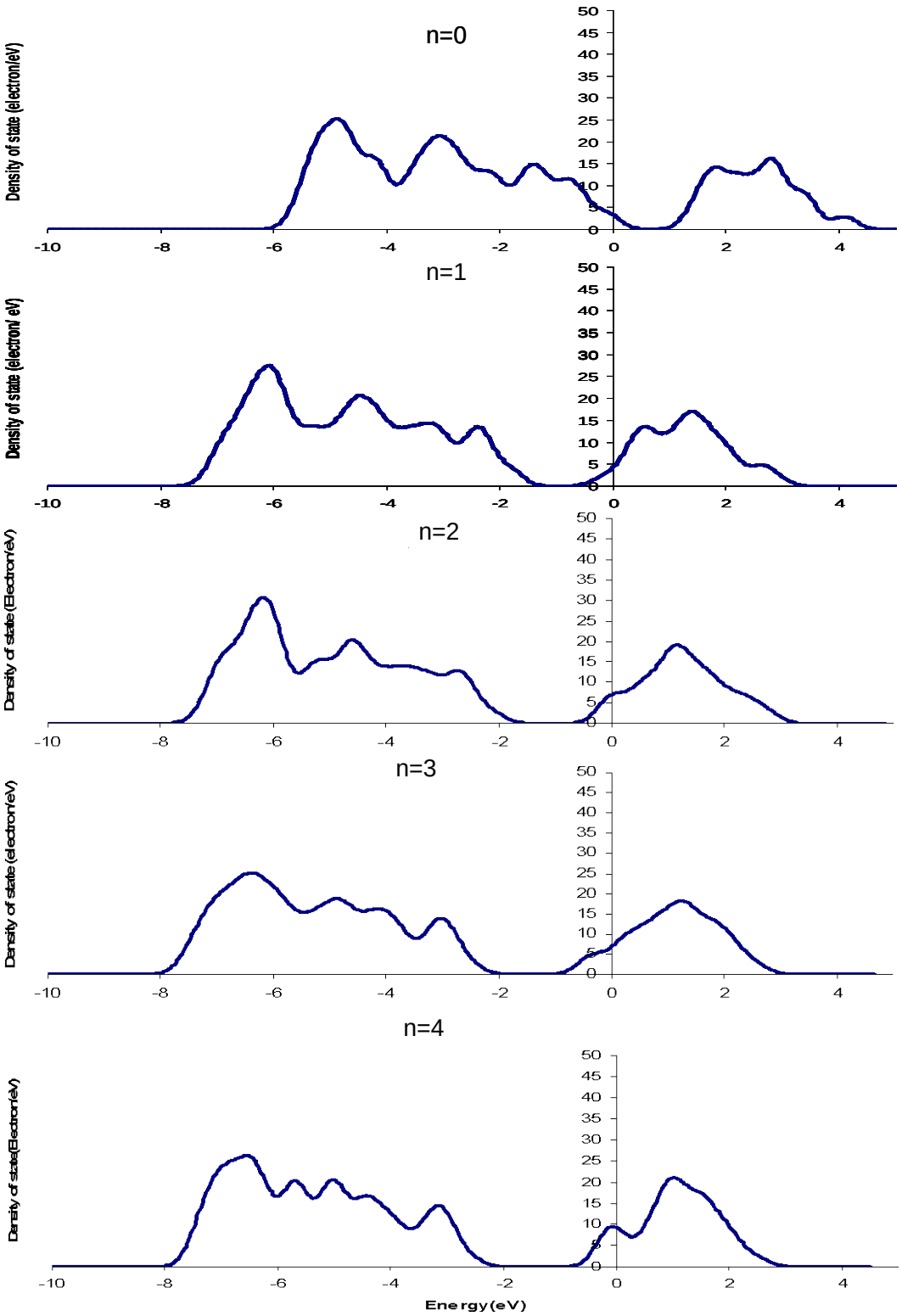

Figure 6.10 Density of state of the $Li_nY_4Ti_4O_{10}S_4$ structure for increasing Li content (n=0-4)

6.4.5 $Li_4Y_4Ti_4O_{10}S_4$

When n=4 all available interstices are occupied by Li ions. The optimised structure is shown in Figure 6.11. The structure is tetragonal *I4/mmm*, with lattice parameters of 4.008 and 21.573 Å, and volume of 346.5 $Å^3$.

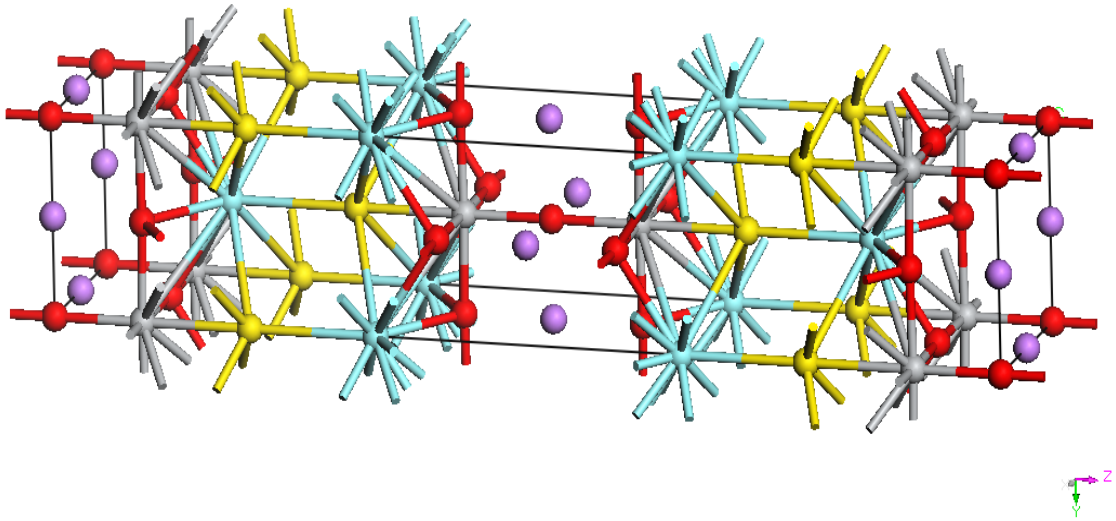

Figure 6.11 $Li_4Y_4Ti_4O_{10}S_4$ structure.

The intercalation energy for the 4th Li ion is -1.69 eV. The Mulliken population analysis (Table 6.7) shows that all changes between n=3 and n=4 are confined to layer B where the Li ion is hosted; Ti ions in layer B are further reduced, causing a further filling of levels in the conduction band as confirmed by the DOS shown in Figure 6.10.

$Li_4Y_4Ti_4O_{10}S_4$											
Li1	1.01	O_e1(A)	-1.03	O_e6(A)	-1.03	S1	-1.24	Ti1(B)	0.04	Y1	2.76
Li2	1.01	O_e2(B)	-1.03	O_e7(B)	-1.03	S2	-1.24	Ti2(A)	0.04	Y2	2.76
Li3	1.01	O_e3(A)	-1.03	O_e8(A)	-1.03	S3	-1.24	Ti3(B)	0.04	Y3	2.76
Li4	1.01	O_e4(B)	-1.03	O_a9(B)	-1.01	S4	-1.24	Ti4(A)	0.04	Y4	2.76
		O_e5(B)	-1.03	O_a10(A)	-1.01						

Table 6.7 Mulliken population charge analysis of the $Li_4Y_4Ti_4O_{10}S_4$ structure.

6.5 Li intercalation energy and structural changes

In order to evaluate the suitability of the $Y_4Ti_4O_{10}S_4$ oxysulfide for applications in Li ion batteries, it is of interest to contrast the Li intercalation energy and structural changes calculated in this chapter, with those of Li_xTiO_2 and carbon nitrides discussed in chapters 4 and 5.

The Li intercalation energy, as a function of Li concentration (n), is shown Figure 6.12, where for each value of n we have chosen the most stable configuration.

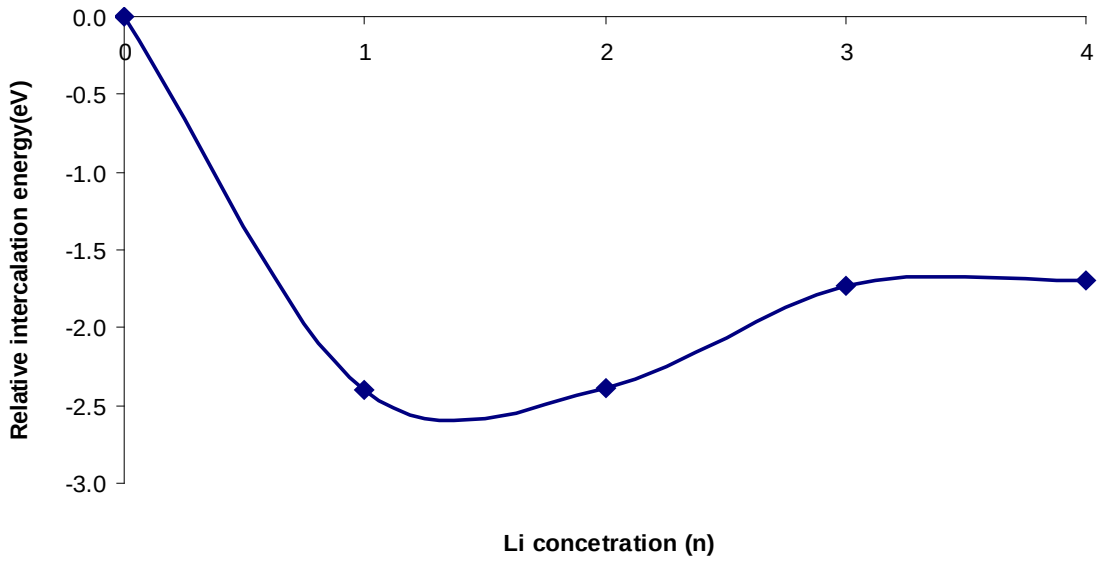

Figure 6.12 Relative intercalation energy as a function of Li concentration (n).

The figure shows that the intercalation energy is relatively high (-2.4 eV) when Li can be hosted in a Li free layer (n= 1 and 2), while it decreases to -1.7 eV for n > 2, when the added Li occupies a layer already partly intercalated. The reduced intercalation energy at n > 2 has 2 likely explanations: first the repulsion between Li ions in the same layer, and second the fact that Ti ions are already partly reduced and provide less stable levels to accept further electrons.

Generally the intercalation energy between -2.4 eV and -1.7 eV appears unsuitable for Li ion batteries operation, as it is too high for anode applications (we ideally require a value of -1.0 eV or less), and too low for cathode materials (requiring values of -4.0 eV or more). The structure also shows too large structural relaxation upon Li intercalation, which is likely to prevent any cyclable application. The structural changes occurring as a function of Li intercalation in $Y_4Ti_4O_{10}S_4$ are summarised in Figure 6.13. We see a larger expansion along the layers (*a* and *b* parameters) of over 8% in the range of n from 0 to 4, and a contraction of similar magnitude in *c*.

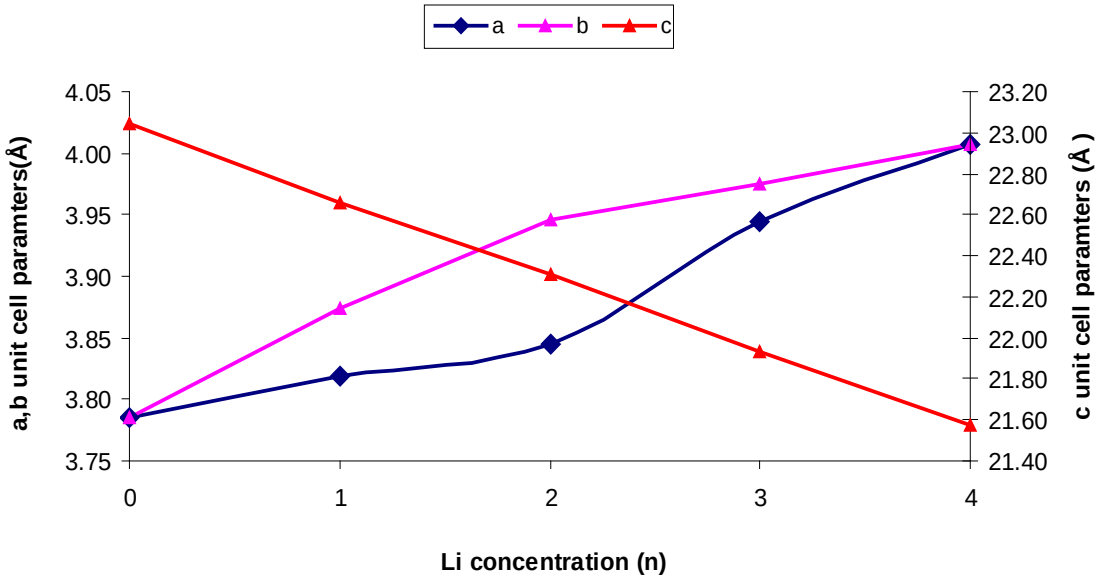

Figure 6.13 The unit cell parameters of $Li_xY_4Ti_4O_{10}S_4$ structure

The calculated structure is tetragonal for the extreme cases of n=0 and n= 4 (all Li interstices empty or occupied), but orthorhombic (*a* and *b* different) at intermediate Li content. The structure has been determined to be still tetragonal experimentally at n=0.66, although this Li concentration cannot be obtained by computational work without use of larger simulation cells.

The unit cell parameters for Li concentrations between n=1.33 and 1.5 measured experimentally by XRD are *a*= 3.818 Å, *b*=3.875 Å, *c*=22.4 Å. Our calculated parameters for n=1.5 (obtained by interpolating the values obtained at n=1 and n=2) are *a* = 3.83 Å, *b* = 3.89Å, *c* = 22.55 Å, in good agreement with the experimental work.

Neutron power diffraction experiments for n=3.04 indicate that the structure has tetragonal *I4/mmm* symmetry, with parameters *a*= *b*= 3.918 Å and *c*= 22.652 Å. Experimental measurements have been performed at 298 K° and above. In the calculations, however, the cell at n=3 is still orthorhombic. The phase transition to tetragonal may be associated with disorder of the Li ions, which is difficult to reproduce computationally.

The total volume of the unit cell increases linearly with the Li concentration (x) as shown in Figure 6.14.

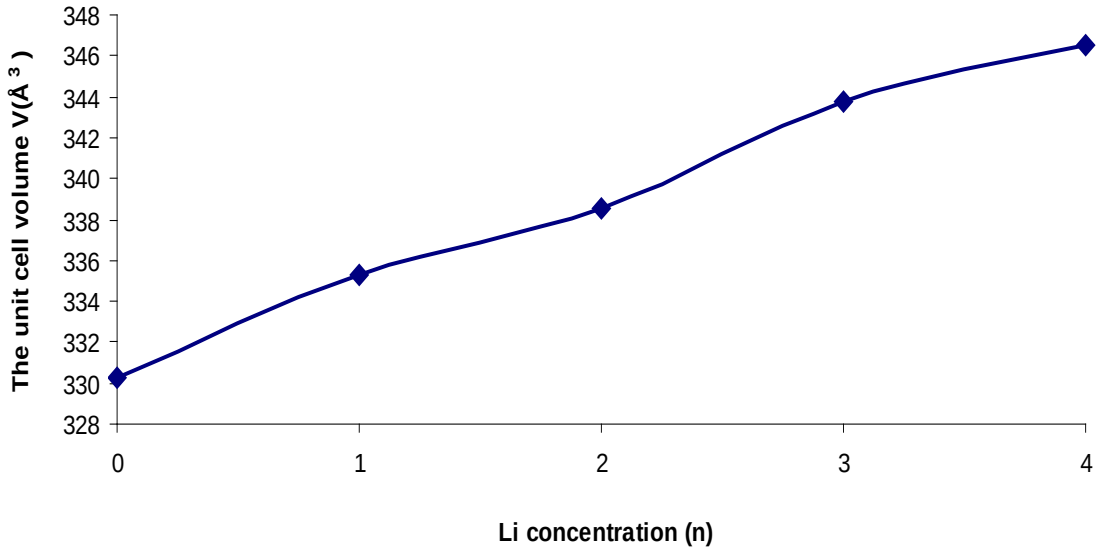

Figure 6.14 Unit cell volume as a function of Li concentration (n).

All previous data confirm the phase transition during the intercalation of Li ions into $Y_4Ti_4O_{10}S_4$, so we need to investigate the internal changes and bond distances in order to explain our results.

As already indicated in previous sections, Li intercalation affects the Ti-O and Ti-S bond distances. To complete the structural analysis of intercalation, here we report plots of equilibrium bond distances (Ti-Oe, Ti-Oa, Ti-S, Li-O and Y-S) and angles (O-Ti-O) as a function of Li content n.

As discussed earlier, only one of the two perovskite layers is modified upon each Li insertion; this is the layer hosting the Li ion. Conversely, when focusing on an individual Ti-X bond distance, we expect to see changes when this bond is in the same layer as the added Li, but not when Li occupies the other layer.

The bonds between Ti and the equatorial oxygen atoms Oe (Oe_1, Oe_2) are shown in Figure 6.15. They elongate from n=0 to n=4, as the Ti ions are reduced and have larger effective size.

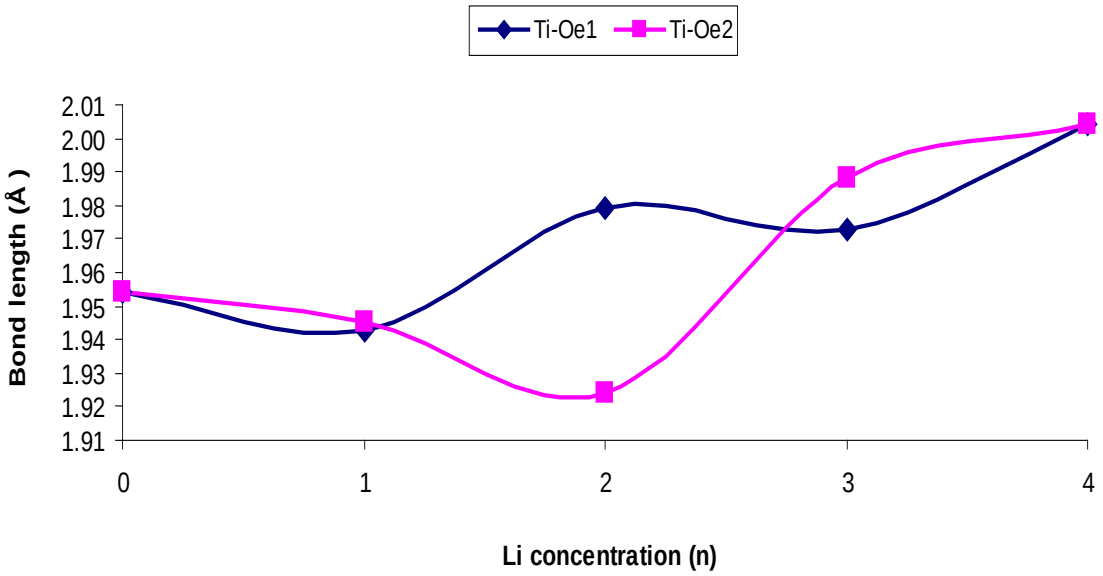

Figure 6.15 The Ti-Oe bond lengths as a function of Li concentration (n).

The Ti-X bonds mostly affected by intercalation are those in the axial direction (Figure 6.16). The $d^{(0)}$ Ti^{+4} ion is displaced off-center in its TiO_5S octahderon, a distortion typical of d^0 metal ions as seen in ferroelectric $BaTiO_3$. Upon localisation of d electrons on the metal the off-center decreases, causing an elongation of the Ti-Oe and shortening of the Ti-S axial bonds. The latter effect is very pronounced, with the Ti-S bond shortening from 2.916 (n=0) to 2.680 (n=2) and 2.447 (n=4). This contraction is reponsible for the large reduction in the *c* lattice parameter upon intercalation.

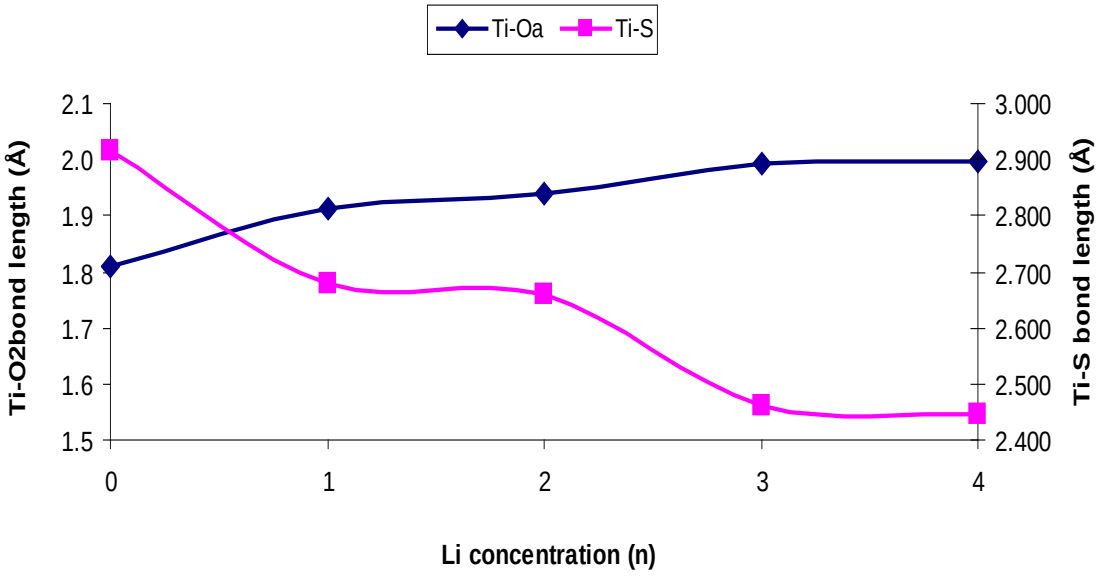

Figure 6.16 Ti-Oe and Ti-S bond lengths of as a function of Li concentration (n).

Equilibrium O-Ti-O angles are shown in Figure 6.17 (angles involving cis oxygens) and Figure 6.18 (trans oxygens). These figures show clearly that the TiO_5S octahedron becomes more regular upon Li intercalation; the cis angles move towards 90° and the trans towards 180°, due to the decreased Ti off-centering on increasing n.

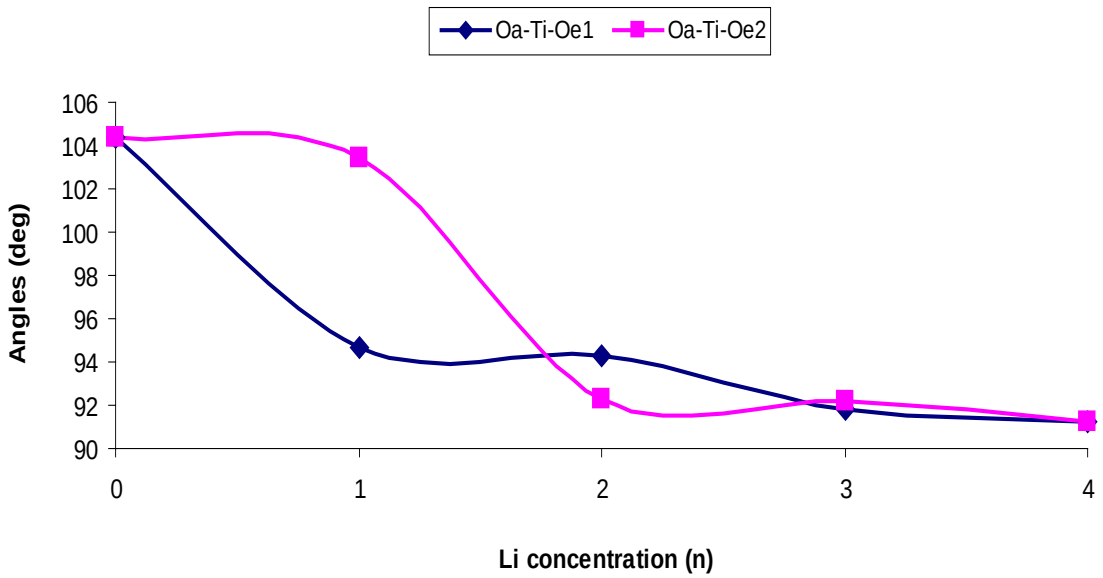

Figure 6.17 Oa-Ti-Oe angles as a function of Li concentration (n).

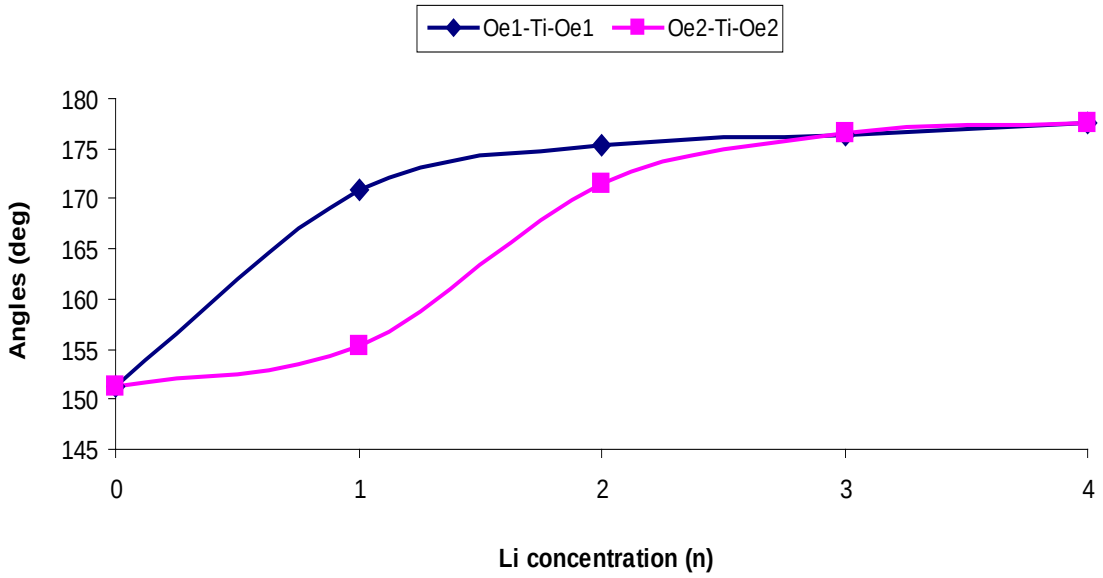

Figure 6.18 Trans Oe-Ti-Oe angles as a function of Li concentration (n).

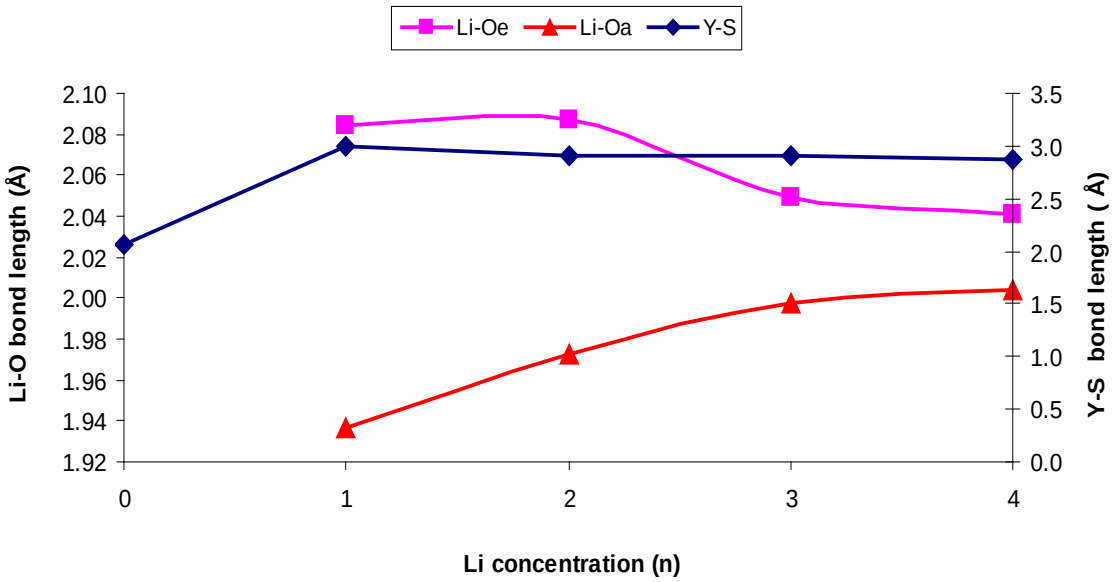

Figure 6.19 Li-O distance and Y-S bond lengths as a function of Li concentration (n).

Li-O and Y-S bond distances (Figure 6.19) are only slightly affected by Li content, confirming that the only electroactive ion during intercalation is Ti.

The Li-Oe distances increase with n, proportionally to the expansion of the *a* and *b* lattice parameters.

6.6 Conclusions

The Li intercalation in an oxysulfide of composition $Li_nY_4Ti_4O_{10}S_4$, with RP structure has been examined. The structural changes are consistent with Ti being progressively reduced on increasing Li content.

Intermediate Li concentrations cause a reduction of symmetry from tetragonal to orthorhombic, consistent with experimental observation.

The material appears unsuitable as electrode for Li-ion batteries: the calculated Li intercalation energy (ranging from -2.4 eV to -1.7 eV depending on the Li content) is too high for anodes, and too low for cathode applications.

In addition, structural changes of nearly 8% in each lattice parameter are too large, and would cause considerable structural stresses upon cycling intercalation and deintercalation of Li.

Chapter 7

Conclusions and Perspectives for Future Work

This PhD thesis has been concerned with the computational work performed on a range of crystalline solids, with comparison with experimental results, when available. The work has examined a range of structures and properties of two classes of materials: materials employed in the manufacturing of anodes for rechargeable Li batteries, and carbon nitrides.

Chapter 4 introduced titanates and considered two important structures: Brookite and TiO_2–B. In the first section brookite which has an orthorhombic structure with *Pbca* symmetry was studied. The structure represents a three dimensional network of TiO_6 octahedra sharing three edges each, with empty zigzag shaped channels along the *c*-direction, which are potentially available for Li-intercalation. The analysis of the connectivity of TiO_6 octahedra has been demonstrated to play an important role in understanding the electronic mechanism of Li-insertion into titanates.

At room temperature, Li-uptake by polycrystalline brookite is negligible while at elevated temperature the intercalation behaviour of brookite at elevated temperatures has not been investigated yet. In the nanophase, the reactivity of brookite towards Li increases with a decrease of the particle size. Recently, it has been shown that nanosized particles of brookite can intercalate Li-ions to high Li-concentrations (x=0.9).

The mechanism of Li-intercalation into Brookite were studied and explained by calculating the most favourable energy sites and calculation of diffusion barriers.

The lowest energy configurations have been identified and their energies computed. It was found that Li intercalation is homogeneous but consists of three domains, corresponding to different ordering patterns: the occupancy of zigzag chains at $0<x\leq0.375$, configurations with maximum separation between Li-ions (x=0.435, 0.5); and random site occupancy at x>0.5. The investigation shows that Li-intercalation is strongly limited by the diffusion of Li-ions, especially at high Li content, resulting in the absence of intercalation at normal conditions, and intercalation to high concentrations at elevated temperature or in the nanophase.

The second section considers the TiO_2-B structure; which contains edge-sharing TiO_2 octahedra and has a monoclinic structure with space group *C2/m*. The most favourable energy sites have been investigated; in addition we identified the possible pathways by calculating the diffusion barriers in all possible directions within the structure.

It is found that the TiO_2-B structure has lower density packing than other titanates like rutile, anatase and brookite. The calculated intercalation energy is in the range of 0.8 to 1.45 eV for low Li content (up to 6 Li ions). We have identified three stable sites in the TiO_2-B structure, and found that the most favourable energy site is the square planar site (signed as B) where Li is in fourfolded coordination with oxygen; a less favourable energy site (signed as A) is a five fold coordinated with oxygen atom, and the lowest favourable energy site (signed as C). We have concluded that the Z direction showing the highest mobility for Li-ions so that the TiO_2-B structure has enough Li mobility is suited for the use as an anode in rechargeable lithium batteries.

Comparing the intercalation energy of the brookite structure, and the TiO_2-B structure up in the low Li content up to 6 Li ions shows the brookite is more reliable to host Li ions, and yields relatively constant voltage values which are good for Li batteries, while the TiO_2-B has quite constant voltage value which is lower than the brookite voltage.
It can be concluded from this investigation that the intercalation process depends on the diffusion process and the temperature. Further work could be done to investigate further Li intercalation in to TiO_2-B structure in order to give an accurate evaluation of the structure suitability as an anode material in rechargeable Li batteries.

In chapter 5 we have used a range of computational methodologies to examine the second type of materials investigated in this work, carbon nitrides.

The first section describes the study of the behaviour of a layered carbon nitride of composition *g*-$C_6N_9H_3$·HCl at high pressure, and particularly investigated the possible occurrence of interlayer bonding under compression/decompression processes.

The results show that upon compression, particularly at 70 GPa, interlayer bonding occurs between C and N atoms of the triazine rings that lie directly on top of each other, forming a new pillared phase: In addition, two bonds are observed: a symmetrical hydrogen bond, and carbon-chloride bonds. We have found that two symmetrical hydrogen bonds are formed upon compression at 70 GPa and become more symmetrical up to 90 GPa, while during decompression the symmetry reduces and restores a more usual donor-acceptor H bond below 50 GPa. On the other hand the carbon chloride bonds that are formed upon compression at 70 GPa are retained up to 0 GPa upon the decompression process.

The symmetrical hydrogen bond is not unusual under pressure and had been observed previously in different compounds such as formic acid (at 12 GPa), ice (ice-X) and potassium hydrogen maleate.

Furthermore, the calculations indicated that the originally inert Cl^- ions at ambient P conditions become 'active' at high pressure and engage in C-Cl bonds. It is also interesting to note here that although the formation of C-Cl bonds requires a significant activation energy, they are quite stable once formed.

The above two points are of interest and require further analysis since these are unusual; our computational study has provided their characterisation, so that their occurrence can be followed up experimentally. According to phonon spectra on the optimised structure:

- At 90 GPa: N-H-N bonding can be detected at 2262, 2228, and 1995 (cm^{-1}) and C-Cl at 1015, 965 (cm^{-1}).
- At 70 GPa: N-H-N bonding can be detected at 2000- 2700 (cm^{-1}) and C-Cl at 833, 923 (cm^{-1}).

- At 50 GPa: N-H-N bonding can be detected at 2200, 2700 (cm^{-1}) and C-Cl at 797, 943 (cm^{-1}).

The second section of chapter 5 examines the graphitic carbon nitride structure as anode for rechargeable Li batteries. It investigates the most favourable Li intercalation sites and it is found that Li insertion causes some local deformation of the host substrate.

Stronger structural deformations occur at Li intercalation beyond 5 atoms per unit cell which lead to a phase transition and creation of interlayer C-C bonds. In such a case, the electron donated by the Li atom form sp^3- hybridised carbanion that favour interlayer bonding.

The new phase with interlayer bonding remains stable upon discharge of the Li atoms. The occurrence of irreversible phase transitions during the first charge/discharge cycle has been observed in other electrode materials, and if the resulting phase is stable upon further cycling it can be used in devices. It would be of interest to examine the effects of loading and discharge in this new interlayer bonded phase and hence determine its potential as use as an electrode for rechargeable Li-ion batteries.

It is interesting to highlight that intercalation to enable new polymerization pathways for phase transformations has never been explored, and it would certainly be of interest to follow our initial results with more extensive studies.

Carbon nitrides display a rich polymorphism; the initial study showed their intercalation properties to be overall similar to those of the corresponding carbon-only structures. For time constraints it was not possible to study the migration of Li in the graphitic carbon nitride phase; due to the layered structure. The presence of large interstices is expected to facilitiate Li migration with respect to graphite and hence the new materials may be promising alternative to graphite as anode materials.

In the next stage of the investigation on the graphitic CN structure, its ion exchange properties were examined. The calculations showed that the extent of deformation of the

base structure is dependent on the type of cation metal inserted in place of the protons that decorated the internal edges of the triangular cavities of the $C_6N_9H_3$ material.

These investigations showed that transition metal ions of 3+ valency (Al, Ga, and In) are too small to fit within the large holes of the structure and caused significant deformations. This was also the case for Cd^{2+}. On the other hand, the Ba^{2+} and Li^{+} ions both fit into the internal vacancies well. Such ions can be used to enable ion exchange and catalytic processes with the key determinant being the type of metal already in the structure and with due note given to steric considerations.

Chapter 6 presented a full explanation of Li intercalation into $Y_2Ti_2O_5S_2$ structure of Ruddlesden-Popper (R-P) type n=2 phase. The structure contains perovskite-like layers Ti_2O_5 separated by rock salt layersY_2S_2. The oxygen ions are exclusively located in the perovskite layer while the sulphide ions occupy the sites in the rock salt layer. The structure contains Ti ions which are reduced from 4+ to 3+ oxidation state during the Li intercalation. The Li intercalation occurs in the centre of the Ti_2O_5 layers, in the empty sites of the perovskite block.

It is found that the structural changes are consistent with Ti being progressively reduced on increasing Li content.

Intermediate Li concentrations cause a reduction of symmetry from tetragonal to orthorhombic consisting with experimental observation.

The material appears unsuitable as electrodes for Li-ion batteries: the calculated Li intercalation energy (ranging from -2.4 eV to -1.7 eV) depending on the Li content is too high for anode, and too low for cathode applications. In addition, structural changes of nearly 8% in each lattice parameter are too large, and would cause considerable structural stresses upon cycling intercalation and deintercalation of Li.

References

1 M. Winter, R. J. Brodd, Chem. Rev. 104, (2004), 4245

2 Picture from http://chemistry.about.com/od/imagesclipartstructures/ig/Science-Clipart/Battery.--0q.htm, (April-2011)

3 J. O'M Bockris , G. J. Hills, D. Inman, L. Young, J. Sci. Instrum. 33, (1956), 438

4 M. S. Whittingham, Chem. Rev. 104, (2004), 4271

5 J. B. Kejha, U.S. Patent No. 5529707 (1996)

6 E. Freg, R. J. Gummow, A. De Kock, M. M. Thackeray, J. Electrochem. Soc. 141, (1994), 147

7 T. Ohzuku, A. Ueda, Solid State Ionics, 69, (1994), 201

8 K. Sawai, Y. Iwakoshi, T. Ohzuku, Solid State Ionics, 69, (1994), 273

9 M. M. Thackeray, W. I. F. David, P. G. Bruce, G. B. Goodenough, Mater. Res. Bull. 18, (1983), 461

10 J. M. Tarascon, D. Guyomard, Solid State Ionics, 69, (1994), 222

11 J. M. Tarascon, W. R. Mckinnon, F. Coowar, T. N. Bowmer, G. Amatucci, D. Guyomard, J. Electrochem. Soc. 141, (1994), 1421

12 I. Nakai, T. Nakagome, Electrochem. Solid State Lett. 1, (1998), 259

13 R. Kanno, T. Shirane, Y. Inaba, Y. Kawamoto, J. Power Sources, 68, (1997), 145

14 R. Kanno, T. Shirane, Y. Kawamoto, Y. Takeda, M. Takano, M. Ohashi, Y. Yamaguchi, J. Electrochem. Soc. 143, (1996), 2435

15 R. Kanno, T. Shirane, Y. Kawamoto, Abstract of the 8th international meeting on lithium batteries, Electrochemical Society, Pennington, NJ, 8, (1996), abstract 133

16 M. S. Whittingham, U.S. Patent 4, 049, (1996), 887

17 A. H. Thompson, M. S. Whittingham, Mater. Res. Bull. 12, (1977), 741

18 A. J. Jacobson, M. S. Whittingham, U.S. Patent 4, 143, (1978), 213

19 M. S. Whittingham, Prog. Solid State Chem. 12, (1978), 41

20 B. Ulrich, N. L. Allinger, Molecular Mechanics, American Chemical Society, Washington, D.C, (1982), 40

21 S. S. Mallajosyula, A. D. MacKerell, Jr., J. Phys. Chem. B 115 (38), (2011), 11215

22 A. D. Case, T. E. Cheatham, T. Darden, H. Gohlke, R. Luo, K. M. Merz, J. A. Onufriev, C. Simmerling, B. Wang, R. J. Woods, J. Comput. Chem. 26, (2005), 1668

23 A. Szabo, N. S. Ostlund, Modern Quantum Chemistry: Introduction to Advanced Electronic Structure Theory. McGraw-Hill, New York, (1989), 191

24 M. Born, J.R Openheimer, Ann.Phys, 84, (1927), 457

25 D. O. Hayward, Quantum Mechanics for chemists, Royal Society of Chemistry, Cambridge, (2002), 3

26 J. C. Slater, Phys. Rev. 36, (1930), 57

27 F. Jensen, Introduction to Computational Chemistry, Wiley, Denmark, (1999), 126

28 U. V. Barth, Physica. Script. 109, (2004), 9

29 P. Hohenberg, W. Kohn, Phys. Rev. 136, (1964), 864

30 A. R. Leach, Molecular Modelling: Principles and Applications, Prentice Hall, (2001), 68

31 W. Kohn, L. J. Sham, Phys. Rev. 140, (1965), 1133

32 V. L. Moruzzi, J. F. Janak, A. R. Williams, Calculated Electronic properties of Metals, Pergamon, New York, (1978), 10

33 R. G. Parr, W. Yang, Density Functional Theory of Atoms and Molecules, Oxford University Press, New York, (1989), 47

34 P. A. M. Dirac, Proc. Camb. Phil. Soc. 26, (1930), 376

35 J. P. Perdew, A. Zunger, Phys. Rev. 23, (1981), 5048

36 J. P. Perdew, Phys. Rev. 33, (1986), 8822

37 J. P. Perdew, Y. Wang, Phys. Rev. 33, (1986), 8800

38 J. P. Perdew, Y. Wang, Phys. Rev. 45, (1992), 13244

39 A. D. Becke, Phys. Rev. 38, (1988), 3098

40 F. A. Hamprecht, A. J. Cohen, D. J. Tozer, N. C. J. Handy, J. Chem. Phys. 109, (1998), 6264

41 J. P. Perdew, K. Burke, Y. Phys. Rev. B 54, (1996), 16533

42 A. D. Becke, J. Chem. Phys. 98, (1993), 5648

43 F. Corà, M. Alfredsson, G. Mallia, D. S. Middlemiss, W. C. Mackrodt, R. Dovesi, R. Orlando, Struct. and Bonding, Berlin, 113 (2004) 171

44 M. Born, T. Von Karman, Phys. Z. 13, (1912), 297

45 M. P. Allen, D. J. Tildesley, Computer Simulations of Liquid, Oxford Science, Oxford, (1987), 208

46 F. Bloch, Phys. Z. 52, (1928), 555

47 F. Jensen, Introduction to Computational Chemistry, Wiley, Chichester, UK, (1999), 192

48 L. P. Bouckaert, R. Smoluchowski, E. Wigner, Phys. Rev. 50, (1936), 58

49 J. C. Philips, L. Kleinman, Phys. Rev. 136, (1959), 287

50 D. R. Hamann, M. Schluter, C. Chiang, Phys. Rev. Lett. 43, (1979), 1494

51 M. T. Yin, M. L. Cohen, Phys. Rev. B 25, (1982), 7403

52 G. Kresse, J. Hafner, J. Physics-Condensed Matter. 6, (1994), 8245

53 B. Z. Christiansen, K. West, T. Jacobson, S. Atlung, Solid State Ionics, 28, (1988), 1176

54 M. A. Reddy, M. S. Kishore, V. Pralong, U.V. Varadaraja and B. Raveau, Electrochem. Solid State Let. 10, (2007), A29

55 M. A. Reddy, M. S. Kishore, V. Pralong, V. Keignaert, U. V. Varadaraju, B. Raveau, Electrochem. Commun. 8, (2006), 1299

56 D. W. Murphy, R. J. Cava, S. M. Zahurak, A. Santoro, Solid State Ionics, 9-10, (1983), 413

57 E. Baudrin, S. Cassaignon, M. Koelsch, J. P. Jolivet, L. Dupont, J. M. Tarascon, Electrochem. Commun. 9, (2007), 337

58 W. J. Macklin, R. J. Neat, Solid State Ionics, 53, (1992), 694

59 M. V. Koudriachova, N. M. Harrison, S. W. de Leeuw, Phys. Rev. Lett., 86, (2001), 1275

60 M. V. Koudriachova, N. M. Harrison and S. W. de Leeuw, Phys. Rev. B 65, (2002), 235423

61 M. V. Koudriachova, N.M. Harrison, S. W. de Leeuw, Phys. Rev. B 69, (2004), 54106

62 M. V. Koudriachova, S. W. de Leeuw, N. M. Harrison, Chem. Phys. Lett. 371, (2003), 150

63 M. V. Koudriachova, N. M. Harrison, S. W. de Leeuw, Solid State Ionics, 174, (2004), 829

64 J. Muscat, V. Swamy, N. M. Harrison, Phys. Rev. B 65, (2002), 224112

65 M. C. Payne, M. P. Teter, D. C. Allan, T.A. Arias, J. D. Joannopoulos, Rev. Mod. Phys. 64, (1992), 1045

66 CASTEP 3.9 Academic version, licensed under the UKCP-MSI agreement,1999

67 J. P. Perdew, Phys. Rev. B 34, (1986), 7406

68 D. Vanderbilt, Phys. Rev. B 41, (1990), 7892

69 V. W. H. Baur, Acta Crystallogr. 14, (1961), 214

70 M. Armand, J. M. Tarascon, Nature 451, (2008), 652

71 M. S. Whittingham, Dalton Trance. 40, (2008), 5424

72 M. R. Palacin, Chem. Soc. Rev. 38. (2009), 2565

73 A. R. Armstrong, G. Armstrong, J. Canales, and P. G. Bruce, Chem. Commun. 17, (2005), 862

74 A. Zhukov, M. Kalbac, L. Kavan, I. Exnar, M. Gratzel, Chem. Mater. 17, (2005), 1248

75 M. C. Tsai, J. C. Chang, H. S. Sheu, H. T. Chiu, C. Y. Lee,. Chem. Mater. 21, (2009), 499

76 D. Deng, M. G. Kim, J. Y. Lee, J. Cho, Energy Environ. Sci. 2, (2009), 818

77 Y. F. Wang, M. Y. Wu, W. F. Zhang, Electrochim. Acta. 53, (2008), 7863

78 M. Wilkening, C. Lyness, A. R. Armstrong, P. G. Bruce, J. Phys. Chem. C 113, (2009), 4741

79 R. J. Cava, D. W. Murphy, S. M. Zahurak, A. Santoro, R.S. Roth;. J. Solid State Chem. 53, (1984), 64

80 C. R. A. Catlow, A. N. Cormack, F. Theobald, Acta Crystallogr, Sect. B 40, (1984), 195

81 D. Panduwinata, J. D. Gale, J. Mater. Chem. 19, (2009), 3931

82 G. Nuspl, K. Yoshikawa, T. Yamabe, J. Mater. Chem. 7, (1997), 2529

83 M. V. Koudriachova, M. Mater, Electrochem. Soc. 16(42), (2009),63

84 A. Corinne, S. C. Parker, M. S. Islam, Chem. Mater. 21, (2009), 4778

85 G. Kresse, J. Hafner, Phys. Rev. B 49, (1994), 14251

86 G. Kresse, D. Joubert, Phys. Rev. B 59, (1999), 1758

87 T.P. Feist, P.K. Davies, J. Solid State Chem. 101, (1992), 275

88 L. Brohan, R. Marchand, Solid State Ionics. 9-10, (1983),419

89 M. V. Koudriachova, N. M. Harrison, S. W. deLeeuw, Solid State Ionics. 157, (2003), 35

90 M. Wagemaker, A. P. M. Kentgens, F. M. Mulder, Nature, 418, (2002), 397

91 C. L. Olson, J. Nelson, M. S. Islam, J. Phys. Chem. B 110, (2006), 9995

92 M. Wagemaker, D. Lützenkirchen-Hecht, A.A. van Well, and R. Frahm, J. Phys. Chem. B 108, (2004), 12456

93 A. Robert Armstrong, C. Arrouvel, V. Gentili, S.C. Parker, M. S. Islam, P. G bruce, Chem. Mater. 22, (2010), 6426

94 M. Deifallah, P. F. McMillan, F. Corà; J. Phys. Chem. C, 112 (14), 2008, 5447

95 A. Y. Liu, R. M. Wentzcovitch, Phys. Rev. B 50, (1994), 10362

96 J. E. Lowther, Phys. Rev. B 59, (1999), 11683

97 Z. Zhang, K. Leinenweber, M. Bauer, L. A. J. Garvie, P. F McMillan, G. H Wolf, J. Am. Chem. Soc. 123, (2001), 7788

98 F. P. Bundy, W. A. Bassett, M. S. Weathers, R. J. Hemley, H. K. Mao, A. F. Goncharov, Carbon, 34, (1996), 141

99 F. P. Bundy, J. S. Kasper, J. Chem. Phys. 46, (1967), 3437

100 S. Scandolo, M. Bernasconi, G. L. Chiarotti, P. Focher, E. Tosatti, Phys. Rev. Lett. 74, (1995), 4015

101 S. Fahy, S. G. Louie, M. L. Cohen, Phys. Rev. B 35, (1987), 7623

102 P. F. McMillan;: Chem. Commun. 8, (2003), 919

103 B. Jürgens, E. Irran, J. Senker, P. Kroll, H. Müller, W. Schnick, J. Am. Chem. Soc. 125, (2003), 10288

104 D. M. Teter, R. Hemley, J. Science, 271, (1996), 53

105 M. Todd, J. Kouvetakis, T. L. Groy, D. Chandrasekhar, D. J. Smith, P. W. Deal, Chem. Mater. 7, (1995), 1422

106 J. Kouvetakis, A. Bandari, M. Todd, B. Wilkens, N. Cave, Chem. Mater. 6, (1994), 811

107 G. Demazeau, H. Montigaud, B. Tanguy, M. Birot, J. Dunogues, Rev. High Pressure Sci. Technol. 7, (1998), 1345

108 G. H. Wolf, M. Bauer, K. Leinenweber, L. A. J. Garvie, Z. Zhang, Frontiers of High Pressure Research II ; Application of High Pressure to Low Dimensional Novel

Electronic Materials, NATO Adv. Res. Workshop. H. D. Hochheimer, B. Kuchta, P. K. Dorhent, J. L. Yarger, Kluwer Academic Press, Boston (2001), 27

109 M. D. Segall; P. J. D. Lindan; M. J. Probert; C. J. Pickard; P. J. Hasnip; S. J. Clark; M. C. Payne;: J. Phys. Cond. Matt. 14, (2002), 2717

110 CASTEP(5.0) UK academic research groups licensed under the terms of an agreement between STFC, York University (for UKCP) and Accelrys Inc, 2010.

111 D. Vanderbilt, Phys. Rev. B 41, (1990), 7892

112 M. Deifallah, "A computational study of the structure and properties of Aluminophosphates and Carbon Nitrides", PhD Thesis, (2009), 207

113 A. F. Goncharov, M. R. Manaa, M. J. Zaug, R. H. Gee, L. E. Fried, W. B. Montgomery, Phys. Rev. Lett. 94, (2005), 065505

114 M. Benoit, A. H. Romero, D. Marx, Phys. Rev. Lett. 89, (2002), 145501

115 R. Caracas, Phys. Rev. Lett. 101, (2008), 085502

116 M. Benoit, M. Bernasconi, P. Focher, M. Parrinello; Phys. Rev. Lett. 76, (1996), 2934

117 T. Glowiak, Z. Malarski, L. Sobczyk, E. Grech, J. Mol. Struct. 270 , (1992), 441

118 H. A. Staab, T. Saupe, C. Krieger, Angew. Chem. Int. Ed. Engl. 22, (1983), 731

119 K. Wozniak, T.M. Krygowski, B. Kariuki, W. Jones, E. Grech, J. Mol. Struct. 240, (1999), 111

120 C. C. Wilson, L. H. Thomas, C. A. Morrison, Chem. Phy. Lett. 381, (2003), 102

121 H. W. Kroto, J. R. Heath, S. C. O'Brien, R. F. Curl, R. E. Smalley, Nature, 318, (1985), 162

122 S. Iijima, Nature, 354, (1991), 56

123 A. Thess, R. Lee, P. Nikolaev, H. Dai, P. Petit, J. Robert, C. Xu, Y.H. Lee, S.G. Kim, A.G. Rinzler, D.T. Colbert, G.E. Scuseria, D. Tomanek, J.E. Fischer, and R. Smalley, Science 273, (1996), 483

124 C. Journet, W.K. Maser, P. Bernier, A. Loiseau, M. Lamydela, Chapelle, S. Lefrant, P. Deniard, R. Lee, J. E. Fischer, Nature, 388, (1997), 756

125 O. Zhou, R. M. Fleming, D.W. Murphy, C. H. Chen, R. C. Haddon, A. P. Ramirez, S. H. Glarum, Science Magazine, 263, (1994), 1744

126 E. Frackowiak, S. Gautier, H. Gaucher, S. Bonnamy, F. Béguin, Carbon, 37, (1999), 61

127 Y. Saito, T. Y. Oshikawa, S. Bandow, M. Tomita, T. Hayashi, Phys. Rev. B 48, (1993), 1907

128 S. Suzukiand, M. Tomita, J. Appl. Phys. 79, (1996), 3739

129 D. Guerard, A. Herold, Carbon, 13, (1975), 337

130 R. Yazami, P. H. Touzain, J. Power Sources 9, (1983), 365

131 N. Dumas, A. Herold, C.R. Acad. Sci. Paris C 268, (1969), 373

132 W. Rüdorff and E. Schulze, Z. Angew. Chem. 66, (1954), 305

133 J. R. Dahn, Phys. Rev. B 44, (1991), 9170

134 R. Fong, U. Von Sacken, J. R. Dahn, J. Electrochem. Soc. 137, (1990), 2009

135 G. Maureen, F. Henn, Encyclopedia of Nanoscience and Nanotechnology 2, 773, Ed. H.S. Nalwa, American Scientific Publisher, Los Angeles (2003), 607

136 V. Meunier, J. Kephart, C. Ronald, J. Bernholc, Phys. Rev. Lett. 88, (2002), 075506

137 J. Young, H. J. Liu, C. T. Chan, Phys. Rev. B 66, (2002), 073415

138 S. Yamazaki, T. Hashimoto, T. Iriyama, Y. Mori, H. Shiroki, N. Tamura, J. Mol. Struct. 441, (1998), 165

139 K. Gurein, M. menetrier, A. Fevrier-Bouvier, S. Flandrois, B. simon, and P. Biensan, Solid State Ion. 127, (2000), 187

140 S. Yata, M. Kinoshita, M.Komori, N. Ando, T. Kashiwamura, T. Harda, K. Tanaka, Tyamabe, Synth. Met. 62, (1994), 153

141 P. F. McMillan, 24, (2004), 67

142 Picture from http://en.wikipedia.org/wiki/Porphyrin (March- 2011)

143 K. Rezouali, M. A. Belkhir, J. Bai, Physica E 41, (2008), 254

144 S. Geller, J. Chem. Phys. 33, (1960), 676

145 Y. Zhao, Z. Zhang, Z. Wu, H. Dang; Langmuir 20, (2004), 27

146 R. W. G. Wykoff, Crystal Structures, John Wiley& Sons, New York, (1963)

147 P. G Bruce, Chem. Commun. (1997), 1817

148 D. W. Murphy, S. A. Sunshine, S. M. Zahurak, NATO Adv. Sci. Inst. Ser. B 172, (1987), 173

149 D. W. Murphy, NATO Adv. Sci. Inst. Ser. E, 101, (1985), 181

150 D. W Murphy, Advances in the Synthesis and Reactivity of Solids: A Research Annual, JAI Press: Greenwich, CT, l, (1991), 237

151 J. Rouxel, M. Tournoux, Solid State Ionics, 84, (1996), 141

152 Picture from http://www.soton.ac.uk/~solids/overview.htm (March-2011)

153 A. M. Chippindale, P. G. Dickens, A. V. Powell, Prog. Solid State Chem. 21, (1994), 133

154 B. W. Eichhorn, In Progress in Inorganic Chemistry, K. D. Karlin, Ed., Wiley, New York, 42, (1994), 139.

155 R. E. Schaak, T. E. Mallouk, Chem. Mater. 12, (2000), 3429

156 R. K. Li, C. Greaves, Phys. Rev. B 62, (2000), 3811

157 S. G. Denis, S. J. Clarke, Chem. Commun. 22, (2001), 2356.

158 J. P. Perdew, Phys. Rev. B 34, (1986), 7406

159 D. Vanderbilt, Phys. Rev. B 41, (1990), 7892

160 S. G. Denis, S. J. Clarke; Chem. Commun., 2001, 2356-2357

161 F. Corà, M. G. Stachiotti, C. R. A. Catlow, J. Phys. Chem. B 101 (20), (1997), 3945

162 F. Corà, C. R. A. Catlow, Faraday Discuss. 114, (1999), 421